

Interferometric Synthetic Aperture Radar Coherence Imagery for Land Surface Change Detection

Submitted to the University of London
for the degree of

Doctor of Philosophy

by

Hoonyol Lee

T. H. Huxley School of Environment, Earth Sciences and Engineering
Imperial College of Science, Technology and Medicine
University of London
United Kingdom

February 2001

To the memory of my father and brother, Byongseop and Hanyeol.

Abstract

Interferometric synthetic aperture radar (InSAR) coherence imagery is a powerful tool for surface random change detection and environmental monitoring. In this study, the methodology of InSAR coherence imagery has been investigated, developed and evaluated through several case studies in the Sahara desert, Algeria and southeast of Spain, using ERS-1/2 SAR data.

InSAR coherence imagery in the Sahara desert reveals various active surface changes in hyper-arid, flat and stable regions, such as movement of sand dunes, ephemeral lakes, river channels and human activities, which are not well detected by other remote sensing methods. An anomalous case in a gully area leads to the study of topographic decorrelation and the development of a new analytical technique: *ratio coherence imagery*. A modified spatial decorrelation function of baseline and terrain slope explains the total topographic decorrelation phenomenon occurring within a slope range defined by *critical terrain slopes* where two SAR signals decorrelate completely regardless of surface stability. The ratio coherence imagery can discriminate spatial decorrelation from temporal decorrelation effectively to improve the accuracy of coherence imagery interpretation.

As a more challenging application for InSAR coherence imagery, the study in semi-arid, mountainous and actively eroding regions in Almeria, Spain provides evidence of rapid erosion on unconsolidated marls and human-disturbance from massive cultivation. Decoherence features with rainfall events in Granada, Spain reveal complicated relationship between coherence and various environmental factors such as vegetation, wind, surface moisture and erosion. The Granada case study triggered the concern of topographic phase fringe effect as a nonstationarity source to degrade coherence. This effect is numerically analysed, and a new method is developed for topographic phase-free, unbiased coherence estimation by using multi-pass differential InSAR (DInSAR) technique. This methodology produces a new by-product of DInSAR, so called the *differential coherence* in addition to the differential interferogram. An example shows up to 16% coherence enhancement selectively on steep slopes.

Acknowledgements

The whole research and this thesis might have been impossible without help of many people. First, I would like to thank my supervisor Dr. Jian Guo Liu. He has been not only an excellent supervisor but also a guardian throughout my first three-year adventure outside homeland, Korea. I also would like to thank:

Mr. John McM Moore for encouragement as a second supervisor.

Professor Howard Zebker in Stanford University for his help on SAR and InSAR software development, which initiated the SAR research in our research group.

Dr. Hiroshi Hanaizumi of Hosei University in Japan for his effort in development of SAR and InSAR software package during his visit to Imperial College from April 1997 to February 1998.

Dr. Yosuke Ito of Takamatsu National College of Technology in Japan for his help upgrading the in-house SAR and InSAR software during his visit to Imperial College from July 1999 to March 2000.

Anna Black and Timothy Pearson for their contributions to image interpretation in their MSc thesis projects.

Members of the Remote Sensing Unit, Imperial College: especially for Dr. Philippa J. Mason and Alex M. Davis for various help and friendship.

Andy Smith in Phoenix Systems and Associates Ltd. for valuable discussion on data processing in PULSAR software.

Dr. Jianguo Chen and Professor Hu of China University of Geosciences for valuable discussion during their visit to Imperial College from April 1999 to September 1999.

This research was funded from Korean Ministry of Education scholarship (1997-2000), Overseas Research Scholarship (ORS) award (1997-2000), and British Chevening Scholarship (2000-2001). The computing and image processing facilities were provided by the University of London Intercollegiate Research Services

(ULIRS). The ERS-1 SAR scenes of the Sahara desert were offered by NPA Group. The ERS-1/2 SAR data of Spain were provided by European Space Agency (ESA) via AO3-113 project. Other valuable information on SAR and InSAR research was obtained through Alaska SAR Facility (ASF) and ESA online.

This work would have been impossible without love of my wife, Miyong Choi, my son, Jejin, my mother, Eunsim Bae, and our families.

Contents

| | |
|---|-----------|
| Abstract | 3 |
| Acknowledgements | 4 |
| List of Figures | 9 |
| List of Tables..... | 13 |
| Chapter 1: Introduction..... | 14 |
| 1.1 The Problem Definition | 14 |
| 1.2 The Objectives of the Research | 17 |
| 1.3 Approach | 18 |
| 1.3.1 SAR Data Selection and Image Processing Facilities | 18 |
| 1.3.2 Case Study of InSAR Coherence Imagery in the Sahara Desert, Algeria – Flat, Hyper-arid and Stable Land Surface | 19 |
| 1.3.3 Spatial Topographic Decorrelation Function and Ratio Coherence Imagery..... | 20 |
| 1.3.4 Another Case Study for InSAR Coherence Imagery in Almeria and Granada regions, Southeast of Spain – Mountainous, Semi-arid and Unstable Land Surface..... | 21 |
| 1.3.5 Topographic Phase-free Coherence: <i>Differential Coherence</i> | 22 |
| 1.4 The Structure of the Thesis..... | 23 |
| 1.5 Summary of the Main Achievements of the Thesis | 24 |
| Chapter 2: Review of Synthetic Aperture Radar, Interferometry, and Coherence Imagery..... | 28 |
| 2.1 Synthetic Aperture Radar | 29 |
| 2.1.1 History of SAR Systems | 29 |
| 2.1.2 SAR Imaging Geometry | 33 |
| 2.2 SAR Interferometry | 35 |
| 2.2.1 History of InSAR | 35 |
| 2.2.2 Definitions | 36 |
| 2.2.3 Topographic Mapping..... | 37 |
| 2.2.4 Coherent Surface Displacement Measurement - DInSAR..... | 41 |
| 2.2.5 Random Surface Change Detection – InSAR Coherence Imagery | 43 |
| 2.3 Phase Statistics of InSAR..... | 44 |
| 2.3.1 The System Model..... | 44 |
| 2.3.2 Statistical Properties of the Interferometric Phase | 45 |
| 2.4 Decorrelation Factors in InSAR | 50 |
| 2.4.1 Thermal Noise..... | 50 |
| 2.4.2 Errors from SAR and InSAR Data Processing | 51 |
| 2.4.3 Spectral Envelope Misalignment | 55 |
| 2.4.4 Volume Scattering | 57 |
| 2.4.5 Temporal Decorrelation..... | 57 |
| Chapter 3: Principles and Algorithms of SAR and InSAR Data Processing for Coherence Imagery..... | 59 |
| 3.1 Introduction | 59 |
| 3.2 SAR Compression and Coregistration..... | 62 |
| 3.2.1 Range Compression | 62 |
| 3.2.2 Azimuth Compression | 66 |
| 3.2.3 Coregistration Offset Functions | 73 |

| | | |
|---|--|------------|
| 3.3 | InSAR Coherence Image Generation | 74 |
| 3.3.1 | Earth Flattening - System Geometric Phase (ϕ_0) Removal | 75 |
| 3.3.2 | Range-varying Spectral Filtering | 76 |
| 3.3.3 | Coherence Calculation | 77 |
| 3.4 | Summary | 78 |
| Chapter 4: Land Surface Change Detection in the Sahara Desert, Algeria using InSAR Coherence Imagery | | 79 |
| 4.1 | Introduction | 79 |
| 4.2 | The Study Area | 80 |
| 4.3 | Data Processing and Evaluation | 82 |
| 4.3.1 | Coherence Image Generation | 82 |
| 4.3.2 | Evaluation | 83 |
| 4.4 | Image Interpretation for Change Detection | 85 |
| 4.4.1 | Interpretation Principle | 85 |
| 4.4.2 | Sand Movement | 86 |
| 4.4.3 | Ephemeral Lakes and Water Bodies | 89 |
| 4.4.4 | Drainage Pattern and Erosion | 93 |
| 4.4.5 | Gully Features – Radar-facing Slopes | 96 |
| 4.4.6 | Geophysical Survey Lines | 99 |
| 4.5 | Discussion | 102 |
| 4.5.1 | Advantages and Potentials of InSAR Coherence Imagery | 102 |
| 4.5.2 | Limitations | 103 |
| 4.6 | Summary | 104 |
| Chapter 5: Analysis of Topographic Decorrelation in SAR Interferometry using Ratio Coherence Imagery | | 106 |
| 5.1 | Introduction | 106 |
| 5.2 | Theory | 108 |
| 5.2.1 | Spatial Decorrelation Function of Baseline and Topography | 108 |
| 5.2.2 | Critical Terrain Slope (or Critical Incidence Angle) | 113 |
| 5.2.3 | Ratio Coherence Imagery: A New Analytical Imagery using Two Coherence Images .. | 115 |
| 5.2.4 | Decorrelation from Volume Scattering | 118 |
| 5.3 | Case Studies of Ratio Coherence Imagery in the Sahara Desert, Algeria | 120 |
| 5.3.1 | Topographic Decorrelation Effects in the Gully Area | 122 |
| 5.3.2 | Discrimination of Topographic and Temporal Decorrelation: Ephemeral Rivers vs. Radar-facing Slopes | 124 |
| 5.3.3 | Rapid Decorrelation from Temporal Change and Volume Scattering on Sand Dunes ... | 126 |
| 5.4 | Summary | 128 |
| Chapter 6: Erosion, Land-use and Change Detection in SE Spain using InSAR Coherence Imagery | | 130 |
| 6.1 | Introduction | 130 |
| 6.2 | Case I: Rapid Erosion along the Rio de Aguas Valley | 131 |
| 6.2.1 | Interpretation of the Coherence Features | 132 |
| 6.2.2 | Ratio Coherence Imagery and Analysis of the Topographic Decorrelation | 134 |
| 6.3 | Case II: Massive Plantation and Decoherence | 143 |
| 6.4 | Case III: A Rainfall Event in the Granada Scene | 148 |
| 6.4.1 | Vegetation & Wind | 149 |
| 6.4.2 | Surface Moisture Change | 151 |
| 6.4.3 | Rainfall/Erosion | 154 |
| 6.4.4 | Bias in Coherence Estimation from Topographic Phase Fringes | 154 |
| 6.4.5 | Interpretation and Discussion | 155 |
| 6.5 | Summary | 170 |

| | |
|--|------------|
| Chapter 7: Topographic Phase-free Coherence Estimation for SAR Interferometry | 172 |
| 7.1 Introduction | 172 |
| 7.2 Coherence Estimation for a Stationary Scene | 173 |
| 7.2.1 Stationary and Ergodic Random Processes | 174 |
| 7.2.2 Stationary and Ergodic Coherence Estimation..... | 177 |
| 7.3 Coherence Estimation for a Nonstationary Scene | 180 |
| 7.3.1 Nonstationary Random Process and the Product Model..... | 180 |
| 7.3.2 Coherence Estimation by Removing the Deterministic Phase..... | 181 |
| 7.4 Topographic Phase-free, Unbiased Coherence Estimation | 184 |
| 7.4.1 Simulation of Coherence Degradation from Topographic Phase Fringes..... | 184 |
| 7.4.2 Differential Coherence..... | 190 |
| 7.4.3 Phase Unwrapping | 191 |
| 7.5 Application Experiment..... | 195 |
| 7.6 Summary..... | 201 |
| Chapter 8. Conclusions and Recommendations | 202 |
| 8.1 Conclusions | 202 |
| 8.2 Recommendations for Future Study..... | 207 |
| 8.2.1 Laboratory Experiments of Coherence Change from Rainfall /Erosion | 207 |
| 8.2.2 The Arrival of New SAR Systems | 210 |
| References..... | 211 |
| Appendix A. Mathematical Symbols | 227 |
| Appendix B: Abbreviations and Acronyms | 231 |

List of Figures

| | |
|--|-----|
| Figure 1.1 The locations of the ERS-1/2 SAR scenes used for the case studies. The square boxes (100 km × 106 km) represent the location of scenes named as GRA, ALM, and ALG, respectively..... | 26 |
| Figure 2.1 SAR imaging geometry (Olmsted, 1993)..... | 34 |
| Figure 2.2 InSAR configuration. | 39 |
| Figure 2.3 SAR imaging models. (a) Two-step linear filter model. (b) Single filter model. (c) The formation of a SAR interferogram. (Just and Bamler, 1994) | 46 |
| Figure 2.4 (a) The $pdf(\phi)$ of the interferometric phase for $\phi_0 = 0$ and different values of ρ . (b) The phase standard deviation σ_ϕ versus ρ . (Bamler and Hartl, 1998; Just and Bamler, 1994)..... | 49 |
| Figure 3.1 Interferometric SAR processing steps: Raw data to coregistered single look complex (SLC) images. | 60 |
| Figure 3.2 Interferometric SAR processing steps: Coregistered SLCs to InSAR products. The steps in bold box will be described in Chapter 7..... | 61 |
| Figure 4.1 Study area: Landsat TM band 421 in RGB (100 km × 106 km)..... | 81 |
| Figure 4.2 Comparison of coherence levels between the three coherence images.... | 84 |
| Figure 4.3 Dune boundary definition and mobile sand detection. (a) Landsat TM band 421 in RGB. db: barchan dune, dl: linear dune. (b) Multi-look amplitude image of ALG1 scene. (c) ALG12_COH: the coherence image of 35-day separation. (d) ALG23_COH: the coherence image of 350-day separation..... | 88 |
| Figure 4.4 Dune migration and change in ephemeral lakes. (a) Colour composite of ALG12_COH, ALG23_COH, and ALG13_COH in RGB. (b) Colour composite of Landsat TM band 421 in RGB. | 91 |
| Figure 4.5 The spectral and coherence properties of an ephemeral lake. (a) TM band 4. (b) TM band 6. (c) ALG12_COH. (d) ALG23_COH. | 92 |
| Figure 4.6 Average monthly precipitation from September 1992 to September 1993 for the study area in the Sahara desert (E7°-9°, N27°-28°) (Rudolf <i>et al.</i> , 1994; GPCC, 1998). | 93 |
| Figure 4.7 Drainage channels. Two major rivers in the region are not visible in (a) the 35 day separation coherence image ALG12_COH but clearly shown in (b) the 350 day separation coherence image ALG23_COH as decoherence features. The boxed area shows a controversial case: low coherence in ALG12_COH but high coherence in ALG23_COH. | 95 |
| Figure 4.8 Gully features – decorrelation on radar-facing slopes. (a) ALG12_COH. (b) ALG23_COH. (c) Colour composite of ALG12_COH, ALG23_COH, and ALG13_COH in RGB. (d) SAR intensity image of ALG2 scene..... | 98 |
| Figure 4.9 Geophysical (seismic) survey lines. (a) ALG12_COH. (b) ALG23_COH. (c) SAR 4-look intensity image of ALG3. (d) Interpretation of linear features..... | 101 |

| | | |
|------------|---|-----|
| Figure 5.1 | Simplified InSAR configuration..... | 109 |
| Figure 5.2 | Spatial decorrelation $\rho_{spatial}$ with $B_{\perp} = 100m$ (upper curve) and $B_{\perp} = 300m$ (lower curve) in case of ERS SAR ($\theta_i^0 = 23^\circ$)..... | 113 |
| Figure 5.3 | Critical terrain slopes α_c as a function of baseline B_{\perp} . Note that the width of the slope of total topographic decorrelation increases with B_{\perp} | 114 |
| Figure 5.4 | Spatial ratio coherence ($\eta_{spatial} = \rho_{spatial}^{13} / \rho_{spatial}^{12}$). Note the abnormally high value within the zone of critical terrain slope centred at the nominal incidence angle of 23° | 117 |
| Figure 5.5 | Topographic decorrelation effect in a gully area (8 km \times 8 km). (a) SAR amplitude image (ALG3), (b) coherence image ALG12_COH with 35 days separation and 263m of B_{\perp} , (c) coherence image ALG23_COH with 350 days separation and 105m of B_{\perp} , and (d) ratio coherence image ALG23_COH/ALG12_COH. The low coherence along the gully edges in the coherence images (b) and (c) could be easily mistaken as a temporal decorrelation effect. In the ratio coherence image (d), it is clear that the total topographic decorrelation effects along the radar-facing slopes are dominant and highlighted as bright features over a grey background..... | 123 |
| Figure 5.6 | An example of discriminating the total topographic decorrelation from the temporal decorrelation features (13 km \times 13 km). (a) SAR amplitude image (ALG3), (b) coherence image ALG12_COH with 35 days separation and 263m of B_{\perp} , (c) coherence image ALG23_COH with 350 days separation and 105m of B_{\perp} , and (d) ratio coherence image ALG23_COH/ALG12_COH. Two different decorrelation effects are not distinguishable from each other in both coherence images (b) and (c), though the gradually decreasing coherence along major river channels is obvious. In the ratio coherence image (d), these are clearly discriminated as dark river channels of temporal decorrelation (upper left part) and bright radar-facing slopes of the total topographic decorrelation (middle to right) on a stable background in grey..... | 125 |
| Figure 5.7 | Rapid temporal decorrelation in the linear type sand dunes due to the continuously moving sand particles and volume scattering (18 km \times 18 km). (a) SAR amplitude image (ALG3), (b) coherence image ALG12_COH with 35 days separation and 263m of B_{\perp} , (c) coherence image ALG23_COH with 350 days separation and 105m of B_{\perp} , and (d) ratio coherence image ALG23_COH/ALG12_COH. The nearly zero coherence level of the sand dunes in the coherence images (b) and (c) results in random spatial distribution of bright and dark spots over a grey stable background in the ratio coherence image (d). | 127 |
| Figure 6.1 | The location map together with a simplified geological map (IGME, 1975a) of the study area of Case I (10 km \times 10 km). The large square represents the locations of the ALM whole scene (100 km \times 106 km)..... | 138 |
| Figure 6.2 | (a) Landsat TM standard false colour composite (band 432 in RGB, 1987). (b) TM NDVI image. | 139 |
| Figure 6.3 | (a) ALM23_COH. (b) ALM34_COH. (c) ALM_24_COH. (d) Colour composite of ALM23_COH in red, ALM34_COH in green and ALM_24_COH in blue. | 140 |

| | | |
|-------------|---|-----|
| Figure 6.4 | Ratio coherence imagery in Almeria, Spain. (a) Coherence image ALM23_COH with 70 days separation and 156m of B_{\perp} . (b) Coherence image ALM34_COH with 140 days separation and 20m of B_{\perp} . (c) Ratio coherence image ALM34_COH/ALM23_COH. (d) SAR amplitude image (ALM4). Complex features of decorrelation of different natures in the coherence images (a) and (b) can be clearly discriminated in the ratio coherence image (c). The curved linear features of low coherence highlighted in white are the total topographic decorrelation along the foreshortened slopes. The dark features are of gradual temporal decorrelation. The black and white noisy spots are from rapid temporal decorrelation of vegetation and agriculture, while grey indicates stable surface..... | 141 |
| Figure 6.5 | (a) The colour composite of ALM23_COH in red, ALM34_COH in green and ALM34_COH/ALM23_COH in blue. 1: Marls subject to rapid erosion. 2: Dense vegetation. 3: Gypsum. 4: Gypsum quarries and dumps. 5: Limestone. 6: Foreshortened slopes (spatial topographic decorrelation effect). (b) Field photo of rapid erosion of Marls (Photo from J. G. Liu)..... | 142 |
| Figure 6.6 | Landsat TM bands 541 in RGB and the location of case study II (20 km × 24 km). The large tilted square represents the ALM whole scene (100 km × 106 km). | 145 |
| Figure 6.7 | Coherence colour composite of ALM34_COH, ALM23_COH, and ALM12_COH in RGB respectively. | 146 |
| Figure 6.8 | Massive plantation (Field photo of southern flank of Sierra de Las, from J. G. Liu)..... | 147 |
| Figure 6.9 | Study area of Case III and Landsat TM bands 432 in RGB colour composite (28 km × 28 km). The large tilted square represents the location of GRA whole scene (100 km × 106 km). | 158 |
| Figure 6.10 | A simplified geological map of the Case III study area (28 km × 28 km; IGME, 1970)..... | 159 |
| Figure 6.11 | Landsat TM bands 531 in RGB colour composite (28 km × 28 km). Red and purple: Jurassic dolomite, limestone, and marls. Light blue: Cretaceous marls and limestone. (Yellow boxes are the locations sub scenes.)..... | 160 |
| Figure 6.12 | Coherence images and interferograms of GRA scenes (28 km × 28 km). (a) GRA12_COH, (b) GRA34_COH, (c) GRA12_INF, and (d) GRA34_INF..... | 161 |
| Figure 6.13 | (a) NDVI-Contour image. Red represents vegetation. (b) GRA12_COH-Contour image. Red represents low coherence. Contours are generated from GRA34_INF. | 162 |
| Figure 6.14 | Wind effect on a lake (11 km × 11 km). (a) GRA1 shows higher radar intensity on the lake surface than that in (b) GRA2. (c) a difference image GRA1-GRA2 that shows higher radar intensity in GRA1 on the lake surface, indicating higher wind speed in GRA1. | 163 |
| Figure 6.15 | (a) Dependence of complex dielectric constant on soil moisture. (b) Dependence of backscattering coefficient on incidence angle and soil moisture (Curlander and McDonough, 1991)..... | 164 |
| Figure 6.16 | SAR intensity images of the study area (28 km × 28 km). | 165 |

| | |
|---|-----|
| Figure 6.17 Difference of SAR intensity images (28 km × 28 km): (a) GRA1-GRA4, (b) GRA2-GRA4, (c) GRA3-GRA4, and (d) GRA2-GRA1..... | 166 |
| Figure 6.18 Decoherence from soil moisture change (9 km × 9 km): (a) GRA2-GRA1, (b) GRA12-Contour, (c) NDVI-Contour, and (d) Landsat TM bands 531 in RGB..... | 167 |
| Figure 6.19 Erosion from rainfall (6 km × 6 km): (a) GRA12_COH-Contour image indicates an area of low coherence from rainfall/erosion. (b) NDVI-Contour shows no vegetation in this area. (c) GRA2-GRA1 indicates no soil moisture change between GRA2 and GRA1. (d) Landsat TM 531 in RGB shows lithology of this area..... | 168 |
| Figure 6.20 Schematic interpretation map of identified decoherence features of GRA12_COH (28 km × 28 km). A (green): Low coherence from wind in vegetated area. B (pink): High coherence area with hard lithology. C (blue): High coherence with soft lithology. D1 (yellow): Soil moisture change in barren area. D2 (yellow): Soil moisture change in vegetated area. E (red): Erosion in barren, soft lithology... | 169 |
| Figure 7.1 Coherence bias for various number of L (Touzi <i>et al.</i> , 1999)..... | 179 |
| Figure 7.2 Coherence ρ as a function of <i>the simulated topographic phase fringe number</i> k^{sim} when window size $N=2,3,4$, and 5. | 186 |
| Figure 7.3 Fringes of the diagonal topographic phase and an averaging window (square box) that result in 10 % degradation in coherence estimation when $k^{sim} = \frac{1}{5.5N}$ | 186 |
| Figure 7.4 <i>Topographic phase fringe number</i> k^{sjs} of an InSAR system as a function of terrain slope α in the Earth-flattened interferogram, where $\theta_i^0 = 23^\circ$ and $B_\perp = 200m$ of ERS system (see Bamler and Hartl, 1998, Fig. 25 for comparison).. | 187 |
| Figure 7.5 Coherence of an InSAR system as a function of terrain slope α in the Earth-flattened interferogram where $N=4$ and $B_\perp = 200m$ of ERS system (thick curve). Thin curve is the spatial decorrelation function of terrain slope (Lee and Liu 2000, or Chapter 5). | 189 |
| Figure 7.6 Generation of differential coherence image of Granada, Spain (10 km × 9 km). (a) GRA32_COH: Coherence image between GRA3 and GRA2, (b) GRA32_INF: Interferogram of GRA3 and GRA2..... | 198 |
| Figure 7.6(continued) (c) GRA34_INF: Reference Interferogram generated from GRA3 and GRA4. (rewrapped after phase unwrapping for illustration purpose) (d) GRA32_DINF: Topographic phase-removed differential interferogram to be used as a phase term in coherence estimator to generate differential coherence. | 199 |
| Figure 7.6(continued) (e) GRA32_DCOH: differential coherence image (the final product). (f) Evaluation: a difference image between (e) and (a). It shows up to 16 % rms coherence improvement on steep terrain slopes (white), degradation in some areas due to low quality in the reference interferogram and phase unwrapping error (black), while other areas remain the same (grey)..... | 200 |

List of Tables

| | |
|---|-----|
| Table 1.1 SAR scenes of the Sahara desert, Algeria (ALG). Track 351, Frame 3051, descending orbit. (ALG1 as a master image) | 27 |
| Table 1.2 SAR scenes of Almeria, Spain (ALM). Track 237, Frame 2853, descending orbit. (ALM1 as a master image)..... | 27 |
| Table 1.3 SAR scenes of Granada, Spain (GRA). Track 051, Frame 2853, descending orbit. (GRA1 as a master image)..... | 27 |
| Table 2.1 Spaceborne SAR systems of past, current, and future..... | 32 |
| Table 4.1 Theoretical and actual coherence (ρ)..... | 82 |
| Table 4.2 Possible coherence scenarios..... | 85 |
| Table 5.1 Coherence images and the slope range of total topographic decorrelation of the Sahara Desert, Algeria data. | 121 |
| Table 5.2 Ratio coherence features in the Sahara Desert, Algeria. | 128 |
| Table 6.1 ERS SAR scenes of Almeria area. | 132 |
| Table 6.2 Coherence images and the critical terrain slopes (Almeria, Spain)..... | 135 |
| Table 6.3 Ratio coherence features in Rio de Aguas valley..... | 136 |
| Table 6.4 ERS SAR Granada scene and weather data of the city of Jaén..... | 149 |
| Table 6.5 Two ERS tandem-pair InSAR coherence images for the case study III in Granada, Spain. | 149 |
| Table 6.6 Interpretation of various decoherence features in GRA12_COH..... | 157 |
| Table 7.1 Three SAR scenes of Granada, Spain used (Track 051, Frame 2853).... | 196 |

Chapter 1: Introduction

1.1 The Problem Definition

Detection of environmental changes of the land surface is important to understand and predict the global ecosystem processes and to either avoid or minimise the potential of catastrophic environmental changes. Spaceborne remote sensing technologies provided the massive amounts of geo-spatial data required for characterising the changing ecosystem processes. The recent development of radar remote sensing technologies enabled scientists to view natural and manmade environmental changes with an aspect different from optical multi-spectral and thermal sensors. One such tool is synthetic aperture radar.

Synthetic aperture radar (SAR) is an active microwave imaging method. It provides cloud-free, all weather, day and night mapping of the scattering properties of the target surface. It achieves very high resolution from sophisticated system configuration and considerable amount of signal processing. SAR images from various systems have contributed to the understanding of the Earth and planetary surfaces using a different imaging geometry and spectral range from conventional optical sensors (Bamler and Hartl, 1998).

By combining multiple SAR images of a target area, interferometric synthetic aperture radar (InSAR) configurations can be achieved. Over the past decade, SAR interferometry has successfully demonstrated, with unprecedented spatial detail and scale, its potential in various applications, such as measurement of terrain elevation, surface motion and deformation, and detection of random land surface changes. SAR interferometry has been mainly used to obtain accurate and cost-effective surface digital elevation models (DEM). One such is the recent US spaceborne single-pass SAR interferometer, Shuttle Radar Topography Mission (SRTM), from which a global DEM can be produced from interferometric SAR data collected during 11 days orbital operation in March 2000 (Hilland *et al.*, 1998). Coherent surface movement can also be detected within an accuracy of a fraction of radar wavelength using

repeat-pass SAR acquisitions, which is called the differential SAR interferometry. It has been used to reveal the co-seismic displacement field (Massonnet *et al.*, 1993; Zebker *et al.*, 1994a), ice motion (Goldstein *et al.*, 1993), and volcanic deflation (Massonnet *et al.*, 1995; Rosen *et al.*, 1996), and land subsidence (Massonnet *et al.*, 1997) within a resolution order of mm to cm.

These achievements of SAR interferometry depend on the phase information from the complex (real and imaginary, I/Q) cross-correlation of two radar acquisitions of the same area. Besides the phase information, the amplitude information of this complex cross-correlation is called *coherence*. Coherence is a statistical measurement of the similarity of the radar interactions with the target surface between two SAR acquisitions. Coherence is sensitive to the surface change so that a half of one wavelength's rms (root mean square) change in radar phase will result in total loss of coherence. Therefore, coherence is a valuable information source with potential for surface stability study and classification.

Compared with the considerable achievements from study of interferometric SAR phase information, studies of the interferometric SAR coherence imagery are so far less reported. The coherence images were initially considered useful only to verify the quality of interferograms for phase-based applications. The potential of the interferometric SAR coherence imagery as a powerful tool for random surface change detection was recognised relatively recently (Ichoku *et al.*, 1998; Liu *et al.*, 1997).

There are several different aspects of InSAR coherence imagery that make it a more challenging technique for applications compared with other applications of InSAR techniques such as DEM generation and coherent surface motion measurement.

Firstly, surface stability and thus coherence is a statistical measurement of "random" processes while topographic or displacement phase field are the measurements of "deterministic" values. The physical representation of true coherence is the temporal stability of dielectric properties and structure of the surface scatterers. However, coherence derived from the real SAR data is only an estimation of the true coherence. This fact diversifies the methods for generating coherence images in both the definition and the approaches of estimation. For example,

coherence can be defined and estimated in several ways, using either SAR intensity data or complex data, though the coherence defined as the complex correlation function gives the most comprehensive information about surface physical stability.

Secondly, because of the nature of SAR data acquisition, that is a single measurement (sample function) of a random physical process, statistical ensemble averaging over multiple sample functions for coherence estimation should be replaced by spatial (or time) averaging over neighbouring pixels in the single sample function under the assumption of stationary and ergodic random processes. However, these assumptions are not always valid with real SAR data. For instance, one of the most technically competing sources of nonstationarity is the topographic phase that tends to reduce the coherence estimation in a high relief area at a false assumption of stationarity. Therefore, topographic phase should be removed to satisfy the stationary and ergodic conditions for the unbiased coherence estimation. As the methods published so far to tackle the problem are not satisfactory, a more systematic and reliable method needs to be developed in order to make reliable interpretation of land surface using coherence image.

Thirdly, the statistics and source of decorrelation that governs coherence imagery should be better understood. There are several different sources of decorrelation which can mislead the interpretation of coherence images. Without an understanding of decorrelation factors, the interpretation of coherence imagery for land surface random change would be hindered by the factors other than temporal decorrelation. In fact, a thorough understanding on the decorrelation sources is essential not only for temporal surface change detection using InSAR coherence imagery but also for other interferometric SAR techniques.

The typical sources that reduce the coherence level are the thermal noise of the sensor, temporal surface change, baseline separation, local terrain slope and phase aberration during image processing. Much effort has been made to reveal the nature of these decorrelation factors but further investigation is needed to understand them fully. In particular, spatial topographic decorrelation needs further investigation. In a side-looking and ranging SAR system, total loss of information along the foreshortened and layover slopes happens in mountainous areas. A consequence is the total topographic decorrelation on these slopes in the SAR interferometric products,

which is a major obstacle in InSAR applications. For DEM generation using interferometry and deformation measurement using differential interferometry, the main technical difficulty is the phase unwrapping. Much research in this field is concentrated on finding efficient ways to avoid low coherence areas during the phase unwrapping procedure to obtain absolute phase information. For coherence imagery, the low coherence features from spatial topographic decorrelation can easily confuse the interpretation for random surface changes. Therefore, analysing the total topographic decorrelation can help to achieve reliable interpretation of the coherence imagery as well as to provide valuable information for other InSAR techniques.

Finally, interpretation of coherence is not as straightforward as the topography or surface motion provided by interferometric phase. The coherence study is highly target dependent and should be treated with consideration of possible factors such as weather, soil, geologic, and geomorphologic conditions.

Therefore, InSAR coherence imagery application needs further refinement in methodology to tackle the problems discussed so far.

1.2 The Objectives of the Research

The main aims of this research are to understand the nature of coherence, to develop the methodologies of using InSAR coherence imagery, and to apply the method to the land surface change detection and environmental monitoring. The detailed objectives of the research are:

- to investigate the applicability of InSAR coherence imagery to surface change detection and environmental monitoring through the interpretation of coherence features on various types of land surface;
- to investigate topography-induced decorrelation in a stationary scene, i.e., the spatial topographic decorrelation;

- to develop an effective interpretation method for various decorrelation features in a series of coherence images;
- to develop a method for coherence estimation in a nonstationary scene, especially for topographic phase-free, unbiased coherence estimation.

1.3 Approach

1.3.1 SAR Data Selection and Image Processing Facilities

For development and application of the methodologies of InSAR coherence imagery, careful selection of data sets and proper image processing facilities are essential. In this research, ERS-1 and ERS-2 SAR raw data were used for the case studies. The data were collected during the 35 days revisit mode or one day separation from ERS-1/2 tandem mode. Data sets adequate for interferometric configuration were selected using the DESCW program of European Space Agency (ESA). This program shows the spatial distance (spatial baseline) and temporal separation (temporal baseline) between two arbitrary satellite orbits available for a specific region. Raw complex SAR data, all from descending orbits, are used in this research.

Only a limited number of SAR scene combinations from the ERS-1/2 mission conform to the InSAR configuration because of the criteria on the spatial and temporal baselines. The spatial baseline is the most important factor in choosing an InSAR data pair. Short baselines are always preferred for repeat-pass InSAR coherence imagery. A baseline component perpendicular to the radar look direction, B_{\perp} , of no more than 500 m is a general criterion used in this research to avoid spatial baseline decorrelation (Zebker and Villasenor, 1992). More frequent revisit of satellite orbit is favoured for intensive surface monitoring, but the available temporal baseline is virtually limited by the satellite's revisit period and the mission plan. Generally, large temporal baseline is not adequate for InSAR coherence imagery,

especially for unstable areas, due to severe temporal decorrelation. Several years of temporal baseline, however, may be acceptable for a highly stable area while no more than one-year temporal baseline is suitable for semi-arid regions. Weather conditions at the time of SAR data acquisition are another important factor that affect the scene coherence. Rainfall events, and thus the moisture change of the land surface, must be particularly accounted for during the interpretation of coherence images.

SAR compression and the subsequent InSAR processing were performed by an in-house software package and the PULSAR software of Phoenix System Ltd. The in-house software package was modified from a software package given by Prof. H. Zebker in Stanford University, USA under the permission from NASA, by the Remote Sensing unit, Imperial College for education purpose. This program was used to generate InSAR products from ERS-1 SAR raw data of the Sahara desert scene. The PULSAR software was then introduced later and used for verification of the in-house software and the data processing of ERS-1/2 SAR data of SE Spain. Most of the post-processing steps and visualisation were performed using ERMMapper software.

The computer hardware used for SAR compression and InSAR software are Silicon Graphics Inc. (SGI) workstations and Sun Ultra Workstations. A SGI Octane is mainly used for SAR and InSAR signal and image processing. It has 333 MHz dual CPUs, 640 MB RAM and the hard disk storage of hundreds of gigabytes linked directly or via network, and is capable of performing SAR compression of one scene (100 km × 106 km) within 30 minutes. A Sun Ultra60 and an Ultra10 workstations with one or half of GB RAM were also used for post-processing.

1.3.2 Case Study of InSAR Coherence Imagery in the Sahara Desert, Algeria – Flat, Hyper-arid and Stable Land Surface

Interpretation of coherence is highly case dependent and should take account of various environmental factors associated with the specific study areas. In most cases, decorrelation features are easily detectable with a highly coherent surface as a

background. Therefore, choosing a stable region as a case study is a good starting point for the methodology development stage.

The first study region is in the east of the Sahara desert, Algeria. It has been investigated as a case study for application of the InSAR coherence imagery in a flat, hyper-arid region. The Sahara study area is an ideal test site for InSAR technology due to the simplicity of topography and highly stable surface properties over a considerable period. The location of the study area is named ALG, as shown in Figure 1.1.

Three ERS-1 SAR scenes of the east of the Sahara desert in Algeria were used as a test dataset for the coherence imagery and also for the development of SAR and InSAR processing algorithms and calibration (Table 1.1). The land surface of this flat, hyper-arid area is characterised by massive sand dunes within which coherence is lost due to micro-scale movement of sand particles and volume scattering by radar penetration into the dry sand mass. Areas of hard bedrock maintain high coherence over a long period. The coherence images of this region show many interesting features such as ephemeral river channel, dry lakes, sand dune migration, and human disturbance of terrain. The observation of these surface change features demonstrates the use of InSAR coherence imagery as a powerful and unique tool for surface change detection and monitoring when the surface background is highly stable. An anomalous case of gully feature leads to the development of spatial topographic decorrelation function and ratio coherence imagery.

1.3.3 Spatial Topographic Decorrelation Function and Ratio Coherence Imagery

There exists a certain topographical condition within which the interferometric coherence is lost completely and not recoverable. This is the case of the foreshortened or layover area where the ground reflectivity spectrums of two SAR observations totally mismatch with each other. Based on a spatial baseline decorrelation function (Zebker and Villasenor, 1992), a modified spatial decorrelation function from the geometrical derivation of the correlation is used to describe the topographic

decorrelation factor, as well as the baseline decorrelation. This function can be verified from another approach using a spectral method (Just and Bamler, 1994; Gatelli *et al.*, 1994). A zone of critical terrain slope (or critical incidence angle) can be defined from the spatial topographic decorrelation function (Lee and Liu, 1999) within which coherence is lost completely.

A new analytical method, ratio coherence imagery, has been developed in this study to identify the area where total loss of coherence occurs due to the topography, so as to reveal various surface characteristics relating to temporal changes. Specific conditions on data sets and surface characteristics have been analysed for successful applications of this methodology.

1.3.4 Another Case Study for InSAR Coherence Imagery in Almeria and Granada regions, Southeast of Spain – Mountainous, Semi-arid and Unstable Land Surface

Mountainous and wet surfaces have been more challenging for SAR and InSAR techniques. With the limited acquisition frequency of the existing spaceborne SAR sensors in monthly order (except for ERS-1/2 tandem mission data of one day separation), the repeat-pass InSAR can be successfully applied only for a limited surface of the entire Earth. Most hyper-arid areas with highly stable land surfaces can be good targets for InSAR technology. However, in a semi-arid area, the choice of suitable datasets may be limited. Even if InSAR pairs of hundreds days of temporal baseline are available, many of them may totally lose coherence as the result of rapid surface changes. Vegetation and humidity variations may result in severe decoherence in a short time.

As a second case study, a semi-arid and mountainous region was investigated: the Almeria and Granada regions in southeast Spain. The locations of the study areas are depicted as ALM and GRA in Figure 1.1. High relief mountainous areas are challenging for SAR and InSAR techniques due to the heavy geometric distortion of the topography. The total topographic decorrelation phenomenon in directly radar-facing slopes is more common. The amount of coherence bias due to topographic

phase can be significant for steep slopes. Therefore, the interpretation of mountainous areas, which are more common on the earth's surface than flat regions, is complicated and should be done with great care.

In the Almeria scene, surface changes by erosion and human activities have been studied based on the ERS SAR images with the interval of the 35-day repetition cycles (Table 1.2). In the Granada scene, surface decoherence features, originated from rainfall events and various environmental factors, have been investigated using ERS-1/2 tandem data (Table 1.3).

Another reason for choosing this region is that it has been a test site for the remote sensing group in Imperial College, London, and for Natural Environment Research Council (NERC) for many years. There is a comprehensive data collection from archived imagery data (e.g. TM, SPOT, and ATM) to geological and topographic maps, together with considerable *in situ* knowledge and data from annual field trips with MSc. students.

The study of this area will show that the interpretation of coherence images should be accompanied by other information sources such as topographic maps, Landsat TM images, geological maps, weather data, and field observation data. This will extend the utility of coherence imagery for surface change detection, monitoring, and surveillance.

1.3.5 Topographic Phase-free Coherence: *Differential Coherence*

Estimation of unbiased coherence from complex SAR data is essential in signal and image processing for InSAR coherence imagery. To satisfy the stationary and ergodic random process condition for coherence calculation, nonstationarity should be removed. Topographic phase fringes are the typical source of nonstationarity that should be compensated to avoid degradation in coherence estimation.

Topographic phase removal has been addressed by many researchers using an existing DEM from other sources such as optical stereo image pairs or topographic

maps. The main common problem of these methods is the coregistration error between coherence imagery and DEM. Alternatively, topographic fringes could be removed by estimating the interferometric phase directly from the interferogram itself. However, this method is very difficult to apply where the phase noise is significant and the coherence level is low. Considering that the application of coherence imagery is mainly based on the features with low coherence, the method is practically not applicable.

Therefore, a novel method is proposed in this thesis, called *differential coherence*, and used to remove topographic phase effects in a low coherence image using a good quality reference interferogram derived from an image pair of the same scene with high coherence (Lee and Liu, 2000b). The method has been developed using multi-pass differential InSAR (DInSAR) technology to obtain topographic phase-free coherence. An extra interferometric image pair of high coherence is essential to the method for generating a reference interferogram. As the reference interferogram has to be phase-unwrapped during the process, the phase unwrapping algorithms for differential coherence image generation has also been investigated.

1.4 The Structure of the Thesis

Chapter 1 introduces objectives, approaches, and structure of the thesis.

Chapter 2 reviews the basic theory of SAR, InSAR, and coherence imagery. The history, systems, and applications of SAR and InSAR are discussed together with phase statistics and decorrelation factors that degrade coherence.

Chapter 3 describes the principles and data processing for SAR and InSAR coherence imagery. It includes descriptions of the data processing procedure and algorithms from SAR compression to coherence image generation.

Chapter 4 is a discussion of an application example of InSAR coherence imagery in a hyper-arid, flat area in the Sahara Desert, Algeria. The study of this area exhibits the potential of coherence imagery for land surface change detection and monitoring

in a highly stable area. A controversial case found in a gully area stimulated the research reported in Chapter 5.

Chapter 5 describes methods for analysis of spatial topographic decorrelation. The origin of total topographic decorrelation has been analysed for foreshortened and layover slopes showing complete loss of coherence. The research led to the design of ratio coherence imagery that enables more effective analysis of various coherence features.

Chapter 6 describes another application example of InSAR coherence imagery in a semi-arid and mountainous area in Almeria and Granada, southeast of Spain. This example extends the potential of coherence imagery to regions with more complicated environment. Postulations on slope dependence of decoherence features initiates the study of Chapter 7.

Chapter 7 presents a novel method to remove topographic phase fringes using a DInSAR technique for unbiased coherence estimation. Coherence estimation is discussed as a statistical measurement of the property of physical stochastic process. A numerical simulation is shown for analysing the effect of topography as a source of nonstationarity that reduces the coherence level. A multi-pass DInSAR technique has been used for topographic phase-free coherence estimation to produce, so called, differential coherence. The limitations and possibility of this method for further application are also discussed.

Chapter 8 summarises the conclusions of the research and the suggestions for future study.

1.5 Summary of the Main Achievements of the Thesis

The main achievements of the author in this thesis are the development of the two methodologies: ratio coherence imagery and differential coherence, and applications of these methods to improve detection of random temporal change on land surface in relief areas in the Sahara desert and SE Spain case studies.

Ratio coherence imagery effectively separates spatial topographic decorrelation from temporal decorrelation. The analysis of spatial topographic decorrelation and the development of a new technique, ratio coherence imagery (Chapter 5), was triggered by controversial gully features in the Sahara desert scenes (Chapter 4) observed during a pilot InSAR project jointly carried out by the Remote Sensing unit, Imperial College and NPA group. As a member of Remote Sensing unit, Imperial College, the author investigated these features and provided a physical and mathematical proof of the total topographic decorrelation phenomenon in the Sahara desert scenes.

The field investigation and interpretation of coherence images of the Almeria and Granada scenes, SE Spain (Chapter 6), were team efforts in the Remote Sensing unit, Imperial College, through the ESA AO3-113 project. Ratio coherence imagery was then used to clarify the origin of complicated decoherence features in this high relief area. A further interpretation of the Granada scenes with rainfall events is also presented in this thesis. Various decoherence features are interpreted in conjunction with lithology, vegetation, wind, surface moisture and erosion.

Observation of the slope dependence of decoherence features in the Granada scenes initiated the development of a new methodology for topographic phase-free coherence estimation and the concept of differential coherence (Chapter 7). Coherence estimation is considered as a statistical representation of random physical processes. For an unbiased coherence estimation, topographic phase fringes should be removed. Multi-pass DInSAR technique is applied to generate topographic phase-free coherence image, differential coherence, which is another product of DInSAR technique in addition to the differential interferogram. Showing up to 16% coherence enhancement selectively on steep slopes, differential coherence imagery demonstrates its potential for refined quantitative analysis.

The development of an in-house SAR and InSAR software was carried out by the author in conjunction with two academic visitors from Japan: Dr. Hiroshi Hanaizumi and Dr. Yosuke Ito, in a research team led by Dr. J. G. Liu. The software was used to process the Sahara desert scenes. A commercial software, PULSAR, was then introduced to process the SE Spain scenes and to qualify the in-house software. A branch-cut phase unwrapping software for differential coherence imagery was also developed and compared with a relevant function in PULSAR.



Figure 1.1 The locations of the ERS-1/2 SAR scenes used for the case studies. The square boxes (100 km \times 106 km) represent the location of scenes named as GRA, ALM, and ALG, respectively.

Table 1.1 SAR scenes of the Sahara desert, Algeria (ALG). Track 351, Frame 3051, descending orbit. (ALG1 as a master image)

| Scene | Mission | Date | Orbit | ΔT (days) | $B_{//}$ (m) | B_{\perp} (m) | Weather |
|-------|---------|----------|-------|-------------------|--------------|-----------------|---------|
| ALG1 | ERS-1 | 19920908 | 06007 | 0 | 0 | 0 | dry |
| ALG2 | ERS-1 | 19921013 | 06508 | 35 | 121 | 263 | dry |
| ALG3 | ERS-1 | 19930928 | 06508 | 385 | 175 | 368 | dry |

Table 1.2 SAR scenes of Almeria, Spain (ALM). Track 237, Frame 2853, descending orbit. (ALM1 as a master image)

| Scene | Mission | Date | Orbit | ΔT (days) | $B_{//}$ (m) | B_{\perp} (m) | Weather |
|-------|---------|----------|-------|-------------------|--------------|-----------------|---------|
| ALM1 | ERS-1 | 19950426 | 19764 | 0 | 0 | 0 | dry |
| ALM2 | ERS-2 | 19961003 | 07606 | 526 | 20 | 131 | dry |
| ALM3 | ERS-2 | 19961212 | 08608 | 576 | -108 | -25 | dry |
| ALM4 | ERS-2 | 19970501 | 10612 | 716 | -34 | -5 | dry |

Table 1.3 SAR scenes of Granada, Spain (GRA). Track 051, Frame 2853, descending orbit. (GRA1 as a master image)

| Scene | Mission | Date | Orbit | ΔT (days) | $B_{//}$ (m) | B_{\perp} (m) | Weather |
|-------|---------|----------|-------|-------------------|--------------|-----------------|------------|
| GRA1 | ERS-1 | 19960502 | 25089 | 0 | 0 | 0 | rain(1mm) |
| GRA2 | ERS-2 | 19960503 | 05416 | 1 | -47 | -91 | rain(21mm) |
| GRA3 | ERS-1 | 19961024 | 27594 | 175 | 36 | 113 | dry |
| GRA4 | ERS-2 | 19961025 | 07921 | 176 | -73 | -18 | dry |

Chapter 2: Review of Synthetic Aperture Radar, Interferometry, and Coherence Imagery

Synthetic aperture radar (SAR) imaging technology has become established since the initial concept of SAR emerged in the 1950s. The use of spaceborne SARs as interferometers became popular relatively recently, although understanding of the basic principles dates back to the early 1970s (Graham, 1974). For terrestrial applications, it was only in the 1980s that the first results were published (Gabriel and Goldstein, 1988; Gabriel *et al.*, 1989; Goldstein and Zebker, 1987; Goldstein *et al.*, 1988; Prati *et al.*, 1989; Zebker and Goldstein, 1986). Today, it is generally appreciated that SAR interferometry (InSAR) is a powerful tool for mapping the land, ice and even sea surface topography. Differential InSAR (DInSAR) provides a unique method for measuring and mapping of surface displacements over large temporal and spatial scales, with precisions of centimetres to millimetres. This is of importance for research into earthquake and volcanic deformation, monitoring glaciology and ice sheet motion, studying tectonic processes, and for mapping the land subsidence due to mining, gas, water, and oil extraction. Repeat-pass InSAR coherence imagery allows the detection of random changes of spatial and dielectric properties of the land surface by using the temporal and spatial coherence information. Coherence can also be used for land cover classification, mapping of flooded areas, studying land surface erosion, and even for detecting human activities (Bamler and Hartl, 1998).

The purpose of this chapter is to review the history, methods, and contemporary aspects of SAR, InSAR, DInSAR and InSAR coherence imagery. Section 2.1 describes the basics of SAR imaging systems. Section 2.2 gives a summary of various InSAR methods and applications. Section 2.3 presents the statistical characteristics of the InSAR system, followed by Section 2.4 in which decorrelation factors of InSAR are discussed.

2.1 Synthetic Aperture Radar

Synthetic Aperture Radar (SAR) is an active microwave radar imaging system. Compared with conventional real aperture radar, it achieves high along-track resolution by synthesising an artificially long antenna through intensive data processing of coherent backscattered radar signals. The microwave bands used are almost free from atmospheric absorption and the radar signal to noise ratio (SNR) is high enough so that all weather, all time (day and night) imaging is possible. To study SAR interferometry, it is essential to understand the basic principles of SAR systems and data processing for SAR image construction. This section briefly describes the history of SAR system development and SAR imaging geometry. More comprehensive descriptions on the topic of SAR are well presented in several textbooks including Curlander and McDonough (1991) and Franceschetti and Lanari (1999).

2.1.1 History of SAR Systems

The history of Synthetic Aperture Radar (SAR) goes back to early 1950s. The SAR concept is usually attributed to Carl Wiley of Goodyear Aircraft Corporation in 1951 and subsequently patented in 1965. Its first experimental validation was carried out in 1953 by a group of scientists at the University of Illinois (Sherwin *et al.*, 1962).

The first operational SAR system was of military purpose. It is believed to have been an X-band (3 cm wavelength) system built in 1957 for the U.S. Department of Defence by Willow Run Laboratories of the University of Michigan, predecessor of Environmental Research Institute of Michigan (ERIM). The successive experiments on X-/L-band co-/cross-polar SAR systems convinced NASA to include an L-band SAR sensor in the SEASAT-A experiment launched in June 1978. Although oriented to oceanographic investigations, the SEASAT-A experiment generated interesting result in other fields as well, such as polar ice studies, geology, subsurface land analysis, etc. The experiment was terminated after 100 days operation due to system failure. Following the SEASAT-A mission, NASA approved the Shuttle Imaging

Radar (SIR) flight series. After the SIR-A and SIR-B experiments with L-band flown in 1981 and 1984 respectively, the SIR-C/X-SAR experiment was conducted in 1994. This is a four-polarisation, C-band and L-band system integrated with an X-band sensor. The SIR-C/X-SAR can simultaneously acquire data of different bands and polarisations, and is currently a unique spaceborne sensor of such. During its second flight in October 1994, successful two-pass interferometric experiments were performed for terrain model reconstruction. In February 2000, Shuttle Radar Topographic Mission (SRTM) has successfully flown for 3D mapping of the land surface between $\pm 60^\circ$ of latitude representing about 80 % of the overall land surface of the Earth. The two antennas mounted on the ends of a 60 m boom form a spaceborne single-pass SAR interferometer.

The European Space Agency (ESA) has also contributed significantly to SAR technology development with the launch of two Earth Resources Satellites in 1991 and 1995 (ERS-1 and ERS-2), each has a C-band VV-polarised SAR onboard. Thanks to the precise orbit control of ERS, many technical exploitations of SAR interferometry have been achieved using these sensors. In particular, by manoeuvring ERS-2 to follow ERS-1 orbits with one day separation, the tandem mission supplied good quality data for repeat-pass SAR interferometry until March 2000 when ERS-1 finally went out of operation after its remarkably long service.

Other countries have also been involved in the development of spaceborne SAR sensors for civilian applications. Russia launched the S-band HH-polarised ALMAZ-1 in 1991; Japan, the HH-polarised L-band SAR on board of JERS-1 in 1992; and Canada, the RADARSAT equipped with a multi-mode C-band HH system in 1995.

New programmes are aimed to make a technological leap and reducing mission and operational costs: ENVISAT (ESA), LIGHTSAR (U.S.), RADARSAT-2 (Canada), PALSAR (Japan), SMART SAR (Germany), and COSMO-SKYMED (Italy). Table 2.1 summarises spaceborne SAR systems of the past, current, and future.

Extraterrestrial applications are very important aspect of SAR. For many years, the surface of the Venus remained a mystery to planetary astronomers due to the dense atmosphere surrounding the planet. In the late 1960s, the NASA 64m deep space

tracking antenna, in conjunction with the 43 m Haystack antenna in Massachusetts and the 300 m Arecibo radar antenna in Puerto Rico produced the first detailed map of Venus using radar interferometry (Pettengill *et al.*, 1980). These images along with the early scientific results from the 1967 Mariner 5 mission to Venus, led to the approval of the Pioneer mission (1978), and the development of Venus Orbiting Imaging Radar (VOIR) system. In 1982, VOIR was modified as the Venus Radar Mapper and renamed as Magellan. During the 1990-1994 mission, Magellan produced a nearly global map of Venus with 150 m resolution together with even more detailed maps of the topography covering 20% of the surface of Venus, using stereo and interferometric SAR imagery data (Roth and Wall, 1995).

The Titan Radar Mapper, the second planetary radar of NASA/JPL, is a major payload on board the Huygens-Cassini mission to Saturn. It was launched in 1997 and will be in operation in 2004 (Elachi *et al.*, 1991). SAR data will be collected in 35 close fly-bys of Titan during the four-year nominal mission, mapping 30% of the moon's surface. Considering the uncertainties on the elevation of the surface and the orbit ephemeris, multi-mode operations were designed with a very flexible radar system to operate at 300 to 600 m resolutions, without attempting to interleave the transmit and receive pulses.

In addition to spaceborne SAR missions, many airborne SAR sensors have also been developed over the years. Airborne SARs with single-pass interferometer capability are useful for regional high-accuracy topographic mapping and for ocean current monitoring by the ATI (Along Track Interferometry) configuration. Today, several national organisations and private companies own interferometric systems in operation such as TOPSAR (JPL, USA), IFSARE (ERIM/Intermap, USA), C/X-SAR (CCRS, Canada), EMISAR (Technical University of Denmark), Ramses (ONERA, France), ESR (DERA, UK), DO-SAR (Dornier, Germany), E-SAR (DLR, Germany), AeS-1 (AeroSensing, Germany), AER-II (FGAN, Germany).

Table 2.1 Spaceborne SAR systems of past, current, and future.

| Sensor | Country | Mission period | Band; polarisation | Look angle (°) | Antenna size (m) | Alt. (km) | Swath (km) | Peak Power (kW) | Data rate (Mbps) |
|-------------------|---------------------|-------------------|-----------------------|----------------|------------------------------|---------------|------------|-----------------|---------------------------|
| SEASAT-A | USA | 6/1978-, 105 days | L; HH | 20 | 10.8×2.2 | 795 | 100 | 1 | 110 (5 bps) |
| SIR-A | USA | 11/1981, 2.5 days | L; HH | 47 | 9.4 ×2.2 | 260 | 50 | 1 | Optical |
| SIR-B | USA | 10/1984, 8.3 days | L; HH | 15-60 | 10.8×2.2 | 224, 257, 360 | 20-40 | 1.1 | 30.4 (3-6 bps) |
| SIR-C/ X-SAR | USA/ Germany, Italy | 4/1994, 11 days | L, C, X; Multipol. | 20-55 | 12×2.9/ 12×0.7/ 12×0.4 | 225 | 15-90, 225 | 4.4/1.2/ 1.4 | 90 (4-8 bps)/45 (4-6 bps) |
| ALMAZ-1 | Russia | 3/1991-, 2.5 yrs | S; HH | 20-65 | 12×1.5 | 300 -70 | 30-45 | 250 | 87.5 (5 bps, I/Q) |
| ERS-1 | EU | 7/1991- 2/2000 | C; VV | 20 | 10×1 | 780 | 100 | 4.8 | 105 (5 bps, I/Q) |
| ERS-2 | EU | 4/1995-present | C; VV | 20 | 10×1 | 780 | 100 | 4.8 | 105 (5 bps, I/Q) |
| JERS-1 | Japan | 2/1992- 10/1998 | L; HH | 38 | 12×2.4 | 570 | 75 | 1.3 | 60 (3 bps, I/Q) |
| RADARS AT-1 | Canada | 11/1995-present | C; HH | 20-60 | 15×1.5 | 790 -820 | 50-500 | 5 | 85, 105 (4 bps, I/Q) |
| SRTM | USA/ Germany | 2/2000, 11 days | C, X; HH, VV | 20-60 | 12×0.7/ 12×0.4 | 233 | 56-225 | 1.2/1.4 | 180 (C), 90 (X) |
| ENVISAT | EU | ca. 2001 | C; HH, VV (VH) | 15-45 | 10×1 | 800 | 57-400 | 0.6-1.3 | 100 |
| RADARS AT-2 | Canada | ca. 2003 | C; multipol. | variable | 15×1.5 | 790-820 | 20-500 | - | - |
| PALSAR | Japan | ca. 2003 | L; Multi-pol. | 8-60 | 8.9×2.9 | 692 | 30-350 | | 120, 240 |
| LightSAR (US SAR) | USA | - | L (C or X); Multipol. | variable | - | - | - | - | - |
| COSMO-SKYMED | Italy | - | X | - | - | 600 | - | - | - |
| SMART SAR | Germany | - | - | - | - | - | - | - | - |

- under development.

2.1.2 SAR Imaging Geometry

SAR illuminates the target surface obliquely (side-looking), as depicted in Figure 2.1, to avoid equal-range ambiguity. While the sensor is moving along its path at an altitude H above some reference (x, y) plane, it transmits microwave pulses into the antenna's illumination footprint at the rate of the pulse repetition frequency (PRF) and receives the echoes of each pulse backscattered from the target surface. For a high slant range resolution and a high SNR, SAR emits a chirp pulse with a bandwidth B_v of tens of MHz modulating a carrier wave frequency f_c . Typical microwave pulse carrier wavelengths λ used are approximately 2 cm (Ku band), 3 cm (X band), 6 cm (C band), 9 cm (S band), 24 cm (L band), and 64 cm (P band). The typical PRFs are in the range of 1 – 10 kHz. The returned signal is demodulated and then is sampled in the order of several tens of MHz for ground signal processing. The data is configured in relation to two co-ordinates: slant range and azimuth. Slant range R corresponds to the two-way signal delay time and azimuth x to the pulse number sequence. The radar beam is nominally oriented orthogonal to the flight path. This is called the non-squint mode, which is never true in reality. Squint mode with a slight angle difference from orthogonal can be applied for specific purposes such as compensation for the effect of the Earth's rotation.

The commonly used SAR imaging geometry is known as strip mode (e.g., ERS-1/2 SAR and JERS-1 SAR). Two other SAR modes are of interest such as scan mode (ScanSAR) and spot mode (Spotlight SAR). The SAR integration time S is defined as the duration of a target illuminated by the radar beam. It determines the azimuth resolution of the SAR image. In the strip mode configuration, the integration time is given by the azimuth extent of the antenna pattern and the relative speed of the vehicle. In the scan mode (Ahmed *et al.*, 1990; Bamler and Eineder, 1996; Cumming *et al.*, 1997; Moore *et al.*, 1981; Moreira *et al.*, 1996; Tomiyasu, 1981), the integration time is deliberately shortened by operating the SAR in a burst fashion, where it periodically transmits bunches of pulses. In the time between bursts, the look angle of the antenna beam is changed in order to illuminate a swath parallel to the previous one. Following this routine, the SAR sweeps its beam in a stepped manner from swath to swath before it returns to the first look direction. A scan mode system

images several, temporarily interleaved swaths at the same time. During data processing, these swaths can be merged to give a total swath of up to 500 km width. One consequence of the increased coverage is reduced azimuth resolution.

Another complementary approach is adopted by using spot mode (Carrara *et al.* 1995; Di Cenco, 1988; Gough and Hawkins, 1997; Munson *et al.* 1983, Walker 1980). The antenna is continuously steered towards a certain patch on ground in order to keep it in view over a longer time. The increased integration time results in a higher azimuth resolution but at the expense of coverage area.

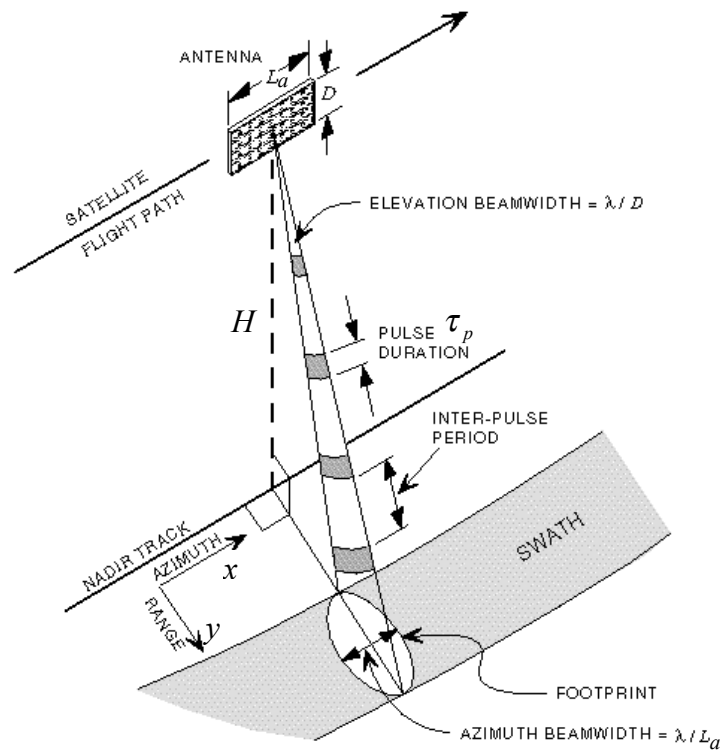


Figure 2.1 SAR imaging geometry (Olmsted, 1993).

2.2 SAR Interferometry

This section reviews the history, definitions and configurations of SAR interferometry for various applications such as topographic mapping, surface displacement measurement, and the surface random change detection.

2.2.1 History of InSAR

SAR interferometry was first used in observation of the surface of Venus and the Moon from InSAR configurations using antennas on the Earth's surface (Rogers and Ingalls, 1969). Graham (1974) was the first to introduce synthetic aperture radar for topographic mapping. Zebker and Goldstein (1986) presented the first practical results of observations with airborne radar. Goldstein *et al.* (1988) was the first to apply InSAR technique to the spaceborne observations to generate highly accurate digital elevation model (DEM) of the Earth's surface using the SEASAT-A L-band SAR system. With the launch of ERS-1 (1991), JERS-1 (1992), and RADARSAT (1995), spaceborne InSAR study has increased dramatically. With the launch of ERS-2 in 1995, the feasibility of spaceborne SAR interferometry has been greatly improved by the use of ERS-1 and ERS-2 in the tandem mission that can provide interferometric data at only one-day separation (Duchossois and Martin, 1995).

Technical refinement of InSAR for DEM generation can be found in Madsen *et al.* (1993) and Zebker *et al.* (1994b). The concept of DInSAR was established by Gabriel *et al.* (1989). Massonnet *et al.* (1993) used a pre-existing DEM to remove the topographic phase from interferogram and retrieved the co-seismic displacement field of the Landers earthquake in California. Zebker *et al.* (1994a) used three-pass DInSAR configurations to remove directly the topographic phase without use of the reference DEM. The use of coherence image for surface stability study is a relatively recent study area in fast development (Massonnet *et al.*, 1995; Hagberg *et al.*, 1995; Rosen *et al.*, 1996; Liu *et al.*, 1997).

2.2.2 Definitions

The relatively recent and rapid development of SAR interferometry has created untidy and multiple definitions and nomenclatures used independently by different groups of scientists. A clear specific nomenclature for SAR interferometry is necessary for this thesis.

Interferometric SAR refers to a SAR system or configuration that incurs coherent correlation between multiple SAR observations of the same target. Several acronyms for interferometric SAR are used. These include InSAR, INSAR, IFSAR, or IfSAR, which are all equivalent. The term “InSAR” is used throughout this thesis. Note that InSAR normally refers to the across-track interferometric configuration rather than *along-track interferometer* (ATI) for moving target detection (Bao *et al.*, 1997; Carande, 1994) or Δk -radar for accurate range measurement using different wavelengths from the same antenna position (Sarabandi, 1997).

InSAR can be operated from either *airborne* or *spaceborne* platforms and configured for *single-pass* or *repeat-pass*. A single-pass interferometer is best for DEM generation while repeat-pass is essential for environmental change monitoring. Repeat-pass is only possible when vehicle revisit control is of high accuracy. An airborne system provides more flexible configuration and operation. However, an *airborne repeat-pass* interferometer is not operationally feasible at present because the motion and position control of aircraft is more difficult than spaceborne systems. An airborne interferometer is usually a single-pass configuration and has been widely used for DEM generation. Given accurate orbit control, *spaceborne repeat-pass* InSAR configuration for change detection of the Earth’s surface is possible. A typical successful case is ERS-1 and ERS-2. SRTM is, so far, a unique example of a *spaceborne single-pass* interferometer.

SAR interferometry (equivalently, the InSAR technique) is a technique to extract surface physical properties by using the *complex correlation coefficient* of two SAR signals. The complex correlation coefficient, γ , of the two SAR observations, u_1 and u_2 , is defined as:

$$\gamma = \frac{E[u_1 u_2^*]}{\sqrt{E[u_1 u_1^*] E[u_2 u_2^*]}} \quad (2.1)$$

where $E[\cdot]$ is the mathematical expectation (ensemble averaging) and $*$ represents the complex conjugate.

The *interferometric phase* is defined as the phase of the complex correlation coefficient as:

$$\phi = \arg\{\gamma\} = \arg\{E[u_1 u_2^*]\}, \quad (2.2)$$

and its two dimensional map is called the *interferogram*.

The *coherence* is the amplitude of the complex correlation coefficient as:

$$\rho = |\gamma|, \quad (2.3)$$

and its two dimensional map is called the *coherence image*.

An interferogram contains the interferometric phase fringes from SAR geometry, together with those from topography and displacement of the surface. The level of coherence can give a measure of the quality of the interferogram. Initially, the InSAR techniques were mainly dedicated to topographic information retrieval from interferograms. Further development resulted in techniques to extract interferometric phase fringes from coherent block displacement of the surface. This is called *differential SAR interferometry* (DInSAR). Coherence itself gives valuable information about the surface temporal stability. This is called *InSAR coherence imagery*, which is the main topic of this thesis.

2.2.3 Topographic Mapping

It is a consequence of SAR geometry that surface scatterers at the same distance from the radar (slant range) but with different look angles are imaged as the same point by SAR. SAR geometry provides only the slant range of the target but no

information about its look angle. If this ambiguity of the radar look angle can be solved, the exact location (elevation and ground range) of each target point can be calculated. The look angle ambiguity in SAR geometry can be solved from the following InSAR geometry.

Consider a cross section of the Earth surface as shown in Figure 2.2. This figure is drawn in a plane perpendicular to the along-track direction. InSAR configuration is normally achieved by imaging a target point P from two radar positions at S_1 and S_2 . The height of S_1 above zero elevation level is H . The radius of the Earth r_e , measured from the Earth's centre O to the datum, is assumed to be a constant along the across-track direction. This assumption usually holds for the case of a spaceborne SAR system with orbit inclination (the angle between the orbit plane and the Earth's equatorial plane) around 90° and having side-looking imaging property. The distance between S_1 and S_2 is called baseline, B . The angle of the baseline with respect to the horizon is β . The look angle is θ_l , and the slant ranges from S_1 and S_2 to the target points are R_1 and R_2 , respectively. If the slant range difference is given by $\Delta R = R_2 - R_1$, then the measured interferometric phase is

$$\phi = \frac{4\pi}{\lambda} \Delta R \quad (2.4)$$

This is 2π times the round-trip distance difference in wavelengths. By applying the law of cosines in $\Delta S_1 P S_2$, ΔR can be solved as

$$\Delta R = \sqrt{R_1^2 + B^2 + 2R_1 B \sin(\theta_l - \beta)} - R_1 \quad (2.5)$$

From the measurement of the interferometric phase ϕ and InSAR geometric parameters, the look angle θ_l in equation 2.5 can be solved. Then, from $\Delta S_1 O P$, the topographic elevation z is calculated as

$$z = \sqrt{(r_e + H)^2 + R_1^2 - 2R_1(r_e + H) \cos \theta_l} - r_e, \quad (2.6)$$

and the ground range R_g is

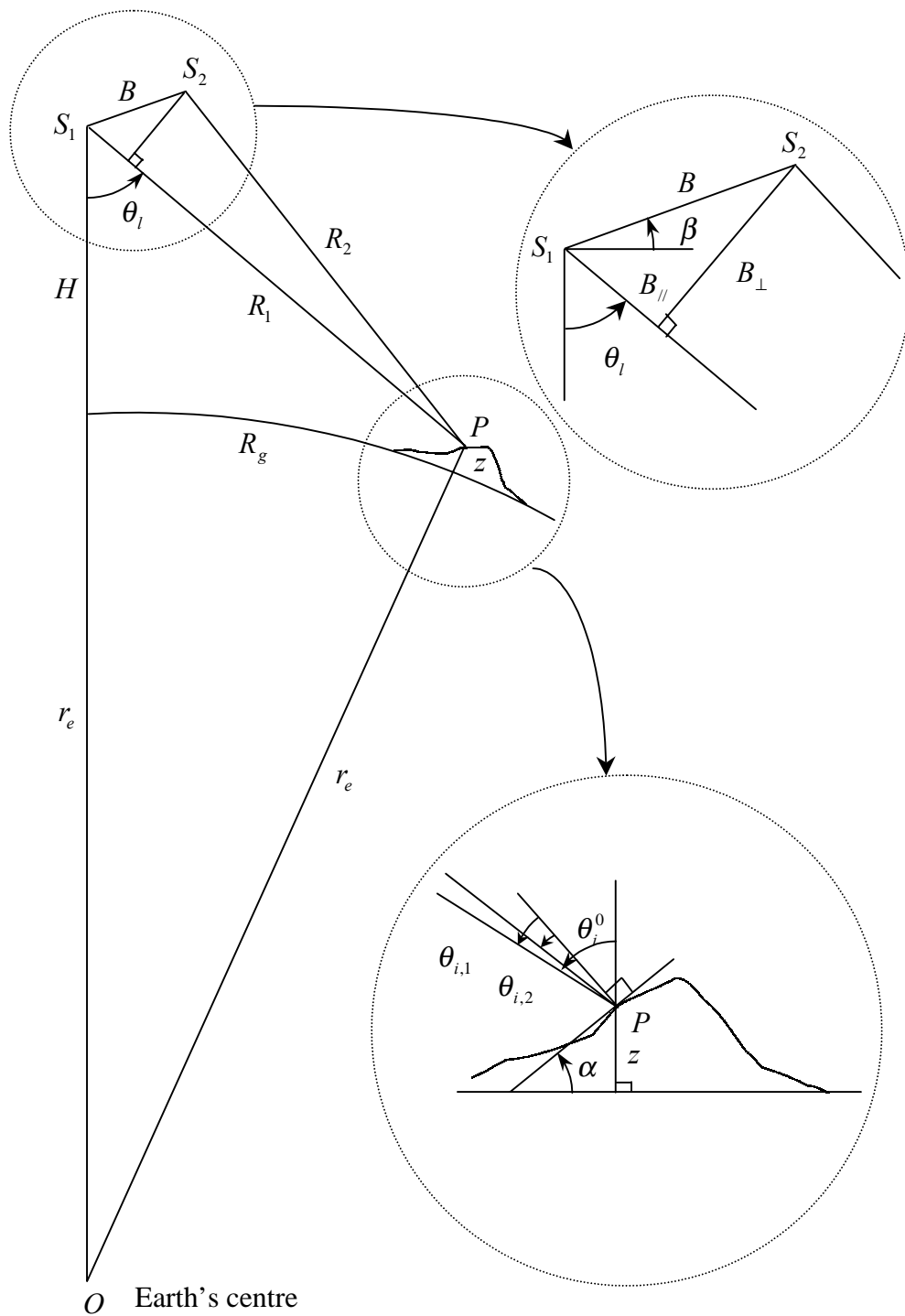


Figure 2.2 InSAR configuration.

$$R_g = r_e \sin^{-1} \left(\frac{R_1}{r_e + z} \sin \theta_l \right). \quad (2.7)$$

From equations 2.4 and 2.6, the *height sensitivity* of InSAR, i.e., the amount of change in interferometric phase from the change of surface elevation, can be calculated as

$$\frac{\partial \phi}{\partial z} = \frac{4\pi}{\lambda} \frac{B \cos(\theta_l - \beta)}{R_1 \sin \theta_l} \cdot \left(\frac{R_1}{r_e + H} \cdot \frac{\sqrt{(r_e + H)^2 + R_1^2 - 2R_1(r_e + H) \cos \theta}}{\sqrt{R_1^2 + B^2 + 2R_1 B \sin(\theta_l - \beta)}} \right) \quad (2.8)$$

Neglecting the minor term in brackets and using a parallel ray approximation (Zebker and Goldstein, 1986), the *height sensitivity* can be simplified as

$$\frac{\partial \phi}{\partial z} \approx \frac{4\pi}{\lambda} \frac{B_{\perp}}{R_1 \sin \theta_l} \quad (2.9)$$

where B_{\perp} is the baseline perpendicular component to the radar look direction while B_{\parallel} is the baseline parallel component, as depicted in Figure 2.2.

Alternatively, the *height of ambiguity* (Bamler and Hartl, 1998) is

$$z_{2\pi} = 2\pi \frac{\partial z}{\partial \phi} \approx \frac{\lambda}{2} \frac{R_1 \sin \theta_l}{B_{\perp}}, \quad (2.10)$$

i.e., the height resulting in a phase change of one fringe (2π) characterises the resolution of topography derived from InSAR. From equations 2.9 and 2.10, it is obvious that a sufficiently large B_{\perp} is necessary for accurate topography mapping. However, the B_{\perp} value is limited in practice due to the spatial decorrelation that reduces the coherence level and the quality of the interferogram (Li and Goldstein, 1990).

Another important property of the interferogram is the *interferometric phase fringe number* in slant range, i.e., the number of interferometric phase (2π) fringes in slant range (Bamler and Hartl, 1998),

$$k_\phi = \frac{1}{2\pi} \frac{\partial \phi}{\partial R_1} \approx \frac{2B_\perp}{\lambda R_1 \tan(\theta_i^0 - \alpha)}, \quad (2.11)$$

where α is the surface slope measured positive towards the radar look direction, and θ_i^0 is the nominal incidence angle when $\alpha = 0^\circ$. Alternatively, the *interferometric phase fringe frequency* in the range time (fast time) domain is given as (Gatelli *et al.*, 1994)

$$f_\phi = \frac{1}{2\pi} \frac{\partial \phi}{\partial t} \approx \frac{cB_\perp}{\lambda R \tan(\theta_i^0 - \alpha)} \quad (2.12)$$

by using the 2-way travel time relation, $2R = ct$.

2.2.4 Coherent Surface Displacement Measurement - DInSAR

The DInSAR technique gives the measurement of block displacement of land surface caused by subsidence, earthquake, glacier movement, volcano inflation, etc., to cm or even mm accuracy. If the surface displacement is as a result of single or cumulative surface movement occurred between the acquisition times of two SAR images S_1 and S_2 , the component of surface displacement in the radar-look direction, ζ , contributes to additional interferometric phase as

$$\phi = \frac{4\pi}{\lambda} (\Delta R + \zeta) \quad (2.13)$$

For the purpose of surface displacement measurement, the zero-baseline InSAR configuration is the ideal as $\Delta R = 0$, so that

$$\phi = \phi_d = \frac{4\pi}{\lambda} \zeta \quad (2.14)$$

This zero-baseline, repeat-pass InSAR configuration is hardly achievable in practice for either spaceborne or airborne SAR system. Therefore, a methodology to remove the topographic phase as well as the system geometric phase in a non-zero

baseline interferogram is needed. If the interferometric phase from the InSAR system geometry and topography can be removed from the interferogram, the remnant phase would be the phase from block surface movement, providing that the surface maintains high coherence.

There are two DInSAR techniques to remove topographic phase from the interferogram: one is the DEM method (Massonnet *et al.*, 1993) and the other is the three-pass method (Zebker *et al.*, 1994). The first method uses a DEM generated from existing topographic information obtained from sources other than InSAR, such as a topographic map or stereo optical imagery. The topographic phase can then be calculated from the DEM and subtracted from the interferogram. The second method requires a reference interferogram, which is believed to contain the topographic phase only. The three-pass approach has the advantage in that all data structure is kept within the SAR data geometry while DEM method can produce errors by misregistration between SAR data and cartographic DEM. The three-pass approach is restricted by the data availability. The three-pass DInSAR technique is further discussed below.

The three-pass DInSAR technique uses another InSAR pair as a reference interferogram that does not contain any surface movement event as

$$\phi' = \frac{4\pi}{\lambda} \Delta R' . \quad (2.15)$$

This motion-free interferogram can be achieved from short-revisit repeat-pass InSAR configuration or single-pass InSAR configuration. Strictly speaking, single-pass InSAR configuration is the only practical way to achieve motion-free interferogram where the motion is continuous such as ice sheets.

Incorporating equations 2.13 and 2.15 gives the phase difference, ϕ_d , only from the surface displacement as

$$\phi_d = \phi - \frac{\Delta R}{\Delta R'} \phi' = \frac{4\pi}{\lambda} \zeta . \quad (2.16)$$

In this processing, phase unwrapping must be applied to the reference interferogram. Phase unwrapping is one of the most challenging problems in InSAR

technology, especially for low coherence areas. Several robust algorithms for phase unwrapping have been developed that are sufficient even for a highly mountainous area. The phase unwrapping algorithms will be discussed further in Chapter 7. For an exceptional case where $\frac{\Delta R}{\Delta R'}$ in equation 2.16 is a positive integer number, phase unwrapping may not be necessary (Massonnet *et al.*, 1996). However, this situation is not realistic and it is very hard to achieve from the system design for a repeat-pass interferometer.

From equation 2.16, the *displacement sensitivity* of DInSAR is given as

$$\frac{\partial \phi_d}{\partial \zeta} = \frac{4\pi}{\lambda}. \quad (2.17)$$

Comparing with height sensitivity of InSAR in equation 2.9, interferometric phase is much more sensitive to surface geometric change than to topography. Therefore, DInSAR technique can measure surface displacement to centimetre or millimetre level while InSAR measures topography to an accuracy of no better than several metres.

The applications of DInSAR have been successful in measurement of glacier and ice sheet dynamics (Fahnestock *et al.*, 1993; Goldstein *et al.*, 1993; Hartl *et al.*, 1994; Joughin *et al.*, 1995; Kwock and Fehnestock, 1996; Thiel *et al.*, 1995; Thiel and Wu, 1996; Wu *et al.*, 1997), seismic deformations (Feigl *et al.*, 1995; Massonnet and Feigl, 1995; Massonnet *et al.*, 1993, 1996a; Meyer *et al.*, 1996; Reigber *et al.*, 1997; Zebker *et al.*, 1994a), volcanic activities (Briole *et al.*, 1997; Massonnet *et al.*, 1995; Roth *et al.*, 1997; Thiel *et al.*, 1997), and land subsidence (Liu *et al.*, 1999c; Massonnet *et al.*, 1997; Raymond and Rudant, 1997).

2.2.5 Random Surface Change Detection – InSAR Coherence Imagery

The coherence of two SAR observations represents the similarity of the radar reflection between them. The main purpose of InSAR coherence imagery is to detect

and monitor surface random change processes. If the reflection or dielectric property of a target has been changed during the observation time interval, the coherence of that target is reduced so that it appears dark in the coherence image.

The coherence image of two time-separated SAR observations provides an automatic detection of the random change of the target surface. Unstable and changing ground objects, which are detectable using InSAR coherence imagery, include lakes, rivers, crop fields, vegetation, surface erosion, sand transformation, and activities of living creatures. Several successful applications have been published describing land cover classification and random change detection in forest canopy (Askne and Hagberg, 1993; Askne *et al.*, 1997; Borgeaud and Wegmuller, 1996; Wegmuller and Werner, 1997; Wegmuller *et al.*, 1995), sand encroachment (Liu *et al.*, 1997, 1999a), rapid erosion (Liu *et al.*, 1999b, 1999d), and for seismic hazard mapping (Ito *et al.*, 2000).

2.3 Phase Statistics of InSAR

This section describes the phase statistics of interferometric SAR signals. It is assumed that SAR data can be statistically modelled as a complex, circular, stationary Gaussian process (Just and Bamler, 1994), assuming that the surface target is spatially homogeneous and the radar backscattering meets Rayleigh approximation requirement, i.e., the particle size is much smaller than the wavelength of the incident wave (Hulst, 1957, p. 270).

2.3.1 The System Model

The interferometric signal is composed of a geometrically induced phase that contains the useful information together with a signal noise (Just and Bamler, 1994). It is assumed that the geometrical part of the phase from system geometry, topography, and possible surface displacement are removed by data processing. In

this case, an undisturbed (noise-free) interferogram will have a constant phase and the highest coherence level.

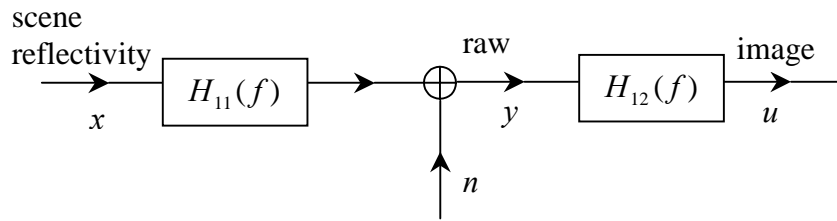
A two-step linear filter model is commonly used to describe the SAR imaging system: the transfer function H_{11} represents data acquisition and H_{12} models the processing system as shown in Figure 2.3(a). The input signal x represents the scene reflectivity. It is contaminated by thermal noise n during the data acquisition process H_{11} . The two-step transfer functions can be combined into a single end-to-end filter function H_1 with thermal noise n added after signal x has passed the filter, as shown in Figure 2.3(b). The transfer functions H_1 and H_2 in Figure 2.3(c) describe the two SAR image processes which are generally different because of the different orbits and possible differential processor aberrations. Thermal noise n_1 and n_2 are added after the transfer functions. Both the signal and the noise are modelled by complex, stationary, white, circular Gaussian processes with power spectral densities of $2\sigma^2$ and $2\sigma_n^2$, respectively. The output signals y_1 and y_2 of the two filters form a complex stationary joint Gaussian process (Papaoulis, 1991).

2.3.2 Statistical Properties of the Interferometric Phase

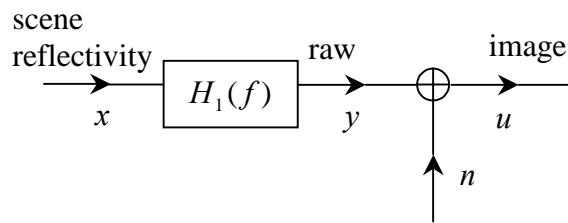
The joint probability density function (*pdf*) of the two complex SAR signals $u_1 = y_1 + n_1$ and $u_2 = y_2 + n_2$ is again Gaussian (Papaoulis, 1991),

$$\begin{aligned} pdf(u_1, u_2) &= pdf(u_{1r}, u_{1i}, u_{2r}, u_{2i}) \\ &= \frac{1}{(2\pi)^2 |\mathbf{C}|^{1/2}} \exp\left[-\frac{1}{2} \mathbf{u}^{*T} \mathbf{C}^{-1} \mathbf{u}\right] \end{aligned} \quad (2.18)$$

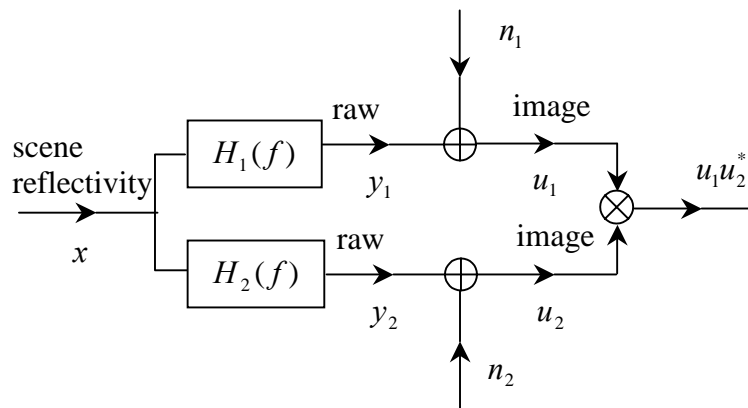
where $\mathbf{u} = (u_{1r}, u_{1i}, u_{2r}, u_{2i})^T$. \mathbf{C} is the covariance matrix of the processes $u_{1r}, u_{1i}, u_{2r},$ and u_{2i} . $|\mathbf{C}|$ and \mathbf{C}^{-1} are the determinant and the inverse of \mathbf{C} , respectively as



(a)



(b)



(c)

Figure 2.3 SAR imaging models. (a) Two-step linear filter model. (b) Single filter model. (c) The formation of a SAR interferogram. (Just and Bamler, 1994)

$$\mathbf{C}^{-1} = \frac{1}{\sigma^2(q - |p|^2)} \begin{bmatrix} q_2 & -\text{Re}\{p\} & 0 & -\text{Im}\{p\} \\ \text{Re}\{p\} & q_1 & \text{Im}\{p\} & 0 \\ 0 & \text{Im}\{p\} & q_2 & -\text{Re}\{p\} \\ -\text{Im}\{p\} & 0 & -\text{Re}\{p\} & q_1 \end{bmatrix} \quad (2.19)$$

and

$$|\mathbf{C}| = \sigma^8 (q - |p|^2)^2 \quad (2.20)$$

with

$$p = \int_{-\infty}^{+\infty} H_1(f) H_2^*(f) df, \quad (2.21)$$

$$q = q_1 q_2, \quad (2.22)$$

$$q_1 = (1 + \text{SNR}_1^{-1}) \int_{-\infty}^{+\infty} |H_1(f)|^2 df, \quad (2.23)$$

$$\text{SNR}_1^{-1} = \frac{\sigma_1^2 \int_{-\infty}^{+\infty} |H_{12}(f)|^2 df}{\sigma^2 \int_{-\infty}^{+\infty} |H_1(f)|^2 df}, \quad (2.24)$$

$$q_2 = (1 + \text{SNR}_2^{-1}) \int_{-\infty}^{+\infty} |H_2(f)|^2 df, \quad (2.25)$$

$$\text{SNR}_2^{-1} = \frac{\sigma_2^2 \int_{-\infty}^{+\infty} |H_{22}(f)|^2 df}{\sigma^2 \int_{-\infty}^{+\infty} |H_2(f)|^2 df}. \quad (2.26)$$

The *pdf* of the interferometric phase $\phi = \arg\{u_1 u_2^*\}$ can be calculated using from equation 2.18 to equation 2.26 as (Lee *et al.*, 1994; Tough, 1991; Just and Bamler, 1994)

$$\begin{aligned} pdf(\phi) &= \frac{1 - \rho^2}{2\pi} \frac{1}{1 - \rho^2 \cos(\phi - \phi_0)}. \\ &\left\{ 1 + \frac{\rho \cos(\phi - \phi_0) \cos^{-1}[-\rho \cos(\phi - \phi_0)]}{[1 - \rho^2 \cos^2(\phi - \phi_0)]^{1/2}} \right\}. \end{aligned} \quad (2.27)$$

where

$$\rho = |\gamma|, \quad (2.28)$$

$$\gamma = \rho / \sqrt{q}, \quad (2.29)$$

$$\phi_0 = \arg\{\gamma\} = \arg\{p\}. \quad (2.30)$$

It can be shown that γ is identical to the complex correlation coefficient of u_1 , u_2 defined in equation 2.1. Equation 2.27 was also derived in the more general context of second-order speckle statistics (Goodman, 1975, pp. 42-46). The statistics of the co-polarised phase difference in polarimetric measurements (Sarabandi, 1992) leads to the same expression of *pdf* as that presented here.

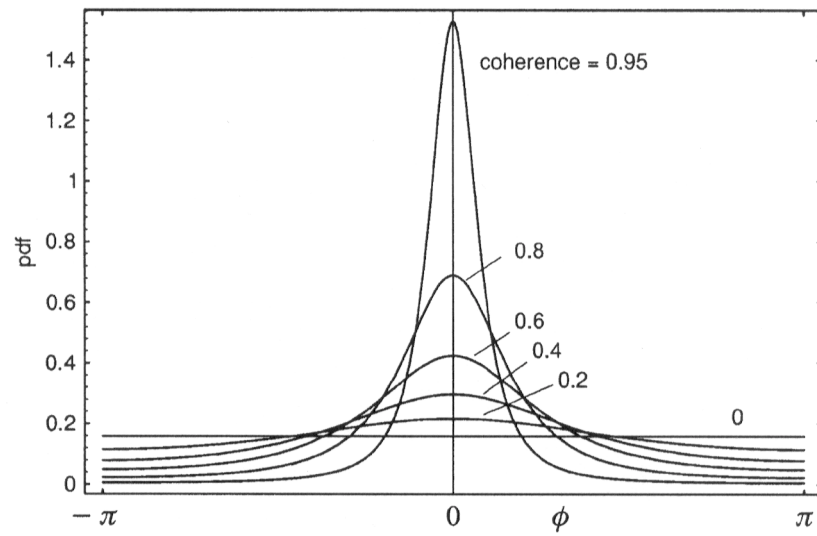
The mean and variance of the phase can be calculated as (Tough, 1991)

$$E[\phi] = \phi_0 = \arg\{\gamma\}, \quad (2.31)$$

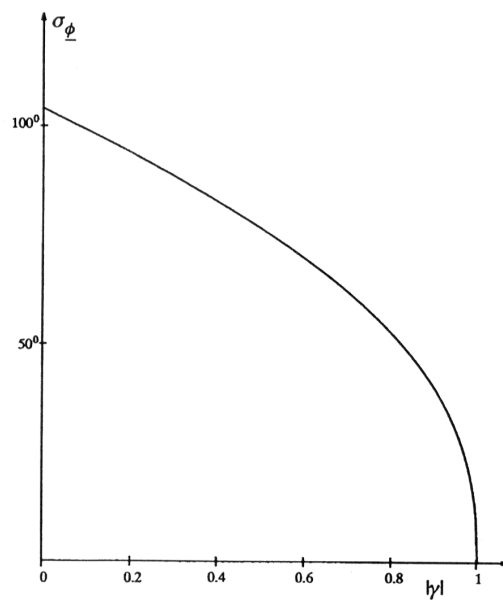
$$\sigma_\phi^2 = E[(\phi - \phi_0)^2] = \frac{\pi^2}{3} - \pi \sin^{-1} \rho + (\sin^{-1} \rho)^2 - \frac{\text{Li}_2(\rho^2)}{2}, \quad (2.32)$$

where $\text{Li}_2(\cdot)$ is Euler's dilogarithm. Figure 2.4(a) shows *pdf*(ϕ) versus ϕ for $\phi_0 = 0$ and four selected values of ρ . The distribution of phase is governed by coherence ρ and mean value ϕ_0 . When $\rho = 0$, the phase is uniformly distributed and carries no information. When the coherence increases, the *pdf* is more concentrated around ϕ_0 , and eventually becomes delta-function when $\rho = 1$. Figure 2.4(b) shows the phase standard deviation σ_ϕ versus ρ .

In summary, the mean value ϕ_0 of the interferometric phase is equal to the phase of the complex correlation coefficient γ , which in turn can be expressed by the transfer functions H_1 and H_2 and it is independent of the SNR. The variance σ_ϕ^2 of ϕ depends on the magnitude of the complex correlation coefficient and it can be determined for any given H_1 , H_2 , and SNR. Thus the effects of specific transfer functions and thermal noise on the interferometric phase and coherence can be statistically evaluated. This will be shown in the next section.



(a)



(b)

Figure 2.4 (a) The $pdf(\phi)$ of the interferometric phase for $\phi_0 = 0$ and different values of ρ . (b) The phase standard deviation σ_ϕ versus ρ . (Bamler and Hartl, 1998; Just and Bamler, 1994)

2.4 Decorrelation Factors in InSAR

SAR is a two-step imaging process that requires coherent radar echo acquisition and coherent processing of raw data as described in Section 2.3. The results are high-resolution complex images that carry not only intensity information but also a phase structure that can be used for interferometry. The achievable accuracy of interferometric SAR signal is affected by several decorrelation factors (Just and Bamler, 1994):

- thermal noise,
- errors from SAR and InSAR data processing,
- spectral misalignment of transfer functions,
- volume scattering,
- temporal decorrelation.

The following sections describe the effect of these factors on decorrelation and phase bias, based on the system model given in the previous section 2.3.

2.4.1 Thermal Noise

For the case of identical transfer functions $H_1 = H_2$ but finite SNR's, p in equation 2.21 becomes

$$p = \int_{-\infty}^{+\infty} |H_1(f)|^2 df \quad (2.33)$$

and hence,

$$\gamma = \rho = \frac{1}{\sqrt{(1 + SNR_1^{-1})(1 + SNR_2^{-1})}}. \quad (2.34)$$

The thermal noise does not introduce a phase bias as γ is real. If the SNR's of both acquisitions are identical, γ reduces to

$$\gamma = \frac{1}{1 + SNR^{-1}}. \quad (2.35)$$

This thermal SNR can only be improved in the system design and manoeuvring stage. One common technique for reducing the thermal noise in the InSAR processing is to spatially average the complex signal values, which is equivalent to the look process (Curlander and McDonough, 1991).

2.4.2 Errors from SAR and InSAR Data Processing

Assuming that the spectral envelopes of the transfer functions H_1 and H_2 are identical but their phases are different, H_1 can be modelled as real valued and the phase difference can be introduced to H_2 . A typical transfer function of rectangular type can be used as (Just and Bamler, 1994)

$$H_1(\mu, \nu) = \text{rect}\left(\frac{\mu}{B_\mu}\right) \text{rect}\left(\frac{\nu}{B_\nu}\right), \quad (2.36)$$

$$H_2(\mu, \nu) = H_1(\mu, \nu) \exp\{j\psi(\mu, \nu)\}, \quad (2.37)$$

where μ is the azimuth frequency, ν is the range frequency, and $\psi(\mu, \nu)$ represents the differential phase aberration between the two imaging processes (Born and Wolf, 1980). Using from equation 2.21 to equation 2.26, the complex correlation coefficient in equation 2.29 is expressed as

$$\gamma = \frac{1}{B_\mu B_\nu} \int_{-B_\nu/2}^{+B_\nu/2} \int_{-B_\mu/2}^{+B_\mu/2} \exp\{j\psi\} d\mu d\nu. \quad (2.38)$$

Assume that the phase aberrations are small enough to be expanded into a Taylor series as

$$\psi(\mu, \nu) = 2\pi\{\psi_{00} + \psi_{10}\mu + \psi_{01}\nu + \psi_{11}\mu\nu + \psi_{20}\mu^2 + \psi_{02}\nu^2 + \psi_{21}\mu^2\nu + \dots\}. \quad (2.39)$$

The coefficients in equation 2.39 represent the following processor aberrations:

ψ_{00} : the constant phase error,

ψ_{10} : the geometric misregistration in azimuth

ψ_{01} : the geometric misregistration in range

ψ_{20} : the defocusing in azimuth

ψ_{02} : the defocusing in range

ψ_{11} : the uncompensated linear range migration

ψ_{21} : the uncompensated quadratic range migration

In the following, the phase bias and decorrelation for each phase aberrations during data processing are evaluated.

Constant Phase Error (ψ_{00})

It is obvious that ψ_{00} simply describes a constant phase factor that adds to any interferometric phase but does not introduce decorrelation. Hence,

$$\phi_0 = 2\pi\psi_{00}, \quad \rho = 1. \quad (2.40)$$

Geometric Misregistration in Azimuth and Range (ψ_{10} or ψ_{01})

A possible error in coregistration of the two complex SAR images can be modelled as a differential linear phase aberration. Only the azimuth misregistration is discussed

here for simplicity. If ε_{10} is the relative shift between the two images in fractions of azimuth time resolution $1/B_\mu$, i.e., $\psi_{10} = \varepsilon_{10} / B_\mu$, then

$$\psi(\mu, \nu) = 2\pi\psi_{10}\mu = 2\pi\varepsilon_{10} \frac{\mu}{B_\mu}. \quad (2.41)$$

Hence

$$\gamma = \rho = \text{sinc}(\varepsilon_{10}), \quad \phi_0 = 0. \quad (2.42)$$

Therefore, misregistration does not introduce a phase bias but does introduce decorrelation.

Defocusing in Azimuth and Range (ψ_{20} or ψ_{02})

Again, consider the azimuth case only. Let ε_{20} be the phase error at the edge of bandwidth $\mu = \pm B_\mu / 2$, i.e., $\psi_{20} = 2/(\pi B_\mu^2)\varepsilon_{20}$. Then the phase aberration is

$$\psi(\mu, \nu) = 2\pi\psi_{20}\mu^2 = 4\varepsilon_{20}\mu^2 / B_\mu^2. \quad (2.43)$$

Hence,

$$\gamma = \frac{1}{\sqrt{2\Psi/\pi}} [\text{C}(\sqrt{2\varepsilon_{20}/\pi}) + j\text{S}(\sqrt{2\varepsilon_{20}/\pi})], \quad (2.44)$$

where C() and S() denote the Fresnel integrals.

The phase bias is then

$$\phi_0 = \arctan \frac{\text{S}(\sqrt{2\varepsilon_{20}/\pi})}{\text{C}(\sqrt{2\varepsilon_{20}/\pi})}, \quad (2.45)$$

and the coherence is

$$\rho = \frac{1}{\sqrt{2\varepsilon_{20}/\pi}} \left[C^2(\sqrt{2\varepsilon_{20}/\pi}) + S^2(\sqrt{2\varepsilon_{20}/\pi}) \right]^{1/2}. \quad (2.46)$$

Unlike the other aberrations, defocusing is characterised by an even phase aberration function and introduces a phase bias as well as decorrelation.

Uncompensated Linear Range Migration (ψ_{11})

Consider the residual range walk in fractions ε_{11} of a range time resolution cell $1/B_v$, i.e., $\psi_{11} = \varepsilon_{11}/(B_\mu B_v)$, then

$$\psi(\mu, \nu) = 2\pi\psi_{11}\mu\nu = 2\pi\varepsilon_{11} \frac{\mu\nu}{B_\mu B_v}. \quad (2.47)$$

Hence

$$\gamma = \rho = \frac{\text{Si}(\pi\varepsilon_{11}/2)}{\pi\varepsilon_{11}/2}, \quad \phi_0 = 0, \quad (2.48)$$

where Si() is the integral sine. Uncompensated linear range migration (range walk) results in decorrelation but does not introduce phase bias.

Uncompensated Quadratic Range Migration (ψ_{21})

The residual range curvature (Wu *et al.*, 1982) is expressed in fraction of ε_{21} of a range resolution cell $1/B_v$, i.e., $\psi_{21} = 4\varepsilon_{21}/B_\mu^2 B_v$, then

$$\psi(\mu, \nu) = 2\pi\psi_{21}\mu^2\nu = 4\pi\varepsilon_{21} \frac{\mu^2\nu}{B_\mu^2 B_v}. \quad (2.49)$$

Hence

$$\gamma = \rho = \frac{1}{\sqrt{\pi\epsilon_{21}/2}} \int_0^{\sqrt{\pi\epsilon_{21}/2}} \text{sinc}(\mu^2) d\mu, \quad \phi_0 = 0 \quad (2.50)$$

Similar to residual range walk, uncompensated quadratic range migration (range curvature) introduces decorrelation but not phase bias.

2.4.3 Spectral Envelope Misalignment

Even in a noise-free and aberration-free case, signal decorrelation will occur if the envelopes of H_1 and H_2 are shifted relative to each other, i.e.,

$$|H_2(\mu, \nu)| = |H_1(\mu - \mu_0, \nu - \nu_0)|. \quad (2.51)$$

For the rectangular transfer function in equation 2.36, the coherence is then

$$\gamma = \rho = \left(1 - \frac{|\mu_0|}{B_\mu}\right) \left(1 - \frac{|\nu_0|}{B_\nu}\right), \quad \phi_0 = 0. \quad (2.52)$$

The physical reason for spectral misalignment both in azimuth and range is the different aspect angles of a scene element in the two observations. This type of decorrelation due to sensor geometry effect is called the *spatial decorrelation*, in contrast to the temporal decorrelation.

Decorrelation caused by spectral misalignment can be avoided if the two data sets are properly band-pass filtered in order to retain only the overlapped part of spectral range between H_1 and H_2 , at the cost of spatial resolution.

Azimuth Spectral Misalignment

In the azimuth frequency dimension, different squint angles result in different Doppler centroid frequencies, $f_{Dc,1}$ and $f_{Dc,2}$, for the two data sets. The azimuth spectral misalignment is then,

$$\mu_0 = f_{Dc,2} - f_{Dc,1}. \quad (2.53)$$

For cross-track interferometry, the Doppler centroid frequency difference μ_0 can be contrived to approach zero by controlling the antenna squint to be the same for both observations. The azimuth spectral misalignment from different squint angles can alternatively be compensated by choosing only the overlapping part of spectrum centred on the average of two Doppler centroids via azimuth spectral filtering, which will be described in Chapter 3.

Range Spectral Misalignment

Spectral misalignment in the range frequency dimension, however, is an inherent feature of cross-track interferometry. Assuming that an area of interest on the ground is seen at incident angles of $\theta_{i,1}$ and $\theta_{i,2}$ in the two orbit paths, then a certain harmonic ground structure transforms into different echo frequency components depending on the incident angles. This effect can be interpreted conversely as a relative shift of $|H_1|$ and $|H_2|$ in the ν direction by the amount of (Just and Balmer, 1994)

$$\nu_0 = f_c \sin \theta_i \left[\frac{1}{\sin \theta_{i,2}} - \frac{1}{\sin \theta_{i,1}} \right], \quad (2.54)$$

where $\theta_i = (\theta_{i,1} + \theta_{i,2})/2$ and f_c is the carrier frequency of the radar. For the baseline perpendicular component B_\perp and slant range R , and considering that B_\perp is significantly smaller than R , then equation 2.54 can be simplified as (Bamler and Hartl, 1998),

$$v_0 \cong \frac{cB_{\perp}}{\lambda R \tan(\theta_i^0 - \alpha)}. \quad (2.55)$$

In fact, the range spectral misalignment v_0 is equivalent to f_{ϕ} , the interferometric phase fringe frequency, as shown in equation 2.12. As the range spectral misalignment is related to the baseline, it is also called as spatial baseline decorrelation (Zebker and Villasenor, 1992). Decorrelation from range spectral misalignment can be partially compensated using range spectral filtering, which will be discussed in Chapter 3.

2.4.4 Volume Scattering

Volume scattering occurs when the radar signal penetrates into the surface (e.g., sand, forest, dry ice), and the returned signal is a summation of the effects of the compound targets encountered in the radar beam. In natural environments, both the surface scattering and the volume scattering contribute to the radar backscattering signals. The inhomogeneity of the medium and the penetration depth determine the presence of volume scattering that reduces the intensity of radar backscattering. In radar interferometry, the presence of volume scattering decreases the coherence level. In particular, the decorrelation from volume scattering increases as the baseline increases (Gatelli *et al.*, 1994; Hagberg *et al.*, 1995).

2.4.5 Temporal Decorrelation

The temporal decorrelation comes from physical changes in the surface over the time period between observations. Temporal decorrelation is a complicated function of detailed change of radar reflectivity between two observations. Individual case studies of the relationship between temporal decorrelation and mobility of surface materials are necessary.

With an assumption of Gaussian random variation of a scatterer, it is possible to relate the coherence to rms scatterer variation between SAR image acquisitions. Zebker and Villasenor (1992) presented a sample calculation as

$$\rho_{temporal} = \exp\left\{-\frac{1}{2}\left(\frac{4\pi}{\lambda}\right)^2 (\sigma_y^2 \sin^2 \theta_i + \sigma_z^2 \cos^2 \theta_i)\right\}, \quad (2.56)$$

where σ_y is the rms variation in ground range direction, σ_z the rms variation in vertical direction. Obviously, from simple geometry, the sensitivity of temporal decorrelation is greater to vertical changes than to horizontal changes for incidence angles less than 45° . As the nominal incidence angle for ERS-1 and ERS-2 SAR is 23° , the contribution to the temporal decorrelation from random change in vertical direction is greater than that in horizontal direction.

It has been shown that only a half radar wavelength of surface rms random variation is large enough to totally decorrelate the signals. In general, surface with significant variation and volume scattering should lose its coherence rapidly with time. Temporal decorrelation is an important error source to degrade the quality of an interferogram in the operation of repeat-pass interferometer for topographic or surface displacement field mapping. In contrast, temporal decorrelation is the main information source of InSAR coherence imagery for surface random change study.

Chapter 3: Principles and Algorithms of SAR and InSAR Data Processing for Coherence Imagery

3.1 Introduction

This chapter describes general processing procedures for generating SAR and InSAR images from raw signal data. For the major interest of this thesis, discussion will be focused on the issues relating to the production and quality of InSAR coherence imagery. The chapter serves as a general reference for the necessary principles relating to the discussions in the following chapters.

InSAR processing needs to be incorporated in the SAR data compression. For example, the range and azimuth compression should follow the range and azimuth spectral filtering, so that only the common part of the ground reflectivity spectrum of the interferometric SAR image pair is processed. Furthermore, the re-sampling of the slave image is performed during the range migration process. These processing schemes are designed to reduce the signal noise during the coregistration of two single look complex (SLC) images, thus to improve the coregistration accuracy. The general procedures for SAR compression and successive InSAR processing are summarised in the flowcharts in Figure 3.1 and 3.2.

The SAR and InSAR data processing steps introduced in this chapter are based on an in-house software package and the PulSAR/INSAR software package of Phoenix Systems and Associates Ltd. (Smith, 1998a, 1998b). More detailed description of various data processing algorithms can be found in textbooks such as Curlander and McDonough (1991) and Franceschetti and Schirinzi (1990).

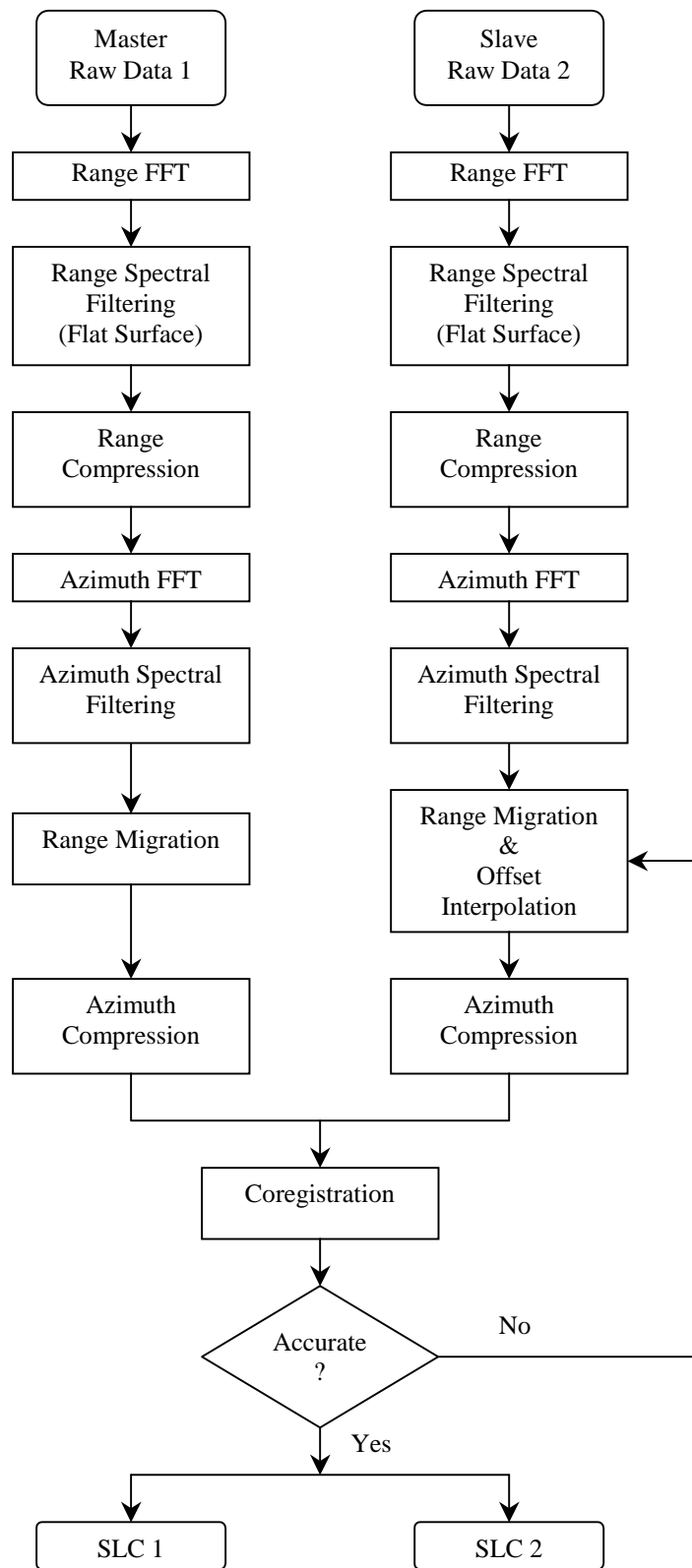


Figure 3.1 Interferometric SAR processing steps: Raw data to coregistered single look complex (SLC) images.

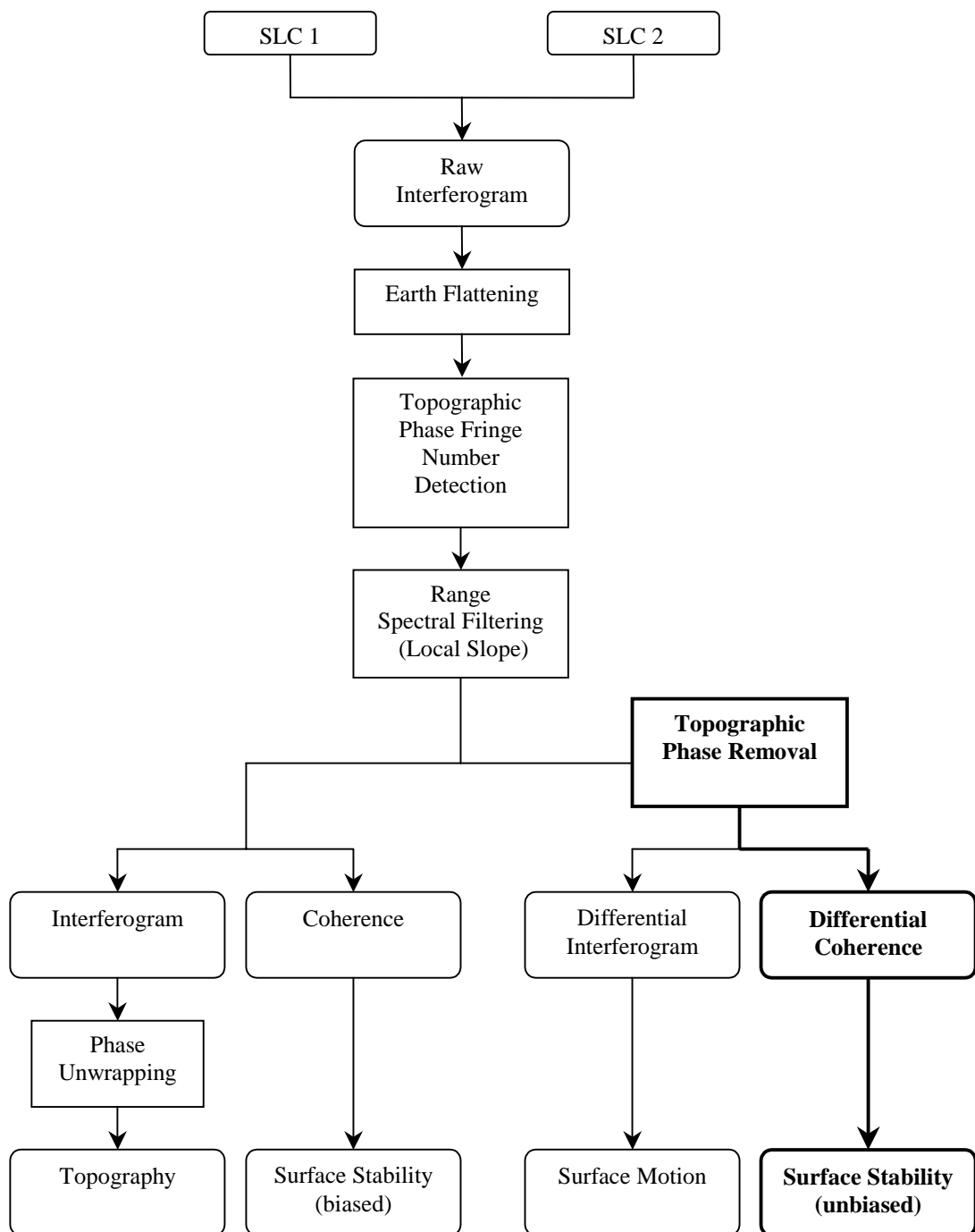


Figure 3.2 Interferometric SAR processing steps: Coregistered SLCs to InSAR products. The steps in bold box will be described in Chapter 7.

3.2 SAR Compression and Coregistration

SAR compression processing in this research uses a typical rectangular algorithm, which consists of the range and the azimuth compression processing (Curlander and McDonough, 1991). This section describes the details of each processing step for SAR SLC image formation and coregistration for further InSAR processing.

3.2.1 Range Compression

The SAR complex raw data is transformed into the range frequency domain via the Fast Fourier Transform (FFT). Range spectral filtering is performed to compensate the spatial baseline decorrelation based on the flat surface (Gatelli *et al.*, 1994). Range compression is performed by matched filtering the recorded data with the transmitted chirp pulse (Whalen, 1971, p.167). Hamming weighting function is used to suppress the sidelobes of the system impulse response function. The data are then transformed back to the time domain via inverse FFT. The following describes the detailed procedures for range compression.

Range Matched Filtering

As the vehicle moves along its path, the radar transmits a linear-FM, or “chirp”, pulse

$$h(t) = \exp[j2\pi(f_c t + Kt^2 / 2)], \quad |t| < \tau_p / 2 \quad (3.1)$$

with frequency (time derivative of phase) $f = f_c + Kt$, which is a linear function of time over the pulse duration τ_p with chirp rate K . The chirp bandwidth is $K\tau_p$ since

the frequency starts at $f_c - K\tau_p / 2$, sweeps through all intermediate frequencies, and ends at $f_c + K\tau_p / 2$. The multi-pulse real transmitted signal is then

$$p(t) = \sum_n h(t - nT_p), \quad (3.2)$$

where T_p is the pulse repetition period and the sum includes all pulses for which the target is in the radar beam.

At an arbitrary time t , the radar is at some slant range $R(t)$ from the target point with image coordinates (x_c, R_c) at the radar beam centre. The received pulse train is then

$$v(t) = \sum_n a_n h[t - nT_p - 2R(t)/c] \quad (3.3)$$

where the slant range $R(t)$ is assumed constant during the time of one pulse width. This assumption enables the general two-dimensional compression problem to be decoupled into a sequence of two one-dimensional compression operations, one in fast time (range) and the other in slow time (azimuth). Since slow time measures a coordinates orthogonal to fast time, this process sequence is called the rectangular algorithm.

Range compression is to correlate the received pulse with $h^*(t)$ (equivalently matched filtering with $h^*(-t)$) as

$$g(t) = \int_{-\infty}^{\infty} h^*(t' - t)v(t')dt' \quad (3.4)$$

which leads approximately to

$$g_n(t) = \tau_p \exp(j\omega_c t) \exp(-j4\pi R_n / \lambda) \text{sinc}[\pi K\tau_p (t - 2R_n / c)] \quad (3.5)$$

The envelope of this has a 3 dB width (range time resolution)

$$\delta t = 1/|K|\tau_p = 1/B_v, \quad (3.6)$$

which corresponds to slant range spatial resolution

$$\delta R = c / 2B_v, \quad (3.7)$$

where $B_v = K\tau_p$ is the range chirp bandwidth. Therefore, a large chirp bandwidth gives enhanced range resolution for a SAR system.

Range Spectral Filtering – Flat Surface

Range spectral filtering is necessary to compensate the decorrelation from range spectral misalignment (or spatial baseline decorrelation) as indicated in section 2.4.3. This processing step is not necessary for conventional single SAR image processing, where only the amplitude image is of concern. For InSAR image processing, however, the spatial baseline decorrelation should be tackled at the SAR compression stage so as to secure the quality of image coregistration between the two SLC images generated. Performing range spectral filtering before image coregistration is a desirable processing scheme in this respect. As shown in equation 2.55, range spectral misalignment is a function of slope as well as baseline. As the local surface slope is not a priori information during SAR compression, the range spectral filtering in this step assumes that the surface is flat. The range spectral misalignment on flat surface is then

$$v_0 \cong \frac{cB_{\perp}}{\lambda R_s \tan \theta_i^0}. \quad (3.8)$$

The filter bandwidths, W_1 and W_2 , and central frequencies, ν_1 and ν_2 , for the two SAR signals can be expressed as (Gatelli *et al.*, 1994)

$$\begin{aligned} W_1 = W_2 &= B_v - v_0, \\ \nu_1 &= \frac{\nu_0}{2}, \quad \nu_2 = -\frac{\nu_0}{2}. \end{aligned} \quad (3.9)$$

The baseline is the most important factor that determines the amount of range spectral misalignment in equation 3.8. For a repeat-pass interferometer, baseline is not known *a priori*. In this case, the baseline has to be estimated based on satellite

position data. Although ERS-1 and ERS-2 orbit control is very accurate compared to other SAR satellite systems, the accuracy of baseline is not high enough for InSAR topography or surface displacement mapping. In this case, tie points are normally used to improve the estimation of baseline up to cm or mm accuracy (Seymour and Cumming, 1996; Singh *et al.*, 1997). For the purpose of the range spectral filtering, however, less accurate estimation of baseline is generally acceptable. Therefore the baseline calculated from satellite state vectors is normally used here.

Hamming Filtering

The amplitude of the range-compressed data, or the system response function, is a sinc function with sidelobes, as shown in equation 3.5. The first sidelobes of $g(t)$ are merely 13 dB lower than the main lobe. Thus, for example, a target 13 dB stronger than an adjacent target one-resolution cell away will mask its weaker neighbour. The usual way to deal with undesirably high levels of range sidelobes in the matched filter output is to unmatch the filter (Curlander and McDonough, 1991, pp. 149-152). This is a trade-off between desirable improvement in sidelobe structure and the risk of broadening the mainlobe of the filter output. For a linear FM transmitted pulse, given in equation 3.1, of which the bandwidth time product is large, the spectrum has a constant amplitude over the band B_v , say unity, as

$$S(v) = \exp[j\psi(v)]. \quad (3.10)$$

The receiver (matched) filter is taken as

$$H(v) = W(v)\exp[-j\psi(v)], \quad (3.11)$$

where $W(v)$ is a real weighting function, which is symmetric around the band centre f_c . Thorough evaluation of the use of various weighting functions has been given by Cook and Bernfeld, 1967; Farnett *et al.*, 1970; Harris, 1978. In this processing, the Hamming function

$$W(v) = 0.54 + 0.46\cos(2\pi v / B_v) \quad (3.12)$$

is used. It provides satisfactory sidelobe behaviour with negligible main lobe broadening. The Hamming filter is also used for azimuth processing as $W(\mu)$ with B_μ replacing B_ν in equation 3.12.

3.2.2 Azimuth Compression

After range compression, the data is transformed into the azimuth frequency domain via FFT. The Doppler centroid frequency f_{Dc} is determined from the data itself via the clutterlock procedure. The Doppler rate f_r can be determined by an autofocus procedure using the azimuth subaperture correlation method. Multiple pulse repetition frequency (PRF) ambiguity of Doppler centroid, which is important for range migration, can be solved by the range subaperture correlation method. Azimuth spectral filtering can be applied on two SAR signals forming an interferometric pair to compensate decorrelation from different Doppler centroids of the two images, as described in section 2.4.3. The signal is azimuth compressed using matched filtering. A Hamming filter can then be applied to reduce the sidelobe effect similar to the one during the range compression as described in section 3.2. The following is the detailed procedures for azimuth compression.

Azimuth Matched Filtering

The angular carrier frequency ω_c in equation 3.5 can be eliminated by demodulation. Selecting the value at $t = t_n$ that gives maximum $|g_n(t)|$, representing t as slow time s , and dropping the scale factor τ_p results in

$$\hat{g}(s|x_c, R_c) = \exp[-j4\pi R(s)/\lambda]. \quad (3.13)$$

The range function $R(s)$ can be expanded as a Taylor series around $s_c = x_c / V_{st}$, the slow time at which the centre of the radar beam crosses the target, where V_{st} is the

speed of the radar platform relative to the target point. Ignoring the terms of order, higher than the quadratic, gives

$$R(s) \approx R_c + \dot{R}_c(s - s_c) + \ddot{R}_c(s - s_c)^2 / 2. \quad (3.14)$$

By definition, the time rate of phase $\phi(s)$ in the exponential term in equation 3.13 is the Doppler frequency f_D as

$$\phi(s) = -j4\pi R(s)/\lambda, \quad (3.15)$$

$$f_D(s) = \dot{\phi}/2\pi = -2\dot{R}(s)/\lambda, \quad (3.16)$$

$$\dot{f}_D(s) = \ddot{\phi}/2\pi = -2\ddot{R}(s)/\lambda. \quad (3.17)$$

Doppler centroid and Doppler rate are thus defined as

$$f_{Dc} = -2\dot{R}_c/\lambda, \quad (3.18)$$

$$f_R = -2\ddot{R}_c/\lambda, \quad (3.19)$$

so that equation 3.14 becomes

$$R(s) = R_c - (\lambda f_{Dc} / 2)(s - s_c) - (\lambda f_R / 4)(s - s_c)^2. \quad (3.20)$$

Then, equation 3.13 can be expressed in terms of f_{Dc} and f_R as

$$\hat{g}(s|s_c, R_c) = \exp(-j4\pi R_c / \lambda) \exp\{j2\pi[f_{Dc}(s - s_c) + f_R(s - s_c)^2 / 2]\},$$

$$|s - s_c| < S/2, \quad (3.21)$$

where S is the azimuth integration time. This is a linear FM wave with centre frequency f_{Dc} and frequency rate f_R . The azimuth compression is to compute the correlation

$$\zeta(s'_c|s_c, R_c) = \int_{s_c - S/2}^{s_c + S/2} h^{-1}(s - s'_c|s_c, R_c) \hat{g}(s|s_c, R_c) ds. \quad (3.22)$$

Similar to range compression, the azimuth compression can be realised approximately using a correlator function

$$h^{-1}(s|s_c, R_c) = \exp[-j2\pi(f_{Dc}s + f_R s^2/2)]. \quad (3.23)$$

The output of azimuth compression is then

$$\zeta(s'_c|s_c, R_c) = S \text{sinc}[\pi f_R S (s'_c - s_c)]. \quad (3.24)$$

The peak of this pulse occurs at $s'_c = s_c$, the target azimuth location. The 3 dB width of this pulse, that determines the azimuth time resolution, is

$$\delta s = 1/|f_R|S = 1/B_\mu \quad (3.25)$$

where $B_\mu = |f_R|S$ is the Doppler bandwidth. The azimuth spatial resolution is then

$$\delta x = V_{st} \delta s = V_{st}/B_\mu = V_{st}/|f_R|S. \quad (3.26)$$

From the simple geometry of a radar antenna, with physical length L_a along track, the nominal beam width is $\theta_H = \lambda/L_a$ so that any particular target point at range R_c is illuminated for a nominal time $S = \lambda R_c / V_{st} L_a$. Given a squint angle θ_s , Doppler parameters can be geometrically determined as

$$f_{Dc} = (2V_{st}/\lambda) \sin \theta_s, \quad (3.27)$$

$$f_R = -2V_{st}^2/\lambda R_c. \quad (3.28)$$

The Doppler bandwidth is therefore $B_\mu = 2V_{st}/L_a$ and the system azimuth resolution is

$$\delta x = L_a/2. \quad (3.29)$$

δx changes in proportion to the physical length of SAR antenna. In contrast, δx of a real aperture radar changes inversely with the physical length of its antenna as

$$\delta x = \lambda R_c / L_a. \quad (3.30)$$

With intensive signal compression processing, high azimuth resolution can be achieved with a SAR in a significantly smaller physical dimension than that in a real aperture radar.

Clutterlock

The nominal value of the Doppler centroid f_{Dc} can be obtained from satellite state vectors via equation 3.27. The satellite height and velocity are calculated by interpolating at the centre of each image from the orbit parameters (velocity and position vectors) included in the header files of the SAR raw dataset.

A more accurate Doppler centroid can be determined by a clutterlock procedure (Curlander and McDonough, 1991, p.223). All SAR clutterlock algorithms for automatic determination of the centre frequency f_{Dc} of the Doppler spectrum are, in one way or another, based on the fact that the power of the Doppler spectrum around the Doppler centre frequency f_{Dc} should form a bell-shaped azimuth power pattern of the antenna. This pattern has the maximum at the centre and gradually decreases off the centre, following a sinc^2 function. The azimuth spectrum of the range-compressed data is used for determination of f_{Dc} at the frequency of the spectral peak.

Autofocus - Azimuth Subaperture Correlation Method

The nominal Doppler rate f_R can be estimated from the orbit parameters using equation 3.28. The Doppler rate can be refined by autofocusing: an algorithm for automatic determination of the azimuth chirp constant f_R of the azimuth filter (Curlander and McDonough, 1991, p. 234). Most SAR processors use the subaperture correlation method (Bennet *et al.*, 1981; Curlander *et al.*, 1982; McDonough *et al.*, 1985; Wu *et al.*, 1982b). The subaperture method depends on the locking relationship between azimuth time or position and Doppler frequency as

$$x - x_c = V_s(s - s_c) = V_s(f_D - f_{Dc}) / f_R. \quad (3.31)$$

Suppose two images are produced from a different part of the Doppler spectrum, as in multilook processing. The outer two looks of a four-look processing are used with the centres of the subbands f_{Dc}^1 and f_{Dc}^4 , respectively, and some trial value f'_R from the orbit parameters via equation 3.28 is used. After formation of the two images, they will be registered in azimuth time by shifting one relative to the other by exactly the amount of

$$\Delta s = (f_{Dc}^1 - f_{Dc}^4) / f'_R. \quad (3.32)$$

If the value f'_R is different from the true value f_R , the registration will be incorrect because the imposed azimuth shift in equation 3.32 will not accord with the actual relation in the image

$$\Delta s = (f_{Dc}^1 - f_{Dc}^4) / f_R. \quad (3.33)$$

The two images, registered using Δs in equation 3.32, will therefore mismatch in azimuth by the amount of

$$\delta s = (f_{Dc}^1 - f_{Dc}^4)(1/f_R - 1/f'_R). \quad (3.34)$$

The procedures described from equation 3.32 to equation 3.34 establish an iteration mechanism. The autofocus procedure starts from an initial trial value f'_R . Two subaperture images are generated and coregistered in azimuth to find the offset value δs to modify f'_R (calculate f_R from equation 3.34 and make it the new trial value f'_R), and then equation 3.32 and equation 3.34 are applied again to calculate the new δs . The procedure is repeated until δs becomes small enough so that the true f_R is approached.

Azimuth Ambiguity Determination - Range Subaperture Correlation Method

The Doppler spectrum, computed as the FFT of the range compressed and base-banded data for an image line, is periodic. The period is the pulse repetition frequency f_p due to the pulsed nature of the radar. The Doppler centroid f_{Dc} determined from the clutterlock procedure still has an ambiguity of whether it is the true f_{Dc} or one of its replications, $f'_{Dc} = f_{Dc} + mf_p$, $m \neq 0$. This periodicity is of no concern in the azimuth compression and filtering operations involved in making a full resolution image, since all calculations are done digitally and all azimuth filter spectra are also periodic. An ambiguity problem, however, can arise in the range migration correction (Curlander and McDonough, 1991, p. 238). For instance, suppose that the true range walk for some particular image range R_c with the true f_{Dc} is described as (Chang and Curlander, 1992)

$$R(s) \approx R_c - (\lambda f_{Dc} / 2)(s - s_c). \quad (3.35)$$

If a different value $f'_{Dc} = f_{Dc} + mf_p$ is used, there will be a difference in the range walk in both the slow time and Doppler frequency domains by

$$\Delta R = R - R' = -(\lambda m f_p / 2)(s - s_c) = -(\lambda m f_p / 2)(f - f_{Dc}). \quad (3.36)$$

Now consider the procedure of registration of the multiple looks of a multilook image. Each frequency f in the subband of the first-look, centred at f_{Dc}^1 , will be associated with a frequency in the fourth subband of the 4-look image, for example, as

$$f' = f + (f_{Dc}^4 - f_{Dc}^1), \quad (3.37)$$

where the look centre frequencies may be ambiguous themselves, but differ by the same amount for any ambiguity number m . If the true migration locus has been used, then the range of the points corresponding to f and f' are the same, and the points of the two sublook images superpose, after azimuth registration as described in equation 3.33. If the wrong Doppler spectral replication is used ($m \neq 0$), the ranges corresponding to f and f' will differ by

$$\Delta R = -\lambda m f_p (f_{Dc}^4 - f_{Dc}^1) / 2 f_R. \quad (3.38)$$

The value of ΔR can be found from the range cross-correlation of the two subaperture images, just as was done in azimuth subaperture correlation to measure f_R in autofocus process in the previous section. The value of m may be calculated from equation 3.38, which yields the true value

$$f_{Dc} = f'_{Dc} - m f_p, \quad (3.39)$$

allowing the full image to be processed with the proper range migration correction.

Azimuth Spectral Filtering

As in range spectral filtering, the decorrelation from the azimuth spectral misalignment between the master and slave image should also be compensated before coregistration. For the difference of the Doppler central frequencies of the two SAR images $\mu_0 = f_{Dc,1} - f_{Dc,2}$ as shown in equation 2.53, an azimuth spectral filter can be designed with the bandwidths W_1, W_2 , with the centre frequencies μ_1 and μ_2 given by

$$\begin{aligned} W_1 = W_2 &= B_\mu - \mu_0, \\ \mu_1 &= \frac{\mu_0}{2}, \quad \mu_2 = -\frac{\mu_0}{2}. \end{aligned} \quad (3.40)$$

Range Migration and Offset Interpolation

The distance from a radar to a surface target changes during the time of view S (azimuth integration time), and so the range-compressed point target response occurs at different ranges for different pulses. This is known as range migration (Curlander and McDonough, 1991, p. 172). The azimuth signal needed for the azimuth compression processing must therefore be assembled from different range resolution cells, depending on the pulse number. The locus of these range cells in the data array

is just a curve of $R(s)$, approximately represented by equation 3.20. The linear part of the curve represents the range walk and the quadratic part represents the range curvature. The total change $\Delta R = R(s) - R_c$ is the range migration, which might involve higher order terms in the expansion of $R(s)$, but is usually unnecessary.

The range migration procedure can be applied in the data array in the azimuth frequency domain after range compression, assuming slow variations in azimuth compression parameters f_{Dc} , f_R with slow time s . Each range bin is interpolated and shifted by the amount of $-\Delta R$ in range direction to assemble the exact locus of each target point.

For a slave image, any necessary offset in range and azimuth direction with respect to a master image can be adjusted in R_c and s_c using the two dimensional offset functions $\Delta R_c(s_c, R_c)$ and $\Delta s_c(s_c, R_c)$ obtainable from the coregistration process.

3.2.3 Coregistration Offset Functions

For InSAR processing, two or more SAR complex images should be accurately coregistered. A registration error of the order of a resolution cell results in total loss of coherence as shown in equation 2.42. Conventionally, one image is set as a master and other slave images are coregistered to that master image. Since the coordinate system of each SAR image is related to the satellite orbit, a very good initial estimation of the coregistration relationship can be achieved from the satellite orbit data. More accurate coregistration is necessary for InSAR purposes, and this can be achieved from analysis of the image itself.

There are several coregistration methods available based on either frequency or spatial data analysis. One efficient method is the amplitude offset method. A small patch of the scene is initially selected from both master and slave images. For sub-pixel coregistration accuracy, two SAR complex images need to be interpolated into the desired sub-pixel. A pixel accuracy of 1/32 is sufficient for most InSAR processing. The amplitude values of two patches of SAR data are cross-correlated,

and the offset value in range and azimuth will be decided at the position of the maximum value of the cross-correlation. This process is performed for several patches over the entire scene so that the two-dimensional offset functions in range and azimuth can be obtained by solving the following equations for coefficients a and b as

$$\Delta R_c(s_c, R_c) = \sum_{n=0}^N \sum_{r=0}^n a_{n-r,r} R_c^{n-r} s_c^r, \quad (3.41)$$

$$\Delta s_c(s_c, R_c) = \sum_{n=0}^N \sum_{r=0}^n b_{n-r,r} R_c^{n-r} s_c^r. \quad (3.42)$$

Approximation up to quadratic order is accurate enough for most InSAR processing, so that $N = 2$.

Some target points give erroneous offset values. These points are mainly from mountainous regions, oceans, or corner reflectors and they can be removed by a number of processing schemes (Smith, 1998b). Firstly, the points having extremely high values of SAR intensity should be avoided to exclude the corner reflectors. Secondly, the points having excessive deviations from the estimated offset function should be removed. The refined offset values are then used to estimate the two-dimensional offset function of azimuth and range. The slave image is then shifted and resampled, according to the offset functions, through interpolation during the range migration procedure.

3.3 InSAR Coherence Image Generation

From the two coregistered SLCs, an interferogram can be generated by calculating the phase difference of two signals pixel by pixel. This “raw” interferogram with a non-zero baseline contains phase fringes mainly from the system geometry and topography. The system geometric phase fringes and the spatial decorrelation factor from local slope variation should be removed so that only the temporal decorrelation can be evaluated from the level of coherence.

The general data processing procedures for coherence map generation are as follows. First, the system geometric phase is removed using the *Earth flattening* procedure. The remnant phase fringes can be assumed as those from topography. The topographic phase fringe number is calculated to determine the parameters for range spectral filtering for local slope variation to compensate the decorrelation from range spectral misalignment.

The following sections describe in detail the processing for InSAR coherence image generation

3.3.1 Earth Flattening - System Geometric Phase (ϕ_0) Removal

The *system geometric phase fringe number* in slant range can be calculated from equation 2.11 when $\alpha = 0^\circ$ as

$$k_{\phi_0} = \frac{2B_{\perp}}{\lambda R \tan \theta_i^0}. \quad (3.43)$$

The fringe number from InSAR geometry ϕ_0 is strongly dependent on the baseline perpendicular component B_{\perp} . The removal of this phase is essential for coherence estimation especially when the InSAR image pair was configured with a large enough baseline to produce sufficient height sensitivity for topographic mapping.

When sufficiently accurate system and orbit data are available, which is generally true for ERS-1/2, Earth-flattening is a relatively easy task. Since the orbit state vectors containing the position and velocity information of the satellite are sparsely time sampled, an orbit propagator program, such as “getorb” of Delft Institute for Earth-Oriented Space Research (DEOS), is necessary to obtain the precise orbit parameters for the scene (Scharroo and Visser, 1998).

The system geometric phase can be compensated by considering the elliptical earth surface (e.g. WGS84) where the surface elevation is zero ($z = 0$). The look angle on

zero-elevation surface, θ_l^0 , is determined from the geometric relations ΔS_1OP in Figure 2.3 as

$$\theta_l^0 = \cos^{-1} \left(\frac{R_1^2 + (r_e + H)^2 - r_e^2}{R_1(r_e + H)} \right), \quad (3.44)$$

then the phase difference from the system geometric phase is determined as

$$\phi_0 = \frac{4\pi}{\lambda} \Delta R|_{z=0}, \quad (3.45)$$

where

$$\Delta R|_{z=0} = \sqrt{R_1^2 + B^2 + 2R_1B \sin(\theta_l^0 - \beta)} - R_1. \quad (3.46)$$

The system geometric phase ϕ_0 is then removed from the interferogram to give the Earth-flattened interferogram,

$$\phi_{flat} = \phi - \phi_0. \quad (3.47)$$

3.3.2 Range-varying Spectral Filtering

To compensate for the spatial baseline decorrelation from range spectral misalignment, the flat-earth approximation, applied in range spectral filtering (section 3.2.1), is not sufficient and the range-varying filter must be used to incorporate the local topographic variation. Although the spectral misalignment is a function of the local slope (equation 2.55), knowledge of the local slope information is not necessary *a priori* in this processing. The reason for this is that the amount of range spectral misalignment v_0 , given in equation 2.55, is equivalent to the interferometric phase fringe frequency f_ϕ in equation 2.12. The estimation of the interferometric phase fringe frequency from the interferogram can therefore be used to design the range-varying spectral filter similar to equation 3.9. The bandwidths and central frequencies of the filter can be estimated from the fringes of interferogram after Earth-flattening.

3.3.3 Coherence Calculation

The coherence is the magnitude of the complex correlation coefficient calculated within an averaging window of the complex Earth-flattened interferogram as

$$\rho = \frac{\left| \sum_{l=1}^L u_1(l) u_2^*(l) e^{j\phi_{flat}} \right|}{\sqrt{\sum_{l=1}^L u_1(l) u_1^*(l)} \sqrt{\sum_{l=1}^L u_2(l) u_2^*(l)}}. \quad (3.48)$$

For unbiased coherence estimation, it should be assumed that the scene is locally stationary and ergodic within the averaging window. The size of the averaging window L is determined by a trade-off between unbiased coherence estimation and spatial resolution. Selecting a small averaging window ensures high spatial resolution, but may risk the bias of coherence estimation towards higher values especially in low coherence area (Touzi *et al.*, 1999). On the other hand, using a large averaging window may underestimate the coherence when the scene is inhomogeneous especially on steep slopes. These relations will also be further explained in Chapter 7.

3.4 Summary

This chapter presents principles and algorithms of SAR and InSAR data processing for coherence image generation. SAR compression uses a rectangular algorithm that consists of range and azimuth compression processing. Range spectral filtering is followed by matched filtering and Hamming weighting filtering for range compression. Doppler parameters are refined by clutterlock and subaperture correlation methods for range migration and azimuth compression. Two SAR SLC images are coregistered to generate “raw” interferogram. Coherence image is then produced after Earth-flattening and range-varying spectral filtering procedures.

The principles and algorithms for SAR and InSAR data processing described in this chapter give a general reference for the interpretation of various surface features using coherence images in the following chapters. The dedicated procedures for coherence estimation described in this chapter cannot overcome the total loss of information on directly radar-facing slopes, which will be investigated further in Chapter 5. In addition, coherence estimation needs further refinement to eliminate artefacts from topographic phase fringes that serves as scene nonstationarity, which will be discussed in Chapter 7.

Chapter 4: Land Surface Change Detection in the Sahara Desert, Algeria using InSAR Coherence Imagery

4.1 Introduction

With the development of radar interferometry techniques, the value of multi-temporal coherence imagery as a useful information source for surface change detection has been widely recognised and many successful application cases have been reported (Corr and Whitehouse, 1996; Ichoku, *et al.*, 1998; Schwäbisch, *et al.*, 1997; Smith and Alsdorf, 1997).

The ERS-1/2 platforms have accurate positional data and can revisit the same area from the same orbit with only a few tens to a few hundred metres drift (baseline). A spaceborne interferometer mechanism can thus be established using repeated multi-temporal SAR imagery data. A SAR image is composed of pixel values recording not only the intensity but also the phase of the signal. Any pixel of such a complex image can be regarded as a vector. The magnitude of the vector (intensity) is mainly dependent on the combined physical properties of the scatterers in a resolution pixel while the phase is sensitive to scatterer geometry and position.

SAR coherence is defined as the vector local correlation in a small neighbourhood between two complex SAR images as described in Chapter 3. If there is absolutely no change on the land surface between two SAR image acquisitions from the same orbit with minor drift, and the two images are perfectly co-registered, the phase difference between the two images in a small neighbourhood will be a constant and thus result in nearly full coherence. Any random changes in scatterers on the land surface during the two acquisitions will cause irregular variation of phase and reduce the coherence. If the random variation exceeds a half wavelength of the radar beam in the slant range direction, the vectors will lose local correlation resulting in decoherence. Therefore, coherence provides a reliable method for detection of random changes on the land surface though it does not give direct information of the nature of these changes.

This chapter presents the results of a case study of land surface change detection and interpretation in an arid area of the Sahara desert in Algeria using ERS-1 SAR multi-temporal coherence images. It will emphasise interpretation and some interesting change phenomena found in these images.

4.2 The Study Area

The area chosen for study is in eastern Algeria near the border with Libya in North Africa, 100 km × 106 km, at approximately $N27^\circ \sim 28^\circ$, and $E8^\circ \sim 9^\circ$. The Atlas Mountains separate the warm and temperate region along the coast of the Mediterranean from the vast hot arid or hyper-arid desert: the Sahara. With very low humidity levels of from 5% to 25%, the rainfall is rare, the solar radiation is intensive and the diurnal variation of temperature is large in the region (Ahrens, 1994).

The very low precipitation and excessive evaporation make the desert hyper dry, barren and almost completely devoid of surface vegetative cover. This absence of a binding agent allows the loose sand or topsoil to migrate according to the prevailing wind patterns. It has been observed that the desert conditions of this region are expanding northwards, with the vegetation of marginal lands being stripped for firewood or animal fodder, further exposing fragile soils to erosion.

As shown in a colour composite of a Landsat TM image in Figure 4.1, the main geographic features of the study area are large expanses of flat bare rock or gravel plains broken up by escarpments, gully networks and ephemeral drainage channels, some of which flow into elongated lakes or depressions. Large parts of the region are covered with sand of linear, barchanoid, and star dune types, as well as thin sand sheets.

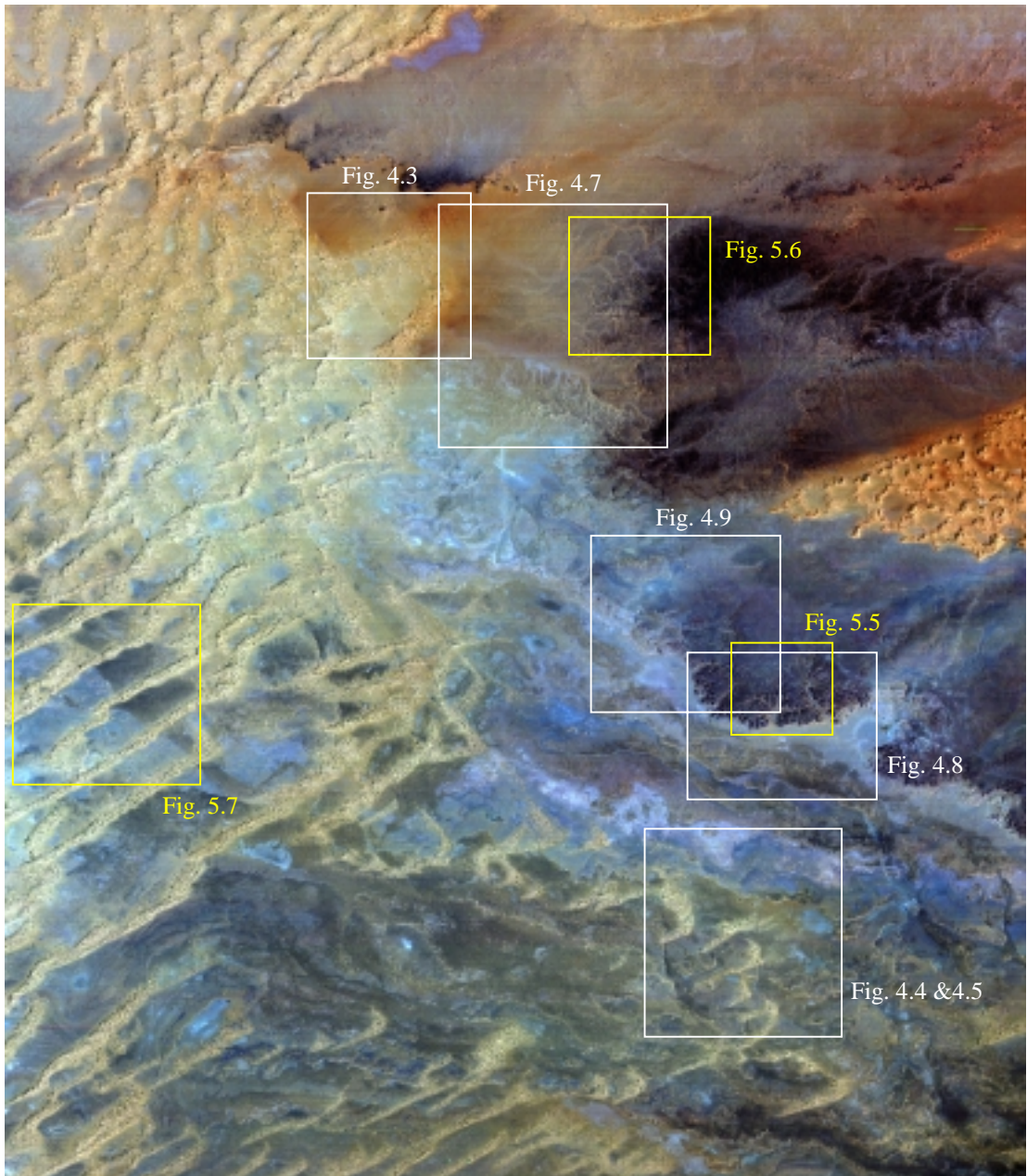


Figure 4.1 Study area: Landsat TM band 421 in RGB (100 km × 106 km).

4.3 Data Processing and Evaluation

4.3.1 Coherence Image Generation

Three scenes of ERS-1 SAR data of a region in the Sahara desert, Algeria, acquired on 8th September 1992 (ALG1), 13th October 1992 (ALG2), and 28th September 1993 (ALG3) have been processed to generate coherence images (Table 1.1). These images were all taken during descending orbits in dry weather conditions. A coherence image between ALG1 and ALG2 is labelled as ALG12_COH (35 days separation and 263m of B_{\perp}) and so on for ALG23_COH (350 days separation and 105m of B_{\perp}) as shown in Table 4.1.

A series of signal processing techniques have been applied to produce unbiased estimations of coherence including accurate image co-registration, range spectral filtering, and use of an optimised sample average window. Single look complex (SLC) images were co-registered within 1/32 of a pixel that is accurate enough for most InSAR techniques. ALG2 was used as a master image to which ALG1 and ALG3 were coregistered. This scheme gives shortest baseline between three images that minimises any possible coregistration error. A relatively small window with 10 pixels only in azimuth direction satisfied both requirements of high contrast coherence image and high spatial resolution in this flat, hyper-arid, and stable region.

Table 4.1 Theoretical and actual coherence (ρ).

| Coherence Image | ΔT (days) | B_{\perp} (m) | ρ_{theory} | $\rho_{actual} \pm \text{std.} (\rho_{actual} / \rho_{theory})$ | | |
|-----------------|-------------------|-----------------|-----------------|---|---------------------------|---------------------------|
| | | | | Stable area | Full scene | Gully area |
| ALG12_COH | 35 | 263 | 0.80 | 0.65 \pm 0.13 (0.81) | 0.52 \pm 0.21 (0.65) | 0.39 \pm 0.18 (0.49) |
| ALG23_COH | 350 | 105 | 0.92 | 0.75 \pm 0.13 (0.81) | 0.56 \pm 0.24 (0.61) | 0.61 \pm 0.18 (0.67) |
| ALG13_COH | 385 | 368 | 0.71 | 0.52 \pm 0.15 (0.73) | 0.43 \pm 0.19 (0.60) | 0.35 \pm 0.16 (0.49) |

4.3.2 Evaluation

There are several decorrelation factors that cause the loss of coherence in multi-temporal coherence imagery. In addition to temporal change of the land surface, which is the objective of the study, a major factor reducing coherence level is the baseline distance. Spatial decorrelation caused by baseline separation is an inherent factor of the multi-pass, multi-temporal interferometric SAR system. The baseline component perpendicular to the radar look direction (B_{\perp}) decides the difference in view angles for the same ground target between the two tracks. The phase of a radar return signal is decided by the vector summation of all the scatterers within a pixel area corresponding to a radar sampling time interval. These scatterers react to radar beams differently depending on the illumination angle. If B_{\perp} is significant, the radar beam will illuminate the same ground target at quite different angles and the collective effects of the relevant scatterers will result in a certain degree of random phase change. Thus the coherence decreases with the increase of B_{\perp} as characterised in the formula below (Zebker and Villasenor, 1992),

$$\rho_{theory} = 1 - \frac{2 \cos \theta R_y}{\lambda R} B_{\perp}, \quad (4.1)$$

where θ is the incidence angle, R_y the ground range resolution, λ the radar wavelength and R the distance from the radar sensor to the centre of a resolution element. (Details of this relationship are in Chapter 5.)

These data together with the actual average coherence values of the whole scene, a high coherence area, and an area with gully features are shown in Table 4.1 and Figure 4.2. The theoretical coherence value declines steadily with the increase of B_{\perp} . The average coherence for the whole scene is much lower than the theoretical values for all the three coherence images because of very low coherence in the large areas covered by mobile sand. The average coherence over a stable barren land surface is 0.74 for ALG23_COH while those for ALG12_COH and ALG13_COH are 0.65 and 0.43, respectively, as the result of spatial baseline decorrelation. The standard deviation of ALG23_COH over the whole scene is the highest (0.24) among the three coherence images due to the shortest B_{\perp} (105 m) resulting in the highest image

contrast. The average coherence over a stable and flat land surface for ALG23_COH is about 30% higher than that for ALG13_COH.

The ratios between the actual and the theoretical coherence values for a coherence image give an evaluation of the relationships between B_{\perp} , the local slope and coherence level. In an area of very stable flat surface, $\rho_{actual}/\rho_{theory}$ is nearly a constant for all the three coherence images as is expected. In the gully area, however, $\rho_{actual}/\rho_{theory}$ values drops down suddenly (26%) as B_{\perp} increases between ALG23_COH and ALG12_COH (from 105m to 263m) due to the decorrelation effect on a directly radar-facing slope (Lee and Liu, 2000a). This phenomenon will be discussed further in section 4.4.5.

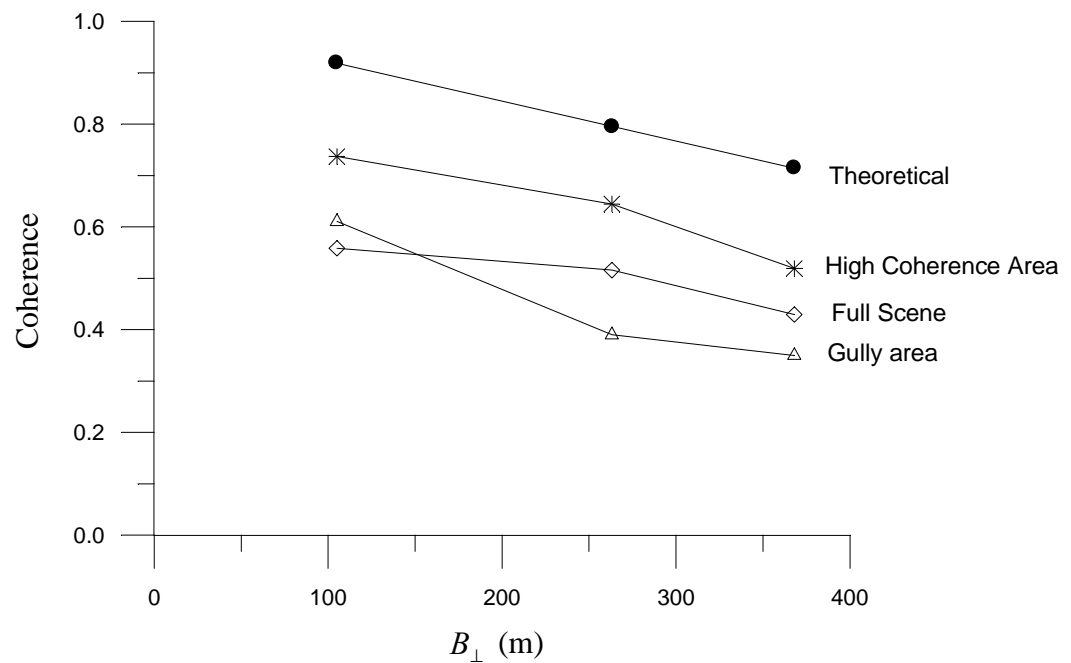


Figure 4.2 Comparison of coherence levels between the three coherence images.

4.4 Image Interpretation for Change Detection

4.4.1 Interpretation Principle

The study area has a very stable climatic environment. The factors causing random changes of land surface are sand movement, erosion and deposition by wind or occasional flash flooding, and very limited human activities mainly relating to oil exploration. These changes will cause the decrease and loss of coherence and form dark features remarkably obvious against the high coherence background of a stable barren land surface. With three images taken with 35, 350 and 385 day temporal separation, simple logical analysis is effective for interpreting the nature of the changes. Typically, there are 6 possible scenarios, as shown in Table 4.2.

Table 4.2 Possible coherence scenarios.

| Scenario | Level of coherence | | Interpretation |
|----------|--|---|---|
| | ALG12_COH 8/9/92 -13/10/92 (35 days) | ALG23_COH 13/10/92-28/9/93 (350 days) | |
| 1 | High | High | Stable, no change. |
| 2 | High | Low | Stable, then substantial change after 13/10. |
| 3 | Low | High | Sudden change within 35 days then stable in the following 350 days. |
| 4 | Low | Low | Continually substantial change over whole period. OR Sudden change in 35 days followed by substantial change in 350 days. |
| 5 | Medium | High | Slight change until 13/10, then stable. |
| 6 | Medium | Low | Slow and progressive change over a whole period. |

4.4.2 Sand Movement

Several types of sand dunes are present in the area, including transverse barchan and linear types, and star dune networks. These are generally evident on TM imagery (Figure 4.1), which shows the morphology and structure of individual dune features. To define the boundaries of a dune or dune-field and to identify thin sheets of mobile sand are not always possible using TM or other types of optical imagery, particularly when the spectral properties of sand are very similar to solid basement, as shown in Figure 4.3(a). SAR amplitude imagery is even less satisfactory for the task as shown in Figure 4.3(b) because the tone variation of the image is relevant to surface roughness rather than spectral or dynamic properties.

In contrast, coherence imagery is very effective for dune boundary delineation and mobile sand sheet identification, enabling assessment of dune movement and sand encroachment. The loose sand grains on dune surfaces or thin sand sheets on a solid basement plain are subject to a continuous movement by the wind even though the dune is static as a whole. The sand movement causes random changes of the micro-geometry of volume scatterers on the sand covered land surfaces and thus results in loss of coherence over a very short period (Liu *et al.*, 1997) as characterised by scenario 4 in Table 4.2. The very dark decoherence features of mobile sand over a bright high coherence background are not only direct evidence of sand mobility but also effectively delineate the outlines of active dunes and optically indiscernible thin sand sheets. These data are not easily obtainable over a large region using conventional means and other earth observation techniques.

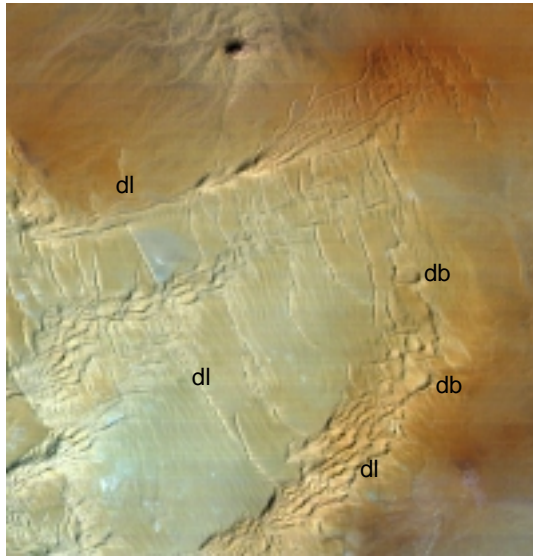
As illustrated in Figure 4.3(c), complex boundaries of three chains of dunes (barchan and linear types) in the region are sharply defined in the ALG12_COH image as decoherence patches over a high coherence background. The boundaries are distinctive and definite. With 350 day temporal separation, ALG23_COH in Figure 4.3(d) reveals a thin sheet of mobile sand spreading into the inter-dune areas making the whole dune field a nearly continuous decoherence patch. The central part of the dune-field is typically characterised by scenario 6 in Table 4.2 as medium coherence

in ALG12_COH and low coherence in ALG23_COH indicating continuous transport of the sand sheet as it is swept over the barren land surface.

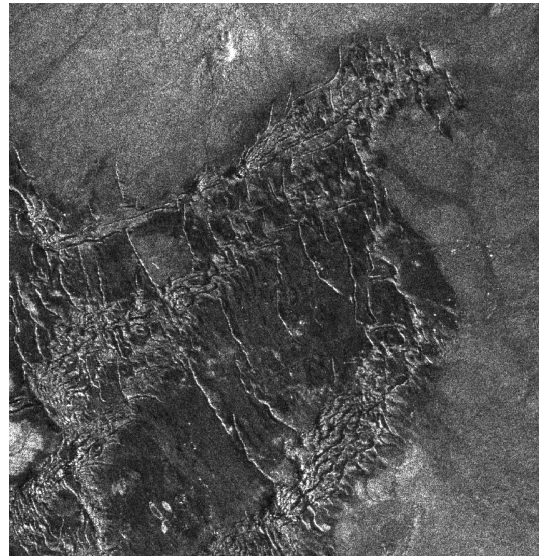
The dune positions are defined effectively in coherence images of 35, 350 and 385 days temporal separation. As the three coherence images are very accurately co-registered to sub-pixel level, a colour composite of them may reveal possible dune migration, which occurred during the 385-day period. For a colour composite of ALG12_COH in red, ALG23_COH in green and ALG13_COH in blue, a migrating barchan dune would be presented as a dark decoherence feature with narrow trailing edge in red and windward edge in green. As illustrated in Figure 4.4(a), this diagnostic pattern is not evident for following reasons:

- The large formations of approximately 1 km wide are static as a whole, as confirmed by comparison between the SAR multi-look amplitude images and the TM image. These large formations consist of small barchanoid ridges 50m wide, which themselves are likely to be the migrating features but the migration cannot be detected in the largely decoherent background of the sand sea.
- Even dunes migrating rapidly at 20 m per year would not produce a substantial signal on images of 35- and 350-day intervals, at a coarse pixel resolution of around 30m.

In order to make a serious attempt to identify dune migration, coherence imagery with a temporal separation of at least two years and a very short B_{\perp} are suggested.



(a)



(b)



(c)



(d)

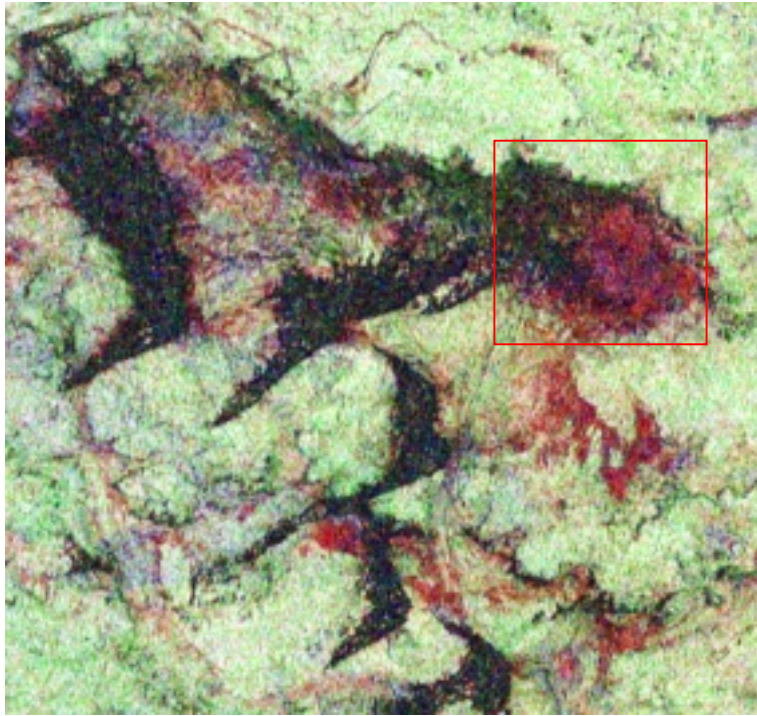
Figure 4.3 Dune boundary definition and mobile sand detection. (a) Landsat TM band 421 in RGB. db: barchan dune, dl: linear dune. (b) Multi-look amplitude image of ALG1 scene. (c) ALG12_COH: the coherence image of 35-day separation. (d) ALG23_COH: the coherence image of 350-day separation.

4.4.3 Ephemeral Lakes and Water Bodies

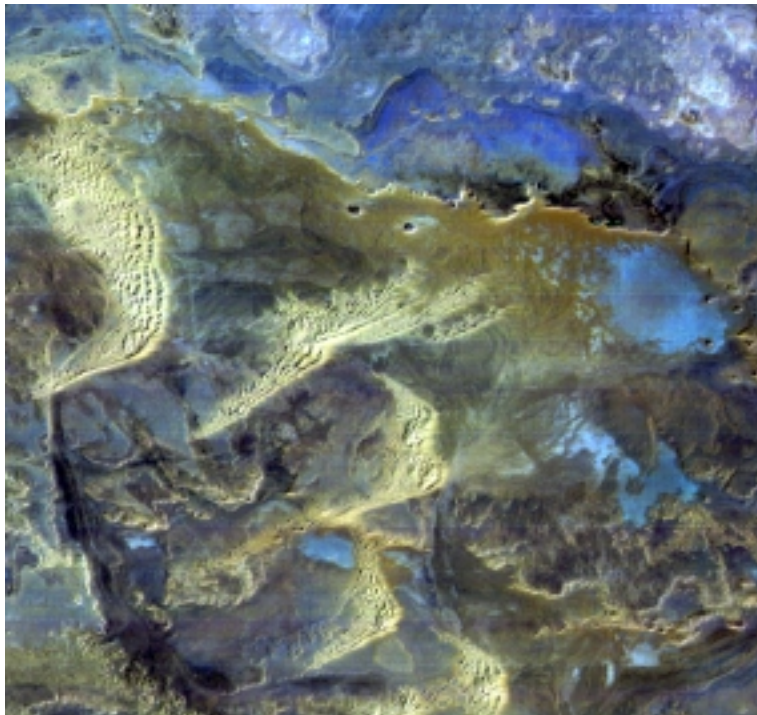
The RGB colour composite of coherence images is an effective aid for logical analysis of various land surface changes events. The area indicated by a box in the coherence colour composite in Figure 4.4(a) presents several well-defined red patches. They appear to correspond closely with the distribution of bright cyan features on the Landsat TM 421 colour composite in Figure 4.4(b), which are defined as shallow ephemeral lakes in a reference map of the area (DMAAC, 1981). However, the analysis of TM multi-spectral information indicates that the lakes were nearly dry when the TM image was taken on 10 February 1987. As shown in Figure 4.5(a) and 4.5(b), the lake patches are not particularly dark in near infrared band TM4 and very bright in the thermal band TM6. This characteristic is contradictory to the typical water spectral signature: strong absorption in TM4. The area in fact presents an unusual spectral property: high albedo and high thermal emission. In general cases, high albedo objects would have low thermal emission (Liu *et al.*, 1997). The exceptional cases may occur for crystallised transparent material with strong internal scattering such as snow, gypsum and salt. It is reasonable to presume that this dried lake basin is covered with salt deposits.

Red pixels in Figure 4.4(a) are those coherent in ALG12_COH (Figure 4.5c), but not in ALG23_COH (Figure 4.5d), logically implying a slow changing environment that appears relatively stable in the short-term (35 days) but the accumulated progressive change is substantial over a much longer period (350 days). It is therefore suggested that the lake basin was dry during the initial 35 days with a relatively stable surface. This condition allows medium to high coherence in ALG12_COH. Then in the following 350 days, the lake possibly experienced recharges of floodwaters, temperature variation over a considerable range and repeated salt mineral crystallisation due to the water level change. Any of these processes can produce random changes significant enough to result in decoherence in ALG23_COH. This explanation is supported by monthly average precipitation data (Rudolf *et al.*, 1994; GPCC, 1998) of the area during the period as shown in Figure 4.6. There was 6-10 mm precipitation in the winter 1992 and 5-6 mm in the autumn 1993, which is adequate to cause seasonal recharge to the lake.

Numerous similar features can be identified in the whole ALG scene using the same logic and methodology, which correspond well with ephemeral lakes in the Landsat TM421 RGB colour composite (Figure 4.1). Reliable identification of these desert lakes cannot be achieved without the TM colour composite. The extra contribution of the multi-temporal SAR coherence imagery is the detection of the ongoing change in these lakes.



(a)

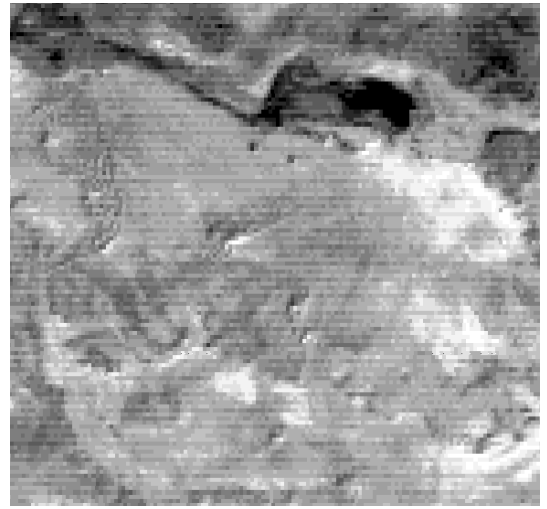


(b)

Figure 4.4 Dune migration and change in ephemeral lakes. (a) Colour composite of ALG12_COH, ALG23_COH, and ALG13_COH in RGB. (b) Colour composite of Landsat TM band 421 in RGB.



(a)



(b)



(c)



(d)

Figure 4.5 The spectral and coherence properties of an ephemeral lake. (a) TM band 4. (b) TM band 6. (c) ALG12_COH . (d) ALG23_COH .

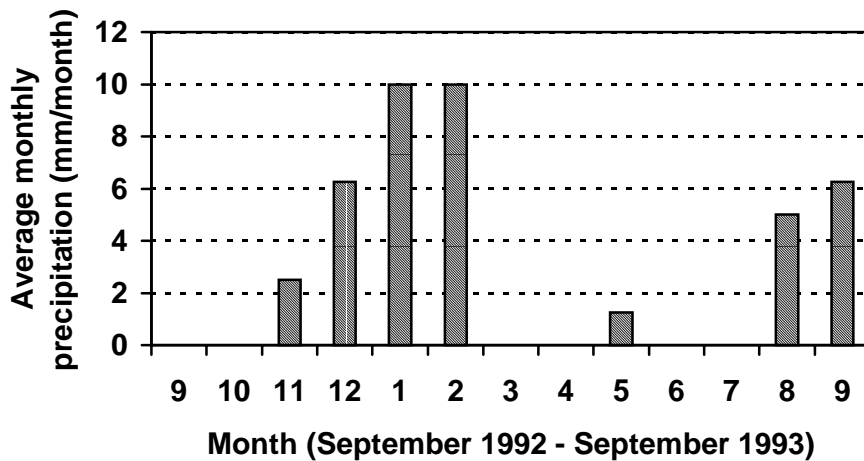


Figure 4.6 Average monthly precipitation from September 1992 to September 1993 for the study area in the Sahara desert (E7°-9°, N27°-28°) (Rudolf *et al.*, 1994; GPCC, 1998).

4.4.4 Drainage Pattern and Erosion

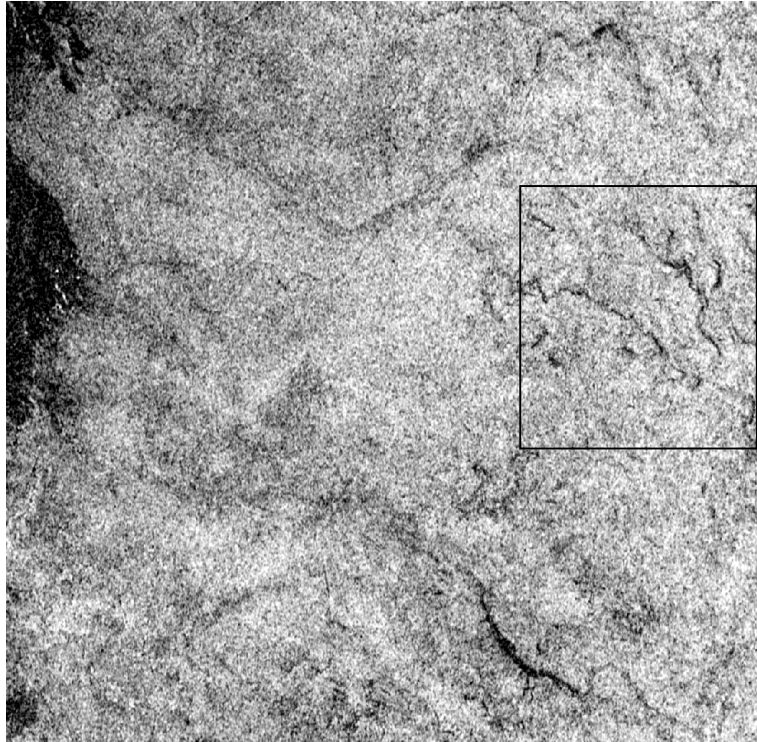
The dominant erosional agent in the Sahara desert is the prevailing wind, but occasional and isolated intense rainstorms can cause local flooding and rapid fluvial erosion/deposition. Multi-temporal SAR coherence imagery provides direct evidence of erosion. As information on the spatial location and temporal frequency of such erosion events is lacking, coherence imagery is a valuable potential source of such data.

As shown in Figure 4.7(a), the coherence image ALG12_COH illustrates an area with high coherence over the initial 35-day period. There are no obvious water channel features except for a small section of channel approximately 30 m wide near the southeast corner with low coherence. The subsequent ALG23_COH image in Figure 4.7(b), on the other hand, exhibits two separate major channels as obvious decoherence features in a high coherence background. These features are very prominent from the east and gradually become less pronounced further downstream towards the west. This characteristic supports a hypothesis of localised flooding from isolated storms, coupled with high transmission losses and evaporation causing

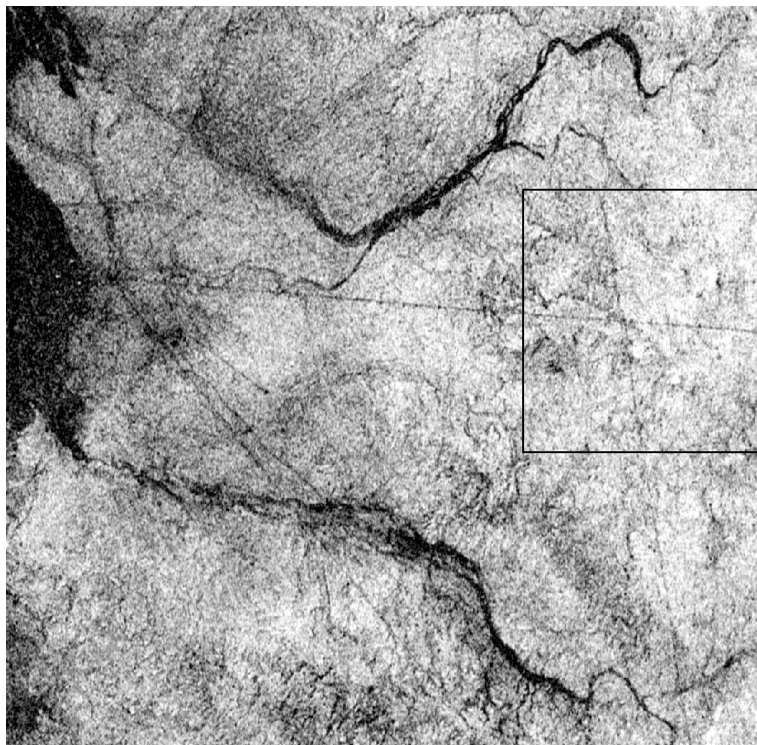
surface flow to diminish downstream. Therefore, it can be assumed that the channels were dry and stable in the initial 35 days, and then in the subsequent 350 days there was active erosion and deposition caused by rainfall (possibly as well as the prevailing wind).

The erosion characteristics of wind and water are very similar, and can be confused. In the case of Figure 4.7, due to the apparent decoherence of tributary stream networks, the braided pattern of the southernmost channel, and the assumption that aeolian erosion would be more constant and less constrained by existing water channels, seasonal flooding is more likely the major cause of these decoherence features.

It is interesting to notice the coherence features in a boxed area in Figure 4.7. The stream-like features can be easily misunderstood as those from temporal decorrelation in river channels. Comparing two coherence images reveals that it has low coherence in 35-day coherence image (ALG12_COH) but high in 350-day coherence image (ALG23_COH). This controversial phenomenon is not easily explicable in terms of temporal surface change relationship. Similar features are found in some other areas, which will be shown in detail in the following section.



(a)



(b)

Figure 4.7 Drainage channels. Two major rivers in the region are not visible in (a) the 35 day separation coherence image ALG12_COH but clearly shown in (b) the 350 day separation coherence image ALG23_COH as decoherence features. The boxed area shows a controversial case: low coherence in ALG12_COH but high coherence in ALG23_COH.

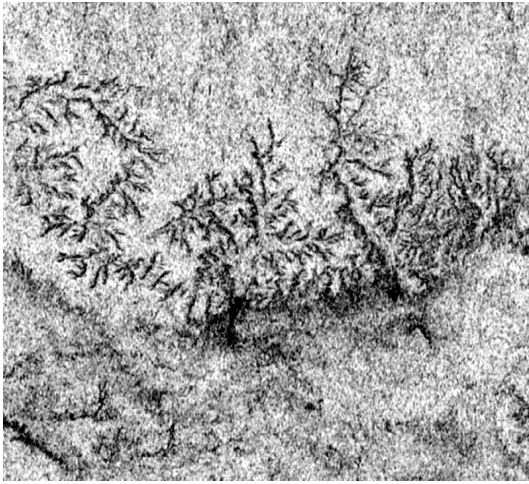
4.4.5 Gully Features – Radar-facing Slopes

Similar to the case shown in the box in Figure 4.7, Figure 4.8 presents an interesting and controversial case of drainage patterns. The ALG12_COH in Figure 4.8(a) illustrates very distinctive gullies which are typical fluvial erosion features in arid lands. These decoherence gully features contrast sharply with a high coherence background, providing evidence of rapid fluvial erosion over a 35-day period in this arid region! Detailed observation does not support this conclusion. The bottoms of major valleys to which the gullies are attributed show high coherence. If there was significant erosion in the gullies, the material transported to the valleys should have caused the valley bottoms to lose coherence.

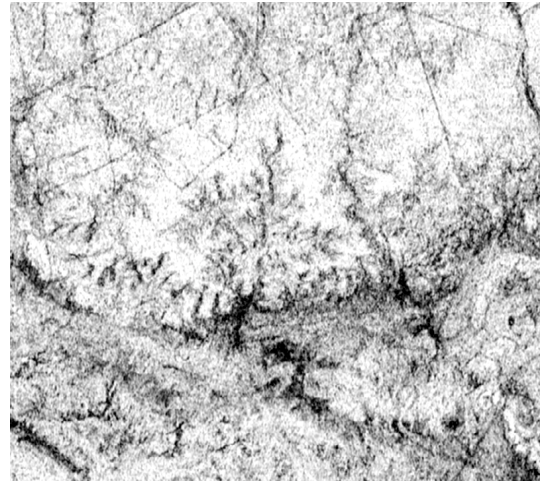
The ALG23_COH image of the same area in Figure 4.8(b) reveals the other side of the coin: the same gully patterns show much higher coherence. The decoherence features along many gully walls in ALG12_COH appear in very high coherence in ALG23_COH. These gully walls are highlighted in bright green in a colour composite of ALG12_COH in red, ALG23_COH in green and ALG13_COH in blue as shown in Figure 4.8(c). This evidence eliminates the possibility of intensive fluvial erosion in 35 days as well as in the subsequent 350 days.

So, what is the cause of the gully decoherence in ALG12_COH? Referring to the amplitude image in Figure 4.8(d), it is obvious that the gully decoherence features in ALG12_COH mainly occur along east-facing slopes where the foreshortening effect is significant under direct radar illumination. As discussed in section 4.3.2, a longer B_{\perp} between two SAR images means a greater difference in view angles to the same target. On a foreshortened slope, the return radar signals from nominal equal range positions will be recorded as one point with enhanced intensity. The phase of such a point is decided by the vector summation of all the overlapping return signals. The change of view angle will change the combination of equal range positions along a foreshortened slope and thus the composition of the overlapped return signals. As a result, the phases of pixels on a foreshortened slope are subject to random variation with the slight change of view angles. The random phase variation is not significant for a short B_{\perp} and the signal can result in strong coherence as in the case of ALG23_COH. However, with a long B_{\perp} , the random phase variation becomes

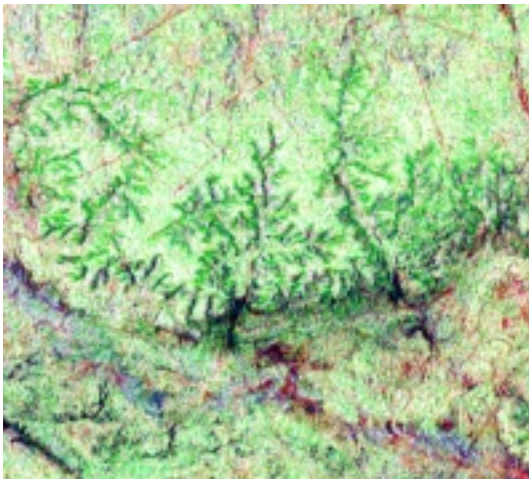
significant and thus results in a dramatic drop of coherence on foreshortened slopes, as in the case of ALG12_COH (as well as ALG13_COH). This explanation is supported by the data in Table 4.1 and Figure 4.2, showing that the decrease of coherence with the increase of B_{\perp} is more significant in this gully area than in other areas. The physical and mathematical proof of this phenomenon will be shown in Chapter 5.



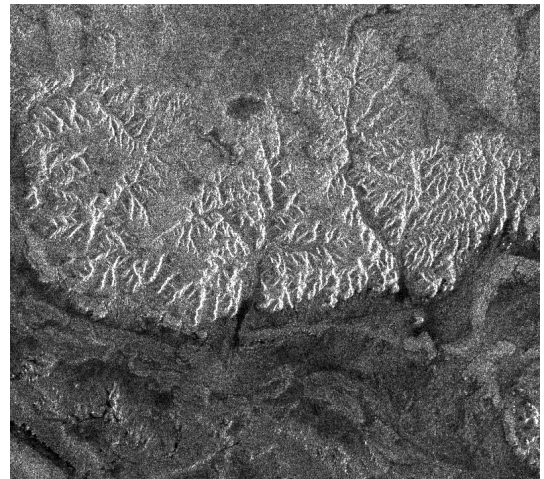
(a)



(b)



(c)



(d)

Figure 4.8 Gully features – decorrelation on radar-facing slopes. (a) ALG12_COH. (b) ALG23_COH. (c) Colour composite of ALG12_COH, ALG23_COH, and ALG13_COH in RGB. (d) SAR intensity image of ALG2 scene.

4.4.6 Geophysical Survey Lines

An unexpected finding of this study is the straight-line network shown in Figure 4.9. Obviously, these are the results of anthropogenic disturbance over the periods between the repeated SAR image acquisitions. These features are not present in the relevant SAR intensity images or Landsat TM image.

The coherence image ALG12_COH observed between 8 September and 13 October 1992 faintly reveals a few long, straight lines of low coherence (Figure 4.9a). The image ALG23_COH observed between 13 October 1992 and 28 September 1993 (Figure 4.9b) shows a much greater number of mostly parallel straight lines in a complex matrix, but with different orientations from those observed in ALG12_COH. They are clearly visible over this approximately 40 km × 40 km sub-scene area, with single lines up to 40 km long at a spacing of 2~3 km.

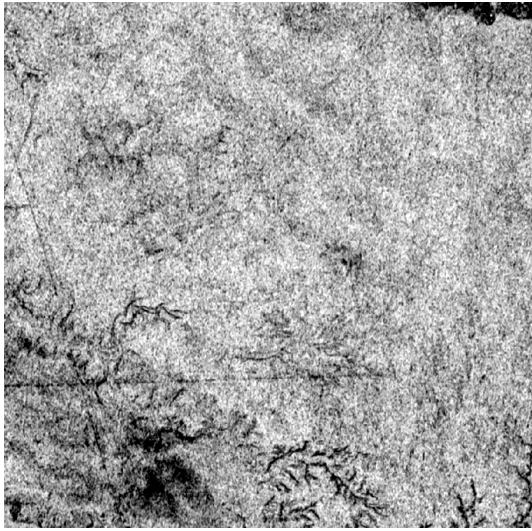
It is known that an oil company has been working in the area and several oil wells are located in the region of study. Thus a logical conclusion is that these straight lines are geophysical seismic survey transects. As the tracks of Vibroseis trucks did not change the average spectral property at a scale relevant to SAR spatial resolution, the features cannot be detected in the intensity image (Figure 4.9c). The disturbance has randomly altered the ground scatterers at a scale much greater than half a wavelength of the radar carrier wave (2.83 cm for C-band), causing decoherence along the survey lines between the SAR images taken before and after the events.

A map depicting all of the observed survey lines deduced from coherence imagery is presented in Figure 4.9(d). The survey engineering work might have been started well before 8 September 1992 but the survey lines generated before this date would not be evident on either ALG12_COH or ALG23_COH. ALG12_COH shows only a few survey lines, produced in the 35 days from 8 September 1992 to 13 October 1992. After 13 October 1992, a matrix of many survey lines was completed in a year. Straight lines in ALG12_COH do not occur in ALG23_COH because the survey lines dug after 8 September 1992 and completed before 13 October 1992 would be left undisturbed in the following 350 days. However, in the sub-scene of Figure 4.9, a few lines appearing in ALG12_COH can be faintly seen as discontinuous segments in

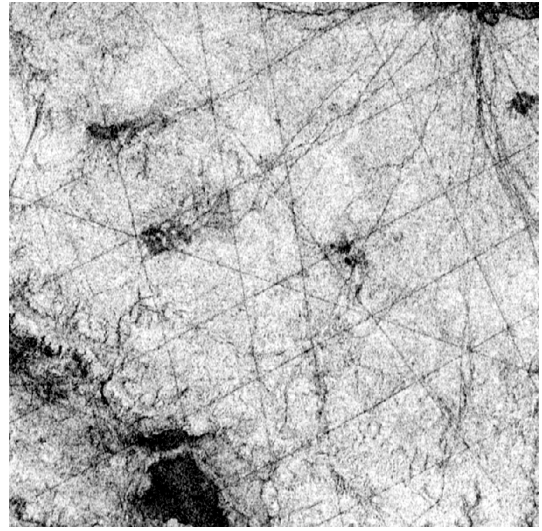
ALG23_COH. One possible explanation is that the seismic surveys along these lines were half way through on the date of 13 October 1992. The further engineering work to complete the survey and recover the land surface disturbed the ground and left a low coherence mark on ALG23_COH.

Besides straight lines, other low coherence linear features can also be observed in Figure 4.9(b). Some curved lines are obviously drainage patterns. A few slightly curved lines may be roads whose surface had been disturbed by vehicles.

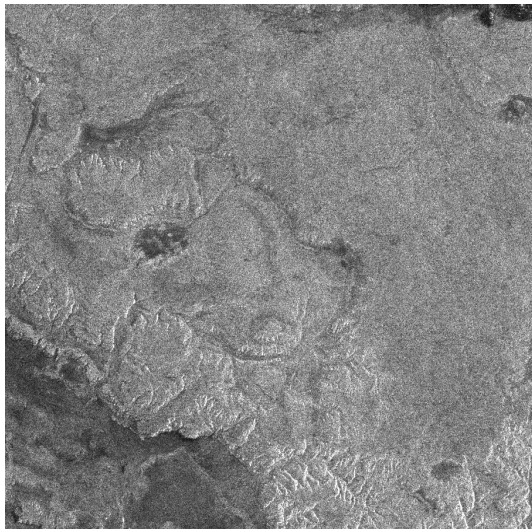
This case demonstrates coherence imagery as a tool for monitoring environmental impact of human activities.



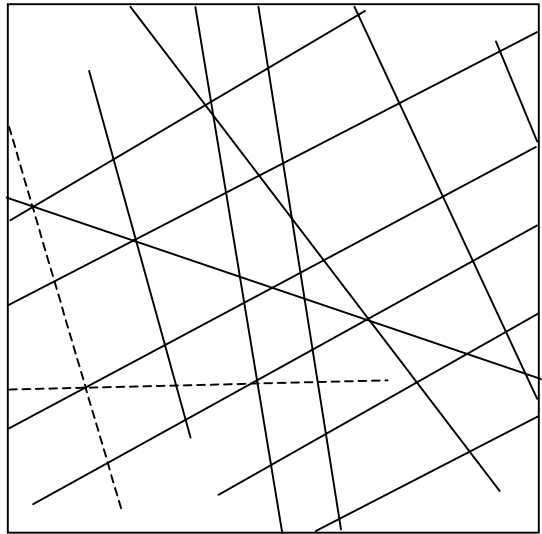
(a)



(b)



(c)



----- Lines in (a)
———— Lines in (b)

(d)

Figure 4.9 Geophysical (seismic) survey lines. (a) ALG12_COH. (b) ALG23_COH. (c) SAR 4-look intensity image of ALG3. (d) Interpretation of linear features.

4.5 Discussion

4.5.1 Advantages and Potentials of InSAR Coherence Imagery

The primary value of the InSAR coherence imagery lies in its ability to record subtle random changes on the land surface in an otherwise stable environment. Changes at this small scale (random change of more than 2.83 cm rms for C-band in the direction of slant range will in theory cause total decorrelation) cannot be detected on conventional optical imagery or SAR intensity image. The change detection technique based on multi-temporal InSAR coherence imagery is fundamentally different from the DInSAR based measurement technique. DInSAR technique is capable of measuring centimetre to millimetre-level land surface deformation but the application is limited only for a highly coherent area. On the other hand, coherence imagery is applicable for more SAR scenes that constitute the InSAR configuration regardless of surface stability.

In an arid environment such as the Sahara example explored here, the bare desert surface is an extremely stable landscape, which retains high coherence over very long periods (over several years). The contrast between this bright background and the dark decoherence signatures of any change elements permits immediate detection and delineation of unstable features. It is this property that permits the spatial and temporal mapping of surface processes with a confidence unrivalled by other earth observation techniques over areas too large or inaccessible for practical field surveys.

The results described in this chapter demonstrate the potential of SAR coherence imagery to detect and interpret changes in a desert environment. For example, persistent decorrelation over short time intervals is a direct evidence of sand mobility. Lack of rainfall data in remote desert regions hampers attempts to research the contribution of sporadic, catastrophic fluvial erosion to arid landscapes. A sequence of short time scale (monthly), frequent coherence images could provide information on the temporal and spatial distribution of the effects of localised sporadic flood

events. Coherence imagery also enables detection of human-induced surface change with time.

4.5.2 Limitations

A multi-temporal InSAR coherence image presents an objective record of unsystematic land surface changes between two SAR image acquisitions. Decoherence phenomena, however, can be presented as meaningful features only when they contrast with highly coherent background. The average stability of the environment limits the nature of processes that can be investigated using this technique. The technique is most effective in detecting changes in a largely stable environment, such as desert. It is not useful particularly in a highly unstable environment with many decorrelation factors, e.g., in tropical areas. Vegetation growth, variation of soil and air moisture, and frequent rainfall can result in decoherence, making interpretation for particular thematic information difficult if not impossible. On the other hand, with a very short time interval (e.g., ERS-1/2 tandem pairs), decoherence phenomena could be used to study vegetation growth (Hagberg *et al.*, 1995), soil moisture change and rainfall/erosion events but the data availability is very restricted.

The length of the baseline is an important factor in image quality. An InSAR image pair with large baseline will show degradation of coherence level especially in radar-facing slopes. Decoherence features from topography complicates the interpretation of InSAR coherence imagery. A zero B_{\perp} would be ideal for coherence based change detection though it is not desirable for DEM generation from SAR interferometry.

4.6 Summary

The results of a comprehensive interpretation of multi-temporal InSAR coherence images derived from three ERS-1 SAR images of eastern Algeria taken on 8 September, 13 October 1992 and 28 September 1993 are summarised as below.

- 1) Decoherence of individual dune features was due to micro-scale surface transport of mobile sand and volume scattering from radar penetration into the dry sand, but not dune migration. Micro-scale movement of sand particles is active over all the dune surfaces in the study area, allowing identification over short time intervals. With 30 m resolution coherence images in just over one year period, there was no definite evidence of any traverse dune migration. Analysis of coherence imagery is an effective and efficient tool in the mapping of mobile sand and dune distribution over large desert areas.
- 2) Ephemeral lakes and temporary water bodies in desert areas can be detected by coherence images and characterised as medium coherence features over a relatively short period (35 days in this study) and decoherence features over a long period (e.g. a year). The lake features detected in coherence images matched accurately with those in a Landsat TM image of the same area. The spectral and thermal properties of a major lake basin imply that the lake is saline. Coherence imagery cannot provide information of the mineral composition of the lake, but it shows evidence of changes of these ephemeral lakes.
- 3) Ephemeral flood courses and streams can be identified by channels which are clearly defined as decoherence features on the coherence image showing change over a year period (350 days) but present no obvious features on the coherence image of 35 days. The decoherence over the longer period is due to either fluvial erosion or deposition, or aeolian dry riverbed activity.
- 4) A long baseline can cause severe decoherence features on foreshortened slopes, resulting in prominent gully patterns which complicate the interpretation of coherence image. An InSAR image pair with a short baseline is therefore preferred for the coherence study.

- 5) Human-induced disturbances such as geophysical seismic survey lines can be identified as decoherence features on InSAR coherence imagery. Coherence images with different time intervals show different seismic lines dug over these periods. The phenomena are not shown in the relevant SAR multi-look intensity images and would probably be less obvious in TM imagery of the relevant date. This unique function of coherence imagery shows that it is a useful reconnaissance tool for monitoring environmental impact of human activities.

The methods used in this research are applicable to other arid desert regions. Recognising the controversial cases in the gully features, a physical and mathematical explanation of the spatial topographic decorrelation phenomenon in the radar-facing slopes and a method to identify such features will be presented in Chapter 5.

Chapter 5: Analysis of Topographic Decorrelation in SAR Interferometry using Ratio Coherence Imagery

5.1 Introduction

Multi-temporal Interferometric SAR (InSAR) coherence imagery is a useful tool to detect and monitor randomly changing land surfaces by measuring the degree of temporal decorrelation between the time-separated multiple SAR acquisitions. This technique has been refined by separating the temporal decorrelation factor from other possible decorrelation sources such as thermal noise, baseline, topography, misregistration, bias on coherence estimation, and atmospheric effects. Among these decorrelation factors, baseline and topographic factors are often called spatial decorrelation because they are relevant to the geometric relations of sensor position and target distribution.

In terrain with strong relief, topographic decorrelation due to the slope is often the dominant decorrelation factor. This type of decorrelation is an intrinsic property of a side-looking and ranging SAR system. It is so overwhelming, particularly on a foreshortened or layover slope that the coherence drops down dramatically towards zero. The low coherence features on these slopes can easily be misinterpreted, in the InSAR coherence imagery, as an unstable land surface subject to rapid random change even for a highly stable slope. The total topographic decorrelation, especially in an area where the local terrain slope is equal or similar to the radar look angle, is generally regarded as an obstacle for SAR interferometry and has not yet been fully investigated. In fact, this particular type of low coherence, once identified, can give useful information on surface topography.

There have been two different approaches to characterizing spatial decorrelation due to the baseline and the local terrain slope: the geometrical method (Zebker and Villasenor, 1992) and the spectral method (Gatelli *et al.*, 1994). In the geometrical method, a baseline decorrelation function is derived by cross-correlating two SAR signals with a given baseline length. This function is simply a Fourier transform of

the radar impulse response. It shows the relationship between the baseline and the coherence level, and gives a criterion for choosing the satellite orbits with baselines suitable for InSAR configuration. However, the effect of local terrain slope, which is the major factor causing the total decorrelation phenomenon on a directly radar-facing slope, has not been fully addressed in this method. In the spectral method, the frequency shift of the ground reflectivity spectrum between two SAR observations explains spatial decorrelation caused by both the baseline and the terrain slope. Applying range-varying spectral filtering by using terrain slope information derived from interferogram or pre-existing Digital Elevation Model (DEM), the local coherence can be enhanced at the expense of range resolution. The spectral method has provided a different aspect of understanding spatial decorrelation and has been used to improve the quality of coherence. However, it does not give a quantitative measure of coherence, which is essential for the analysis of the coherence image. Moreover, the spectral method cannot deal with the situation when the shift of the ground reflectivity spectrum exceeds the radar bandwidth, which is the case of total topographic decorrelation.

This chapter presents the study of identification and analysis of the total topographic decorrelation to provide a refined technique for change detection and environmental monitoring using InSAR coherence images. This study will show the critical conditions for the total topographic decorrelation to occur and how to benefit from this intrinsic limitation on the SAR system by turning it into useful information for the analysis of the coherence image.

A modified spatial decorrelation function will be derived geometrically as a function of both the baseline and the local terrain slope. This function will be verified by proving that the geometrical method leads to the same spatial decorrelation function as that derived from the spectral method. From the modified spatial decorrelation function, a critical terrain slope (or critical incidence angle) and a slope of total topographic decorrelation can be defined within which the image of the slope surface completely loses its coherence under any circumstance. The width of the slope of total topographic decorrelation is proportional to the baseline. A new technique, the ratio coherence imagery is then introduced to separate the spatial decorrelation from temporal decorrelation for more effective and reliable

interpretation of coherence images. This new technique is then applied to the same ERS-1 data of the case study in Chapter 4, a hyper-arid and relatively flat land surface in the Sahara desert, Algeria.

5.2 Theory

5.2.1 Spatial Decorrelation Function of Baseline and Topography

Decorrelation from spectral misalignment in range frequency, discussed in section 2.4.3, is also called the *spatial baseline decorrelation* (Li and Goldstein, 1990; Rodriguez and Martin, 1991; Zebker and Villasenor, 1992). The spatial baseline decorrelation function can be obtained directly from the imaging geometry of an InSAR configuration. Consider a radar interferometer operating with geometry shown in Figure 5.1. The along-track (azimuth) distance is x and the across-track distance (ground range) is y . Two antennas S_1 and S_2 illuminate the same ground patch centred at (x_0, y_0) , with different incidence angle of $\theta_{i,1}$ and $\theta_{i,2}$, respectively. The averaged distance from the sensor to the centre of a resolution element is R . The returned signals u_1 and u_2 are the summations of radar backscattering from the targets $P(x, y)$ on the Earth's surface to each antenna, which can be represented as (Zebker and Villasenor, 1992)

$$u_1 = \iint \sigma(x - x_0, y - y_0) \exp\left\{-j \frac{4\pi}{\lambda} (R + y \sin \theta_{i,1})\right\} h(x, y) dx dy + n_1, \quad (5.1)$$

$$u_2 = \iint \sigma(x - x_0, y - y_0) \exp\left\{-j \frac{4\pi}{\lambda} (R + y \sin \theta_{i,2})\right\} h(x, y) dx dy + n_2, \quad (5.2)$$

where $\sigma(x, y)$ is the complex backscatter function, $h(x, y)$ is the system impulse response, and n_1 and n_2 are the noise associated with the receivers.

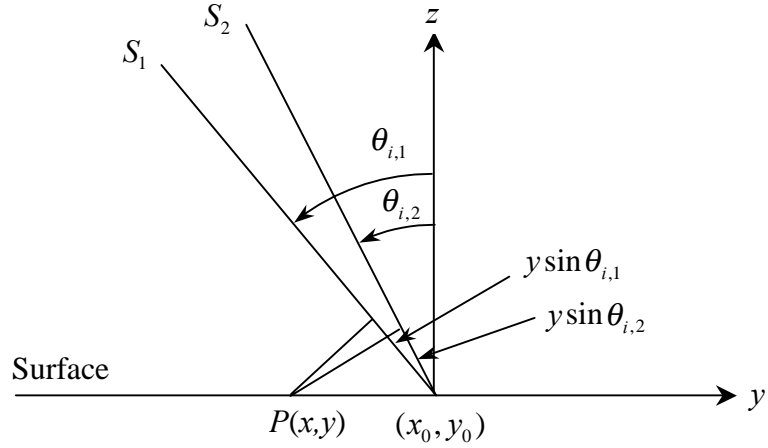


Figure 5.1 Simplified InSAR configuration.

The cross-correlation of the two signals is

$$u_1 u_2^* = \iiint \sigma(x - x_0, y - y_0) \sigma^*(x' - x_0, y' - y_0) \exp\left\{-j \frac{4\pi}{\lambda} y(\sin \theta_{i,1} - \sin \theta_{i,2})\right\} h(x, y) h^*(x', y') dx dy dx' dy' \quad (5.3)$$

If the interferometer is arranged so that the range R is unequal at the two antennas, only the mean phase of the correlation changes but not the correlation magnitude.

In general, the input signal may consist of both deterministic and random parts but only the latter is considered here in order to represent natural scenes where the surface is assumed to consist of uniformly distributed and uncorrelated scattering centres. Then the complex backscattering is a zero-mean circular Gaussian white noise process with an autocorrelation given by

$$E[\sigma(x, y) \sigma^*(x', y')] = \sigma^0 \delta(x - x', y - y'), \quad (5.4)$$

where σ^0 is the average radar cross section and $\delta(x, y)$ is the two dimensional Dirac delta function. Then, equation 5.3 is simplified as

$$E[u_1 u_2^*] = \sigma^0 \iint \exp\left\{-j \frac{4\pi}{\lambda} y \delta \theta_i \cos \theta_i\right\} |h(x, y)|^2 dx dy, \quad (5.5)$$

where $\theta_i = (\theta_{i,1} + \theta_{i,2})/2$ and $\delta\theta_i = \theta_{i,1} - \theta_{i,2}$. The exponential term can be interpreted as a Fourier kernel as it is linear in y . Therefore, the correlation function is simply the Fourier transform of the intensity impulse response.

The typical radar impulse response function is

$$h(x, y) = \text{sinc}(x/\delta x) \text{sinc}(y/\delta y), \quad (5.6)$$

where δx and δy are the azimuth resolution and ground range resolution, respectively, and the sinc function is taken as $\frac{\sin \pi x}{\pi x}$. Evaluation of equation 5.5 followed by normalisation leads to the spatial baseline decorrelation function (Zebker and Villasenor, 1992)

$$\rho_{\text{spatial}} = 1 - \frac{2 \cos \theta_i |\delta\theta_i| \delta y}{\lambda}. \quad (5.7)$$

The correlation falls off linearly as $\delta\theta_i$ increases. This effect can be described equivalently in terms of the antenna baseline. The difference of incidence angles $|\delta\theta_i|$ can be approximated as the ratio between the perpendicular component of the baseline B_{\perp} , and the averaged slant range R as

$$|\delta\theta_i| = \frac{B_{\perp}}{R}. \quad (5.8)$$

Substituting equation 5.8 for $|\delta\theta_i|$ in equation 5.7 gives

$$\rho_{\text{spatial}} = 1 - \frac{2 \cos \theta_i \delta y B_{\perp}}{\lambda R}. \quad (5.9)$$

The correlation decreases linearly as B_{\perp} increases, and falls to zero at the critical baseline

$$B_{\perp,c} = \frac{\lambda R}{2 \delta y \cos \theta_i}. \quad (5.10)$$

Therefore, the effect of spatial decorrelation can be minimised by choosing SAR observations nearly repeating the same orbit positions. On the other hand, a short B_{\perp} will reduce the height sensitivity of the interferogram to the variation of elevation change according to equation 2.9 for DEM generation.

Note that the spatial baseline decorrelation function in equation 5.9 is not only inversely proportional to B_{\perp} , the baseline component perpendicular to radar look direction, but also δy , the ground range resolution.

Let $\theta_i = \theta_i^0 - \alpha$, where θ_i^0 represent the nominal incidence angle of the radar on the ellipsoidal Earth (23° for ERS-1 and ERS-2 at the image centre) and α the local terrain slope measured upward from the horizon away from the radar direction. The ground range resolution is a function of the local terrain slope as (Curlander and McDonough, 1991, p. 15)

$$\delta y = \frac{c}{2B_v |\sin(\theta_i^0 - \alpha)|}, \quad (5.11)$$

where c is the speed of light, B_v the frequency bandwidth of the transmitted chirp signal. The magnitude of ground range resolution δy increases rapidly when the surface is nearly orthogonal to the radar beam and becomes infinite if the terrain slope is equal to the nominal incidence angle (i.e., $\alpha = \theta_i^0$). Note that δy is practically limited to a finite length even when $\alpha = \theta_i^0$ because the terrain is not an infinite plane. However, the effect of a large value of δy on the decorrelation is significant in the case of the surface slope facing the radar.

According to equation 5.9, the correlation linearly decreases as the magnitude of ground range resolution increases. SAR achieves resolution by emitting a chirp pulse and then sampling the returned signal with a time sampling interval no longer than the theoretical pulse width after range compression. In each slant range resolution cell of a SAR image, the total scattered field is a coherent summation of radar backscattering from many scatterers within the ground range resolution cell. As the ground range resolution cell increases, the width of the main lobe of the impulse

response function broadens and thus the correlation between two SAR signals diminishes.

Substituting equation 5.11 into equation 5.9 results in a modified *spatial decorrelation function of baseline and topography*

$$\rho_{spatial} = 1 - AB_{\perp} |\cot(\theta_i^0 - \alpha)|, \quad (5.12)$$

where $A = c/\lambda RB_v$, a constant for a SAR system. This spatial decorrelation function describes the behaviour of topographic decorrelation as well as baseline decorrelation. For a given baseline, the correlation decreases as the local terrain slope approaches the value of the nominal incidence angle, and the increase of baseline will speed up the deterioration of the correlation (Figure 5.2).

The spatial decorrelation function above can be verified by deriving it from a different approach based on the spectral shift in the ground reflectivity spectrum between two radar signals in equation 2.55,

$$v_0 \cong \frac{cB_{\perp}}{\lambda R} \cot(\theta_i^0 - \alpha). \quad (5.13)$$

Substituting equation 5.13 into equation 5.12 gives an alternative spatial decorrelation function,

$$\rho_{spatial} = 1 - \left| \frac{v_0}{B_v} \right|. \quad (5.14)$$

If the spectral shift v_0 , a function of the baseline and the local slope, exceeds the bandwidth of a radar chirp signal B_v , the two SAR spectra become totally disjointed with each other and thus result in total decorrelation. This function is identical to equation 2.52, the correlation function derived from range spectral misalignment of transfer functions. This means that the two different approaches – the geometrical and the spectral methods – reach the same relationship for the spatial decorrelation function in terms of the baseline and topography.

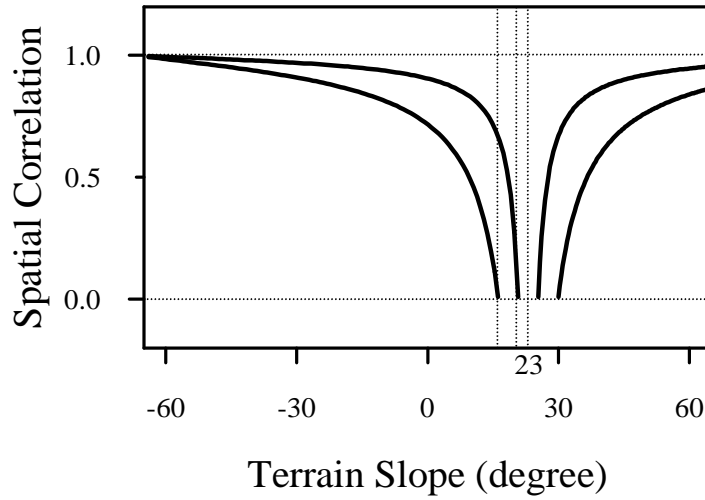


Figure 5.2 Spatial decorrelation $\rho_{spatial}$ with $B_{\perp} = 100m$ (upper curve) and $B_{\perp} = 300m$ (lower curve) in case of ERS SAR ($\theta_i^0 = 23^\circ$).

It should be noted that the radar impulse response is assumed as a square frequency weighting function (equation 5.6) that is a typical radar model in derivation of equation 5.12. For a different type of impulse response, these equations need to be modified but the basic relationships remain the same.

5.2.2 Critical Terrain Slope (or Critical Incidence Angle)

From equation 5.12, *critical incidence angle*, $\theta_{i,c}$ (or *critical terrain slope*, α_c , where $\alpha_c = \theta_i^0 - \theta_{i,c}$) and *slope of total topographic decorrelation*, θ_d , can be defined within which the spatial decorrelation function falls to a meaningless value (below zero):

$$\theta_d \leq |\theta_{i,c}|, \quad \text{where } \theta_{i,c} = \tan^{-1}(AB_{\perp}). \quad (5.15)$$

The width θ_d becomes wider as B_{\perp} increases, as shown in Figure 5.3. The definition of $A = c/\lambda RB_v$ suggests that a SAR system with wider chirp signal bandwidth B_v or

a longer wavelength λ can reduce the slope range of total topographic decorrelation. At the image centre (mid-swath), for example, $A = 0.4041 \times 10^{-3} [m^{-1}]$ for the C-band SAR on board ERS-1 and ERS-2, and $A = 0.1174 \times 10^{-3} [m^{-1}]$ for the L-band SAR on board JERS-1. This simple calculation indicates that an ERS-1 and ERS-2 InSAR coherence image is about 4 times more likely to produce the total topographic decorrelation phenomenon than that of JERS-1.

The total topographic decorrelation is most relevant to the interferometric measurements where the incidence angle equals the actual terrain slope. For example, ERS-1 and ERS-2 SAR have a nominal incidence angle range across the swath of $19.4^\circ - 26.5^\circ$. This angle range coincides with slope angles of moderate relief terrain, a common case of land surface, and therefore the ERS SAR is very likely to produce the total topographic decorrelation. Aircraft measurements, on the other hand, may have a mid-swath look angle of 45° and a range of look angles across the swath of $20^\circ - 70^\circ$. Terrain slope angles equalling the critical incidence angle, in this case, are only in a particular range of the image. In practice, the total topographic decorrelation is a problem mainly for interferometric measurements from satellite SAR systems such as SEASAT, ERS-1, ERS-2, JERS-1 and RADARSAT with a relatively narrow incidence angle coinciding with common slope angles of terrain.

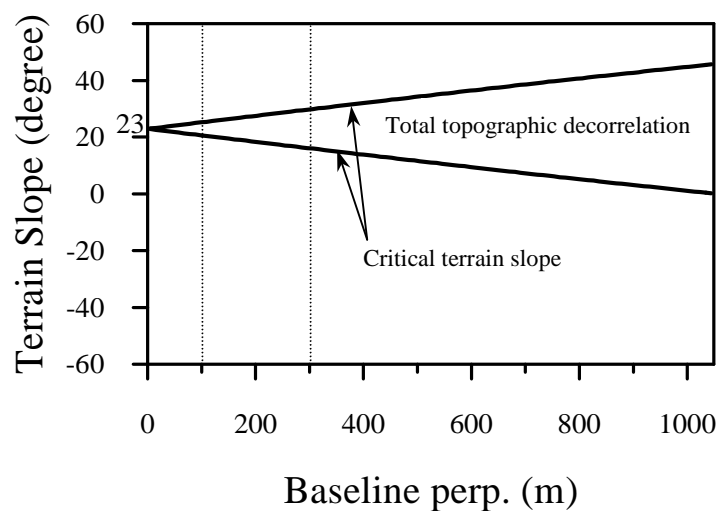


Figure 5.3 Critical terrain slopes α_c as a function of baseline B_\perp . Note that the width of the slope of total topographic decorrelation increases with B_\perp .

5.2.3 Ratio Coherence Imagery: A New Analytical Imagery using Two Coherence Images

A new method is introduced in this section for analysing coherence images. Ignoring other competing decorrelation factors such as thermal noise, misregistration, and atmospheric effects, the total observed correlation of the returned radar signals can be generalized as a product of temporal and spatial correlation as

$$\begin{aligned}\rho_{total} &= \rho_{temporal} \cdot \rho_{spatial} \\ &= \rho_{temporal} \cdot \left(1 - AB_{\perp} |\cot(\theta_i^0 - \alpha)|\right).\end{aligned}\quad (5.16)$$

Now, consider three SAR observations named 1, 2, and 3 in time sequence. A ratio coherence image can then be established by dividing a coherence image with long temporal separation by the other with relatively short temporal separation as

$$\frac{\rho_{total}^{13}}{\rho_{total}^{12}} = \frac{\rho_{temporal}^{13}}{\rho_{temporal}^{12}} \cdot \frac{1 - AB_{\perp}^{13} |\cot(\theta_i^0 - \alpha)|}{1 - AB_{\perp}^{12} |\cot(\theta_i^0 - \alpha)|}, \quad (5.17)$$

where the superscripts represent the SAR image pair for each coherence image. Alternatively, it can be said that the total ratio coherence, η , consists of a temporal ratio part and a spatial ratio part as

$$\eta_{total} = \eta_{temporal} \cdot \eta_{spatial}. \quad (5.18)$$

Assuming that the temporal change is a cumulative process and as the temporal separations are $\Delta T^{13} > \Delta T^{12}$, the temporal ratio part generally satisfies $\eta_{temporal} \leq 1$ as $\rho_{temporal}^{13} \leq \rho_{temporal}^{12}$. If the baselines are $B_{\perp}^{13} \geq B_{\perp}^{12}$, the total ratio is $\eta_{total} < 1$ for all slopes. For the case of $B_{\perp}^{13} < B_{\perp}^{12}$ ($\alpha_c^{12} < \alpha_c^{13}$ as shown in Figure 5.2 and 5.4, excluding layover zone where $\alpha > \theta_0$ for simplicity), however, the spatial ratio part is abnormally high ($\eta_{spatial} \gg 1$) when the terrain slope approaches from zero slope (flat surface) to the critical terrain slope α_c^{12} , thus producing very high total ratio coherence ($\eta_{total} \gg 1$) as shown in Figure 5.4. For flat areas and slopes facing away

from the radar, $\eta_{spatial} \approx 1$ and $\eta_{total} \approx 1$ for stable surface (grey in ratio coherence image) and $\eta_{total} < 1$ for temporally changing surface (dark in a ratio coherence image).

Within the slope range of $\alpha_c^{12} < \alpha < \alpha_c^{13}$, the theoretical spatial decorrelation function $\rho_{spatial}^{12}$ falls down to below zero but the actual coherence level is limited to $\rho_{spatial}^{12} = 0$, while $\rho_{spatial}^{13} > 0$ (Figure 5.2). In this case, the spatial ratio part in equation 5.18 may not be well defined theoretically (Figure 5.4), but the ratio coherence will always result in $\eta_{total} \gg 1$ by protecting computational division from overflow.

The behaviour of the spatial ratio part within the slope of total topographic decorrelation of the shorter baseline ($\alpha > \alpha_c^{13}$) is ambiguous and cannot be clearly defined because the spatial decorrelation functions of the two coherence images both fall down to below zero. Considering that the estimation of the coherence is an ensemble averaging process with neighbouring pixels, the effect of this ambiguity in the theoretical spatial ratio coherence function (equation 5.18) can be averaged out and becomes negligible if the critical terrain slope zone of the coherence image with the shorter baseline is very narrow. Otherwise the ratio coherence will show random mixtures of white and black spots due to the singularity problem of the ratio calculation in the spatial ratio part.

In summary, the feasible working condition for the ratio coherence is as follows:

$$\eta_{total} = \frac{\text{Coherence of large } \Delta T \text{ and short } B_{\perp}}{\text{Coherence of small } \Delta T \text{ and long } B_{\perp}}. \quad (5.19)$$

If the baseline of the larger temporal separation coherence image (numerator) is shorter than that of the smaller temporal separation coherence image (denominator), the abnormally bright feature in the ratio coherence image provides an effective identification of the total topographic decorrelation along the radar facing slopes in contrast to the dark temporal decorrelation features over a stable background in grey.

It is not always possible to acquire an adequate dataset satisfying the temporal and baseline conditions necessary to establish the ratio coherence imagery in (5.19). Alternatively, one may use two coherence images of which the temporal separations do not overlap with each other (for example, $\eta_{total} = \rho_{total}^{23} / \rho_{total}^{12}$ where $\Delta T^{23} > \Delta T^{12}$ and $B_{\perp}^{23} < B_{\perp}^{12}$) taking the risk of $\eta_{temporal} > 1$. For an area where surface change processes can be considered as gradually progressive and continuous so that temporal decorrelation is proportional to the temporal separation, the temporal ratio part can then be assumed to be $\eta_{temporal} < 1$, and the above discussions of ratio coherence imagery will hold.

However, the assumption between temporal separation and the degree of temporal decorrelation could be overturned by some environmental factors. For example, if an erosion event by an unusual storm or human disturbances occurs between the first and second image acquisitions and only, then the coherence between 1 and 2 ($\rho_{temporal}^{12}$) would be poor, while the coherence $\rho_{temporal}^{23}$ might be fine even if $\Delta T^{23} > \Delta T^{12}$. In this case, the non-overlap temporal separation approach for ratio coherence is not desirable.

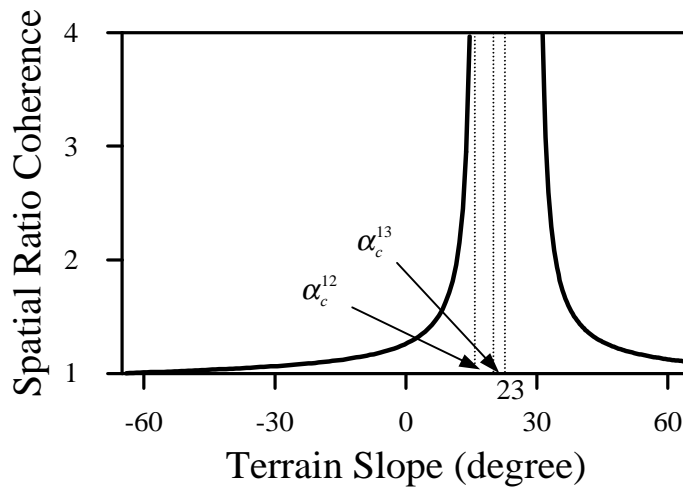


Figure 5.4 Spatial ratio coherence ($\eta_{spatial} = \rho_{spatial}^{13} / \rho_{spatial}^{12}$). Note the abnormally high value within the zone of critical terrain slope centred at the nominal incidence angle of 23°.

5.2.4 Decorrelation from Volume Scattering

So far, it is assumed that backscattering from each resolution cell is dominated by scatterers on a tilted plane in an open terrain. In practice, there may be a significant contribution from volume scattering effects such as penetration into dry sand or forest canopy. It is known that the presence of volume scattering reduces coherence level (Gatelli *et al.*, 1994; Hagberg *et al.*, 1995). Moreover, decorrelation from volume scattering also increases as the baseline increases. This relationship can be derived by expanding the spatial baseline decorrelation from surface scattering defined in equations 5.1-5.9 to the three dimensional case as

$$u_1 = \iiint \sigma(x-x_0, y-y_0, z-z_0) \cdot \exp\left\{-j \frac{4\pi}{\lambda} (R + y \sin \theta_{i,1} - z \cos \theta_{i,1})\right\} h_1(x, y, z) dx dy dz + n_1 \quad (5.20)$$

$$u_2 = \iiint \sigma(x-x_0, y-y_0, z-z_0) \cdot \exp\left\{-j \frac{4\pi}{\lambda} (R + y \sin \theta_{i,2} - z \cos \theta_{i,2})\right\} h_2(x, y, z) dx dy dz + n_2 \quad (5.21)$$

Note that different system impulse response functions h_1 and h_2 are used for u_1 and u_2 , respectively. This is because the volume scattering is of temporal as well as of spatial due to possible changes of target condition such as penetration depth between two time-separated SAR observations for repeat-pass InSAR. The cross-correlation of the two signals is then,

$$u_1 u_2^* = \iiint \iiint \sigma(x-x_0, y-y_0, z-z_0) \sigma^*(x'-x_0, y'-y_0, z'-z_0) \cdot \exp\left\{-j \frac{4\pi}{\lambda} y (\sin \theta_{i,1} - \sin \theta_{i,2})\right\} \exp\left\{j \frac{4\pi}{\lambda} z (\cos \theta_{i,1} - \cos \theta_{i,2})\right\} \cdot h_1(x, y, z) h_2^*(x', y', z') dx dy dz dx' dy' dz' \quad (5.22)$$

Again, the complex backscattering is assumed to be a zero-mean circular Gaussian white noise process with autocorrelation given by

$$E[\sigma(x, y, z) \sigma^*(x', y', z')] = \sigma^0 \delta(x-x', y-y', z-z'), \quad (5.23)$$

where σ^0 is the average radar cross section and $\delta(x, y, z)$ is the three dimensional Dirac delta function. Then, equation 5.22 reduces to

$$E[u_1 u_2^*] = \sigma^0 \iiint \exp\left\{-j \frac{4\pi}{\lambda} y \delta\theta_i \cos\theta_i\right\} \exp\left\{-j \frac{4\pi}{\lambda} z \delta\theta_i \sin\theta_i\right\} \cdot h_1(x, y, z) h_2(x, y, z) dx dy dz \quad (5.24)$$

The exponential terms can be interpreted as a Fourier kernel as they are linear in y and z , respectively. Therefore, the correlation function is simply the Fourier transform of the intensity impulse response.

The typical radar impulse response function in 3D is

$$h(x, y, z) = \text{sinc}(x/\delta x) \text{sinc}(y/\delta y) \text{sinc}(z/\delta z), \quad (5.25)$$

where δz is the rms penetration depth. For further simplification, temporal penetration depth change is excluded in the following evaluation to let $h_1 = h_2 = h$. Evaluation of equation 5.24 followed by normalisation leads to the spatial decorrelation function both from surface scattering and volume scattering as

$$\begin{aligned} \rho_{\text{spatial}} &= \rho_{\text{surface}} \cdot \rho_{\text{volume}} \\ &= \left(1 - \frac{2 \cos\theta_i \delta y B_{\perp}}{\lambda R}\right) \left(1 - \frac{2 \sin\theta_i \delta z B_{\perp}}{\lambda R}\right) \end{aligned} \quad (5.26)$$

If the penetration depth is equal to zero ($\delta z = 0$), then the spatial decorrelation function from surface and volume scattering (equation 5.26) is simplified to the form of equation 5.9 for surface scattering only. The penetration depth is dependent on the surface dielectric properties as well as surface geometry, and needs to be modelled specifically for individual cases.

Similar to the effect of surface scattering, the correlation from volume scattering effect decreases linearly as B_{\perp} increases. Therefore, the phenomenon of the high values of ratio coherence on radar facing slopes becomes more significant in the presence of volume scattering and the principle and application of ratio coherence imagery are valid.

Finally, it is important to note that both temporal and spatial decorrelation features can only be highlighted over a stable background. If a region is subject to rapid temporal decorrelation everywhere, any two coherence images of the region will both be dominated by low values and the ratio coherence image between the two will be a mixture of randomly distributed black and white spots as the result of the singularity problem of ratio processing in the temporal ratio part. Therefore, the ratio coherence is only applicable to the area where temporal and volume scattering decorrelation factors only affect specific targets over a largely stable background. This condition is usually satisfied in arid to semi-arid areas where the InSAR coherence technique is to be used to detect temporal changes.

The weather conditions at the time of image acquisition are another complex factor for correct interpretation of ratio coherence imagery. For instance, if there is rainfall at the time of the second image acquisition and dry and stable weather conditions for the first and third images, the coherence between 1 and 2 could be lower than that between 1 and 3. The low coherence between 1 and 2 is largely due to the scattering properties of the microwave for penetration that decreases quickly with the increase of moisture. The volume scattering between wet and dry land surface can therefore be considerably different. Therefore, it should be emphasised that the ratio coherence imagery should be applied in conjunction with adequate information of precipitation and weather conditions on the days of SAR image acquisitions.

5.3 Case Studies of Ratio Coherence Imagery in the Sahara Desert, Algeria

As a further development of the case study in the Sahara desert, Algeria, described in Chapter 4, the ratio coherence imagery was tested and evaluated using the same dataset: three scenes of ERS-1 SAR data acquired on 8 September 1992 (ALG1), 13 October 1992 (ALG2), and 28 September 1993 (ALG3).

The critical incidence angles and the slopes of total topographic decorrelation of these coherence images are shown in Table 5.1. Among three possible coherence

images, a ratio coherence image ALG23_COH/ALG12_COH satisfies the condition stated in (5.19). This ratio coherence configuration is ideal for the discrimination of topographic and temporal decorrelation phenomena because the temporal separation of ALG23_COH is significantly greater than that of ALG12_COH while the baseline B_{\perp} of ALG23_COH is much shorter than that of ALG12_COH. Though it is not a time-overlapping configuration, the temporal ratio can be generally assumed to be $\eta_{temporal} \leq 1$ in this hyper-arid and stable region.

Several interesting coherence features have been shown in Chapter 4 in this hyper-arid desert: 1) a gully area subject to topographic decorrelation showing higher coherence level for longer temporal separation coherence image as the result of a shorter baseline; 2) ephemeral flood streams having lost coherence gradually, and stream-like topographic decorrelation features on steep slopes; and 3) low coherence of the sand dunes due to the micro-scale rapid movement of sand particles driven by the wind and the volume scattering from radar penetration into the dry sand.

The following sections describe and explain how these features appear in the ratio coherence image, and show the advantages of using the ratio coherence imagery in terms of methodology verification.

Table 5.1 Coherence images and the slope range of total topographic decorrelation of the Sahara Desert, Algeria data.

| Coherence image | ΔT (days) | B_{\perp} (m) | Critical incidence angle ($ \theta_{i,c} $) | Slope range of total topographic decorrelation, θ_d ($\theta_i^0 = 23^\circ$) |
|-----------------|-------------------|-----------------|---|--|
| ALG12_COH | 35 | 263 | 6.0° | 17.0°~ 29.0° |
| ALG23_COH | 350 | 105 | 2.4° | 20.6°~ 25.4° |
| ALG13_COH | 385 | 368 | 8.4° | 14.6°~31.4° |

5.3.1 Topographic Decorrelation Effects in the Gully Area

Figure 5.5 shows the decorrelation features of radar-facing slopes in a dense gully network. The radar facing (east facing) slopes have high backscattering in the SAR intensity image (a) ALG3, but low coherence in (b) ALG_COH12 and (c) ALG_COH23. Having high coherence on the bottom of the valleys both in ALG12_COH and ALG23_COH excludes the possibility of rapid fluvial erosion in this hyper arid region between three SAR observations. Furthermore, the coherence on these radar facing slopes in ALG23_COH ($\Delta T=350$ days) is much higher than that in ALG12_COH ($\Delta T=35$ days), which cannot be explained in terms of temporal changes. This is a typical case of the total topographic decorrelation on radar-facing slopes. The theoretical slope range of total topographic decorrelation for ALG23_COH ($20.6^\circ \sim 25.4^\circ$) is less than half of that for ALG12_COH ($17.0^\circ \sim 29.0^\circ$) as shown in Table 5.1. Comparing the topographic decorrelation features on Figure 5.5(b) and 5.5(c), it is obvious that the wider the critical terrain slope range, the wider the slope area of total decorrelation. On these stable radar-facing slopes, the temporal ratio part can be assumed to be $\eta_{temporal} \approx 1$ while the spatial ratio part is $\eta_{spatial} \gg 1$. This results in the highlighted spatial decorrelation features in the ratio coherence, i.e. $\eta_{total} \gg 1$. The network of high ratio coherence values along the east-facing sides of the gullies forms eminent bright features over a grey background in Figure 5.5(d) ALG23_COH/ALG12_COH, isolating the total topographic decorrelation on the radar-facing slopes over the flat and stable bedrock.

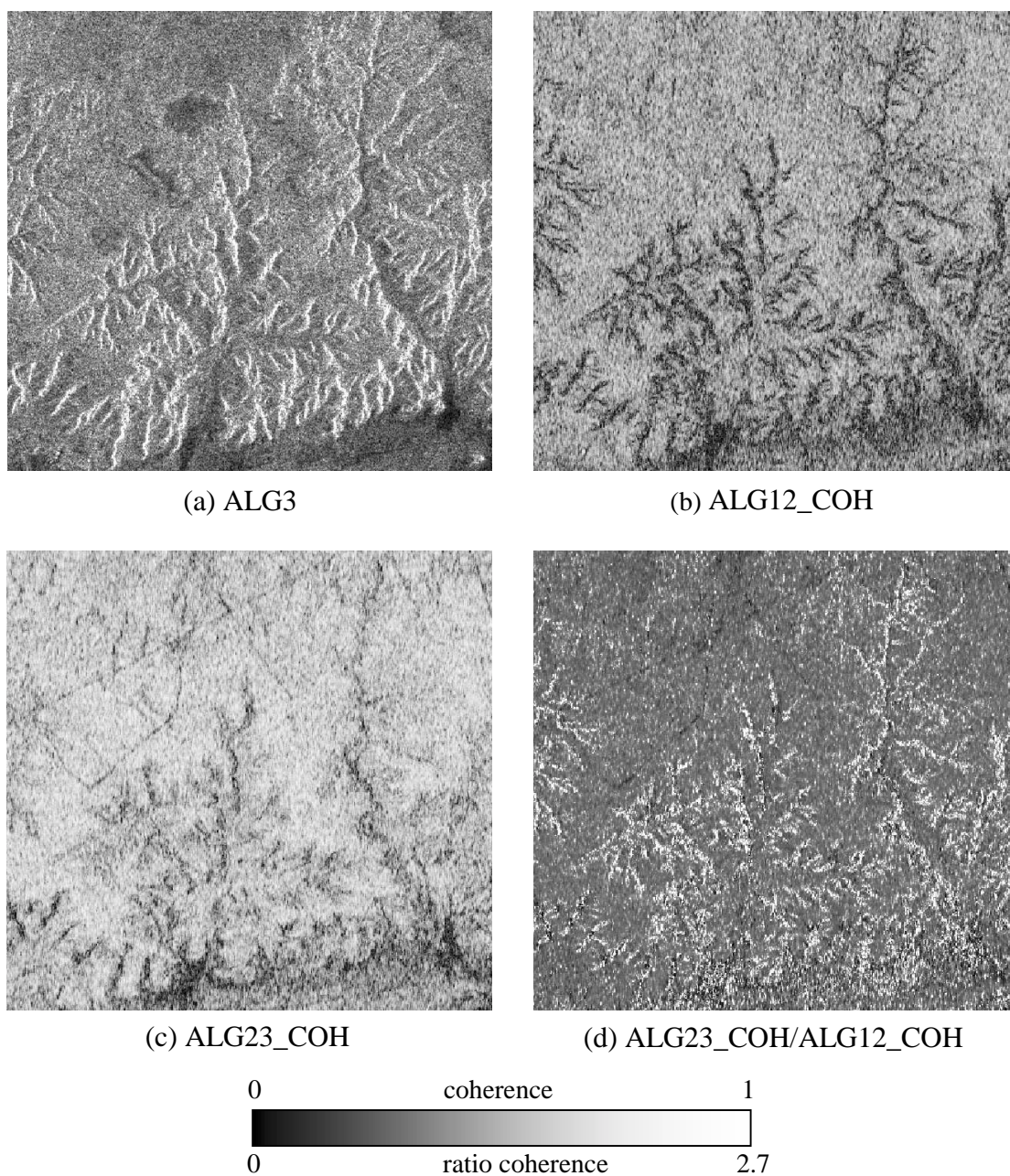


Figure 5.5 Topographic decorrelation effect in a gully area ($8 \text{ km} \times 8 \text{ km}$). (a) SAR amplitude image (ALG3), (b) coherence image ALG12_COH with 35 days separation and 263m of B_{\perp} , (c) coherence image ALG23_COH with 350 days separation and 105m of B_{\perp} , and (d) ratio coherence image ALG23_COH/ALG12_COH. The low coherence along the gully edges in the coherence images (b) and (c) could be easily mistaken as a temporal decorrelation effect. In the ratio coherence image (d), it is clear that the total topographic decorrelation effects along the radar-facing slopes are dominant and highlighted as bright features over a grey background.

5.3.2 Discrimination of Topographic and Temporal Decorrelation: Ephemeral Rivers vs. Radar-facing Slopes

Figure 5.6 shows an example of separating topographic decorrelation features from temporal decorrelation features. The coherence images (b) ALG12_COH and (c) ALG23_COH show the decorrelation features that cannot be seen in the SAR amplitude image (a) ALG3. These are the temporal decorrelation features of erosion process in ephemeral river channels in the upper part of the image, as well as some unknown stream-like decorrelation features in the middle to right of the coherence images. These unknown features, possibly the results of a different decorrelation factor, are not distinguishable from the river channel features in the two coherence images.

Comparing the variation of the coherence features of the river channels in the two coherence images, it is obvious that surface change caused by episodic rainfall had occurred mainly between ALG2 and ALG3 SAR observations. For these relatively flat river channels, the temporal ratio part is $\eta_{temporal} < 1$, while the spatial ratio part is $\eta_{spatial} \approx 1$, resulting in a low value of the ratio coherence $\eta_{total} < 1$. On the stable radar facing slopes near or within the slope of total topographic decorrelation, the temporal ratio part is $\eta_{temporal} \approx 1$ while the spatial ratio part is $\eta_{spatial} \gg 1$, resulting in a high value of the total ratio coherence $\eta_{total} \gg 1$. As shown in the ratio coherence image (d) ALG23_COH/ALG12_COH, the total topographic decorrelation in the radar-facing slopes in the middle to right part of the image is convincingly recognised as bright features against dark features of river channels over a stable and flat background in grey. This example has demonstrated the effectiveness of the ratio coherence imagery for the discrimination between topographic and temporal decorrelation features.

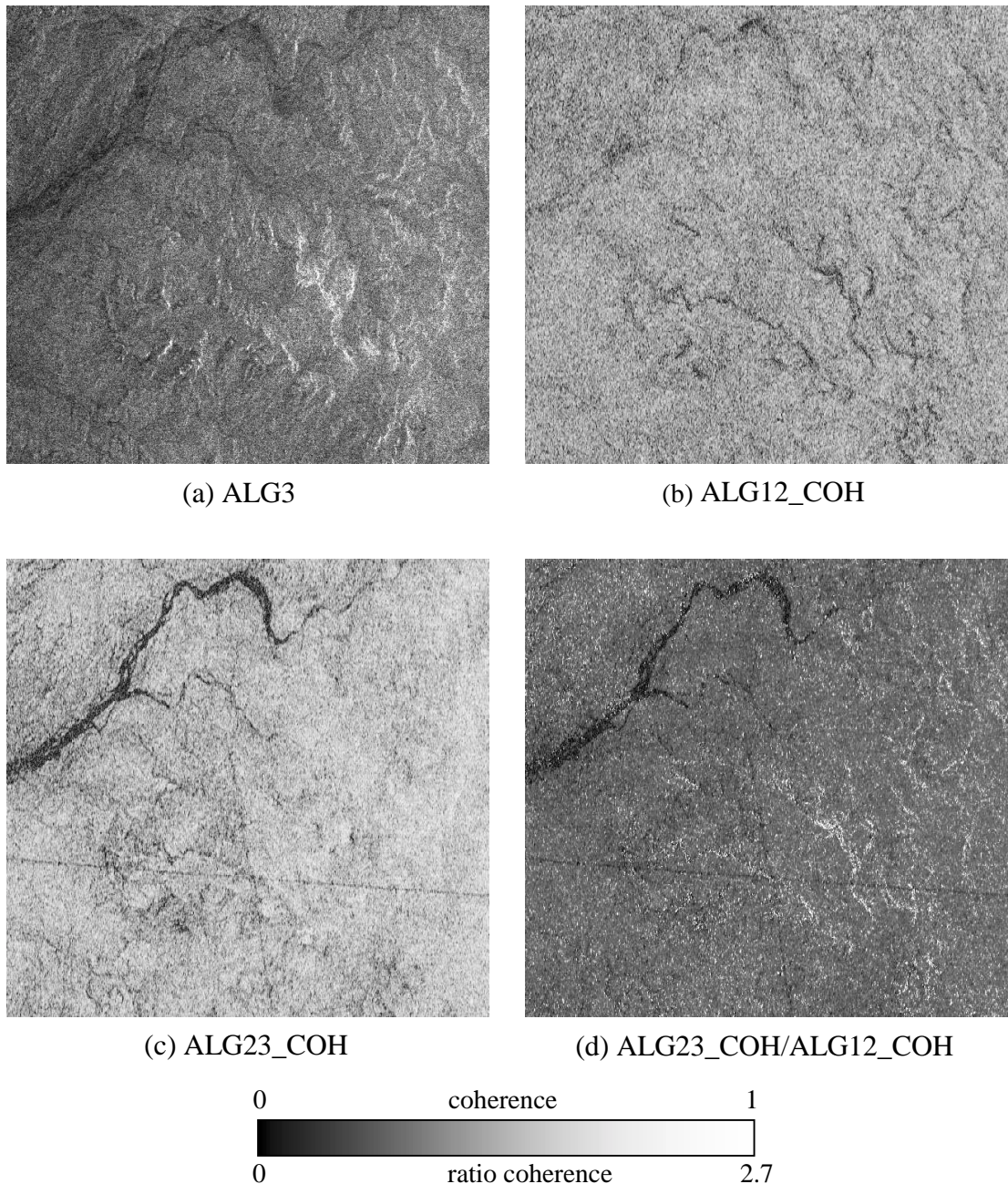


Figure 5.6 An example of discriminating the total topographic decorrelation from the temporal decorrelation features ($13 \text{ km} \times 13 \text{ km}$). (a) SAR amplitude image (ALG3), (b) coherence image ALG12_COH with 35 days separation and 263m of B_{\perp} , (c) coherence image ALG23_COH with 350 days separation and 105m of B_{\perp} , and (d) ratio coherence image ALG23_COH/ALG12_COH. Two different decorrelation effects are not distinguishable from each other in both coherence images (b) and (c), though the gradually decreasing coherence along major river channels is obvious. In the ratio coherence image (d), these are clearly discriminated as dark river channels of temporal decorrelation (upper left part) and bright radar-facing slopes of the total topographic decorrelation (middle to right) on a stable background in grey.

5.3.3 Rapid Decorrelation from Temporal Change and Volume Scattering on Sand Dunes

Figure 5.7 shows linear type sand dunes on stable flat bedrock. Since three SAR scenes were acquired in dry weather conditions, there was a considerable amount of radar penetration into the dry sand causing volume scattering. The sand dunes show low radar backscattering in the SAR amplitude image (a) ALG3 due to the volume scattering. As shown in the coherence images (b) ALG12_COH and (c) ALG23_COH, the sand dunes also have consistently low coherence level due to both rapid temporal decorrelation and volume scattering. The micro-scale movement of the sand particles driven by the wind continuously changes the distribution of scatterers resulting in rapid temporal decorrelation. The volume scattering also has contributed to decorrelation in the sand dunes.

On these sand dunes, the temporal ratio part $\eta_{temporal}$ can have random spatial distribution of values from extremely high to extremely low because of the singularity behaviour of the ratio operation. The slope of each sand dune can also be regarded as continuously varying in micro-scale, which results in a random variation of the spatial ratio part $\eta_{spatial}$, thus producing random values of the ratio coherence η_{total} . In the ratio coherence image (d) ALG23_COH/ALG12_COH, the sand dunes appear as a random mixture of bright and dark spots over grey background of stable and flat bedrock.

To conclude the case study of the Sahara desert, Table 5.2 summarizes the contribution of the temporal and spatial part of the ratio coherence for the several surface types in the region discussed so far.

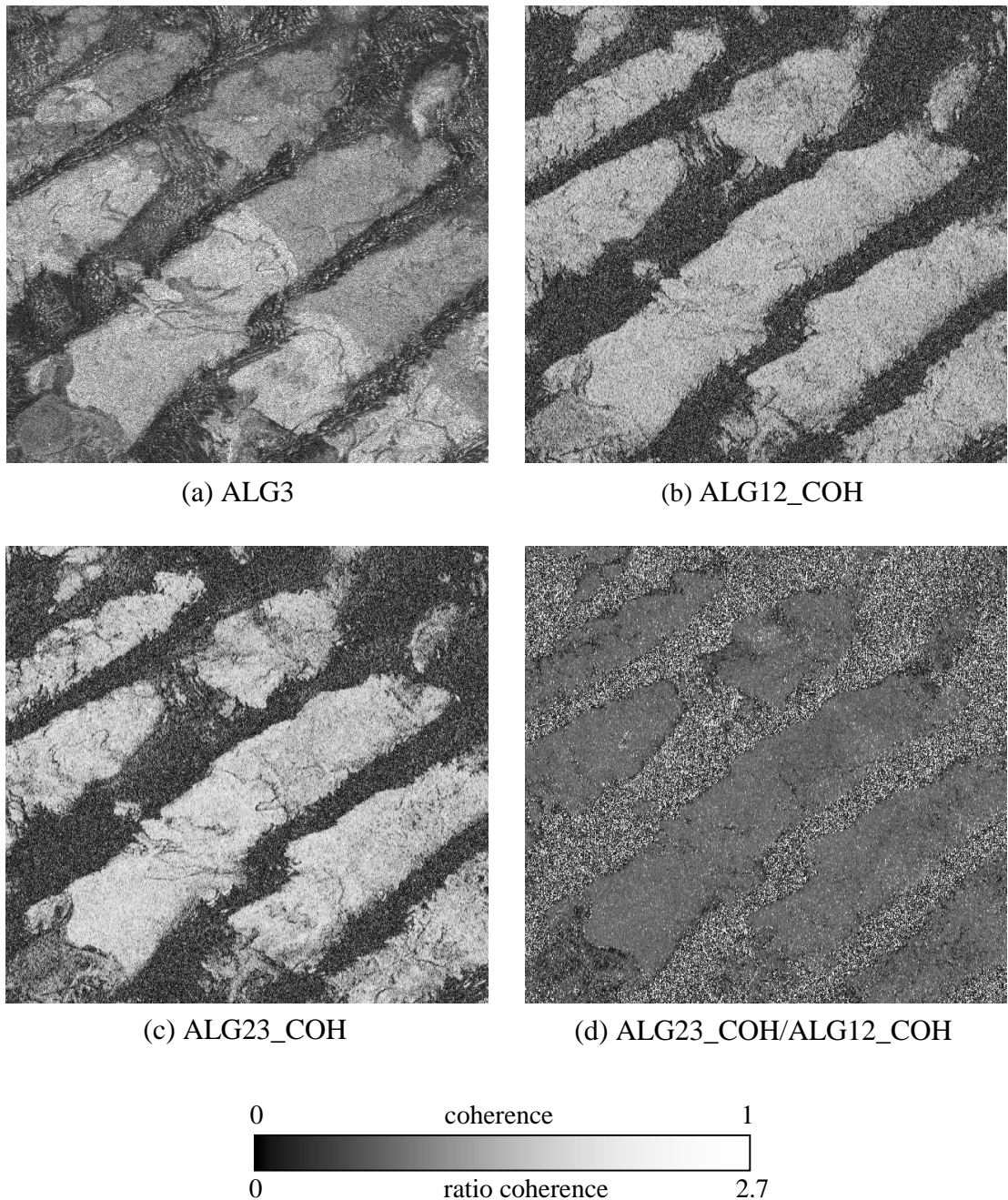


Figure 5.7 Rapid temporal decorrelation in the linear type sand dunes due to the continuously moving sand particles and volume scattering ($18 \text{ km} \times 18 \text{ km}$). (a) SAR amplitude image (ALG3), (b) coherence image ALG12_COH with 35 days separation and 263m of B_{\perp} , (c) coherence image ALG23_COH with 350 days separation and 105m of B_{\perp} , and (d) ratio coherence image ALG23_COH/ALG12_COH. The nearly zero coherence level of the sand dunes in the coherence images (b) and (c) results in random spatial distribution of bright and dark spots over a grey stable background in the ratio coherence image (d).

Table 5.2 Ratio coherence features in the Sahara Desert, Algeria.

| Surface type | $\eta_{temporal}$ | $\eta_{spatial}$ | η_{total} | Feature on ratio coherence image |
|---|-------------------|------------------|----------------|----------------------------------|
| Flat bedrock (highly stable) | ≈ 1 | 1.198 | 1.176 | homogeneously grey |
| Radar-facing slope (total topographic decorrelation) | ≈ 1 | $\gg 1$ | $\gg 1$ | bright |
| Flood stream (gradual temporal decorrelation) | < 1 | ≈ 1 | < 1 | dark |
| Sand dunes (rapid temporal and volume scattering decorrelation) | random | random | random | random bright and dark spots |

5.4 Summary

Topographic decorrelation due to local terrain slope is a dominant decorrelation factor on a surface under direct radar illumination. A highly stable surface may lose its coherence completely when the terrain slope angle is near or within the critical terrain slope zone. This phenomenon can mislead the interpretation of a coherence image.

The topographic decorrelation has been analysed by deriving a modified spatial decorrelation function using the geometrical approach. This function was verified by the fact that the same result can also be derived based on the spectral approach. The definition of the critical terrain slope (or critical incidence angle) is then proposed, which, for a given baseline, defines the criterion angle between radar illumination and terrain slope for total decorrelation to occur. It has been shown that the slope range of total topographic decorrelation broadens as the baseline increases.

A new technique, ratio coherence imagery, is proposed as a further development of this study. A ratio between a short-baseline, long-temporal separation coherence image (numerator) and a long-baseline, short-temporal separation coherence image (denominator) can effectively enhance and separate topographic decorrelation in

white (high ratio values) from temporal decorrelation in black (low ratio values) on a grey background (stable areas).

Volume scattering is a complicated factor that should be dealt with in analysing coherence imagery. Similar to spatial decorrelation from surface scattering, volume scattering degrades the coherence level as the baseline increases. Therefore, volume scattering affects the ratio coherence imagery in a similar way to surface scattering.

Application examples using ERS-1 SAR data in a hyper-arid flat area in the Sahara desert, Algeria have demonstrated that the technique is useful to eliminate incorrect interpretation of coherence images for detection of random temporal changes on land surface. Weather data, geological information, and adequate temporal and baseline separations between SAR data sets are needed for correct interpretation and effective use of the ratio coherence imagery.

Chapter 6: Erosion, Land-use and Change Detection in SE Spain using InSAR Coherence Imagery

6.1 Introduction

Soil erosion is a widespread problem in Mediterranean countries. Irregular and often intense rainfalls in this semi-arid region can result in rapid erosion in areas where the slope is steep, the lithology is soft and the vegetation is sparse. Tremendous damage to the vulnerable ecosystems can be triggered by inappropriate land use (e.g., excessive cultivation) and engineering work (e.g., road cut). For environmental management in the region, it is important to detect and monitor the areas subject to rapid erosion.

Multi-temporal interferometric SAR (InSAR) coherence imagery is a useful technique for detection of erosive land surface changes by measuring temporal decorrelation. The erosion process randomly changes the micro-topography of the slope surface and thus the geometry of radar scatterers. As a result, the phase and amplitude of the signal from each pixel are randomly altered. The signal coherence, a measure of consistency of the average random signal between the initial and the later state, estimated over a convenient number of neighbouring pixels, will therefore be gradually reduced. Eventually coherence will be lost completely when the average random phase change among pixels in a neighbourhood exceeds half the radar wavelength. It has been shown that erosion can be effectively detected using ERS SAR coherence imagery (Liu *et al.*, 1999d, 1999e).

This chapter reports part of the research results of the ESA ERS AO3-113 project on rapid erosion detection based on the above principle. The study area is in SE Spain (Almeria and Granada Provinces), which is one of the most arid areas in Europe, where the annual precipitation is less than 300 mm. In this semi-arid region, badlands are eroded from poorly cemented Tertiary molasses debris, marls, and thin soils derived from mica-schist and phyllite. They are vulnerable to flash flood erosion

caused by occasional torrential storms (Harvey, 1984, 1987). Rapid erosion will occur especially when the natural land surface is disturbed and vegetation is destroyed.

Three case studies are presented: 1) rapid erosion along a road cut in the Rio de Aguas valley near Sorbas in ALM scene; 2) recent massive plantation and its possible consequences for erosion on the southern flank of Sierra de Las in ALM scene; and 3) rainfall events caught by an ERS-1/2 tandem pair, east of Jaén in GRA scene.

6.2 Case I: Rapid Erosion along the Rio de Aguas Valley

Raw SAR data of ERS-1/2 for Almeria region is shown in Table 6.1. The scenes are chosen based on temporal separation, perpendicular baseline and weather conditions. Weather data (The Weather Underground, Inc.) shows that there was no precipitation on any of the dates when these images were acquired. Dry weather conditions are essential to eliminate the decorrelation caused by moisture change, which is a key factor to affect the dielectric property of the surface scatterers. These images were used for the studies of Case I and II.

The ERS SAR raw complex data were processed using a SAR processor to produce Single Look Complex (SLC) images. For interferometric processing, the SLC images were accurately co-registered to no less than 1/32 pixel accuracy. Coherence images and interferograms were then derived from pairs of co-registered SLC images. In this study, coherence images were produced by ensemble averaging 4×16 pixels in range and azimuth direction, respectively, after Earth-flattening. Note that range spectral filtering has not been applied for spatial decorrelation compensation here because analysis of the spatial decorrelation effect itself is another object of this research.

The study area is within the ALM scene. The location is shown in Figure 6.1 together with a simplified geological map illustrating the main lithologies. Coherence and ratio coherence images were analysed in conjunction with Landsat TM images and stereo air-photos, topographic maps (1:10,000; ICA, 1997a) and geological maps

Table 6.1 ERS SAR scenes of Almeria area.

| Scene | Mission | Date | Weather | Wind Speed (kph) | B_{\perp} (m) | | | ΔT (days) | | | | |
|-------|---------|----------|---------|------------------|-----------------|-----|----|-------------------|--|----|-----|-----|
| | | | | | | | | | | | | |
| ALM1 | ERS-1 | 19950426 | dry | 17.8 | 131 | | | 526 | | | | |
| ALM2 | ERS-2 | 19961003 | dry | 13.5 | | | | | | | | |
| ALM3 | ERS-2 | 19961212 | dry | 15.7 | | 156 | 20 | 136 | | 70 | 140 | 210 |
| ALM4 | ERS-2 | 19970501 | dry | 21.9 | | | | | | | | |

(1:50,000; IGME, 1975a). The TM images were used to illustrate the environment of the study area and to verify decoherence features of dense vegetation. Stereo air-photos and topographic maps provide slope information that is useful for separating erosion from deposition and for eliminating decoherence features caused by spatial topographic decorrelation. Air-photos also show details of sparse natural vegetation. The image interpretation was checked in a field investigation.

6.2.1 Interpretation of the Coherence Features

Erosion phenomena appearing in coherence images are expected to be features gradually losing coherence with time. Vegetation and human activities (e.g., agriculture) are the other two major temporal decorrelation factors in the study area. Dense vegetation can result in total loss of coherence within a few days or even shorter time lapse. On the other hand, according to field investigation, sparse and dry natural vegetation (shrubs) typical in the region does not expose a significant effect to coherence level for months to even a year. Human activities such as field ploughing, engineering construction and quarrying can result in sudden loss of coherence in a specific period in clearly defined shapes illogical to natural processes. The general guidance for interpretation is summarised as below.

- Rapid erosion: High to intermediate coherence in a few days to months depending on if there are rainfall events. Gradually lost coherence over a long period (several months to more than a year).

- Dense vegetation: Lost coherence in very short period (within a few days).
- Human activities: Usually not relevant to the length of the temporal separation. The decoherence features often show regular spatial patterns. Agriculture related decoherence features are controlled by seasons.

As shown in the Landsat TM 432 RGB colour composite and NDVI (Normalized Difference Vegetation Index; Rouse *et al.*, 1974) image in Figure 6.2, the Rio de Aguas valley cuts through a sequence of Tertiary strata tilting toward the west. On the western side of the valley, there are steep slopes of marls capped by thick block layers of gypsum. The eastern side of the valley is mainly composed of thick limestone with several fossil landslides. The bottom of the valley (low terraces) is covered by dense vegetation mainly of orange orchards, and farmhouses. A motorway (the dark curved line in the NDVI image), built in the middle of the 1990s based on limestone, cuts through the marls on high terraces. Gypsum and limestone are very resistant lithologies especially in arid regions where there is little surface and shallow groundwater. The marls are loose and soft and nearly completely barren. Marls are therefore vulnerable to erosion when heavy rainfalls happen.

Figure 6.3 shows ALM23_COH, ALM34_COH, ALM24_COH and the RGB colour composite using the three coherence images. The dense vegetation in the valley bottom shows persistently low coherence in 70, 140 and 210 days intervals as very dark patches in all the coherence images. These dark patches accurately match the bright patches of TM NDVI image in Figure 6.2. However, there are several persistently low coherence patches in the upper-left part of coherence images that are not shown in the TM NDVI image. These patches correspond to a large gypsum quarry and the quarry dumps in operation.

The gypsum plateau to the west of the valley is the most stable feature in the area retaining high coherence in 210 days. The limestone on the eastern side of the valley also shows considerable stability. These features appear as bright tones in each individual coherence image and bright grey to white in the coherence colour composite. The distribution of these features generally matches with the geological map in Figure 6.1.

The western side of the valley is seen to have lost coherence gradually from an intermediate level in 70 days (average coherence of 0.42) to low coherence in 140 days (average coherence of 0.25) and nearly complete loss of coherence in 210 days. This progressive change is effectively recognised in red colours in the coherence colour composite shown in Figure 6.3(d). Comparing the coherence colour composite with the geological map, the gradually changing area matches well with the distribution of the marls (Figure 6.1). This progressive change is believed to be caused by rapid erosion.

Most temporal changes are accumulative with time. Therefore, the coherence level in ALM23_COH (70 days) is generally higher than ALM34_COH (140 days). However, there are exceptional cases such as sudden temporal changes during the 70 days of ALM23_COH and then stable in the 140 days of ALM34_COH. These features are presented as bright green in the coherence colour composite shown in Figure 6.3(d), and are a result of high coherence only in ALM34_COH and usually correspond to human activities such as newly ploughed fields appearing as small regular or irregular patches.

6.2.2 Ratio Coherence Imagery and Analysis of the Topographic Decorrelation

For further study on the temporal changes relating to possible rapid erosion in the region, it is essential to separate spatial decorrelation from temporal decorrelation. In this section, the topographic decorrelation features on steep slopes will be analysed using the ratio coherence technique.

There are distinctive linear features in bright green in Figure 6.3(d). These features appear along east facing steep slopes of valleys and cliffs, which are produced by the much shorter baseline of ALM34_COH (20 m) compared to ALM23_COH (156 m) and ALM24_COH (136 m). In a high relief terrain, the spatial topographic decorrelation due to the terrain slope and baseline may overwhelm other decorrelation factors including the temporal decorrelation. This effect is dominant particularly on directly radar-facing foreshortened slopes and layover zones. For a foreshortened

slope, the width of spatial decorrelation zone increases with the increase of baseline (Lee and Liu, 1999, 2000a; Chapter 5). As a result, the spatial decoherence zones along east-facing slopes are significantly narrower in the case of ALM34_COH than that of ALM23_COH and ALM24_COH, producing bright green edge features in Figure 6.3(d).

Among the three possible coherence images listed in Table 6.2, the ratio coherence image of ALM34_COH/ALM23_COH meets the condition of ratio coherence imagery in equation 5.19. Figure 6.4 shows two coherence images (a) ALM34_COH and (b) ALM_COH23, the ratio coherence image (c) ALM34_COH/ALM23_COH, and the SAR amplitude image (d) ALM4 of the Rio de Aguas valley nearby Sorbas town. Coherence images show complex features of decorrelation from either temporal decorrelation or spatial topographic decorrelation.

It is not really possible to distinguish the two using a single coherence image. For instance, the curved linear features of low coherence in Figure 6.4(a) ALM23_COH can be easily misinterpreted as temporal decorrelation in streams. With the aid of the ratio coherence image, one can confidently recognize them as the topographic total decorrelation features along the foreshortened or layover slopes of cliff scarps because they are highlighted in white in the ratio coherence image in Figure 6.4(c) ALM34_COH/ALM23_COH. The dark areas in Figure 6.4(c) are the temporal decorrelation features possibly related to progressive erosion in the unconsolidated Tertiary molasses debris and marls. The rapid temporal decorrelation of vegetation in the agricultural field in the valley shows randomly distributed black and white spots, while grey in the upper left part of Figure 6.4(c) corresponds to the stable gypsum plateau. Table 6.3 summarizes the contribution of the temporal and spatial part of the ratio coherence for several surface types in this region.

Table 6.2 Coherence images and the critical terrain slopes (Almeria, Spain).

| Coherence image | ΔT (days) | B_{\perp} (m) | Critical incidence angle ($ \theta_{i,c} $) | Slope range of total topographic decorrelation, θ_d ($\theta_i^0 = 23^\circ$) |
|-----------------|-------------------|-----------------|---|--|
| ALM23_COH | 70 | 156 | 3.6° | $19.4^\circ \sim 26.6^\circ$ |
| ALM34_COH | 140 | 20 | 0.5° | $22.5^\circ \sim 23.5^\circ$ |
| ALM24_COH | 210 | 136 | 3.1° | $19.9^\circ \sim 26.1^\circ$ |

Table 6.3 Ratio coherence features in Rio de Aguas valley.

| Surface type | $\eta_{temporal}$ | $\eta_{spatial}$ | η_{total} | Feature on ratio coherence image |
|--|-------------------|------------------|----------------|----------------------------------|
| Gypsum plateau (highly stable) | ≈ 1 | 1.152 | 1.003 | homogeneously grey |
| Radar facing slope (topographic decorrelation) | ≈ 1 | $\gg 1$ | $\gg 1$ | bright |
| Unconsolidated Tertiary marls (gradual temporal decorrelation) | < 1 | ≈ 1 | < 1 | dark |
| Vegetation and agriculture (rapid temporal decorrelation) | random | random | random | random bright and dark spots |

It is interesting to notice that the location of the total topographic decorrelation features partially matches the high backscattering area (the usual case for foreshortened slopes) in the SAR amplitude image in Figure 6.4(d). Furthermore, comparison of the two coherence images Figure 6.4(a) and (b), ALM34_COH is little affected by topographic decorrelation. This is because of the very short baseline of ALM34_COH ($B_{\perp} = 20$ m). However, it is difficult to say that the low coherence features appearing in ALM23_COH but absent in ALM34_COH are the features of topographic decorrelation without using the ratio coherence image. It is more difficult to pin-point the features of such kind in practice. In this case, the ratio coherence image Figure 6.4(c) gives a definite identification and it is much easier to interpret than by comparing two coherence images or SAR amplitude images side by side.

As a further enhancement, a colour composite of ALM23_COH in red, ALM34_COH in green and ALM34_COH/ALM23_COH in blue is produced (Figure 6.5). In this image, spatial decorrelation effects are shown as bright edges in cyan because of the high values in both ALM34_COH and ALM34_COH/ALM23_COH and low values in ALM23_COH. Stable land surfaces (gypsum and limestone) correspond to yellow tones because of the high coherence in both ALM23_COH and ALM34_COH and intermediate values in ALM34_COH/ALM23_COH. The dense vegetation appears as blue tones as a result of consistently low coherence and intermediate ratio values. The large area of marls in the middle part of the image is distinctively illustrated as reddish orange tones as a result of gradual temporal change

characterised by intermediate coherence in ALM23_COH, low coherence in ALM34_COH and low ratio values in ALM34_COH/ALM23_COH.

In field investigations conducted in May 1999 and 2000, fresh rills and gullies were observed on the marl slopes. The rills on the surfaces of steep slopes along the road cut present firm evidence of erosion and give an estimation of the erosion rate. When the motorway was completed in 1993, these man-made slope surfaces should be smooth. After six years, the accumulated erosion process has produced dense rills with depths ranging from a few centimetres to 70 centimetres. Erosion at this rate will significantly reduce the coherence in a few months. Supported by the field observation (fresh erosion evidences and acute lack of vegetation), it is obvious that rapid erosion is the only major factor causing the temporal change that has gradually reduced the coherence. Figure 6.5 presents a convincing detection of rapid erosion occurring in the marls situated in the study area.

Comparing Figure 6.5 with the TM NDVI image shown in Figure 6.2(b), the geological map (Figure 6.1) and topographic maps, it becomes clear that rapid erosion is most likely to happen in soft lithologies where the slope is relatively steep and vegetation cover is very poor. The rapid erosion detected in this case study happens to be along a new motorway road cuts. It implies that there is a direct or indirect impact of this large-scale engineering work to the rapid erosion. Outcrops of marls with similar topography in an undisturbed environment are often protected by thin calcareous crusts from rapid erosion so that they may show high coherence in an equivalent period (Hilton, 2000)

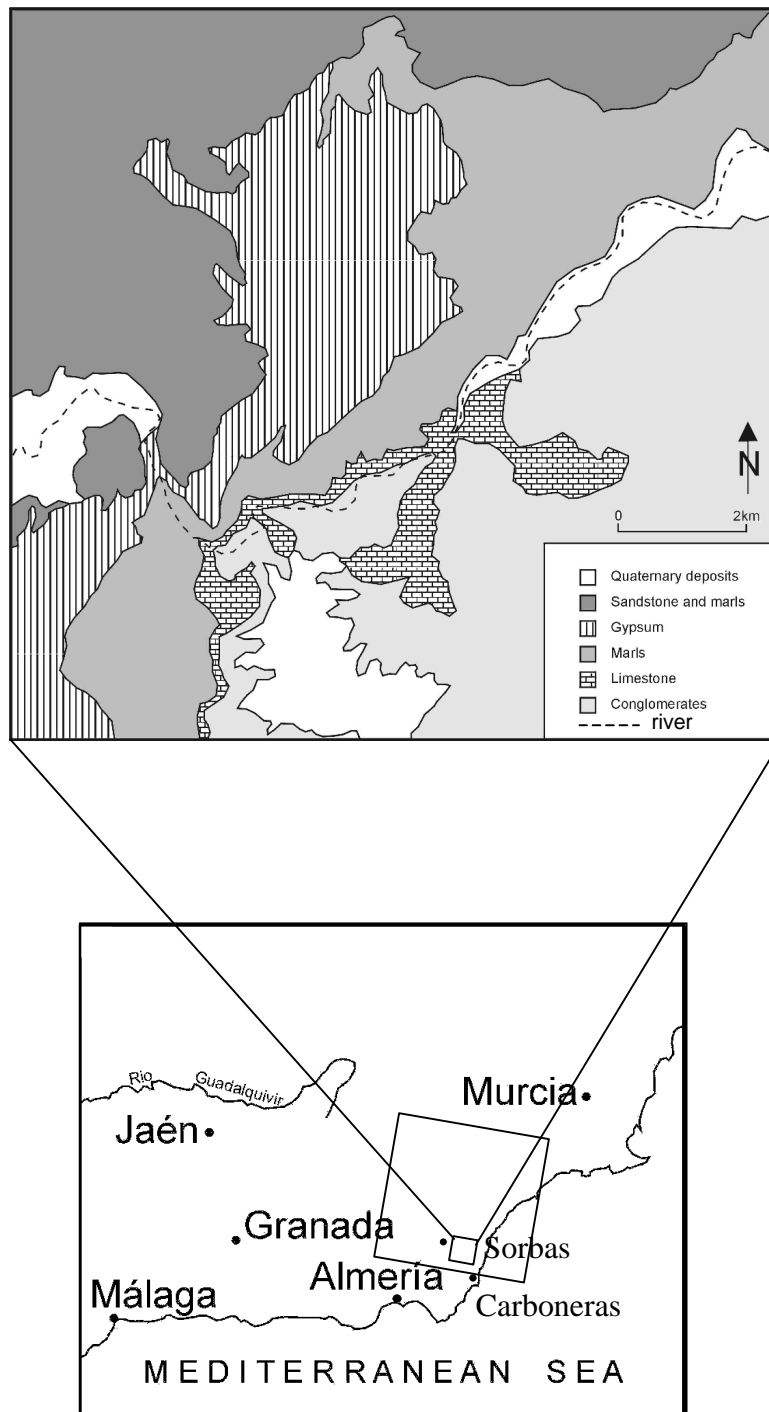
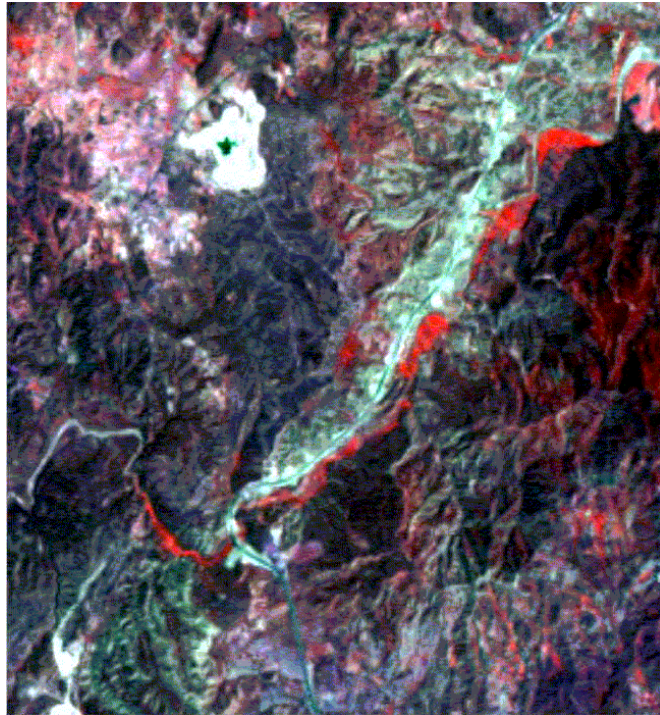
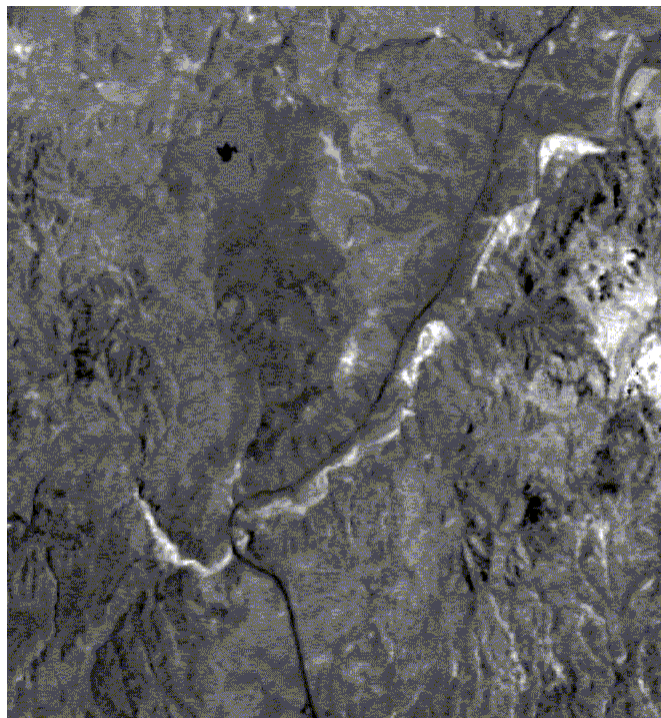


Figure 6.1 The location map together with a simplified geological map (IGME, 1975a) of the study area of Case I (10 km × 10 km). The large square represents the locations of the ALM whole scene (100 km × 106 km).

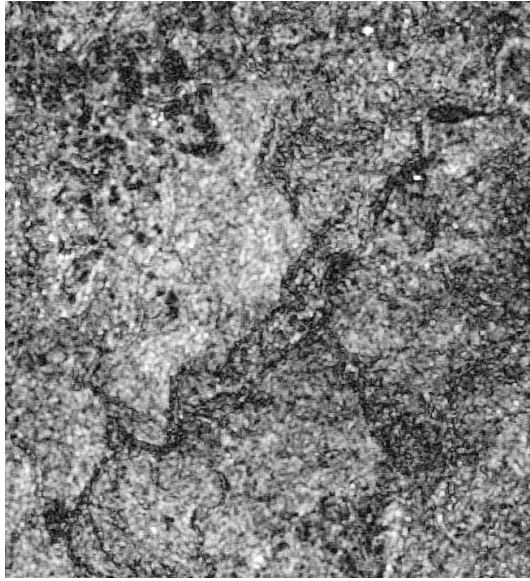


(a) Landsat TM 432

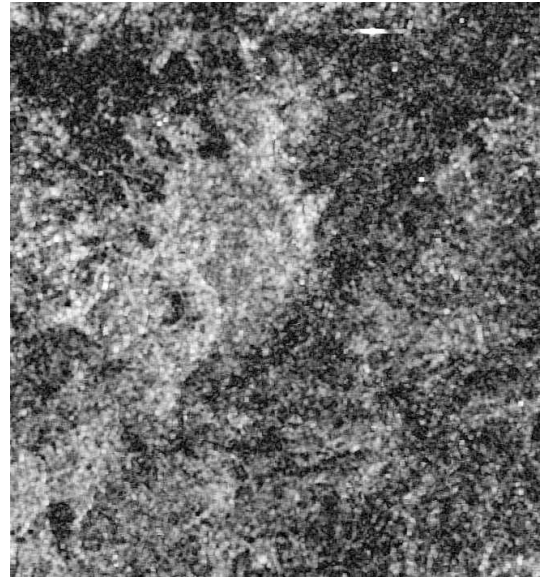


(b) NDVI

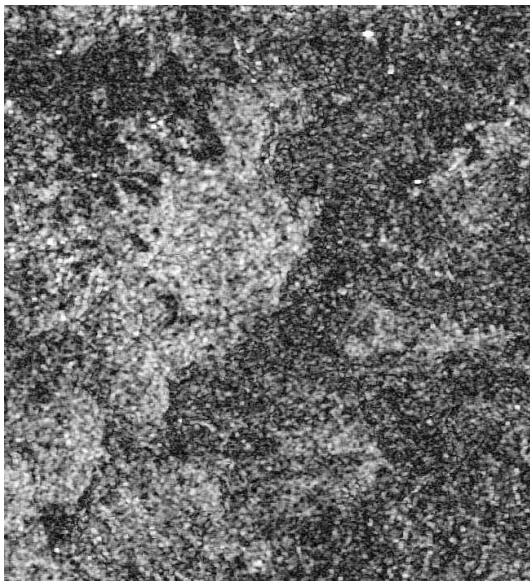
Figure 6.2 (a) Landsat TM standard false colour composite (band 432 in RGB, 1987). (b) TM NDVI image.



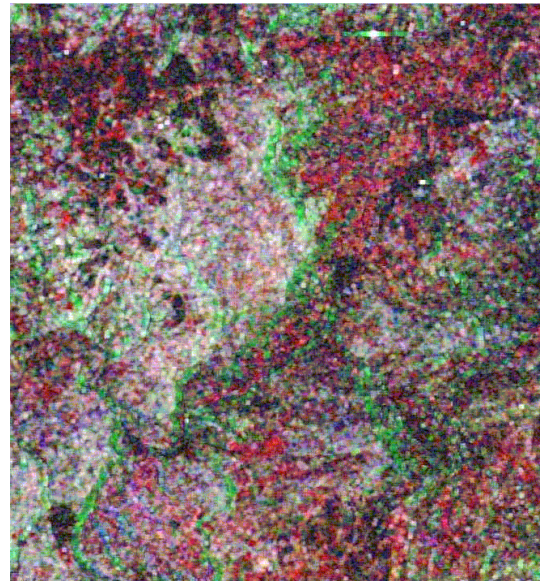
(a) ALM23_COH



(b) ALM34_COH



(c) ALM24_COH



(d) RGB

Figure 6.3 (a) ALM23_COH. (b) ALM34_COH. (c) ALM_24_COH. (d) Colour composite of ALM23_COH in red, ALM34_COH in green and ALM_24_COH in blue.

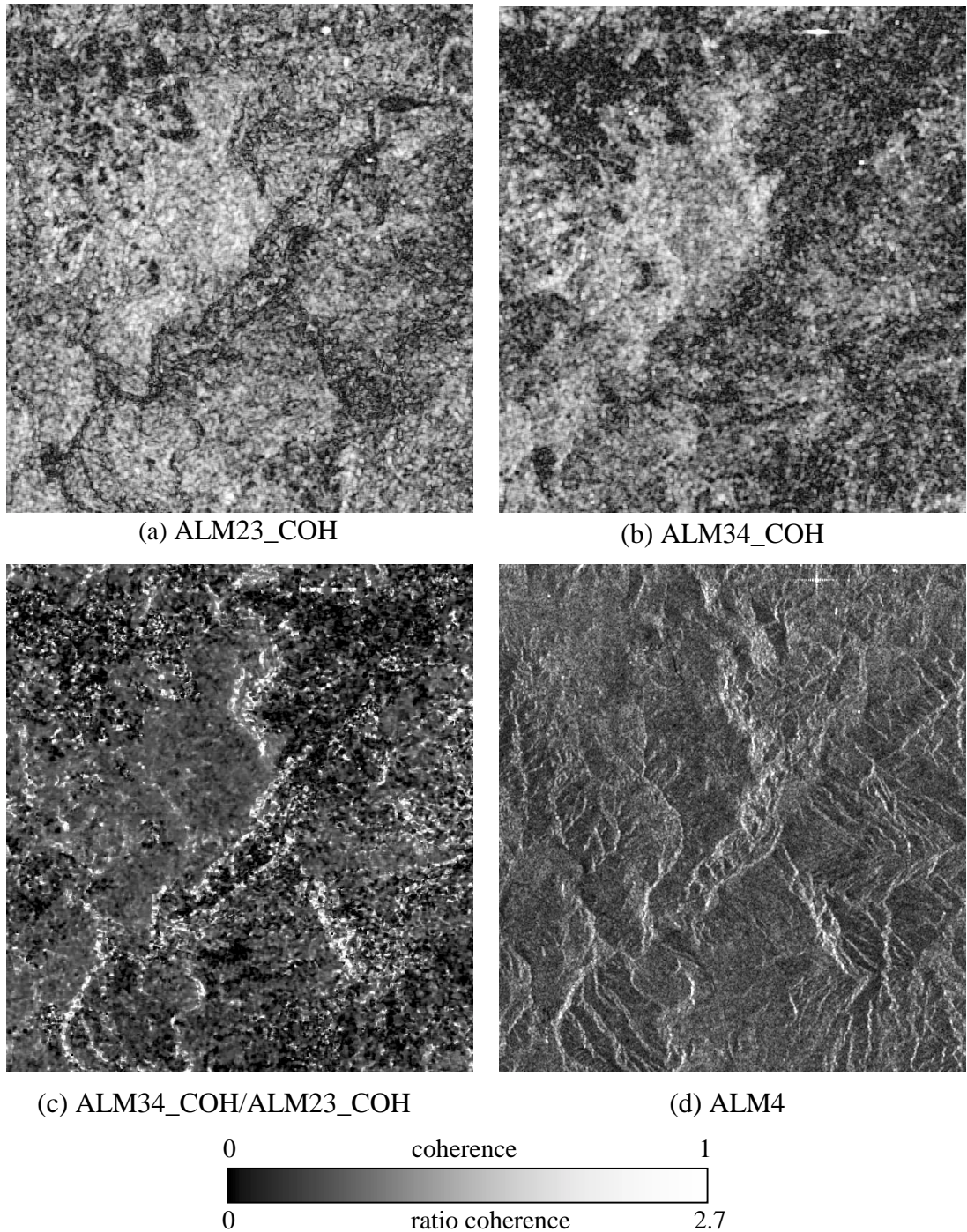
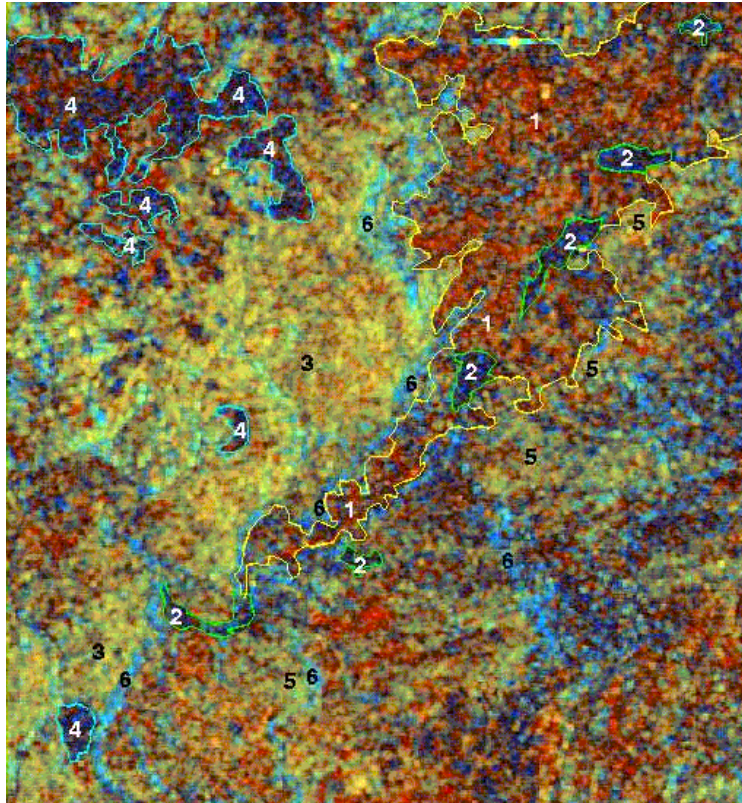


Figure 6.4 Ratio coherence imagery in Almeria, Spain. (a) Coherence image ALM23_COH with 70 days separation and 156m of B_{\perp} . (b) Coherence image ALM34_COH with 140 days separation and 20m of B_{\perp} . (c) Ratio coherence image ALM34_COH/ALM23_COH. (d) SAR amplitude image (ALM4). Complex features of decorrelation of different natures in the coherence images (a) and (b) can be clearly discriminated in the ratio coherence image (c). The curved linear features of low coherence highlighted in white are the total topographic decorrelation along the foreshortened slopes. The dark features are of gradual temporal decorrelation. The black and white noisy spots are from rapid temporal decorrelation of vegetation and agriculture, while grey indicates stable surface.



(a)



(b)

Figure 6.5 (a) The colour composite of ALM23_COH in red, ALM34_COH in green and ALM34_COH/ALM23_COH in blue. 1: Marls subject to rapid erosion. 2: Dense vegetation. 3: Gypsum. 4: Gypsum quarries and dumps. 5: Limestone. 6: Foreshortened slopes (spatial topographic decorrelation effect). (b) Field photo of rapid erosion of Marls (Photo from J. G. Liu)

6.3 Case II: Massive Plantation and Decoherence

This case study is mainly based on field investigation. The study area is in the north region of Almeria from Rio Almanzora in the south to the mountain range of Sierra de Las in the north. A Landsat TM 541 RGB colour composite (Figure 6.6) shows the topography, lithology and vegetation in the area clearly. From the north-west to south east, the main rock types are dolomite mountains in orange, mica-schist range land in deep blue, the highly dissected Pliocene alluvial plain in purple to brown and Quaternary badlands in white (IGME, 1975b). The vegetation is in green.

Figure 6.7 is a colour composite of ALM34_COH in red, ALM23_COH in green and ALM12_COH in blue with temporal separation of 140, 70 and 526 days (Table 6.1). A long temporal separation coherence image ALM12_COH was used to present highly stable areas. Dense vegetation along the Rio Almanzora and other rivers is black because of coherence loss in each time period. The white areas are sparsely vegetated Permian-Triassic dolomites and marbles, such as the mountain range of Sierra de Las and hills along the both sides of Rio Almanzora. The red edge features are spatial decorrelation on foreshortened slopes as the result of a very short baseline of ALM34_COH ($B_{\perp} = 20m$) that is displayed in red. The ratio coherence image is not shown because the major decoherence features are in a gentle undulated terrain with no confusion from spatial decorrelation along steep east-facing slopes.

The most significant features are the green patches which coincide with the distribution of badland in the Albox area and a belt of mica-schist and phyllite forming the southern flank of Sierra de Las. The colour indicate that these areas had quite a high coherence in the 70 days from October to December 1996 but lost coherence completely in the following 140 days from December 1996 to May 1997. What is the principal cause for this phenomenon? The initial interpretation was that it is possibly a rapid erosion event particularly in the hilly region of soft lithology like mica-schist and phyllite. However, the field investigation provided an unexpected answer. The green belt in the southern flank of Sierra de Las accurately defines a massive plantation of olive and almond trees planted recently, as shown in a field photo (Figure 6.8). These trees were planted in the thin soil developed from mica-schist and phyllite. Field observation indicates that the terrain is vulnerable to erosion

once the natural sparse vegetation is stripped off. The decoherence effects may be partially due to the irrigation and ploughing in spring and partially due to natural erosion. This case study demonstrates that coherence imagery can reliably detect and define temporal changes.

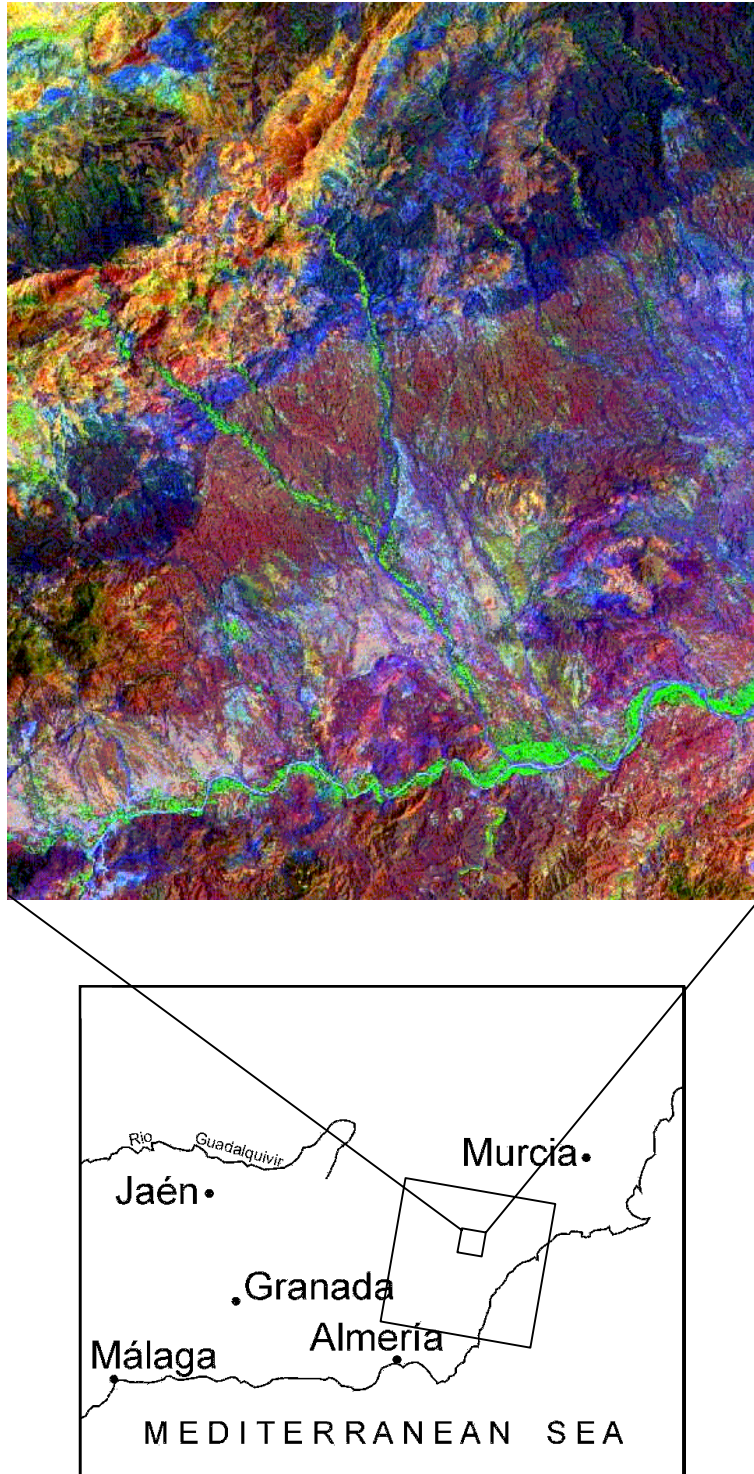


Figure 6.6 Landsat TM bands 541 in RGB and the location of case study II (20 km × 24 km). The large tilted square represents the ALM whole scene (100 km × 106 km).

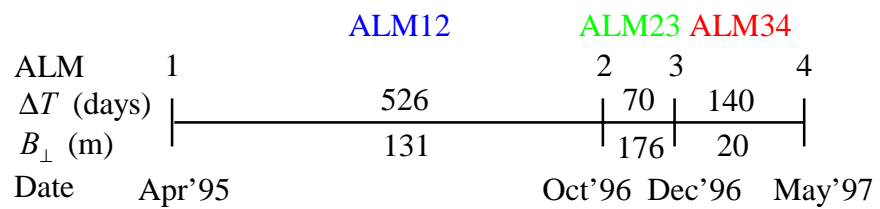
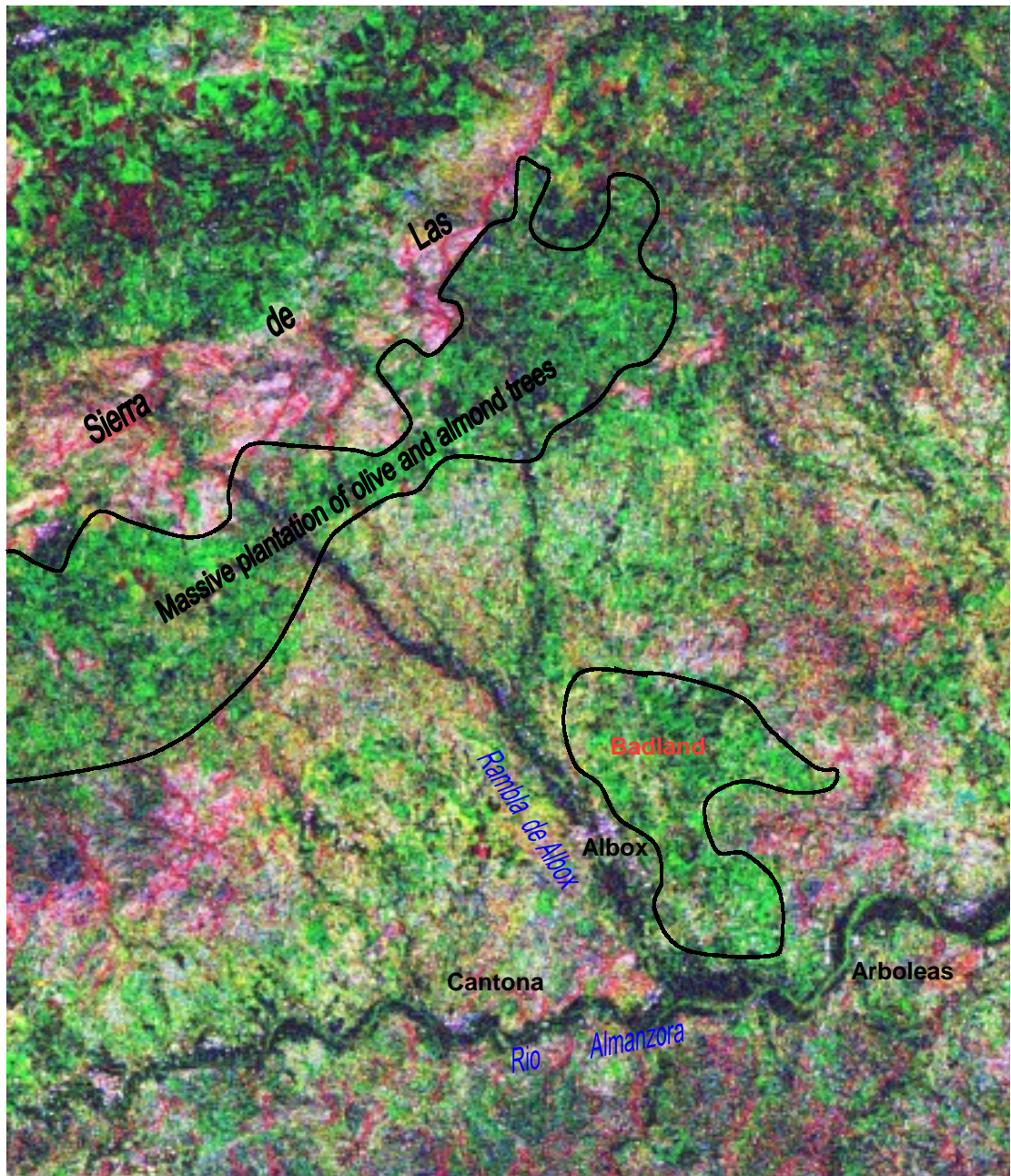


Figure 6.7 Coherence colour composite of ALM34_COH, ALM23_COH, and ALM12_COH in RGB respectively.



Figure 6.8 Massive plantation (Field photo of southern flank of Sierra de Las, from J. G. Liu).

6.4 Case III: A Rainfall Event in the Granada Scene

An area southeast of Jaén in the Granada scene was selected for the third case study. The study area, measuring 28 km by 28 km, is shown in a Landsat TM band 432 in RGB colour composite, together with a location map (Figure 6.9). Figure 6.10 illustrates a simplified geological map of this area (IGME, 1970). Figure 6.11 shows Landsat TM band 531 in RGB for more detailed interpretation of lithology,. The massifs to the north and south (red to purple) are the Jurassic basement rock of the South Iberian Domain composed of limestone, dolomite and marls. Between them is a broad basin of Cretaceous marls, limestone and dolomite (light blue). The basin is partially filled with Neogene and Quaternary sediments.

Raw data of two ERS-1/2 tandem pairs of Granada area were acquired as shown in Table 6.4. The first tandem pair brackets a rainfall event. At the weather station in the city of Jaén, 1 mm of precipitation was recorded on 2 May 1996, the acquisition date of GRA1, and 21 mm on 3 May 1996, the acquisition date of GRA2 (The Weather Underground, Ltd.). The wet weather conditions significantly altered the moisture and micro-geometry of the radar scatterers to reduce coherence during the first tandem pair GRA12_COH, shown in Figure 6.12(a). In comparison, the second tandem pair GRA34_COH acquired under dry condition is shown in Figure 6.12(b). The average coherence level of GRA12_COH (0.46) is significantly lower than that of GRA34_COH (0.72), as shown in Table 6.5. It is particularly low in most regions of the GRA12_COH image, except the spatial topographic decorrelation phenomena in the mountainous area in GRA34_COH due to its larger baseline (131 m) than that of GRA12_COH (91 m).

Four possible major causes that may have reduced the coherence in GRA12_COH are to be discussed here: 1) vegetation & wind, 2) surface moisture change, 3) rainfall/erosion, and 4) bias of coherence estimation from topographic phase fringes.

Table 6.4 ERS SAR Granada scene and weather data of the city of Jaén.

| Scene | Mission | Date | Weather | Average wind speed (kph) | Maximum wind speed (kph) |
|-------|---------|----------|--------------|--------------------------|--------------------------|
| GRA1 | ERS-1 | 19960502 | rain (1 mm) | 20.4 | 24.1 |
| GRA2 | ERS-2 | 19960503 | rain (21 mm) | 6.3 | 14.8 |
| GRA3 | ERS-1 | 19961024 | dry | 4.3 | 7.6 |
| GRA4 | ERS-2 | 19961025 | dry | 1.1* | 7.6* |

* data measured at the city of Granada.

Table 6.5 Two ERS tandem-pair InSAR coherence images for the case study III in Granada, Spain.

| Scene | B_{\perp} (m) | Average coherence | Standard deviation |
|-----------|-----------------|-------------------|--------------------|
| GRA12_COH | 91 | 0.46 | 0.21 |
| GRA34_COH | 131 | 0.72 | 0.12 |

6.4.1 Vegetation & Wind

According to the Landsat TM band 432 in RGB colour composite, in Figure 6.9, many parts of the study area are covered with vegetation. Dense vegetation (bright red) is concentrated along the river channels while forest (dark red) is also widespread over the entire region. Vegetation may have a considerable effect to reduce the coherence level in GRA12_COH in these areas.

To localise the low coherence areas affected by vegetation and to visualise the slope dependence of them, Landsat TM NDVI and GRA12_COH are overlain by topographic contours derived from GRA34_INF, as shown in Figure 6.13. GRA34_INF is a good quality interferogram that presents topographic variation in SAR geometry. Red colour represents vegetated area in (a) NDVI-contour image and low coherence area in (b) GRA12_COH-contour image.

The coregistration error between the TM NDVI image and the interferogram GRA34_INF is significant in mountainous regions. The SAR image of this high relief area is severely distorted, resulting in *foreshortening* and *layover* effects. This local geometric distortion is due to the fact that the SAR (actually any radar) is a ranging device and therefore generates a cross-track reflectivity map based on the sensor to target range distance. For instance, the topographic contours are foreshortened on the east side slope of Monte Prieto, located in the upper left part of the study area, while expanded on the west side as ERS SAR looks from the east. The actual vegetation cover in Monte Prieto is wider than that shown in Figure 6.13(a) NDVI-Contour image. It should spread over all contours of the west side slope to the top of this mountain. Correction of SAR geometric distortion needs an accurate DEM and computer software, which was not available during this research period. For qualitative comparison to verify the concept of the application, the dataset is adequate though caution must be applied in interpretation. In the interpretation of NDVI-contour image, a rule of thumb is that vegetation cover over the contours of the west side slope should be expanded towards the contours of uphill while those of the east side slope should be shrunk towards the east. The coregistration is relatively accurate in flat region where the effects of geometric distortion can be ignored.

Two images show high correlation with each other. The distribution of forest on mountain slopes and dense vegetation along rivers in NDVI-contour image matches most of the decoherence patches in the GRA12_COH-contour image. The existence of vegetation alone cannot provide evidence of low coherence. Vegetated areas can sustain high coherence in dry and calm (low wind speed) weather conditions, as seen from GRA34_COH. It can, therefore, be assumed that all the vegetated areas in GRA12_COH lost coherence due to movement of tree canopies caused by rainfall and wind.

Wind accompanying rainfall event can significantly change the stability of the surface covered with vegetation. According to the weather data in Table 6.4, the wind speed was relatively high at the acquisition day of GRA1 (20.4 kph) compared with the others: GRA2 (6.3 kph), GRA3 (4.3 kph), and GRA4 (1.1 kph). High wind speed in GRA1 swung vegetation canopies thus intensified decoherence phenomena in the areas covered with vegetation. The higher wind speed of GRA1 compared to that of

GRA2 can be verified by observing the high radar intensity of a lake in GRA1 near the study area. An example is shown in Figure 6.14. The smooth water surface in calm weather acts as a specular reflector that reflects most of the energy away from the radar, resulting in a very low return signal. The lake appears dark in (b) GRA2. Rough water surfaces in windy condition return radar signals of varying strengths resulting much brighter lake surface in (a) GRA1. The difference image between GRA1 and GRA2 in (c) GRA1-GRA2 shows higher radar intensity in GRA1 than GRA2, indicating higher wind speed in GRA1.

6.4.2 Surface Moisture Change

Surface moisture is an important factor that changes the radar backscattering properties of the target surface, thus changing coherence level as well as radar intensity. Most natural surfaces are subject to penetration by the electromagnetic wave. The penetration depth is dependent on both the surface condition and the wavelength of the electromagnetic wave. Thus the scattering from natural terrain is generally a combination of surface scattering and volume scattering. A useful quantity for characterising the volume scattering is the penetration depth. Given a wave incident on a surface, the depth at which the refracted portion of the wave is attenuated by $1/e$ of its value at the layer boundary is given by (Ulaby *et al.*, 1982)

$$\delta z = \lambda \sqrt{\epsilon'} / (2\pi\epsilon'') \quad (6.1)$$

where the relative dielectric constant, a complex number $\epsilon_r = \epsilon' + j\epsilon''$, must satisfy $\epsilon''/\epsilon' < 0.1$ for equation 6.1 to be valid.

The volumetric content of the water in the soil, for example, is directly related to the dielectric constant. When water is added to the soil, the real part of the relative dielectric constant increases more rapidly than the imaginary part as shown in Figure 6.15(a). The net effect is that the penetration depth δz decreases as the soil moisture increases according to (6.1). Thus, the signal received by the radar is a result predominantly from surface scattering of the non-refracted portion of the incident

wave. The backscattering coefficient, therefore, increases as the soil moisture volume content m_v increases as shown in Figure 6.15(b).

A SAR intensity image is brighter in wet weather conditions than in dry weather conditions, as the result of stronger surface scattering. This general observation is supported by the fact that GRA1 and GRA2 SAR intensity images, obtained in wet condition, show higher intensity than GRA3 and GRA4 (Figure 6.16). In the areas of soft lithology, penetration depth was reduced significantly by the rainfall event so that surface scattering dominates volume scattering, resulting in high radar backscattering in GRA1 and GRA2 compared with GRA3 and GRA4, shown as bright in a difference image (a) GRA1-GRA4 and (b) GRA2-GRA4 in Figure 6.17. In the areas of hard lithology, penetration depth was not changed by the rainfall events, shown as grey in (a) GRA1-GRA4 and (b) GRA2-GRA4. No change of radar intensity was found between GRA3 and GRA4 both obtained in dry condition, as shown in (c) GRA3-GRA4.

If two SAR scenes of an area are obtained in a similar wet condition, then radar intensities and coherence between them will be high. This is the case of the basins showing high intensity both in GRA1 and GRA2 and high coherence in GRA12_COH. High wind speed of GRA1 did not contribute to decoherence in this barren surface (nearly no vegetation cover). The rainfall events, occurred both in GRA1 and GRA2 of these regions, gave more or less the same effect on radar backscattering coefficient. The absence of volume scattering due to wet surface conditions and no significant surface moisture change in two images resulted in high coherence in GRA12_COH in these areas. It implies that 1 mm precipitation of GRA1 was sufficient to increase the soil moisture to the level that hindered the C band radar penetration. Therefore, there was no further increment of radar intensity even though 21 mm rainfall was added in the next day when GRA2 image was taken. This is in accordance with a laboratory experiment performed by Nesti *et al.* (1998), which indicated that the scattering property and coherence becomes insensitive to further moisture change for an initially wet surface.

Change of moisture content on tree canopy and trunk, as well as the soil moisture under the trees, may have caused different radar reflectivity between GRA1 and GRA2, resulting in decoherence in GRA12_COH. According to Figure 6.17,

however, SAR intensity images of GRA1 and GRA2 in the vegetated areas show no change of radar reflectivity between wet and dry conditions, shown as grey in (a) GRA1-GRA4 and (b) GRA2-GRA4. The same phenomenon is also shown in the difference image (d) GRA2-GRA1 indicating no difference between GRA1 and GRA2. As most vegetated areas are based on hard lithology with thin soil in this study area, there was no significant change surface moisture or change of radar intensity even in case of rainfall events. Areas of resistant lithology without vegetation cover also show no change in radar intensity but have high coherence. Moisture may not be relevant in this case because there is no radar penetration to solid rock surface in whatever weather conditions. Therefore, it can be concluded that low coherence of GRA12_COH on vegetated surface, mostly based on stable lithology, was not affected by decoherence from surface moisture change. Movement of trees by high wind speed in GRA1 is the main cause of decoherence in the vegetated area, as discussed in the previous section.

An area is detected that shows significantly different radar intensities between GRA1 and GRA2, in the right bottom of the study area. This is shown as bright in a difference image of (d) GRA2-GRA1 in Figure 6.17. Figure 6.18 (a) shows a zoomed image of this area. The SAR intensity of GRA1 was low in this area, but increased the next day (GRA2). The southern part of this patch is covered with vegetation while the northern part is not, as shown in (b) NDVI-Contour. If the rainfall events are not localised in this area, it can be concluded that surface lithology and soil type in this area must be sensitive enough to react differently between 1 mm (GRA1) and 21 mm (GRA2) precipitations, resulting in low coherence in (c) GRA12_COH. Surface moisture change is the major decoherence factor in this area, while wind also contributed to decoherence in the vegetated area in the southern part. In the case of very localised rainfall, this interpretation may not be valid. For example, if there were no rainfall in GRA1 in this area but GRA2, one cannot conclude that the lithology of this area is different from that of other areas. Therefore, more localised weather conditions is needed for interpretation of coherence images.

6.4.3 Rainfall/Erosion

Figure 6.19 shows a patch of area in the upper right part of the study area, having low coherence in (a) GRA12_COH-Contour image. This area is not covered with vegetation as shown in (b) NDVI-Contour. Wind could not be a contributing factor in this barren area. Responses of radar reflectivity are similar to those of areas with hard lithology, which have consistently low reflectivity regardless of rainfall event, as shown in (c) GRA2-GRA1 image. Soil moisture change is therefore not an effective decoherence factor in this area. From the geological map and (d) TM 531 RGB image, this area is covered with soft lithology (mica-schist and phyllite) vulnerable to erosion. Rapid erosion associated with rainfall event could be a major factor to lose coherence in GRA12_COH in this specific area. Further verification is necessary from field investigation.

6.4.4 Bias in Coherence Estimation from Topographic Phase Fringes

It is known that coherence estimation is biased towards lower value in the presence of topographic phase fringes (Touzi *et al.*, 1999). Topographic phase fringes within the averaging window during the coherence calculation will act as a scene nonstationarity that causes degradation of coherence level. Therefore, in principle, it is necessary to remove topographic phase fringes in the coherence calculation.

The coherence degradation effect of topographic phase is expected more significantly in GRA34_COH than in GRA12_COH because the baseline perpendicular component of GRA34_COH (131 m) is longer than that of GRA12_COH (93 m). This is shown as denser topographic phase fringes in the interferogram GRA34_INF than in GRA12_INF. Therefore, if the effect of topographic phase fringes on degrading coherence level on a steep slope is significant, GRA34_COH should have more serious coherence degradation than GRA12_COH on steep slopes. As the argument here is to find the explanation of low coherence features on steep slopes which are selectively in GRA12_COH but not

obvious in GRA34_COH, the possibility of coherence bias from topographic phase fringes as a reason of these low coherence features can be easily ruled out.

However, this study raised an important issue: coherence imagery would be more objective and reliable for temporal change detection in a relief area if the bias (or degradation) in coherence estimation from topographic phase fringes can be removed. This is the topic of Chapter 7.

6.4.5 Interpretation and Discussion

It is found that different decoherence factors contributed to different areas of low coherence in GRA12_COH, as summarised in Table 6.6. Lithology, vegetation cover characterises the surface feature. Wind, surface moisture change, and erosion are possible decoherence factors. Figure 6.20 shows interpretation results of decoherence features of GRA12_COH.

Most vegetated areas (A, green) are believed to have lost coherence from high wind speed on the day of GRA1. Based on hard lithology, these areas show no change of radar reflectivity in all Granada scenes, indicating that surface moisture change was not significant in this area even in the case of rainfall events. It was found that many areas of low coherence coincide with steep slopes. In the early stage of the research, the roles of this widespread forest vegetation (dark red in Landsat TM band 432 in RGB composite, see Figure 6.9) to decoherence of GRA12_COH were overlooked. This led to an incorrect interpretation that decoherence features of GRA12_COH, selectively on steep slopes, were possibly caused by rapid erosion from a rainfall event from an assumption that the non-vegetated, bare surface with high gradient is more vulnerable to erosion (Liu *et al.*, 1999e). Vegetation of such kind tends to remain only in high relief regions while flat areas are cultivated. The distribution of vegetation, therefore, coincides with slopes in high relief areas, and decoherence effect of vegetation is not negligible in the rainy and windy weather condition. Assumption of the slope dependence of rainfall/erosion rate (Liu *et al.*, 1999e) is also proved inappropriate by observing the high coherence areas of steep slope with no vegetation cover. These areas, having resistant lithology with no

vegetation cover were not affected by surface moisture change (B, pink) because radar penetration into solid rock surface is irrelevant to surface moisture.

In areas of soft lithology (C, blue), 1 mm precipitation changed soil moisture significantly, resulting in high radar reflectivity in GRA1 compared with GRA4 obtained in dry surface condition. No further change of soil moisture and radar reflectivity was produced when 21 mm precipitation was added in the next day (GRA2), resulting in high coherence in GRA12_COH. However, there are exceptional cases. An area is found showing significant changes in radar reflectivity between GRA1 and GRA2 (D1 and D2, yellow). Soil moisture change between GRA1 and GRA2 is possibly the main cause of decoherence in GRA12_COH in this area. The southern part of this patch (D2), covered with vegetation, may have also been affected by high wind in GRA1. This phenomenon could be from moderately resistant lithology of this area that did not allow significant change of surface moisture with 1mm rainfall, and allowed significant change when 21mm rainfall was added. However, the possibility of the localised rainfall only in GRA2 in this area cannot be excluded. In the upper-right part of the study area (E, red), a low coherence area was detected, which is non-vegetated, showing no radar intensity change. Erosion from rainfall in this soft lithology may have caused decoherence in this limited area.

It should be noted that the amount of rainfall was assumed to be evenly distributed over the study area. In the case of localised rainfall events, the interpretation of coherence images, discussed so far, could be changed accordingly. More localised weather conditions as well as detailed surface morphological information should be taken account of during the interpretation of coherence images.

This case study shows how interpretation of coherence images becomes complicated when a rainfall event has occurred. Interpretation of coherence images should be incorporated with many other environmental factors such as vegetation cover, wind speed, precipitation, land-use, and lithology. InSAR coherence images, together with images from optical sensors, topographic map, geological map, meteorological data, and field investigation, enables comprehensive study of environmental surface change and morphology.

Table 6.6 Interpretation of various decoherence features in GRA12_COH.

| Area Code (colour) | Land Surface | | Decoherence Factors | | | Coherence GRA12_COH |
|-----------------------|--------------|------------|---------------------|---|------------|------------------------|
| | Lithology | Vegetation | Wind | Surface moisture change (GRA1 – GRA2) | Erosion | |
| A (green) | Hard | Yes | Yes | No (low–low) | No | Low |
| B (pink) | Hard | No | No | No (low–low) | No | High |
| C (blue) | Moderate | No | No | No (high–high) | No | High |
| D1 (yellow) | Moderate | Yes | Yes | Yes (low–high) | No | Medium to Low |
| D2 (yellow) | Moderate | No | No | Yes (low–high) | No | Medium to Low |
| E (red) | Soft | No | No | No (low–low) | Yes | low |

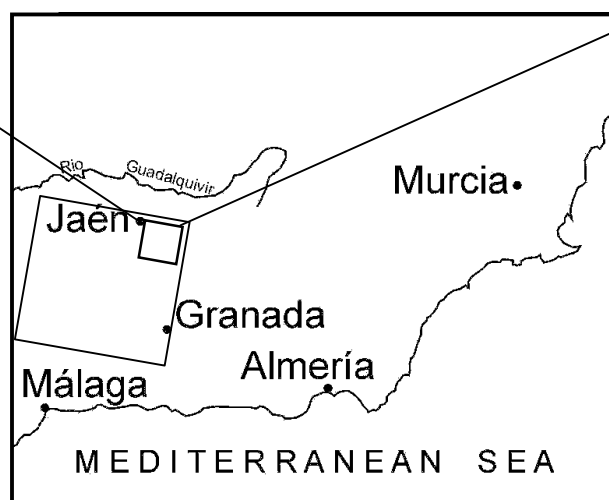
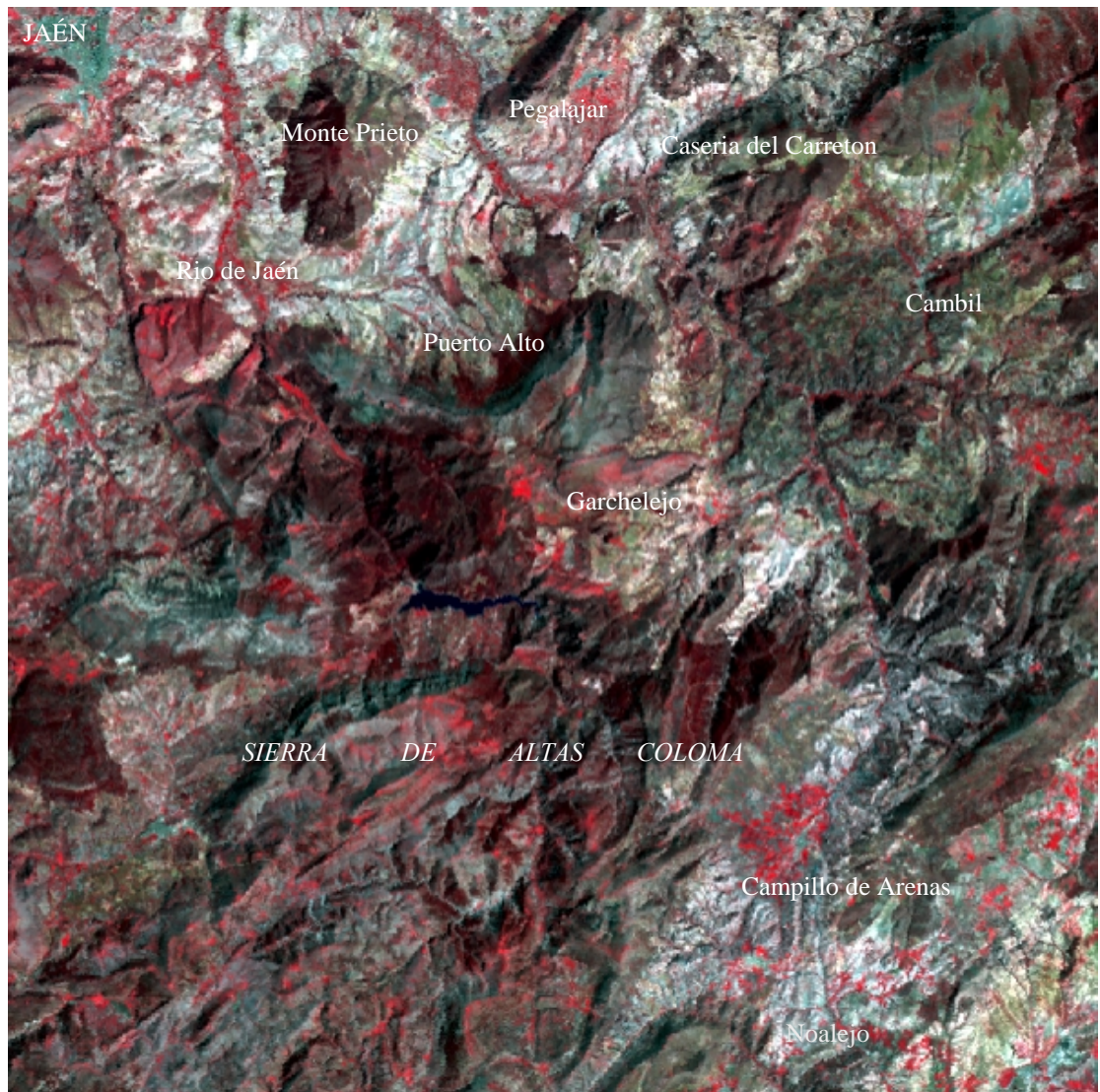


Figure 6.9 Study area of Case III and Landsat TM bands 432 in RGB colour composite (28 km × 28 km). The large tilted square represents the location of GRA whole scene (100 km × 106 km).

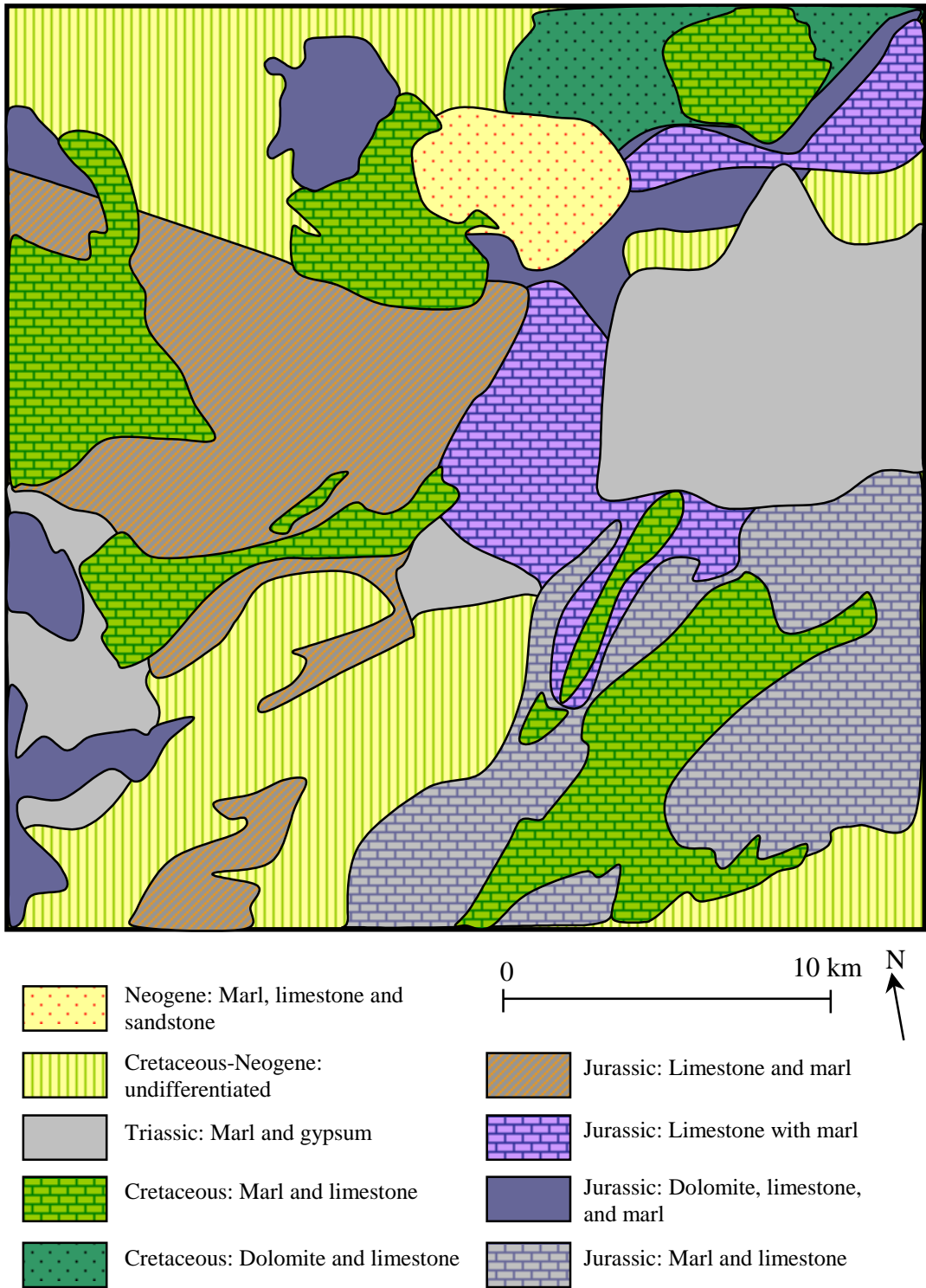


Figure 6.10 A simplified geological map of the Case III study area (28 km × 28 km; IGME, 1970).

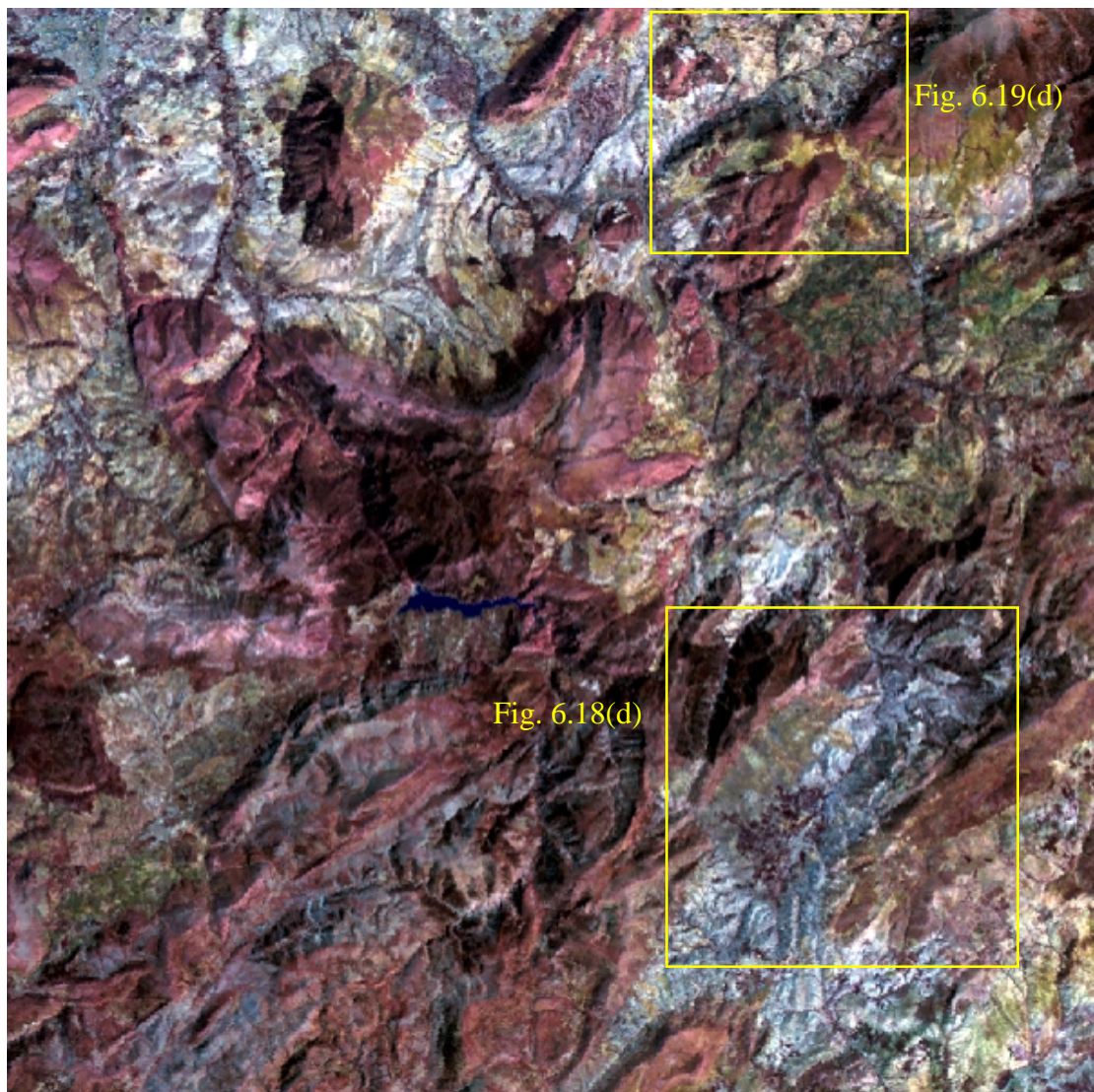
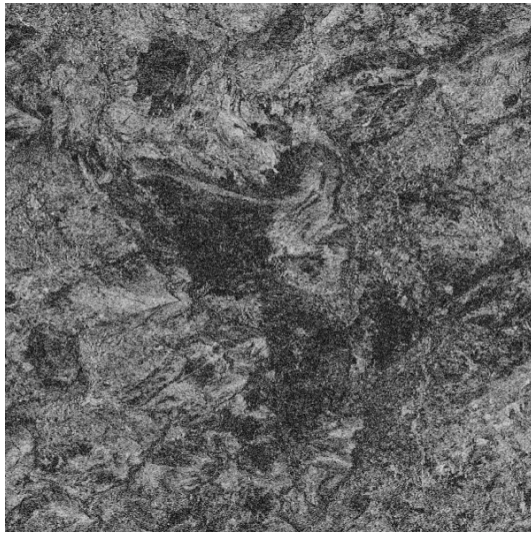
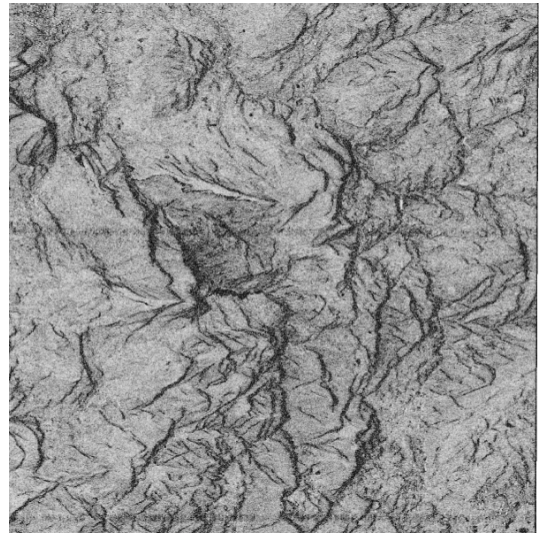


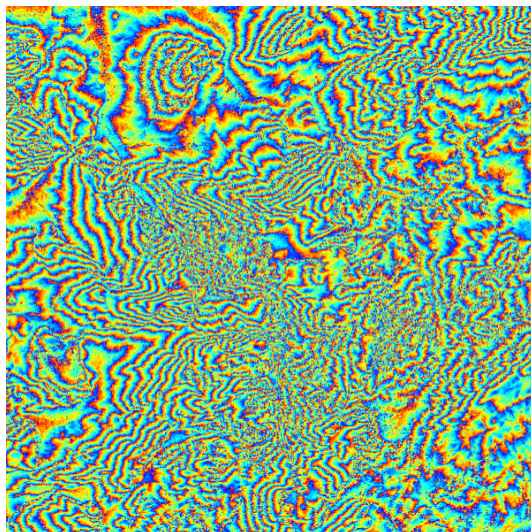
Figure 6.11 Landsat TM bands 531 in RGB colour composite (28 km \times 28 km). Red and purple: Jurassic dolomite, limestone, and marls. Light blue: Cretaceous marls and limestone. (Yellow boxes are the locations sub scenes.)



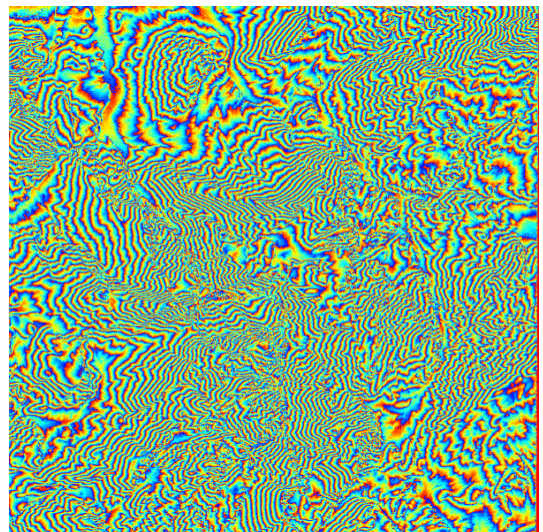
(a) GRA12_COH



(b) GRA34_COH

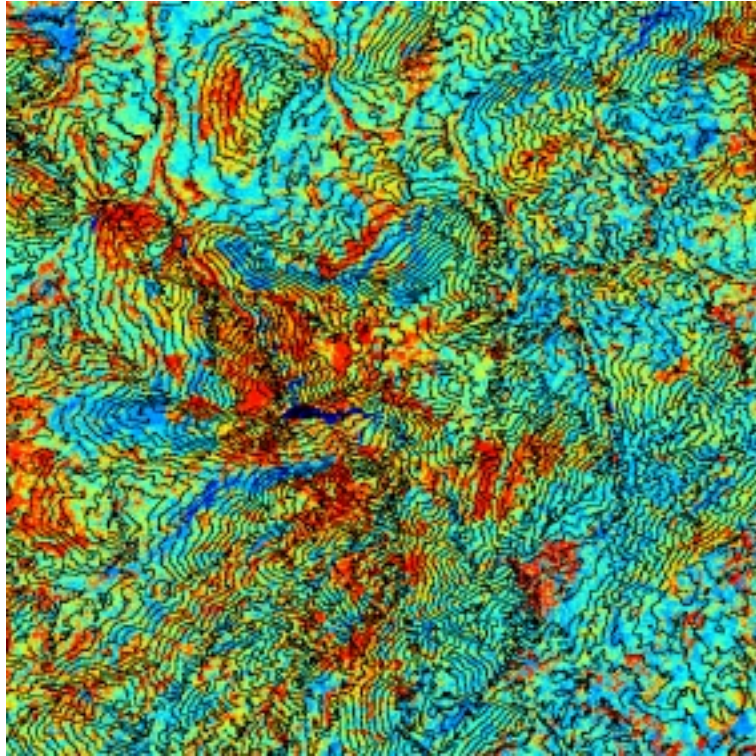


(c) GRA12_INF

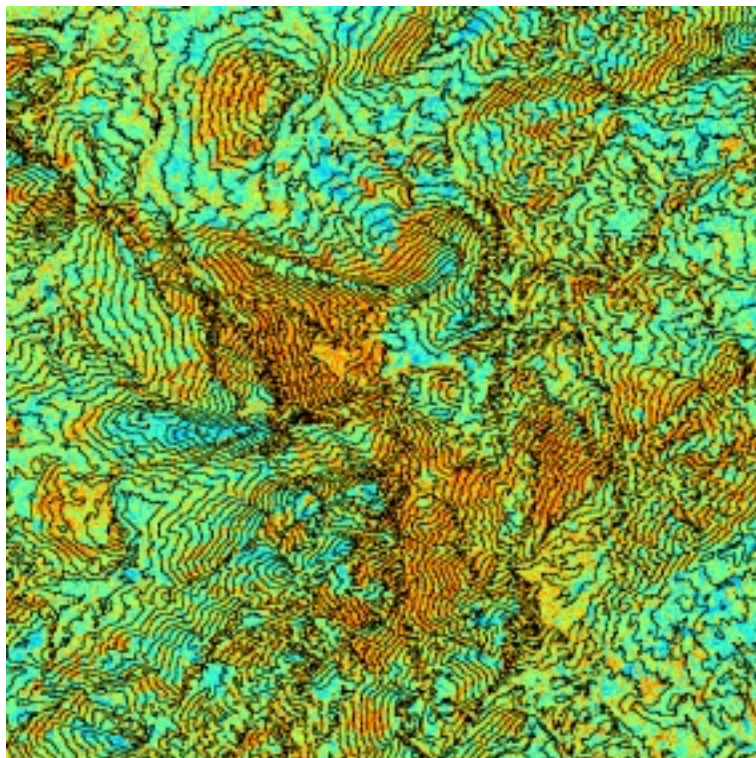


(d) GRA34_INF

Figure 6.12 Coherence images and interferograms of GRA scenes (28 km \times 28 km). (a) GRA12_COH, (b) GRA34_COH, (c) GRA12_INF, and (d) GRA34_INF.

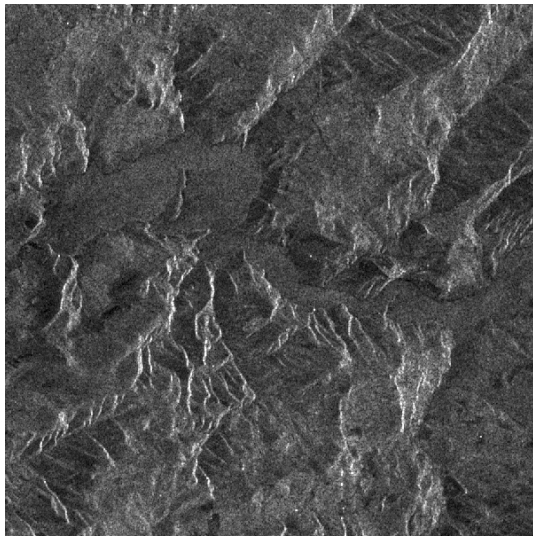


(a) NDVI-Contour

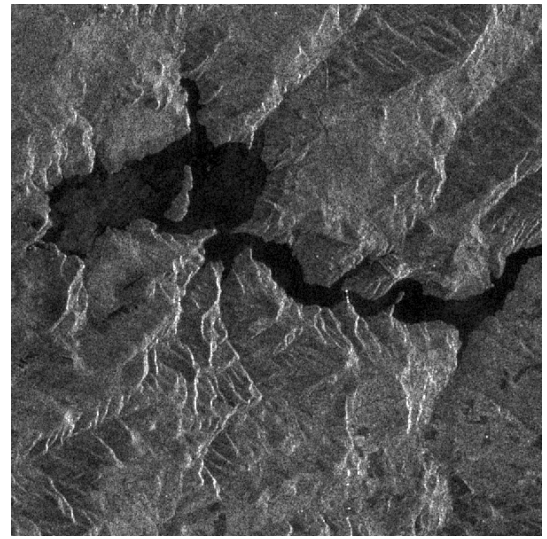


(b) GRA12_COH-Contour

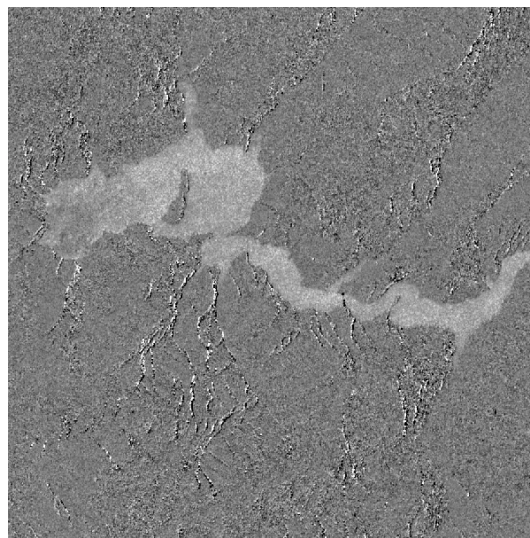
Figure 6.13 (a) NDVI-Contour image. Red represents vegetation. (b) GRA12_COH-Contour image. Red represents low coherence. Contours are generated from GRA34_INF.



(a) GRA1

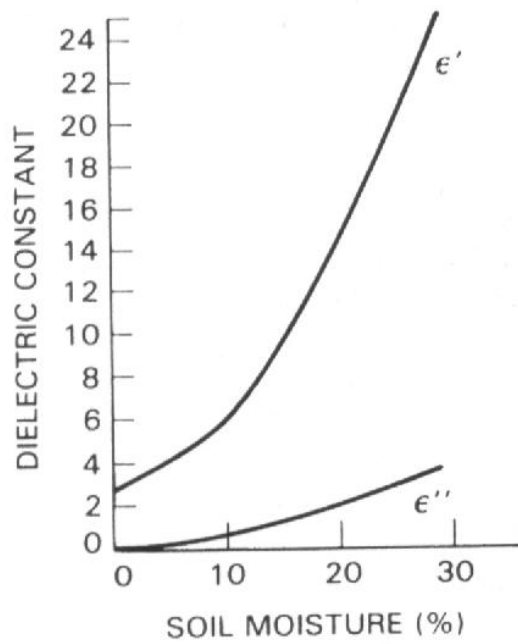


(b) GRA2

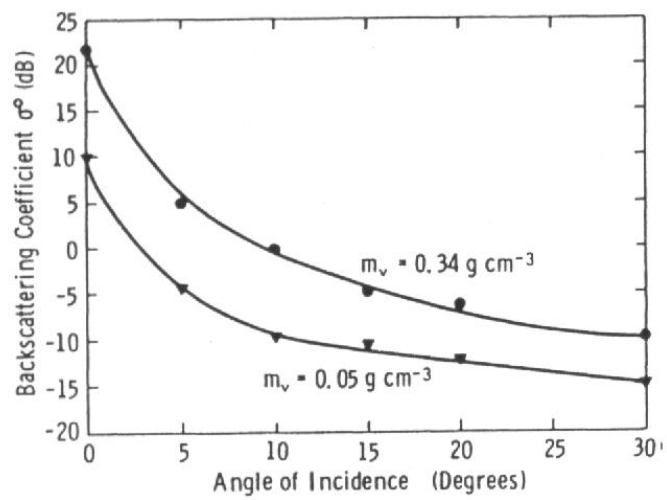


(c) GRA1-GRA2

Figure 6.14 Wind effect on a lake ($11 \text{ km} \times 11 \text{ km}$). (a) GRA1 shows higher radar intensity on the lake surface than that in (b) GRA2. (c) a difference image GRA1-GRA2 that shows higher radar intensity in GRA1 on the lake surface, indicating higher wind speed in GRA1.

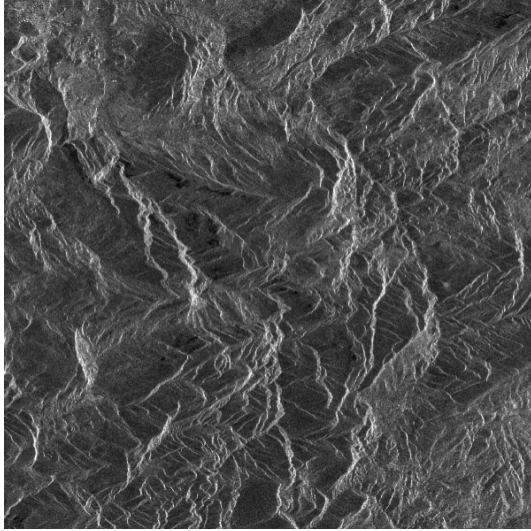


(a)

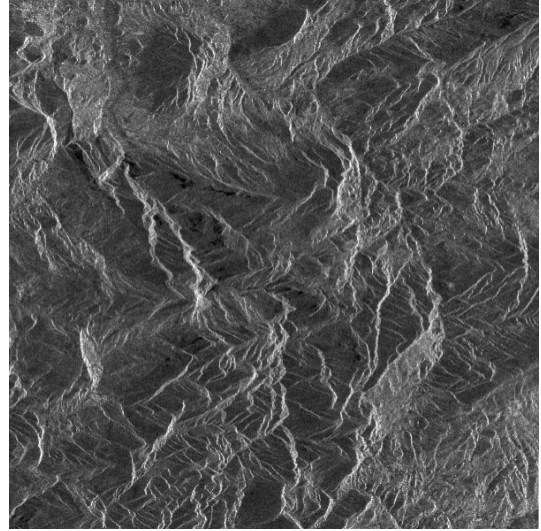


(b)

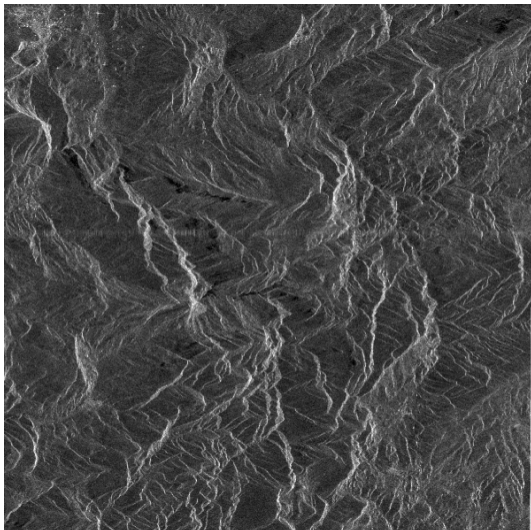
Figure 6.15 (a) Dependence of complex dielectric constant on soil moisture. (b) Dependence of backscattering coefficient on incidence angle and soil moisture (Curlander and McDonough, 1991).



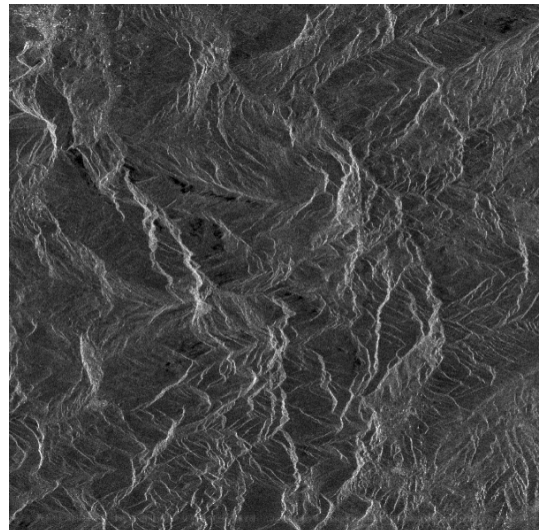
(a) GRA1



(b) GRA2

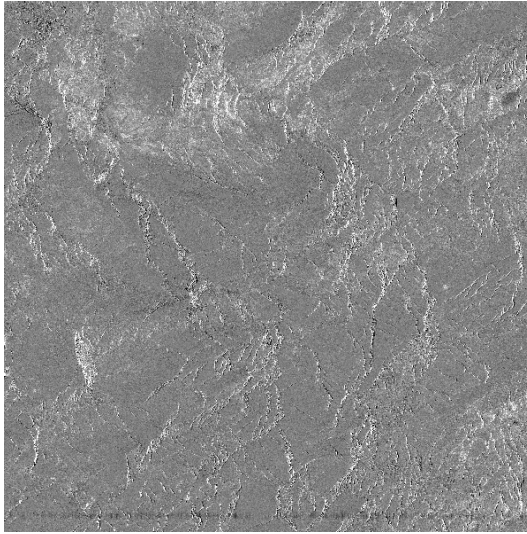


(c) GRA3

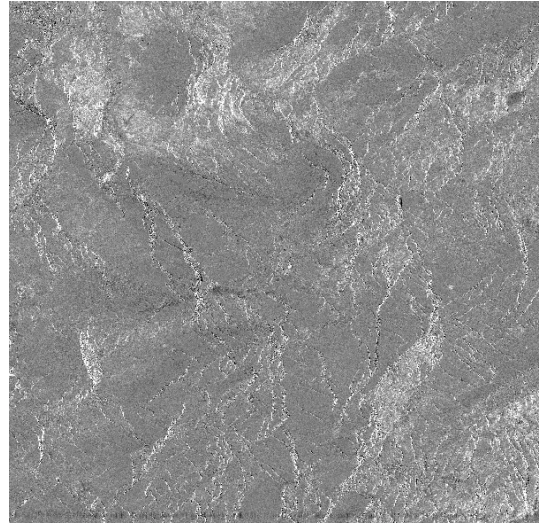


(d) GRA4

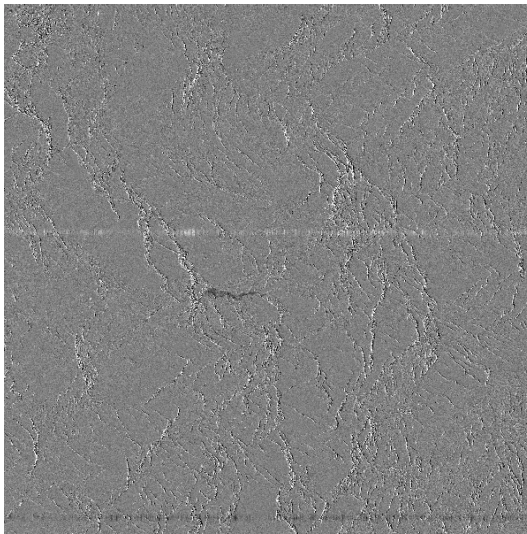
Figure 6.16 SAR intensity images of the study area (28 km \times 28 km).



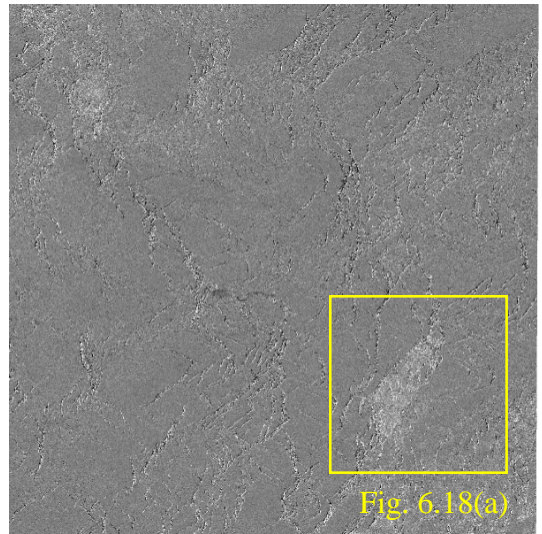
(a) GRA1-GRA4



(b) GRA2-GRA4

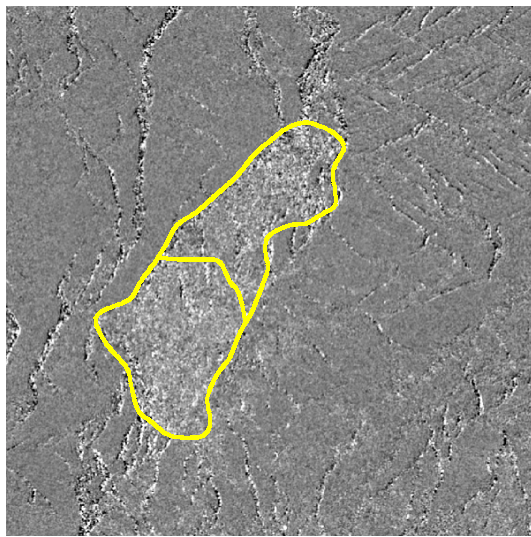


(c) GRA3-GRA4

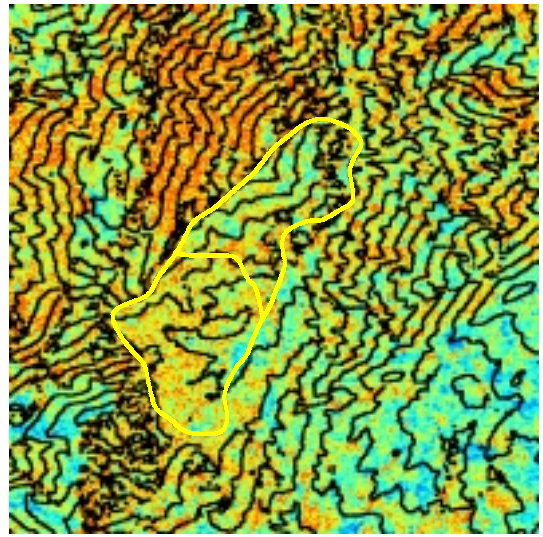


(d) GRA2-GRA1

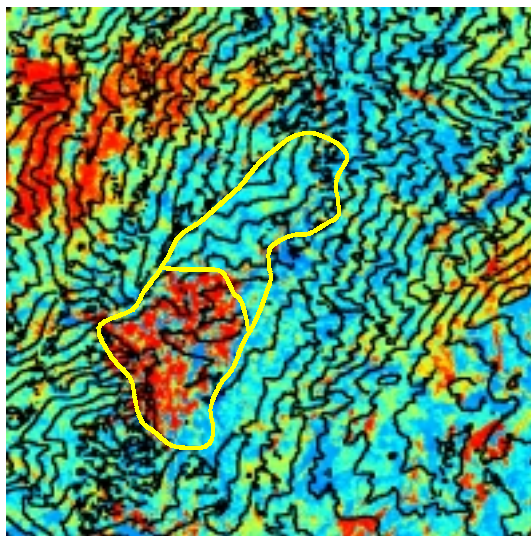
Figure 6.17 Difference of SAR intensity images ($28 \text{ km} \times 28 \text{ km}$): (a) GRA1-GRA4, (b) GRA2-GRA4, (c) GRA3-GRA4, and (d) GRA2-GRA1.



(a) GRA2-GRA1



(b) GRA12_COH-Contour

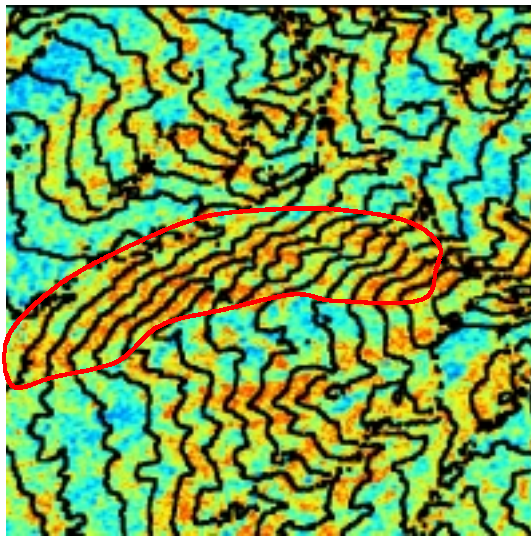


(c) NDVI-Contour

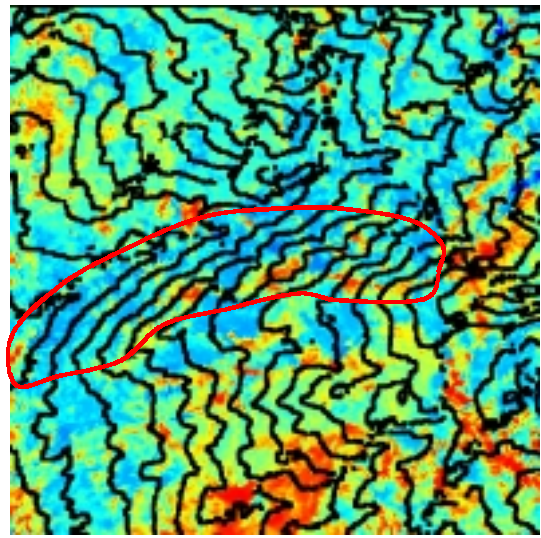


(d) TM 531

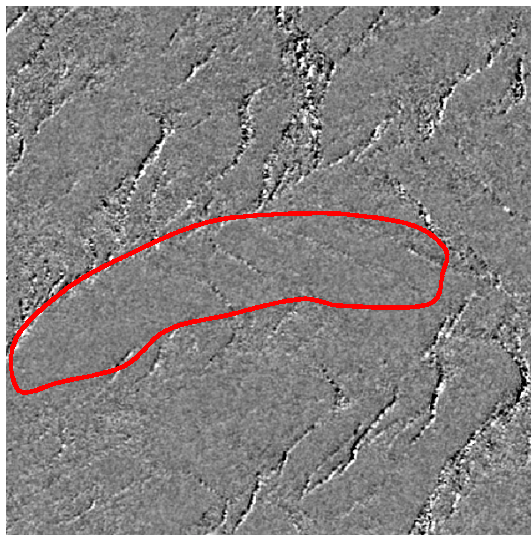
Figure 6.18 Decoherence from soil moisture change ($9 \text{ km} \times 9 \text{ km}$): (a) GRA2-GRA1, (b) GRA12-Contour, (c) NDVI-Contour, and (d) Landsat TM bands 531 in RGB.



(a) GRA12_COH-Contour



(b) NDVI-Contour



(c) GRA2-GRA1



(d) TM 531

Figure 6.19 Erosion from rainfall ($6 \text{ km} \times 6 \text{ km}$): (a) GRA12_COH-Contour image indicates an area of low coherence from rainfall/erosion. (b) NDVI-Contour shows no vegetation in this area. (c) GRA2-GRA1 indicates no soil moisture change between GRA2 and GRA1. (d) Landsat TM 531 in RGB shows lithology of this area.

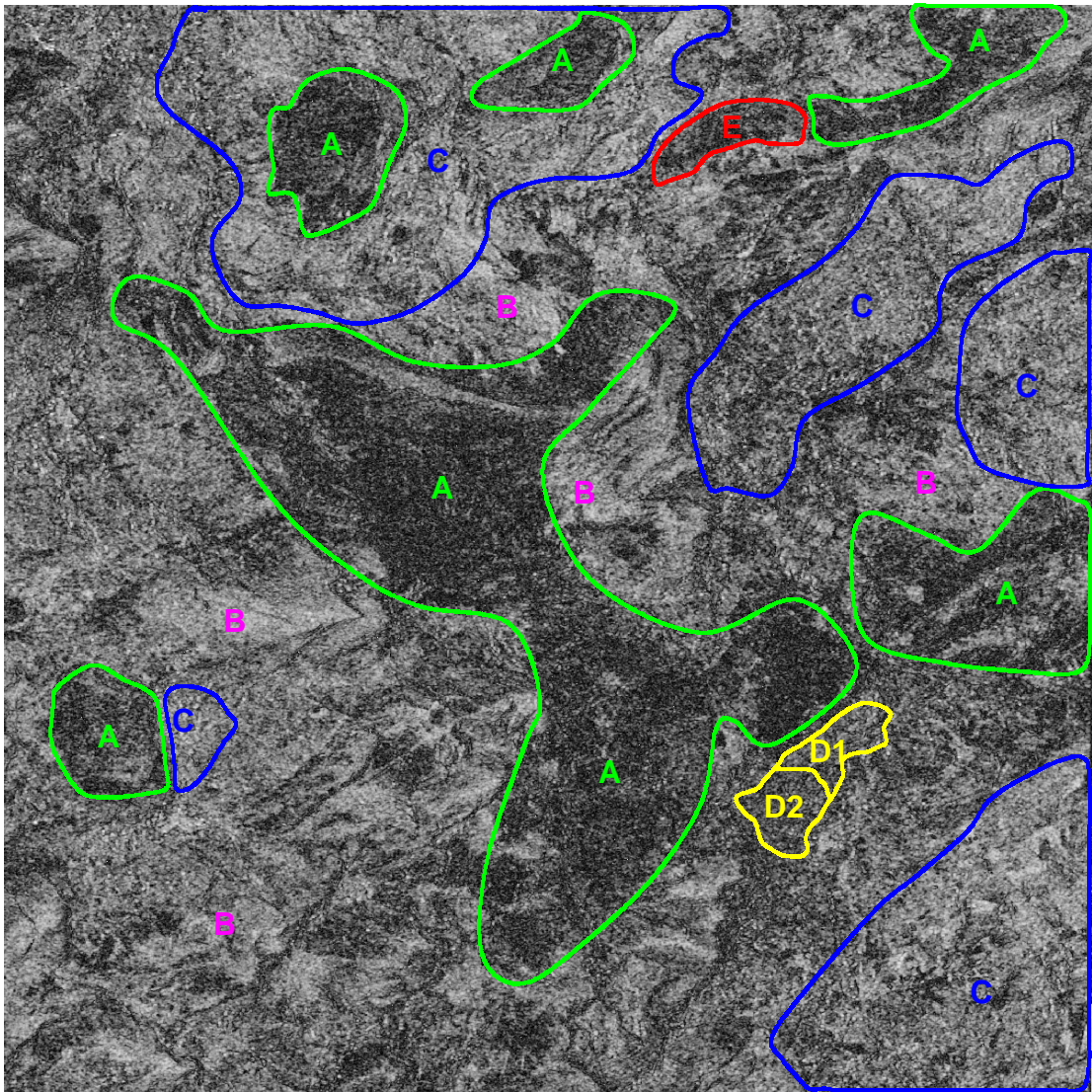


Figure 6.20 Schematic interpretation map of identified decoherence features of GRA12_COH (28 km × 28 km). A (green): Low coherence from wind in vegetated area. B (pink): High coherence area with hard lithology. C (blue): High coherence with soft lithology. D1 (yellow): Soil moisture change in barren area. D2 (yellow): Soil moisture change in vegetated area. E (red): Erosion in barren, soft lithology.

6.5 Summary

This chapter presents three case studies of applications of ERS InSAR coherence imagery for erosion and land-use change detection in Almeria and Granada, southeast of Spain.

In the Case I study, evidence of rapid erosion was found on steep slopes of marls along a motorway cut. A new technique, the ratio coherence imagery presented in Chapter 5, was applied to separate the spatial decorrelation from decoherence features caused by rapid erosion that is characterised as areas losing coherence gradually over several months. Field observation provided direct evidences of active erosion such as gullies on the man-made smooth slopes along the motorway.

In the Case II study, large patches of de-coherence features in the coherence image from an SAR image pair taken in December 1996 and May 1997 were found to coincide with a massive plantation of olive and almond trees, discovered during a field investigation. Young trees with little canopy leave the large proportion of thin soil above mica-schist and phyllite unprotected and vulnerable to erosion though the de-coherence effects may not necessarily be the result of erosion but the irrigation and ploughing in spring.

In the Case III study, coherence image of a tandem pair that brackets a rainfall event (GRA12_COH) is compared with that of a tandem pair taken in dry conditions (GRA34_COH). The main decoherence factor of vegetated areas was proved to be the relatively high wind speed of GRA1 (21 kph). Soil moisture change from rainfall events did not occur in the areas of resistant lithology, which coincide with vegetation cover. Areas of moderately resistant lithology without vegetation cover show high coherence in GRA12_COH, indicating that 1 mm of precipitation was enough to raise soil moisture to the level preventing effective penetration in GRA1, so that there was no further decoherence effect for the further increase of soil moisture content when 21 mm precipitation was added in the next day when the GRA2 image was acquired. Only very limited areas show evidence of moisture change causing decoherence. For instance, an area was found to have different radar backscattering coefficient between

GRA1 and GRA2, resulting in low coherence in GRA12_COH due to soil moisture change. Rapid erosion due to one rainfall event in this region is rare. An area of soft lithology without vegetation cover, showing no sign of soil moisture change, was detected to have lost coherence in GRA12_COH. For this specific case, the most convincing explanation so far is rainfall/erosion but field investigation is needed. It should be noted that the interpretation of coherence images above could be changed in the case of localised rainfall events. More localised weather conditions and detailed surface environmental information must be used for accurate interpretation of coherence images.

Postulations on slope dependence of degradation of coherence estimation in this high relief region lead to the development of a new method for topographic phase-free coherence estimation in Chapter 7.

Chapter 7: Topographic Phase-free Coherence Estimation for SAR Interferometry

7.1 Introduction

The development of techniques for coherence estimation has been focused on isolating only the effects of temporal surface stability from other decorrelation factors such as thermal noise, baseline, terrain slope, co-registration, and even atmospheric refraction. Apart from these decorrelation factors, scene homogeneity also affects the coherence estimation which is defined as an ensemble average, i.e., the average over multiple observations of a physical random process at a specific time or spatial coordinates. Coherence of InSAR data is conventionally estimated by calculating the cross-correlation of two radar echoes over neighbouring pixels (averaging over time or space, rather than ensemble average), under the assumptions that the scene is stationary and ergodic (Touzi *et al.*, 1999). In a non-homogeneous area where topographic phase is dominant, these assumptions are not generally valid and the coherence estimation will be biased. In this case, the data can be treated as a nonstationary random process that contains the topographic phase as a deterministic value. Only after the topographic phase has been removed, can the process be considered as stationary for unbiased coherence estimation.

Many researchers have proposed methods to compensate topographic phase by simulating it from a DEM or estimating local slope based on interferometric phase fringe frequency (equation 2.12). The latter approach has the advantage of not depending on a DEM from a different data source that may introduce co-registration errors and may not be available in some areas. However, it cannot provide adequate topographic information in the case where temporal decorrelation is significant, which is a common case for a scene with the purpose of random change detection using coherence imagery.

This chapter presents the stochastic view of coherence estimation as a statistical representation of stationary and ergodic random processes. A numerical simulation

shows the degrading effects of topographic phase to the coherence estimation. A new method is then proposed to generate topographic phase-free coherence, so called *differential coherence*, by using multipass differential interferometry (DInSAR). This method can benefit from the recently on-going development of SAR interferometry; for example, the advent of spaceborne single-pass SAR Interferometer i.e. SRTM. This method is a short cut for topographic phase removal compared with the DEM method because there is no need to use DEM taking the risk of co-registration error when image pair preserving SAR coordinates is available.

7.2 Coherence Estimation for a Stationary Scene

Any observed data representing a physical phenomenon can be broadly classified as being either deterministic or nondeterministic. Deterministic data are those that can be described by an explicit mathematical relationship, while nondeterministic data cannot (Bendat and Piersol, 2000). InSAR data contain information of both deterministic and nondeterministic types. Topography and surface displacement are deterministic information that can be extracted from the deterministic part of InSAR data defined explicitly from InSAR geometry in the form of interferograms, as described in Chapter 2. On the contrary, the coherence is a statistical representation of surface disturbance derived from the nondeterministic part of InSAR data. Compared to other InSAR applications, many different aspects arise in coherence estimation due to the fact that the coherence is a statistical expectation value of a nondeterministic, random physical process.

InSAR coherence is a mathematical expectation $E(\cdot)$ of the physical processes $u_1(t)$, $u_2(t)$, and $u_1u_2^*(t)$. It should be noted that two time-separated SAR observations for InSAR configuration $u_1u_2^*(t)$ are considered as one single observation for coherence estimation. Also, the physical dimension of observation, t , can be considered in either the time or space domains. This is true for SAR observations where the slow time (s) or fast time (t) data sampling is the measurement of slant range (R) or azimuth distance (x). The mathematical expectation should be

calculated by averaging multiple observations, i.e., ensemble average. As InSAR data has only one single observation, ensemble averaging is intrinsically not applicable for InSAR data. Instead of an ensemble average, the coherence is conventionally estimated using a local correlation approach by averaging over the data itself (time or space domain) in a limited neighbourhood from a single observation. Two important assumptions make this operation valid: stationarity and ergodicity.

In this section, coherence estimation is discussed from the viewpoint of random data measurement. The definition of the stationary and ergodic random process is introduced in section 7.2.1, and applied to InSAR coherence estimation in 7.2.2.

7.2.1 Stationary and Ergodic Random Processes

A single time history representing a random phenomenon is called a *sample function* (or a *sample record* when observed over a finite time interval). The collection of all possible sample functions that the random phenomenon might have produced is called a *random process* or a *stochastic process* (Bendat and Piersol 2000).

When a physical phenomenon is considered in terms of a random process, the properties of the phenomenon can be hypothetically described at any instant of time by computing average values over the collection of sample functions that describe the random process. For example, consider the collection of sample functions (also called the *ensemble*) $x_k(t)$, $k = 1, 2, \dots, N$, that forms the random process. For the random process $\{x(t)\}$, where the symbol $\{\}$ is used to denote an ensemble of sample functions, the mean value (first moment), μ , and the autocorrelation function (joint moment), R , of the random process at some t_1 can be computed as

$$\mu_x(t_1) = \lim_{N \rightarrow \infty} \frac{1}{N} \sum_k^N x_k(t_1), \quad (7.1)$$

$$R_{xx}(t_1, t_1 + \tau) = \lim_{N \rightarrow \infty} \sum_{k=1}^N x_k(t_1) x_k(t_1 + \tau). \quad (7.2)$$

where τ is the time displacement.

For the general case where $\mu_x(t_1)$ and $R_{xx}(t_1, t_1 + \tau)$ vary as time t_1 varies, the random process $\{x(t)\}$ is said to be non-stationary. For the special case where $\mu_x(t_1)$ and $R_{xx}(t_1, t_1 + \tau)$ do not vary with time t_1 , the random process $\{x(t)\}$ is said to be *weakly stationary* or stationary in the wide sense. For weakly stationary random processes, the mean value is a constant and the autocorrelation function is dependent only on the time displacement τ , that is,

$$\mu_x(t_1) = \mu_x, \quad (7.3)$$

$$R_{xx}(t_1, t_1 + \tau) = R_{xx}(\tau). \quad (7.4)$$

An infinite collection of higher-order moments and joint moments of the random process $\{x(t)\}$ could also be computed to establish a complete family of probability distribution functions describing the process. For the special case where all possible moments and joint moments are time invariant, the random process $\{x(t)\}$ is said to be *strongly stationary* or stationary in the strict sense. For many practical applications, verification of weak stationarity will justify an assumption of strong stationarity.

The properties of a stationary random process can be determined by computing ensemble averages at specific instants of time. In most cases, however, it is also possible to describe the properties of a stationary random process by computing time averages over a specific sample function in the ensemble. The mean value and the autocorrelation function of the k th sample function are given by

$$\mu_x(k) = \lim_{T \rightarrow \infty} \frac{1}{T} \int_0^T x_k(t) dt, \quad (7.5)$$

$$R_{xx}(\tau, k) = \lim_{T \rightarrow \infty} \frac{1}{T} \int_0^T x_k(t) x_k(t + \tau) dt. \quad (7.6)$$

If the random process $\{x(t)\}$ is stationary, and $\mu_x(k)$ and $R_{xx}(\tau, k)$ defined in equations 7.5 and 7.6 do not differ when computed over different sample functions, the random process is said to be *ergodic*. For ergodic random processes, the time-

averaged mean value and autocorrelation function are equal to the corresponding ensemble averaged values. That is,

$$\mu_k(k) = \mu_x, \quad (7.7)$$

$$R_{xx}(\tau, k) = R_{xx}(\tau). \quad (7.8)$$

Note that only stationary random processes can be ergodic. Ergodic random processes are an important class of random processes since all properties of ergodic random processes can be determined by performing either time averages over a single sample function or sample function averages at an instant time. Fortunately, in practice, random data representing stationary physical phenomena are generally ergodic. It is for this reason that the properties of stationary random phenomena can be measured properly, in most cases, from a single observed time history record.

Now, consider two arbitrary random processes $\{x(t)\}$ and $\{y(t)\}$. The ensemble means at an arbitrary fixed value of t , where $x_k(t)$ and $y_k(t)$ are random variables over the index k , are defined as below:

$$\mu_x(t) = E[x_k(t)], \quad (7.9)$$

$$\mu_y(t) = E[y_k(t)], \quad (7.10)$$

where $E[\]$ represents the expected value, averaged over each sample function of the ensemble. The *covariance functions* at arbitrary fixed values of $t_1 = t$ and $t_2 = t + \tau$ are defined by

$$C_{xx}(t, t + \tau) = E[(x_k(t) - \mu_x(t))(x_k(t + \tau) - \mu_x(t + \tau))], \quad (7.11)$$

$$C_{yy}(t, t + \tau) = E[(y_k(t) - \mu_y(t))(y_k(t + \tau) - \mu_y(t + \tau))], \quad (7.12)$$

$$C_{xy}(t, t + \tau) = E[(x_k(t) - \mu_x(t))(y_k(t + \tau) - \mu_y(t + \tau))]. \quad (7.13)$$

In a special case when $\tau = 0$,

$$C_{xx}(t, t) = E[(x_k(t) - \mu_x(t))^2] = \sigma_x^2(t), \quad (7.14)$$

$$C_{yy}(t, t) = E[(y_k(t) - \mu_y(t))^2] = \sigma_y^2(t), \quad (7.15)$$

$$C_{xy}(t, t) = E[(x_k(t) - \mu_x(t))(y_k(t) - \mu_y(t))] = C_{xy}(t), \quad (7.16)$$

Thus the covariance functions $C_{xx}(t, t)$ and $C_{yy}(t, t)$ represent the ordinary variances of $\{x(t)\}$ and $\{y(t)\}$ at a fixed value of t , whereas $C_{xy}(t, t)$ represents the covariance between $\{x(t)\}$ and $\{y(t)\}$.

If the mean values $\mu_x(t)$ and $\mu_y(t)$, together with the covariance functions $C_{xx}(t, t + \tau)$, $C_{yy}(t, t + \tau)$, and $C_{xy}(t, t + \tau)$, yield the same results for all fixed values of t , then the random processes $\{x(t)\}$ and $\{y(t)\}$ are said to be *weakly stationary*. If all possible probability distributions involving $\{x(t)\}$ and $\{y(t)\}$ are independent of time translations, then the random processes are said to be *strongly stationary*. If the mean values and the covariance functions calculated from time averages are independent of sample functions, then the random processes are said to be *ergodic*.

7.2.2 Stationary and Ergodic Coherence Estimation

For an InSAR configuration, two SAR observations $x(t)$ ($=u_1(t)$) and $y(t)$ ($=u_2(t)$) can be considered as arbitrary sample functions of random processes $\{x(t)\}$ and $\{y(t)\}$, respectively. From the definitions in equations 7.14-7.16, the complex coherence can be defined as the complex correlation coefficient function (normalised cross-correlation function) of two random processes $\{x(t)\}$ and $\{y(t)\}$ of zero-time (equivalently zero-position) shift ($\tau = 0$) as,

$$\gamma_{xy}(t) = \frac{C_{xy}(t)}{\sigma_x(t)\sigma_y(t)}. \quad (7.17)$$

As only one single sample function exists for each random process, ensemble averaging over sample functions is not applicable. Here lies the importance of ergodic

random process because all properties of ergodic random processes can be determined by performing time averages over a single sample function.

Coherence defined as an ensemble average in equation 2.1 can be estimated by time (or space) averages over a single sample function. Time (or space) averaging in InSAR scene corresponds to the averaging of L independent neighbouring pixels as

$$\hat{\gamma} = \frac{\sum_{l=1}^L u_1(l)u_2^*(l)}{\sqrt{\sum_{l=1}^L u_1(l)u_1^*(l)} \sqrt{\sum_{l=1}^L u_2(l)u_2^*(l)}}. \quad (7.18)$$

The estimated phase and coherence are,

$$\hat{\phi} = \arg\{\hat{\gamma}\} = \arg\left\{\sum_{l=1}^L u_1(l)u_2^*(l)\right\} \quad (7.19)$$

$$\hat{\rho} = |\hat{\gamma}|. \quad (7.20)$$

As discussed so far, this estimation is only valid under the assumption that the processes $u_1(t)$ and $u_2(t)$ are stationary and ergodic random processes. Ergodic random processes are an important class of random processes since all properties of ergodic random processes can be determined by performing time (or space) averages over a single data acquisition. Thus the mean value and autocorrelation of a process do not differ when computed over different data acquisitions. Note that only stationary random process can be ergodic. These conditions are generally met in homogeneous scenes. In the case of an inhomogeneous scene, the stationary condition is broken and the coherence estimation in equation 7.18 will be biased.

The *pdf* of the multi-look phase estimation is (Joughin *et al.*, 1994; Lee *et al.*, 1994; Touzi and Lopes, 1996)

$$pdf(\hat{\phi}) = \frac{\Gamma(L+1/2)(1-\rho^2)^L \rho \cos(\hat{\phi} - \phi_0)}{2\sqrt{\pi}\Gamma(L)(1-\rho^2 \cos^2(\hat{\phi} - \phi_0))^{L+1/2}} + \frac{(1-\rho^2)^L}{2\pi} {}_2F_1(L, 1; \frac{1}{2}; \rho^2 \cos^2(\hat{\phi} - \phi_0)), \quad (7.21)$$

where ${}_2F_1$ is the hypergeometric function and L the look number.

The *pdf* of coherence estimation is (Touzi and Lopes, 1996; Touzi *et al.*, 1999)

$$pdf(\hat{\rho}) = 2(L-1)(1-\rho^2)^L \hat{\rho}(1-\hat{\rho}^2)^{L-2} {}_2F_1(L, L; 1; \rho^2 \hat{\rho}^2), \quad (7.22)$$

and the moments of order k is

$$E(\hat{\rho}^k) = \frac{\Gamma(L)\Gamma(1+k/2)}{\Gamma(L+k/2)} {}_3F_2(1+k/2, L, L; L+k/2; 1; \rho^2)(1-\rho^2)^L. \quad (7.23)$$

As shown in Figure 7.1 for the case of $k=1$, i.e., $E(\hat{\rho})$, the coherence estimation is biased. It tends to overestimate the low coherence part. For large value of L , it becomes asymptotically unbiased. Therefore, choosing a large value of L is preferred for unbiased coherence estimation in homogeneous scene for stationary and ergodic data. However, in practice, the large averaging window size underestimates the true coherence due to the nonstationary of the real SAR data. Therefore the nonstationarity should be removed before coherence estimation, and the proper window size should be taken to ensure *local stationarity* within the averaging window.

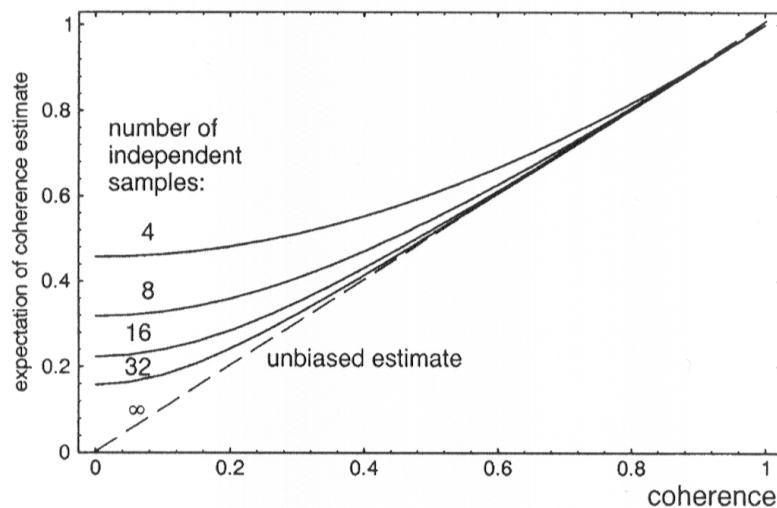


Figure 7.1 Coherence bias for various number of L (Touzi *et al.*, 1999).

7.3 Coherence Estimation for a Nonstationary Scene

For the study of coherence imagery as a tool for surface random change detection and monitoring, it is obvious that coherence should be the representation of surface temporal changes only. If two observations are made in the same sensor position (zero baseline) at different times, stationary coherence estimation in (7.18) can be used as a surface physical parameter relating to the surface temporal stability, ignoring the minor bias caused by the effect of atmospheric phase. However, this is not a usual case. Time-separated observations are often acquired at slightly different sensor positions (non-zero baseline), which lead to decorrelation of the interferometric signals and bias in the coherence estimation as the result of scene nonstationarity relating to radar geometry and topography. For the purpose of the coherence imagery as a tool to detect and monitor surface random changes, these deterministic factors should be eliminated.

This section starts with discussion on the nonstationary random process followed by the removal of the deterministic phase from an interferogram to make the scene stationary for unbiased coherence estimation.

7.3.1 Nonstationary Random Process and the Product Model

Nonstationary random processes include all random processes that do not meet the requirements for stationarity. Unless further restrictions are imposed, the properties of a nonstationary random process are generally time-varying functions that can be determined only by performing instantaneous averages over the ensemble of sample functions forming the process. Under certain conditions, the nonstationary random process $\{x(t)\}$ of particular physical phenomena can be simplified as a product of a stationary random process $\{u(t)\}$ and a deterministic multiplication factor $a(t)$ as given by (Bendat and Piersol, 2000)

$$x(t) = a(t)u(t). \quad (7.24)$$

In other words, the data might be represented by a nonstationary random process consisting of sample functions with a common deterministic time (or spatial) trend. If nonstationary random data fit a specific model of this type (*product model*), ensemble averaging is not always necessary to describe the data. The statistical properties can be estimated from a single sample record as in the case for ergodic stationary data.

7.3.2 Coherence Estimation by Removing the Deterministic Phase

The interferometric phase with a non-zero baseline contains contributions from InSAR geometry, target topography, and possibly the surface displacement field. As all of these nonstationary factors are deterministic values of an InSAR system, the process fits the product model. If these sources of nonstationarity are all removed, the properties of the random process can be considered to satisfy the assumption of stationarity and ergodicity for unbiased coherence estimation.

Therefore, equation 7.18 should be modified to compensate the phase fringes from InSAR system geometry (ϕ_0), topography (ϕ_{topo}), block surface displacement (ϕ_d), and even atmosphere-induced phase (ϕ_a) as (Touzi *et al.*, 1999),

$$\hat{\gamma} = \frac{\sum_{n=1}^L u_1(n)u_2^*(n)e^{-j\phi}}{\sqrt{\sum_{n=1}^L u_1(n)u_1^*(n)}\sqrt{\sum_{n=1}^L u_2(n)u_2^*(n)}}, \quad (7.25)$$

where

$$\phi = \phi_0 + \phi_{topo} + \phi_d + \phi_a. \quad (7.26)$$

The system geometric phase is routinely removed by the Earth-flattening procedure during InSAR coherence image generation as described in Chapter 3. Here, the discussion is focused on removal of the other deterministic phase fringes remained in the Earth-flattened interferogram.

Topographic Phase Removal (ϕ_{topo})

The topographic phase is the source of information and development of InSAR technology for topographic mapping. However, for the sake of coherence estimation, it is a source of nonstationarity that should be removed. One method to remove the topographic phase from the interferogram is the case when the topographic elevation z is known as *a priori* (Massonnet *et al.*, 1995). Digital elevation models (DEM) can be used to compensate topographic phase. From Figure 2.2, the topographic phase is

$$\phi_{topo} = \frac{4\pi}{\lambda} \left[\sqrt{R^2 + B^2 + 2RB \sin(\theta_i - \beta)} - \sqrt{R^2 + B^2 + 2RB \sin(\theta_i^0 - \beta)} \right], \quad (7.27)$$

where

$$\theta_i = \cos^{-1} \left(\frac{R^2 + (r_e + H)^2 - (r_e + z)^2}{2R(r_e + H)} \right). \quad (7.28)$$

Therefore, if the elevation z is available from a DEM, the topographic phase can be calculated and removed from the interferogram.

The other method is to use the surface slope as *a priori*. The *topographic phase fringe number* in range is given from equations 2.11 and 3.41 as

$$k_{\phi_{topo}} = k_{\phi} - k_{\phi_0} = \frac{2B_{\perp} \sin \alpha}{\sin \theta_i^0 \sin(\theta_i^0 - \alpha)}. \quad (7.29)$$

If the local slope α can be estimated from a topographic map or DEM, the topographic phase can be estimated and compensated. These methods using DEM or slope information are restricted by the limited availability of such information and the difficulty of accurate co-registration with SAR data.

Additionally, topographic phase fringes can be detected and removed directly from the interferogram itself (Hagberg *et al.*, 1995). This method is effective only for highly coherent surfaces, as the data in a low coherent area cannot produce clear and continuous topographic fringes. Since the main interests of coherence imagery application are related to the features of low coherence or the variation from high

coherence to low coherence, a method that is only usable at the condition of high coherence does not help much for practical applications of coherence imagery.

Acknowledging the limitations of existing methods, an efficient approach to generate topographic phase-free coherence estimation has been developed using multi-pass DInSAR techniques, which will be fully discussed in section 7.4.

Coherent Surface Displacement Phase Removal (ϕ_d)

Surface coherent movement such as the displacement from earthquake, volcano, and land subsidence also generates interferometric phase. This phase is highly sensitive to the surface displacement compared with the topographic phase, as shown in section 2.2.4. For unbiased coherence estimation, the surface displacement phase is again a factor causing nonstationarity that deteriorates the coherence estimation. Therefore, the surface displacement phase should be removed. The removal of the phase from surface displacement needs an accurate displacement field map obtained from an independent source. However, the data collection is often too sparse (e.g. GPS) to be useable for the InSAR purpose. One practical way is to estimate the phase fringes directly from the differential interferogram showing the displacement. This has the same problem as the topographic removal discussed previously because the phase fringes are hardly detectable in low coherence areas. There is so far no effective solution for this problem, which remains as a topic for further research.

Atmospheric Phase Removal (ϕ_a)

The underlying hypothesis in the InSAR techniques is that wave propagation through the atmosphere/ionosphere of the earth follows a straight line. However, it is reported that the atmosphere and ionosphere have a non-negligible influence on the quality of the interferogram (Tarayre and Massonnet, 1994). The refraction of the rays in the atmosphere can cause pixel misregistration and phase artefacts. In the

worst case, the misregistration can be as large as about 15m and the phase artefacts about 6 fringes for a full scene area of the ERS SAR scene.

For the purpose of coherence estimation, only a few phase fringes over the entire scene can hardly affect the quality of coherence estimation, and are generally negligible. However, misregistration caused by atmospheric refraction can result in the decrease of image correlation as discussed in section 2.4.2. This error could be reduced to some extent by simulating the phase from atmospheric physical data. However, the attempt is hindered because the atmospheric data available usually have much less density of spatial sampling than the satellite radar itself. This is one of the ongoing research fields of InSAR technology and applications.

7.4 Topographic Phase-free, Unbiased Coherence Estimation

7.4.1 Simulation of Coherence Degradation from Topographic Phase Fringes

Coherence of complex radar signals $u_1 = |u_1|e^{i\phi_1}$ and $u_2 = |u_2|e^{i\phi_2}$ can be estimated by

$$\rho = \frac{\left| \sum_{l=1}^L |u_1(l)| |u_2(l)| e^{j\phi_{12}} \right|}{\sqrt{\sum_{l=1}^L |u_1(l)|^2} \sqrt{\sum_{l=1}^L |u_2(l)|^2}}, \quad (7.30)$$

where $\phi_{12} = \phi_1 - \phi_2$ and L is the number of averaging pixels. After spectral filtering to compensate for baseline decorrelation, the phase factor ϕ_{12} is usually Earth-flattened as discussed in Chapter 3.

A numerical simulation is presented in this section to demonstrate the effect of topographic phase fringes on the degradation of coherence. Consider an averaging

window of $L = M \times N$ pixels in range and azimuth direction, respectively, for coherence estimation. A linear topographic phase at a pixel (m, n) can be modelled as

$$\phi(m, n) = 2\pi(k_m^{sim} m + k_n^{sim} n) \quad (7.31)$$

where k_m^{sim} and k_n^{sim} are the simulated *topographic phase fringe number* per pixel in m and n direction, respectively. Assuming $|u_1| = |u_2| = 1$ for simplicity, coherence at a pixel (p, q) can be estimated as

$$\begin{aligned} \rho(p, q) &= \left| \frac{1}{MN} \sum_{m=0}^{M-1} \sum_{n=0}^{N-1} \exp[2\pi j k_m^{sim} m] \exp[2\pi j k_n^{sim} n] \right| \\ &= \left| \frac{\text{sinc}(\pi k_m^{sim} M)}{\text{sinc}(\pi k_m^{sim})} \cdot \frac{\text{sinc}(\pi k_n^{sim} N)}{\text{sinc}(\pi k_n^{sim})} \right|. \end{aligned} \quad (7.32)$$

Note that the coherence is independent of the pixel position (p, q) for this linear topographic phase fringe. For simplicity, let $k_m^{sim} = k_n^{sim} = k^{sim}$, a diagonal phase, and $M = N$, a square averaging window, then

$$\rho = \frac{\text{sinc}^2(\pi k^{sim} N)}{\text{sinc}^2(\pi k^{sim})}. \quad (7.33)$$

Figure 7.2 shows a numerical evaluation of ρ as a function of k^{sim} with various N values. Coherence decreases as k^{sim} increases and becomes zero at

$$k_c^{sim} = 1/N, \quad (7.34)$$

the *critical topographic fringe number* of simulation. The condition of having more than 10% degradation of coherence from topographic phase can be found numerically as

$$k^{sim} > \frac{1}{5.5N}. \quad (7.35)$$

This condition is depicted in Figure 7.3.

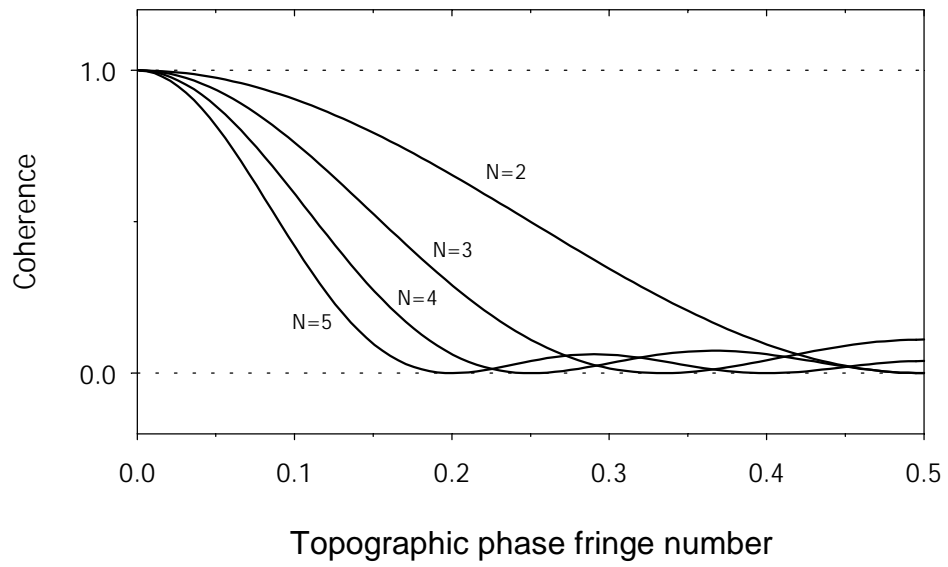


Figure 7.2 Coherence ρ as a function of the simulated topographic phase fringe number k^{sim} when window size $N=2,3,4$, and 5.

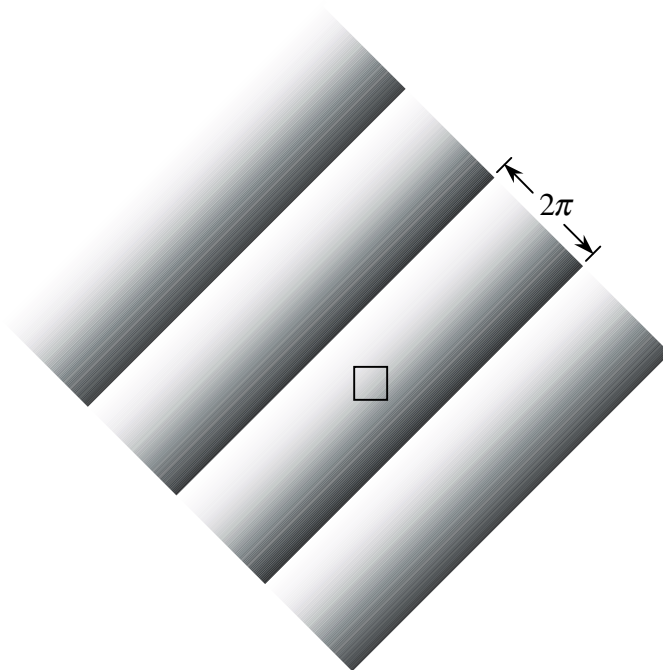


Figure 7.3 Fringes of the diagonal topographic phase and an averaging window (square box) that result in 10 % degradation in coherence estimation when $k^{sim} = \frac{1}{5.5N}$.

For an InSAR system, *topographic phase fringe number* per pixel k^{sys} in range direction for Earth-flattened phase ϕ_{flat} can be derived similarly to equation 7.29 as

$$k^{sys} = \frac{\delta R}{2\pi} \frac{d\phi_{flat}}{dR} = \frac{2\delta R B_{\perp} \sin \alpha}{\lambda R \sin \theta_i^0 \sin(\theta_i^0 - \alpha)}, \quad (7.36)$$

where δR is the slant range pixel size (not necessarily equivalent to slant range resolution). As shown in Figure 7.4, there is no topographic fringe for a flat surface ($k^{sys} = 0$ when $\alpha = 0$) while $k^{sys} = \infty$ on a directly radar facing slope ($\alpha = \theta_i^0$). In practice, k^{sys} is limited to k_c^{sys} , *critical topographic phase fringe number* of InSAR system, by the critical terrain slope α_c (Lee and Liu, 1999; Chapter 5) as

$$k_c^{sys} = \frac{2\delta R B_{\perp}}{c} \left(\pm 1 - \frac{B_{\perp}}{B_{\perp,c}} \right), \quad (7.37)$$

where,

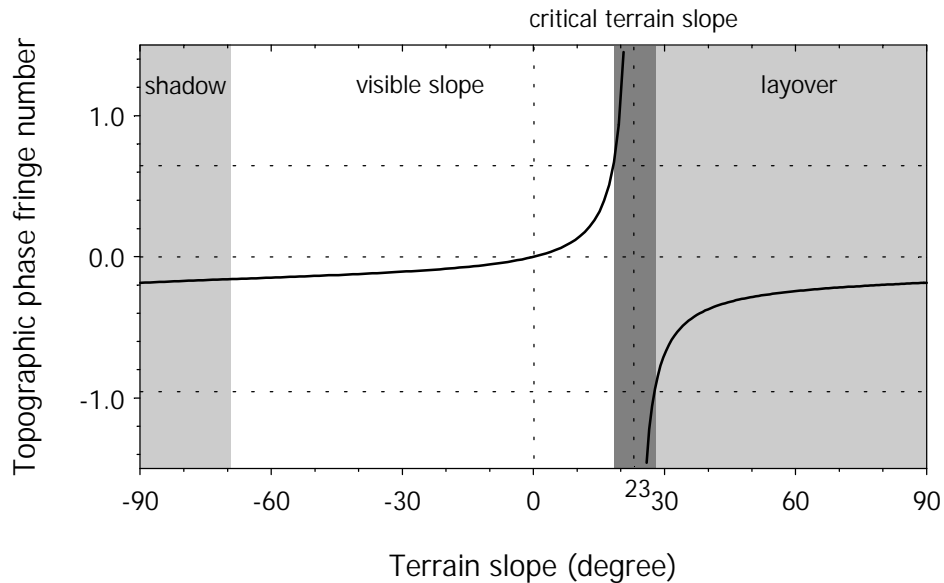


Figure 7.4 *Topographic phase fringe number* k^{sys} of an InSAR system as a function of terrain slope α in the Earth-flattened interferogram, where $\theta_i^0 = 23^\circ$ and $B_{\perp} = 200m$ of ERS system (see Bamler and Hartl, 1998, Fig. 25 for comparison).

$$B_{\perp,c}^{\circ} = \lambda R B_v \tan \theta_i^0 / c, \quad (7.38)$$

the *critical baseline* for flat surface. The sign +1 is for non-layover angles of incidence and –1 for layover cases.

From equations 7.34 and 7.37, topographic phase fringe number of an InSAR system k^{sys} in the range of

$$k_c^{sim} < k^{sys} < k_c^{sys} \quad (7.39)$$

will deteriorate coherence estimation completely (excluding layover where –1 applies in equation 7.37).

For an ERS InSAR pair of $B_{\perp} = 200m$ and $N = 4$ (i.e., 4×4 averaging window), for example, topographic phase fringe number of $k^{sys} > 0.045$ (i.e., *topographic phase fringe length* smaller than 22 pixels per one phase fringe (2π)) will degrade sample coherence by more than 10%, according to equation 7.35. The topographic phase fringe number in the range of $0.25 < k^{sys} < 0.66$ will cause complete deterioration of coherence estimation unless removed, according to equation 7.39.

Substituting k^{sys} in equation 7.36 for k^{sim} in equation 7.32 gives the coherence as a function of terrain slope as

$$\rho(\alpha) = \frac{\text{sinc}^2\left(\frac{2\pi\delta R B_{\perp} \sin \alpha}{\lambda R \sin \theta_i^0 \sin(\theta_i^0 - \alpha)} N\right)}{\text{sinc}^2\left(\frac{2\pi\delta R B_{\perp} \sin \alpha}{\lambda R \sin \theta_i^0 \sin(\theta_i^0 - \alpha)}\right)}. \quad (7.40)$$

Figure 7.5 shows the coherence of an InSAR system as a function of terrain slope α in the Earth-flattened interferogram where $N = 4$ and $B_{\perp} = 200m$ of ERS system (thick curve). For a flat surface ($\alpha = 0^{\circ}$), there is no degradation of coherence due to topographic phase. As the slope approaches towards the critical terrain slope, the sample coherence drops down to zero very rapidly. As the slope approaches the shadow area, the coherence also decreases but relatively slowly. Obviously, the topographic phase fringes should be removed to obtain the unbiased coherence estimation. The thin curve shows the spatial decorrelation function of terrain slope for

a comparison, which has been discussed in Chapter 5 (Lee and Liu, 2000). The spatial (topographic and baseline) decorrelation and the coherence bias due to the terrain slope are in principle different from each other. Even after the range spectral filtering to compensate for the spatial decorrelation (Chapter 3), the topographic phase fringes still remain and the problem of nonstationarity in coherence estimation exists.

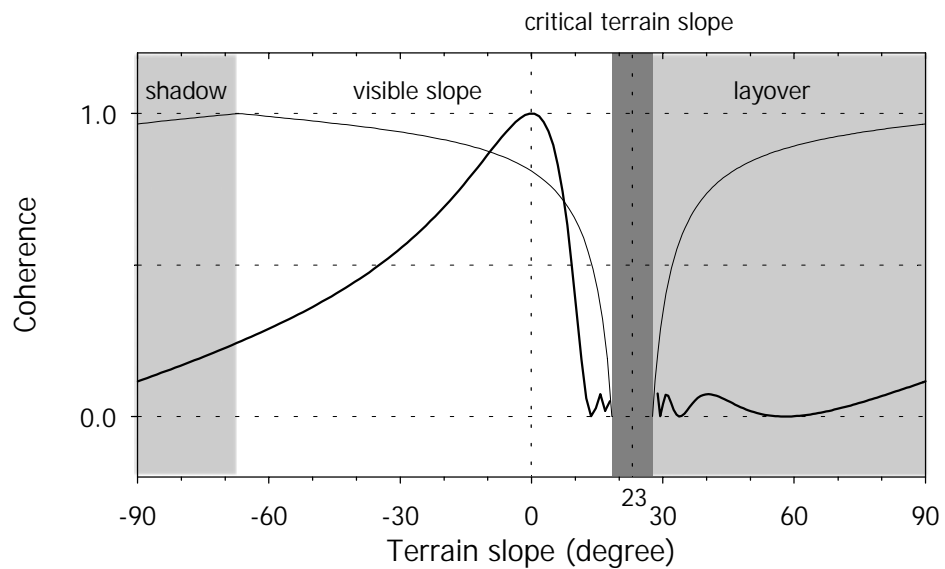


Figure 7.5 Coherence of an InSAR system as a function of terrain slope α in the Earth-flattened interferogram where $N=4$ and $B_{\perp} = 200m$ of ERS system (thick curve). Thin curve is the spatial decorrelation function of terrain slope (Lee and Liu 2000, or Chapter 5).

7.4.2 Differential Coherence

To remove topographic phase in calculating sample coherence, a method using multi-pass differential SAR interferometry is proposed. Consider three SAR acquisitions 1, 2 and 3 in time sequence. Let 1 and 2 be the InSAR pair to analyse surface random change and ground deformation. If the temporal separation between 2 and 3 is short enough to assume that there is no surface change, then the phase is determined only by topography (for example, ERS-1 and ERS-2 tandem pair or a single-pass interferometer, e.g., SRTM). This interferogram is called a reference interferogram. Topographic phase-free differential interferometric phase can be approximately derived from equation 2.16 as (Zebker *et al.*, 1994)

$$\phi_d = \phi_{flat}^{12} - \frac{B_{\perp}^{12}}{B_{\perp}^{23}} \phi_{flat}^{23} = \frac{4\pi}{\lambda} \zeta, \quad (7.41)$$

where ζ is the displacement in the radar look direction caused by either coherent block or decoherent random surface movement between 1 and 2. For the purpose of differential interferometry to detect surface block displacement, the condition that multi-pass radar echoes have to be correlated restricts its application only to relatively stable areas. For InSAR coherence imagery, however, decoherent random change of ζ will result in low coherence that enables us to detect surface instability.

Substituting the phase term in equation 7.41 for equation 7.30 results in the topographic phase-removed coherence estimation, so called, *differential coherence*:

$$\rho_d = \frac{\left| \sum_{l=1}^L |u_1(l)| |u_2(l)| e^{j\phi_d} \right|}{\sqrt{\sum_{l=1}^L |u_1(l)|^2} \sqrt{\sum_{l=1}^L |u_2(l)|^2}}. \quad (7.42)$$

Differential coherence, in conjunction with the differential interferogram, can be considered as an additional product of DInSAR processing, which is a function of coherent surface displacement and/or decoherent random surface change. If the surface is subject to block movement, ϕ_d changes accordingly and ρ_d will be

reduced depending on the scale of deformation (*displacement phase fringe frequency*) as depicted in equation 7.32. If the surface is subject to random change, ϕ_d varies randomly, however, without further degradation by topographic phase. Therefore, differential coherence selectively improves coherence on terrain slopes by removing topographic phase fringes and retains temporal decorrelation effects and it will help the study of surface stability using coherence imagery.

7.4.3 Phase Unwrapping

Phase unwrapping is an important processing step to generate a topographic map or surface displacement field map using InSAR or DInSAR techniques. It is also essential for the development of the new method to refine coherence estimation by removing topographic decorrelation using DInSAR techniques. In calculation of equation 7.41, the phase of the reference interferogram ϕ_{flat}^{23} should be unwrapped before it is scaled by the factor of $\frac{B_{\perp}^{12}}{B_{\perp}^{23}}$. For successful application, a robust phase unwrapping algorithm is essential. A general introduction of phase unwrapping methods is therefore necessary.

SAR interferometry makes use of the phase difference to measure the actual slant range difference between two slightly separated observations of the same target. However, the measured phase $\hat{\phi}$ is within one cycle (2π). The absolute phase can be described as

$$\phi = 2\pi n + \hat{\phi} \quad (7.43)$$

where $0 \leq \hat{\phi} < 2\pi$, which is called as *local phase* obtained from the interferogram, and n is the value that needs to be determined by phase unwrapping process. To find the absolute phase, the 2π -fold measured phase must be unwrapped into continuous phase values beyond 2π .

Various phase unwrapping methods has been developed recently such as a region growing method (Xu and Cumming,1999), multi-grid or multi-resolution method (Pritt, 1996; Davidson and Bamler, 1999), Green's function method (Fornaro *et al.*, 1996), local frequency estimation method (Spagnolini, 1995; Trouve *et al.*, 1998), a finite element method (FEM) based technique (Fornaro *et al.*, 1997), and one using network programming (Costantini, 1998).

The review of all of those methods is out of the scope of this research. However, in principle, all these various phase unwrapping methods belong to either the least squares type (Pritt and Shipman, 1994) or the branch-cut type (Goldstein *et al.*, 1988). The least squares method is a kind of statistical iterative approach that needs an initial model to ensure the convergence of iteration. This method does not produce global error propagation. However, the convergence is highly dependent on the proper choice of the initial model, as is always the case for iterative solutions to inverse problems. Another problem of the least squares method is that it may introduce local deviation into the absolute phase deviation. This means that $\hat{\phi}$ values may be changed after phase unwrapping. This is not an appropriate result especially for the purpose of this chapter for topographic phase-free coherence estimation. On the contrary, the branch-cut method may cause propagation of local error to global error that results in $2\pi n$ discontinuity in unwrapped values ϕ where the branch cuts are not neutral. However, it at least produces accurate values of local estimation $\hat{\phi}$, which is desirable for the purpose of topographic phase-removal for unbiased coherence estimation. Therefore, the branch-cut method is used in this study.

Branch-cut Phase Unwrapping Method

The branch-cut phase unwrapping method consists of three major processing steps: residue detection, define and connect branch-cuts, and integration (Goldstein *et al.*, 1988).

The residue detection process is relatively straightforward. The differences of the interferometric phase are calculated through the four neighbouring pixels following a given direction, making a complete closing path. The direction of integration is

clockwise by convention. Assuming that the phase is smoothly changing and that the phase changes are no greater than π between two adjacent pixels, the phase difference between any two of the neighbouring pixels is adjusted within this limit by adding or subtracting 2π . If the four pixels are analytical, (i.e. the values and their derivatives are piecewisely continuous) then the sum of the phase differences is zero by the law of Cauchy's integration theorem (Kreyszig, 1988). Otherwise, the phase difference integration along a closed path will produce a non-zero value that is a residue. The residual value of this integration of phase difference will be any integer fold of π . The residue is called positive or negative depending on the sign of the integration result. The number of residues of a scene depends on the SNR of the image that affects the spatial continuity of phase pattern in the interferogram. In particular, temporal and spatial coherence and layover effects in high relief topography can cause frequent discontinuity in phase. A region of high residue population is difficult to unwrap properly. The number of residues can be reduced significantly by averaging with neighbouring pixels in the interferogram.

Once residues are defined, the next step is to connect the residues as a branch-cut to make it uncharged. The integration path is not allowed to penetrate the branch-cut. Determining branch-cut is a crucial procedure that affects the result most significantly. The residues are caused by either noisy fluctuation of phase or real discontinuity of layover effect of side looking antenna in high relief mountainous region. Spectral filtering in range and azimuth, as discussed in section 3.2 and 3.3, can reduce the number of residues. On the other hand, residues of real discontinuity should be maintained so that there is real discontinuity in unwrapped phase for such a case.

The algorithm starts by scanning the image to find a residue. Once found, the algorithm searches for another residue nearby. If another residue is found, a branch line is connected between the two residues. If the two residues have opposite signs, then the net charge of the branch line is zero. In this case the branch-cut is closed and the algorithm continues from the beginning for another new residue pixel. If the net residue is not zero, the algorithm searches for another residue until the net charge of the branch-cut is zero. If the length of a branch-cut exceeds a certain limitation or there are no more residues within a given limitation, the algorithm ceases and

declares this branch line “charged”. A charged branch line should be either connected with another charged branch line that has preferably opposite charge, or extended to the nearest image border with a criterion of the shortest branch line.

The next step is integration of phase difference. Once the branch-cuts are well defined so that they have zero net charge, the result of integration of phase difference is consistent everywhere and independent of the integration path (Kreyszig, 1988).

Absolute Phase Determination

At least one ground true value (seed) for each area isolated by branch-cuts is necessary to reconstruct the absolute phase. The branch-cuts can be determined by the criteria of minimising branch-cut length, and maximising the open space that is reachable from the minimum number of seed values. A seed value can be obtained during co-registration of interferometric SAR image pairs or ground control points (GCP) as *a priori* information.

To obtain a seed value from image coregistration within the accuracy of SAR interferometry, the accuracy of the coregistration should be sub-wavelength. During coregistration, the image shift in slant range ΔR is the measurement of the absolute phase as shown in equation 2.4. The accuracy of the co-registration $\sigma_{\Delta R}$ is therefore related to the accuracy of the absolute phase determination σ_{ϕ} as

$$\sigma_{\phi} = \frac{4\pi}{\lambda} \sigma_{\Delta R} \quad (7.44)$$

For example, 2π accuracy in phase determination ($\sigma_{\phi} = 2\pi$), which can resolve $2\pi n$ ambiguity for absolute phase, requires

$$\sigma_{\Delta R} = \frac{\lambda}{2} \quad (7.45)$$

This means, for the case of ERS C-band ($\lambda = 5.6$ cm) SAR where the nominal slant range per pixel is 7.9 m, 1/282 of a pixel size (2.8 cm) accuracy of co-

registration is necessary. However, the current co-registration algorithm ensures only 1/32 of pixel accuracy practically, which corresponds to the phase error, $\sigma_\phi = 2\pi n = 2\pi \times 4.3$. Though the current co-registration algorithm is not accurate enough to determine the absolute phase or an exact seed value, it may constrain the global propagation of the phase error in the branch-cut phase unwrapping algorithm within approximately $n = 4.3$ cycles of 2π in this particular case.

7.5 Application Experiment

An example of differential coherence imagery in Granada, Spain using ERS-1 and ERS-2 SAR data (Table 7.1) is presented here. This area mainly consists of relatively stable dolomite with high relief. GRA32 is the interferometric pair of GRA3 and GRA2. The ERS-1/2 tandem pair GRA34 from GRA3 and GRA4 is used as a reference interferogram.

Figure 7.6 shows the production sequence of a differential coherence image and its evaluation. Figure 7.6(a) is the coherence image GRA32_COH generated without compensating topographic phase fringes shown in its interferogram (b) GRA32_INF. As the coherence has been calculated in the presence of many topographic phase fringes, coherence estimation is intrinsically biased and degraded in high relief areas because of the nonstationarity of the scene. The topographic phase fringes in the interferogram (b) need to be removed before calculating the coherence. Though large parts of the area consist of stable dolomite, this interferometric pair contains a noisy phase and low coherence features due to large temporal separation ($\Delta T = 174$ days). Direct detection and removal of topographic phase fringes from this noisy interferogram is not feasible in this case, as discussed in section 7.3.2.

Table 7.1 Three SAR scenes of Granada, Spain used (Track 051, Frame 2853).

| Scene | Mission | Date | Orbit | Weather | B_{\perp} (m) |
|-------|---------|----------|-------|------------|-----------------|
| GRA2 | ERS-2 | 19960503 | 5416 | rain(21mm) | 204 |
| GRA3 | ERS-1 | 19961024 | 27594 | dry | 0 |
| GRA4 | ERS-2 | 19961025 | 7921 | dry | 131 |

The unbiased estimation of coherence can be achieved by removing topographic phase using the multi-temporal DInSAR technique as described in the previous section. A tandem pair of GRA3 and GRA4 was used for a reference interferogram. A short temporal separation ($\Delta T = 1$ day) between GRA3 and GRA4 obtained during ERS-1/2 tandem mission enables high interferogram quality. The reference interferogram is phase unwrapped using the branch-cut method. Figure 7.6(c) is the reference interferogram GRA34_INF (rewrapped for illustration purpose).

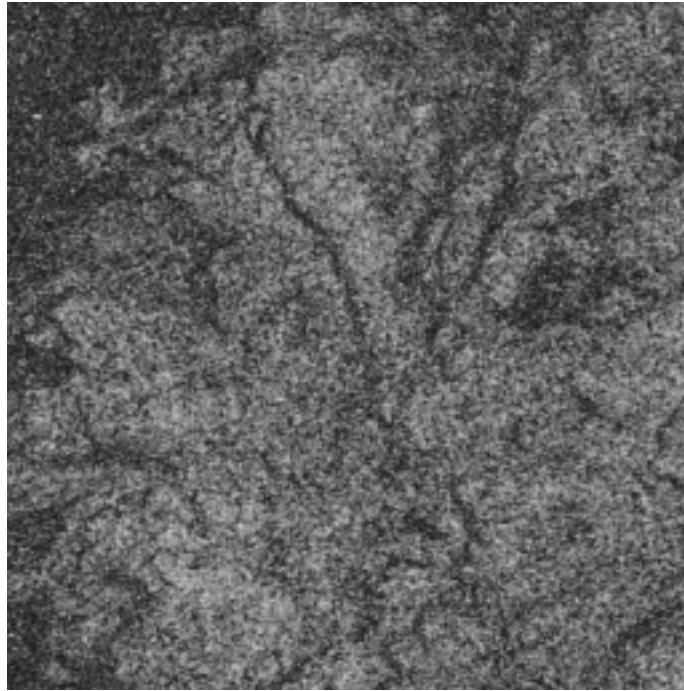
A topographic phase-removed differential interferogram is derived according to equation 7.41 as shown in Figure 7.6(d) GRA32_DINF. Due to errors of the branch-cut method used for phase unwrapping, there are many ill posed branch-cuts in this image that appear as a sudden change of differential phase between two areas dissected by the linear branch-cuts. There also exists approximately one-cycle (2π) remnant phase fringe over the study area ($10 \text{ km} \times 9 \text{ km}$). One-cycle phase fringe in the differential interferogram (d) corresponds to 2.8cm range difference between GRA2 and GRA3, according to equation 7.41. The origin of this remnant phase fringe could be the change of atmospheric conditions or surface displacement. However, one cannot exclude the possibility of the effect from inaccurate baseline information in calculating equation 7.41. This remnant phase is so sparse that it can hardly affect the quality of coherence estimation, according to the discussion in section 7.4.1.

Now, the phase of the differential interferogram in (d) is then used as a phase term in the coherence estimator (equation 7.42) to generate differential coherence GRA32_DCOH in Figure 7.6(e). Figure 7.6(f) is an evaluation image showing the improvement of coherence level from (a) GRA32_COH to (e) GRA32_DCOH, by differencing the two images. It shows that there is up to 16 % coherence improvement selectively on steep terrain slopes (white). These areas correspond to dense

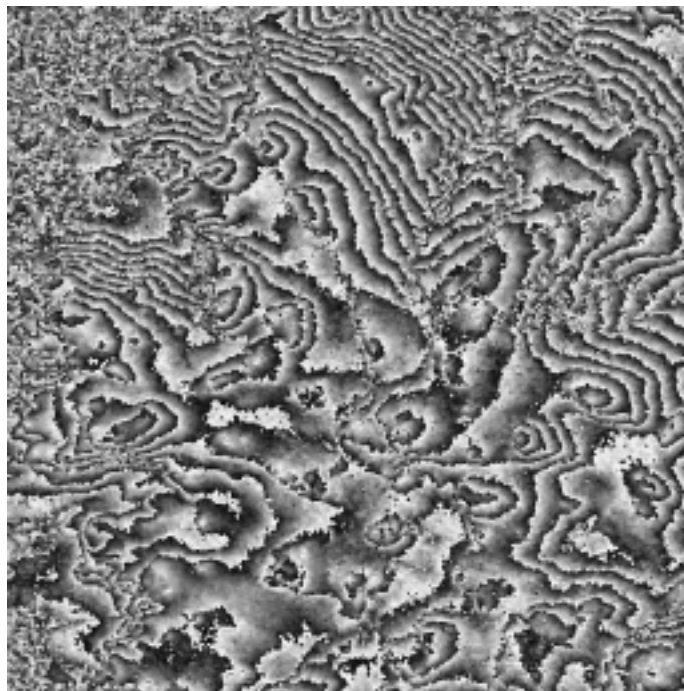
topographic phase fringe areas in the original interferogram GRA32_INF as shown in Figure 7.6(b). The coherence of the flat surfaces with sparse topographic phase fringes remains unchanged (grey).

In some areas, coherence degrades due to the low quality of the reference interferogram and the phase unwrapping errors that appear as black in Figure 7.6(e). The degradation of the differential coherence occurs mainly in the areas having topographic total decorrelation along the foreshortened slope, temporal decorrelation on the reference image, and errors of the phase unwrapping algorithm.

It is interesting to notice that the degradation of coherence from inappropriate branch-cut lines happens only on these very lines. Other areas are not affected by the ill posed branch-cuts. This is because, even though the absolute phase determination from the branch-cut method fails, the locally true phase gives accurate compensation of topographic phase fringes in the area that is not on the branch-cut lines. Though the quality of this differential interferogram is poor because of errors in phase unwrapping and inaccurate baseline information, it is still adequate for the purpose of removing topographic phase for unbiased coherence estimation.



(a) GRA32_COH



(b) GRA32_INF

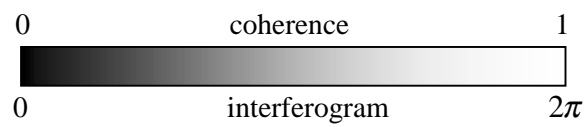
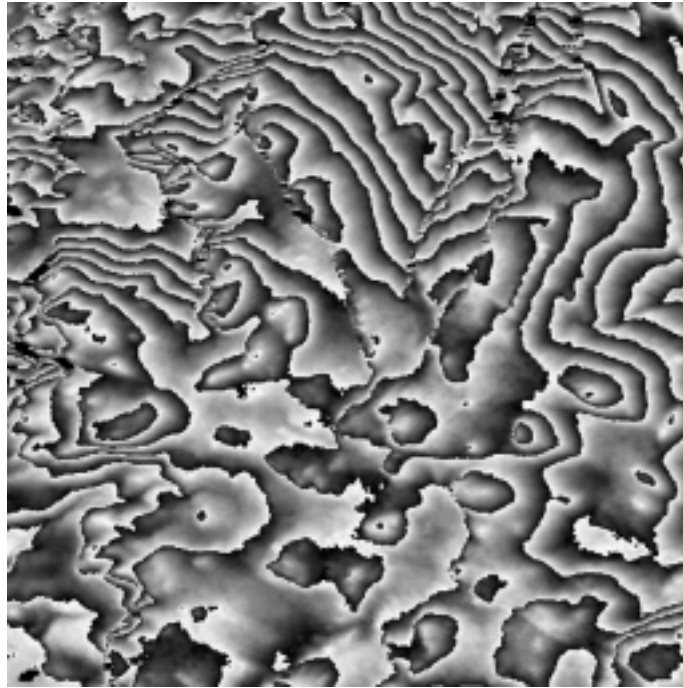
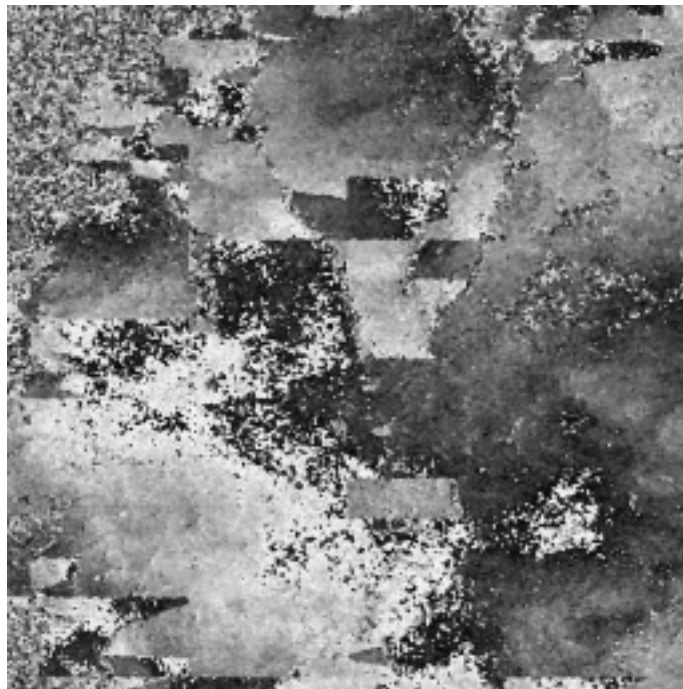


Figure 7.6 Generation of differential coherence image of Granada, Spain ($10 \text{ km} \times 9 \text{ km}$). (a) GRA32_COH: Coherence image between GRA3 and GRA2, (b) GRA32_INF: Interferogram of GRA3 and GRA2.



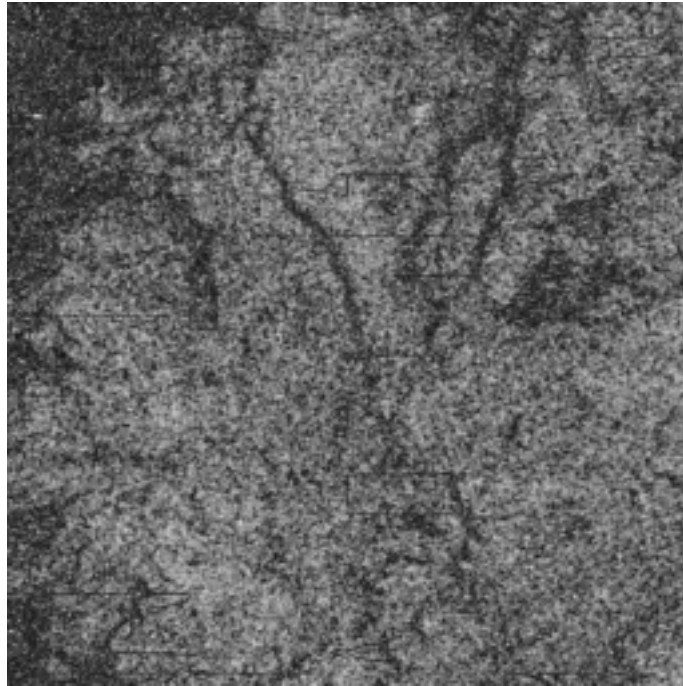
(c) GRA34_INF: Reference interferogram



(d) GRA32_DINF



Figure 7.6(continued) (c) GRA34_INF: Reference Interferogram generated from GRA3 and GRA4. (rewrapped after phase unwrapping for illustration purpose) (d) GRA32_DINF: Topographic phase-removed differential interferogram to be used as a phase term in coherence estimator to generate differential coherence.



(e) GRA32_DCOH: Differential Coherence



(f) Evaluation: (e)-(a)



Figure 7.6(continued) (e) GRA32_DCOH: differential coherence image (the final product). (f) Evaluation: a difference image between (e) and (a). It shows up to 16 % rms coherence improvement on steep terrain slopes (white), degradation in some areas due to low quality in the reference interferogram and phase unwrapping error (black), while other areas remain the same (grey).

7.6 Summary

Coherence is a representation of a physical random process. Ensemble averaging can be substituted by averaging over neighbouring SAR image pixels within an averaging window where the scene can be regarded as homogeneous so that the data are stationary or locally stationary and ergodic.

Topographic phase fringes are the main source of nonstationarity in coherence estimation that should be removed for unbiased coherence estimation. Numerical simulation shows that topographic phase fringe degrades coherence level significantly especially when the surface slope is steep and facing the radar illumination.

Using multi-pass differential SAR interferometry, a novel method to calculate topographic phase-removed sample coherence, so called, *differential coherence* in conjunction with a differential interferogram, has been proposed and applied to Granada, Spain using ERS-1 and ERS-2 SAR data. A differential coherence image shows improved coherence (up to 16%) and image contrast on steep terrain slopes.

A reference interferogram of high quality and a robust phase unwrapping algorithm are essential for this method as is also the case for other InSAR techniques. For coherence estimation, the locally true phase should be retained but the absolute phase is not essential. Therefore, the branch-cut method for phase unwrapping is preferred to the least square method. Ill-posed branch-cuts may not be avoidable, but it results in degradation of coherence only on branch-cut lines leaving adjacent areas not affected.

Only one successful application example was available during this research period due to limited dataset suitable for DInSAR technique. More experiments on generating differential coherence using DInSAR technique should be followed to verify whether this technique is applicable to different areas, datasets, and systems. This remains as a future work.

Chapter 8. Conclusions and Recommendations

8.1 Conclusions

The primary goal of this research project is to explore and to evaluate the potential of InSAR coherence imagery for the detection of random changes on land surface. After a comprehensive review of theory and data processing algorithms and experiments on change detection applications, several new functions and algorithms have been developed for unbiased coherence estimation and interpretation including:

- spatial topographic decorrelation function,
- ratio coherence imagery, and
- differential coherence.

The potential of InSAR coherence imagery as a powerful tool for land surface random change detection and monitoring has been successfully demonstrated in the following application examples in:

- the Sahara desert, Algeria and
- the southeast of Spain (Almeria and Granada).

The major findings and contributions of the research are as follows.

Application in the Sahara Desert, Algeria – Hyper-arid, Flat, and Stable Region

The results in Chapter 4 show the possibility of InSAR coherence imagery for surface random change detection and monitoring in hyper-arid, flat, and stable areas. A comprehensive interpretation of multi-temporal InSAR coherence images derived

from three ERS-1 SAR images of the Sahara desert, Algeria revealed several interesting surface characteristics such as the decoherence pattern of sand dunes, ephemeral lakes, ephemeral flood streams, and human-induced disturbances, which can not be easily detected by other remote sensing techniques.

The location of sand dunes are positively identified in coherence images due to decoherence features from the micro-scale movement of sand particles and volume scattering effects. Evidence of erosion is found along ephemeral flood courses and streams by comparison between coherence images of short and long temporal separations. Dynamic seasonal changes of ephemeral lakes are detected by observing medium to low coherence over a year together with spectral analysis using a TM image. Geophysical seismic survey lines are clearly detected and mapped using a long temporal separation coherence image. This unique function of coherence imagery implies that it can be used as an effective reconnaissance tool for monitoring environmental impact of human activities.

A controversial case is then revealed in a gully area that cannot be explained from the temporal relationship of coherence images, showing low coherence in short period (35 days) and high coherence in long period (350 days). The finding led to the investigation on topographic decorrelation and the development of a new algorithm, ratio coherence imagery in Chapter 5.

Topographic Decorrelation Function & Ratio Coherence Imagery

The analysis of spatial topographic decorrelation in Chapter 5 refines the methodology of InSAR coherence imagery especially in high relief areas where the interpretation of coherence features is more complex than in a flat surface. A modified spatial decorrelation function (equation 5.12) was derived as a function of the baseline and topography. This function explains the origin of the total topographic decorrelation phenomenon on slopes directly facing radar illumination and layover. Based on this function, the *critical terrain slope* (or *critical incidence angle*) and the *slope range of total topographic decorrelation* are defined as the slope for which two SAR signals completely decorrelate regardless of surface physical conditions. It is

found that the slope range of total topographic decorrelation increases with the increase of the component of the baseline perpendicular to the radar look direction.

A new analytical method, the ratio coherence imagery, was then developed and applied to highlight topographic decorrelation against the temporal decorrelation features. A ratio coherence image between a long temporal separation and short baseline (numerator) and a short temporal separation and long baseline (denominator) will separate spatial decorrelation in bright tones and temporal decorrelation in dark tones leaving stable areas as grey background. The effectiveness of this methodology has been demonstrated successfully in selected locations in the Sahara desert, Algeria.

Application in the Southeast of Spain (Almeria and Granada): Semi-arid, Mountainous and Unstable Region

The results in Chapter 6 extend the application potential of multi-temporal InSAR coherence imagery as a tool for surface change detection and monitoring to environmentally unstable and technically challenging semi-arid and mountainous region in the southeast of Spain. Coherence images derived from ERS-1/2 InSAR pairs with temporal separation from 70 to 526 days of the Almeria region and from two one-day tandem pairs of Granada region were analysed in conjunction with interferograms, topographic maps, TM images and geological maps.

Evidence of rapid erosion were found on the slopes of marls in the Sorbas area, Almeria, where the vegetation cover is sparse. Ratio coherence imagery was used to identify the spatial topographic decorrelation features on critical terrain slopes, making the interpretation of the complicated coherence features in this high relief region reliable.

Large areas of disturbed lands in the Almeria scene were defined by image features with high coherence in 70 but decoherence in 140 days. These features closely correspond to the recent massive plantation of olive and almond trees on gentle slopes of phyllites and schists. Stripping off the natural vegetation and surface crust of the land makes the thin soil vulnerable to erosion.

The comparison between two coherence images of tandem pairs in the Granada scene, one taken across a rainfall event and the other in dry conditions, revealed the rainfall/decoherence features in relation to vegetation cover, wind, surface moisture change, and erosion. It was proved that vegetated areas on resistant lithology lost coherence from relatively strong winds of GRA1. Moisture change of thin soil on hard lithology did not seem to change radar penetration depth because there is no penetration to solid rock. In a relatively soft lithology, soil moisture changed significantly by 1 mm precipitation in GRA1 to prevent radar penetration into the ground completely. Therefore, no further change of radar backscattering occurred when 21 mm precipitation was added in GRA2, resulting in high coherence in GRA12_COH. A region of exception was identified that shows difference in radar intensity between GRA1 and GRA2, resulting in low coherence from soil moisture change. A patch of unvegetated area with soft lithology and steep slope was also found to have lost coherence from rainfall/erosion. Further field investigation and intensive studies are needed to verify the vegetation status, lithology and soil types in the areas of these decoherence features and to reveal the nature of coherence as a result of combined effects of these environmental conditions and processes. Postulations on slope dependence of degradation of coherence estimation in this case study triggered further study and development of a new method for topographic phase-free coherence estimation in Chapter 7.

These case studies show that InSAR coherence images, together with images from optical sensors, topographic map, geological map, meteorological data, and field investigation, enables comprehensive study of environmental surface changes.

Differential Coherence: Topographic Phase-free Coherence Estimation using a DInSAR Technique

Coherence estimation is reconsidered as a statistical representation of random processes in Chapter 7. For unbiased coherence estimation, stationary and ergodic assumptions in InSAR data are necessary to allow “averaging over neighbouring pixels” instead of “ensemble average” for coherence calculation. Topographic phase in the interferogram is the main source of nonstationarity that should be removed for

unbiased coherence estimation. A new method was then developed to remove topographic phase from the interferogram so that the scene is homogeneous and the processes are stationary and ergodic. In this method, multi-pass differential SAR interferometry (DInSAR) is applied to produce topographic phase-corrected coherence estimation, so called differential coherence. The topographic phase can be removed using a high quality reference interferogram scaled by the ratio of baselines after phase unwrapping. It has advantages that the data is kept within the SAR geometry without causing a coregistration problem as in the approach of using DEMs from other sources. On the other hand, compared with a method that directly detects and removes topographic phase fringes in the interferogram, which is only applicable to high coherence areas, differential coherence is a more adequate method for InSAR coherence imagery application where both low and high coherence regions are of concern.

An example using ERS-1 and ERS-2 SAR data of Granada, Spain, shows up to 16% rms improvement of coherence on steep terrain slope compared with the coherence in the presence of topographic phase and the overall contrast of the coherence image is slightly enhanced. The phase unwrapping for differential coherence requires locally true phase values while the absolute phase in global sense is not essential. The branch-cut method for unwrapping is therefore preferred as it preserves local true phase. Differential coherence degrades in the areas where phase unwrapping cannot proceed properly because of low coherence of the reference interferogram.

The concept of differential coherence and the methodology presented here is currently limited by the availability of proper DInSAR datasets as well as robust unwrapping algorithms. However, the arrival of new SAR and SAR interferometer systems will make this new method more practical.

8.2 Recommendations for Future Study

8.2.1 Laboratory Experiments of Coherence Change from Rainfall/Erosion

An intensive laboratory experiment will give more concrete results. For surface erosion study using InSAR coherence imagery as discussed in Chapter 6, for example, a laboratory experiment can be designed to simulate rainfall/erosion process over a slope soil surface under the simplest repeat radar observation condition: zero baseline and in an isolated environment. An experimental study of decoherence induced by moisture changes was performed by Nesti *et al.* (1998) at the European Microwave Signature Laboratory (EMSL). An experimental setting similar to this can be used for the rainfall/erosion study, but now changing the micro-scale geometry of soil, i.e. erosion, by artificial rainfall irrigation steps. The laboratory experiment allows a full control to eliminate certain parameters so as to derive the possible quantitative relationship between radar back-scattering signal coherence level and scale of random disturbance (micro-geometric change of scatterers) caused by erosion. Several scientific issues can be clarified based on laboratory data as below. These issues are essential to make an optimal choice of radar configuration and to develop operational methodology for monitoring erosion processes in various landscapes using coherence imagery.

Coherence vs. Noise

Though it is presumed that the minor moisture change between different observation cycles impose negligible effects to coherence for a wet surface (Nesti *et al.* 1998), the radar observation data may still be affected by other unknown parameters. These effects form a minor random variation in coherence. In order to remove this noise thus refining the coherence data, a method based on a accumulative approach can be applied. Two groups of plots will be produced: one for the coherence between the initial status and each erosion cycle, the other for the coherence between

every two different erosion status (including the initial status). Numerical analysis of these data will enable us to minimise the random noise and produce a refined coherence dataset. With this dataset, coherence can be plotted against the volume of soil loss and the standard deviation of differential micro-DEM for every wavelength, look angle and polarisation. The two groups of plots will be used to verify each other. Depending on the shapes of these plots, linear or higher order statistical fitting will be applied to characterise the relationship as functions. If plots show systematic shapes but cannot be easily characterised to a function, LUTs (Look-Up-Table) can be generated alternatively.

Coherence vs. Incidence Angle

The main purpose for using different incidence angles is to simulate general cases of topography. The land surface is generally regarded as a rough surface (non-Lambertian) to radar radiation. The intensity of the back-scattered return signal is known to be affected by the actual incident angle (topography). However the dependence of the phase and thus the coherence (for zero baseline) on different incidence angle is unknown. From the experience of ERS SAR coherence imagery, coherence will be significantly reduced only on steep slopes. The comparison of coherence/erosion plots of different look angles can reveal the relationship. If look angle does not affect coherence within a considerable angle range, then the erosion monitoring using coherence imagery can be relatively independent of topography in a low relief area. If the plots are similar in shapes but different in values, then offset values can be interpolated for every incident angle as a LUT. If the plots are different in shape, then functions (or LUTs) have to be interpolated for every incident angle. For the last two cases, coherence imagery must be used in combination with topographic information in an operational method.

Coherence vs. Polarisation

Coherence/erosion plots for co- and cross-polarisation (HH, VV, HV, and VH) will reveal differences between the two modes and which mode is more sensitive to erosion. The data are essential as standard references for the evaluation of the coherence data especially for a sparsely vegetated land surface.

Coherence vs. Soil Type

With different soil types, erosion will be developed at different rates under the same rainfall intensity. The less resistant soil should lose coherence more rapidly than the more resistance one. However, considering the coherence as a function of the micro-geometrical change of (or the total soil loss from) the sample surface, which is irrelevant to the time (erosion speed), this function should be independent of soil samples. An experiment using two soil samples will verify this assumption. Coherence can be considered as a measure of erosion only when it is independent of soil/regolith types.

Coherence vs. Radar Wavelength

Current spaceborne and airborne SAR systems use various ranges of microwave bands such as P-, L-, C-, X-, and S-band. In general, a longer wavelength will allow greater tolerance of radar signal decorrelation factors. For the same time interval, coherence images derived from SAR systems of different wavelength can reveal different erosion rates. Possible quantitative coherence/erosion functions for various radar wavelengths are essential for the study of InSAR coherence imagery.

8.2.2 The Arrival of New SAR Systems

InSAR coherence imagery will become more important for the new SAR systems that are designed for environmental change monitoring with intensified spatial and temporal data coverage. Further development of applications and algorithms of InSAR coherence imagery is expected with the arrival of future SAR and InSAR systems aimed at smaller, lighter, cheaper, and more flexible design as well as shorter revisit cycles such as ESA's ASAR onboard ENVISAT (Karnevi et al., 1994), the *Starlite* concept (Fulghum and Anselmo, 1997), and NASA's LightSAR (Hilland et al., 1998).

One of the most exciting results concerning InSAR is the establishment of a new discipline: polarimetric interferometry (Cloude and Papathanassiou, 1997, 1998; Hellman et al., 1997; Papathanassiou and Cloude, 1997). Coherence study using multi-polarization SAR and InSAR system are still under development due to the lack of data sources currently, but will be increased with the arrival of new SAR systems in the near future.

References

- Ahmed, S., Warren, H. R., Symonds, D., and Cox, R. P., 1990. The Radarsat System, *IEEE Transactions on Geoscience and Remote Sensing*, vol. 28, no. 4, pp. 598-602.
- Ahrens, C. D., 1994. *Meteorology Today: An introduction to weather, climate, and the environment*, West Publishing Company, Minnesota, pp. 514-521.
- Askne, J., Dammert, P. B. G., Ulander, L. M. H., and Smith, G., 1997. C-band repeat-pass interferometric SAR observations of the forest. *IEEE Transactions on Geoscience and Remote Sensing*, vol. 35, pp. 25-35.
- Askne, J. and Hagberg, J. O., 1993. Potential of interferometric SAR for classification of land surfaces. *Proceedings of the IEEE International Geoscience and Remote Sensing Symposium (IGARSS'93), Tokyo, Japan*, pp. 985-987.
- Bamler, R., 1992. A comparison of range-Doppler and wavenumber domain SAR focusing algorithms. *IEEE Transactions on Geoscience and Remote Sensing*, vol. 30, no. 4, pp. 706-713.
- Bamler, R. and Eineder, M., 1996. ScanSAR processing using standard high precision SAR algorithms. *IEEE Transactions on Geoscience and Remote Sensing*, vol. 34, pp. 212-218.
- Bamler, R. and Hartl, P., 1998. Topical review – synthetic aperture radar interferometry. *Inverse Problems*, vol. 14, pp. R1 - R54.
- Bamler, R. and Schattler, B., 1993. SAR data acquisition and image formation. *SAR Geocoding: Data and Systems*, ed. Schreier, G., Wichmann, Karlsruhe, pp. 53-102.
- Bao, M., Bruning, C., Alpers, W., 1997. Simulation of ocean waves imaging by an along-track interferometric synthetic aperture radar. *IEEE Transactions on Geoscience and Remote Sensing*, vol. 35, pp. 618 –631.
- Barber, B. C., 1985. Theory of digital imaging from orbit synthetic-aperture radar. *International Journal of Remote Sensing*, vol. 6, pp. 1009-1057.
- Bendat, J. S. and Piersol, A. G., 2000. *Random Data: Analysis and Measurement Procedures*, 3rd ed., John Wiley & Sons, Inc., New York.

- Bennet, J. R., Cumming, I. G., McConnell, P. R., and Gutteridge, L., 1981. Features of a generalized digital synthetic aperture radar processor. *15th International Symposium on Remote Sensing of the Environment, Ann Arbor, Michigan.*
- Blackledge, J. M., 1987. Theory of imaging with airborne synthetic aperture radar. *Optik*, vol. 78, pp. 1-11.
- Bonne, B. G., Scott, A. G., Shukla, O. B., and Terry, D. H., 1989. Optical processing for radar signal analysis. *Johns Hopkins APL Technical Digest*, vol. 10, pp. 14-28.
- Borgeaud, M. and Wegmuller, U., 1996. On the use of ERS SAR interferometry for the retrieval of geo- and bio-physical information. *Workshop on Applications of ERS SAR Interferometry (FRINGE96), Zurich*, <http://www.geo.unizh.ch/rsl/fringe96/>
- Born, M. and Wolf, E., 1980. *Principles of Optics*, 6th ed., Pergamon, London, pp. 203-207.
- Briole, P., Massonnet, D., and Delacourt, C., 1997. Post-eruptive deformation associated with the 1986-87 and 1989 lava flows of Etna, detected by radar interferometry. *Geophysical Research Letters*, vol. 24, pp. 37-40.
- Brown, W. M., 1967. Synthetic aperture radar. *IEEE Transactions on Aerospace and Electronic Systems*, vol. AES-3, no. 2, pp. 217-229.
- Brown, W. M. and Porcello, L. J., 1969. An introduction to synthetic aperture radar. *IEEE Spectrum*, September, pp. 52-62.
- Cafforio, C., Prati, C., and Rocca, F., 1991. Full resolution focusing of Seasat SAR images in the frequency-wavenumber domain. *International Journal of Remote Sensing*, vol. 12, pp. 491-510.
- Carande, R. E., 1994. Estimating ocean coherence time using dual-baseline interferometric synthetic aperture radar. *IEEE Transactions on Geoscience and Remote Sensing*, vol. 32, pp. 846-854.
- Carrara, W. G., Goodman, R. S., and Majewski, R. M., 1995. *Spotlight Synthetic Aperture Radar: Signal Processing Algorithms*, Artech House, Boston, MA.
- Chang, C. Y. and Curlander, J. C., 1992. Application of the multiple PRF technique to resolve doppler centroid estimation ambiguity for spaceborne SAR, *IEEE Transactions on Geoscience and Remote Sensing*, vol. 30, no. 5, pp. 941-949.

- Cloude, S. R. and Papathanassiou, K. P., 1997. Coherence optimisation in polarimetric SAR interferometry. *Proceedings of the IEEE International Geoscience and Remote Sensing (IGARSS'97), Singapore*, vol. 4, pp. 1932 –1934.
- Cloude, S. R. and Papathanassiou, K. P., 1998. Polarimetric SAR interferometry. *IEEE Transactions on Geoscience and Remote Sensing*, vol. 36, no. 5, pp. 1551 –1565.
- Cook, C. E. and Bernfeld, M., 1967. *Radar Signals*, Academic Press, New York.
- Corr, D. G. and Whitehouse, S. W., 1996. Automatic change detection in spaceborne SAR imagery. *Proceedings of AGARD Conference - Remote Sensing: a Valuable Source of Information*, AGARD-CP-582, paper no. 39, NATO.
- Costantini, M., 1998. A novel phase unwrapping method based on network programming. *IEEE Transactions on Geoscience and Remote Sensing*, vol. 36, no. 3, pp. 813 –821.
- Cumming, I. G., Guo, Y., and Wong, F., 1997. A comparison of phase-preserving algorithms for burst-mode SAR data processing. *Proceedings of the IEEE International Geoscience and Remote Sensing Symposium (IGARSS'97), Singapore*, pp. 731-733.
- Curlander, J., 1982. Location of spaceborne SAR imagery. *IEEE Transactions on Geoscience and Remote Sensing*, vol. GE-20, pp. 359-364.
- Curlander, J. C. and McDonough, R. N., 1991. *Synthetic Aperture Radar Systems and Signal Processing*, John Wiley & Sons Inc., New York.
- Curlander, J. C., Wu, C., and Pang, A., 1982. Automated preprocessing of spaceborne SAR data. *Proceedings of the IEEE International Geoscience and Remote Sensing Symposium (IGARSS'82), Munich*, pp. FA-1-3 – 1-6.
- Davidson, G. W. and Bamler, R., 1999. Multiresolution phase unwrapping for SAR interferometry. *IEEE Transactions on Geoscience and Remote Sensing*, vol. 37, no. 1, pp. 163 –174.
- DEOS (Delft Institute for Earth-Oriented Space Research). <http://www.deos.tudelft.nl/ers/precorbs/>
- Di Cenco, A., 1988. Strip mode processing of spotlight synthetic aperture radar. *IEEE Transactions on Aerospace and Electronic Systems*, vol. 24, pp. 225-230.

- DMAAC, 1981. *Tactical Pilotage Chart of Algeria, Libya Series TPC*, sheet H-3D, ed. 1. Scale 1:500,000. Defence Mapping Agency Aerospace Center, Missouri.
- Duchossois, G. and Martin, P., 1995. ERS-1 and ERS-2 tandem operations. *ESA Bulletin*, vol. 83, pp. 54-60.
- Elachi, C., Im, E., Roth, L. E., and Werner, C. L., 1991. Cassini Titan Radar Mapper. *Proceedings of the IEEE*, vol. 79, pp. 867-.
- Fahnestock, M. A., Bindschadler, R., Kwok, R., and Jezek, K., 1993. Greenland ice sheet surface properties and ice dynamics from ERS-1 synthetic aperture radar imagery. *Science*, vol. 262, pp. 1530-1534.
- Farnett, E. C., Howard, T. B., and Stevens, G. H., 1970. Pulse-compression Radar. *Radar Handbook* (Skolnik, M. I., ed.), chap. 20, McGraw-Hill, New York.
- Feigl, K., Sergaent, A., and Jacq, D., 1995. Estimation of an earthquake focal mechanism from a satellite radar interferogram: application to the December 4, 1992 Landers aftershock. *Geophysical Research Letters*, vol. 22, pp. 1037-1048.
- Fornaro, G., Franceschetti, G., and Lanari, R., 1996. Interferometric SAR phase unwrapping using Green's formulation. *IEEE Transactions on Geoscience and Remote Sensing*, vol. 34, no. 3, pp. 720-727.
- Fornaro, G., Franceschetti, G., Lanari, R., Rossi, D., and Tesauro, M., 1997. Interferometric SAR phase unwrapping using the finite elements method, *IEE Proceedings - Radar, Sonar and Navigation*, vol. 144, pp. 266-.
- Franceschetti, G. and Lanari, R., 1999. *Synthetic Aperture Radar Processing*, CRC Press.
- Franceschetti, G. and Shirinzi, G., 1990. A SAR processor based on two-dimensional FFT codes. *IEEE Transactions on Aerospace Electronic Systems*, vol. AES-26, pp.356-366.
- Fulghum, D. A. and Anselmo, J. C., 1997. DARPA pitches small sats for tactical reconnaissance. *Aviation Week and Space Technology*, vol. 9, p. 29.
- Gabriel, A. K. and Goldstein, R. M., 1988. Crossed orbit interferometry: theory and experimental results from SIR-B. *International Journal of Remote Sensing*, vol. 9, pp. 857-872.

- Gabriel, A. K., Goldstein, R. M., and Zebker, H. A., 1989. Mapping small elevation changes over large area: Differential radar interferometry. *Journal of Geophysical Research*, vol. 94, no. B7, pp. 9183-9191.
- Gatelli, F., Guarnieri, A. M., Parizzi, F., Pasquali, F., Prati, C., and Rocca, F., 1994. The wavenumber shift in SAR interferometry. *IEEE Transactions on Geoscience and Remote Sensing*, vol. 32, no. 4, pp. 855-865.
- Gens, R. and Genderen, J. L. 1996. SAR interferometry - issues, techniques, applications. *International Journal of Remote Sensing*, vol. 17, no. 10, pp. 1803-1835.
- Goldstein, R. M., Engelhardt, H., Kamb, B., and Frolich, R. M., 1993. Satellite radar interferometry for monitoring ice sheet motion: Application to an Antarctic ice stream, *Science*, vol. 262, pp. 1525-1534.
- Goldstein, R. M. and Zebker, H. A., 1987. Interferometric radar measurement of ocean surface currents. *Nature*, vol. 328, pp. 707-709.
- Goldstein, R. M., Zebker, H. A., and Werner, C. L., 1988. Satellite radar interferometry: Two dimensional phase unwrapping. *Radio Science*, vol. 23, pp. 713-720.
- Goodman, J. W., 1967. Film-grain noise in wavefront-reconstruction imaging. *Journal of Optical Society of America*, vol. 57, pp. 493-502.
- Goodman, J. W., 1975. Statistical properties of laser speckle patterns. *Laser Speckle and Related Phenomena*, Springer-Verlag, Berlin, pp. 29-35.
- Gough, P. T. and Hawkins, D. W., 1997. Unified framework for modern synthetic aperture imaging algorithms. *International Journal of Imaging Systems and Technology*, vol. 8, pp. 343-358.
- GPCC, 1998. The Global Precipitation Climatology Centre. <http://www.dwd.de/research/gpcc>
- Graham, L. C., 1974. Synthetic interferometer radar for topographic mapping. *Proceedings of the IEEE*, vol. 62, 763-768.
- Hagberg, J. O., Ulander, L. M. H., and Askne, J., 1995. Repeat-pass SAR-interferometry over forested terrain. *IEEE Transactions on Geoscience and Remote Sensing*, vol. 33, no. 2, pp. 331-340.

- Harger, R. O., 1970. *Synthetic Aperture Radar Systems: Theory and Design*, Academic, New York.
- Harris, F. J., 1978. On the use of windows for harmonic analysis with the discrete Fourier Transform. *Proceedings of the IEEE*, vol. 66, no. 1, pp. 51-83.
- Hartl, P., Thiel, K-H., and Wu, X., 1994. Information extraction from ERS-1 SAR data by means of InSAR and D-InSAR techniques in Antarctic research. *Proceedings of the Second ERS-1 Symposium, Hamburg, Germany*, pp. 697-701.
- Harvey, A. M., 1984. Geomorphological response to an extreme flood: a case from Southeast Spain. *Earth Surface Processes and Landforms*, vol. 9, pp. 267-279.
- Harvey, A. M., 1987. Patterns of Quaternary aggradational and dissectional landform development in the Almeria region, southeast Spain: a dry-region, tectonically active landscape. *Regionaler Beitrag*, vol. 118, pp. 193-215.
- Haykin, S., 1985. Radar signal processing. *IEEE Acoustics, Speech and Signal Processing Magazine*, April, pp. 2-18.
- Hellman, M., Cloude, S. R., Papathanassiou, K. P., 1997. Classification using polarimetric and interferometric SAR-data. *Proceedings of the IEEE International Geoscience and Remote Sensing Symposium (IGARSS'97), Singapore*, vol. 3, pp. 1411 –1413.
- Hilland, J. E., Stuhr, F. V., Freeman, A., Imel, D., Shen, Y., Jordan, R. L., and Caro, E. R., 1998. Future NASA spaceborne SAR missions. *IEEE Aerospace and Electronic Systems Magazine*, vol. 13, issue 11, pp. 9-16.
- Hilton, F. I., 2000. *An integrated remote sensing-GIS study of rapid erosion in southeast Spain using ERS SAR multi-temporal coherence imagery*, unpublished MSc. Dissertation, University of London.
- Hulst, H. C., 1957. *Light Scattering by Small Particles*, John Wiley and Sons, Inc., New York.
- ICA, 1997a. Provincia de Almeria, *Mapa Topográfico de Andalucía, 1:10,000*, Instituto de Cartografía de Andalucía, (CD-ROM, ISBN: 84-8095-125-7).
- ICA, 1997b. Provincia de Granada, *Mapa Topográfico de Andalucía, 1:10,000*, Instituto de Cartografía de Andalucía, (CD-ROM, ISBN: 84-8095-125-7).

- Ichoku, C., Karnieli, A., Arkin, Y., Chorowicz, J., Fleury, T., and Rudant, J. P., 1998. Exploring the utility potential of SAR interferometric coherence images. *International Journal of Remote Sensing*, vol. 19, no. 6, pp. 1147-1160.
- IGME, 1970. *Mapa Geologico de Espana, 1:200,000 – Jaen*, sheet 77, Instituto Geológico y Minero de España.
- IGME, 1975a. *Mapa Geologico de Espana, 1:50,000 – Sorbas*, sheet 1031, Instituto Geológico y Minero de España.
- IGME, 1975b. *Mapa Geologico de Espana, 1:50,000 – Tabernas*, sheet 1030, Instituto Geológico y Minero de España.
- Ito, Y., Hosokawa, M., Lee, H., and Liu, J. G., 2000. Extraction of damaged regions using SAR data and neural networks. *XIXth International Society for Photogrammetry and Remote Sensing (ISPRS) Congress, Amsterdam, The Netherlands*, vol. XXXIII, part B1, pp. 156-163.
- Jin, M. Y. and Wu, C., 1984. A SAR correlation algorithm which accommodates large-range migration. *IEEE Transactions on Geoscience and Remote Sensing*, vol. GE-22, pp. 592-597.
- Joughin, I. R. and Winebrenner, D. P., 1994. Effective number of looks for a multilook interferometric phase distribution. *Proceedings of the IEEE International Geoscience and Remote Sensing Symposium (IGARSS'94), Pasadena, California*, pp. 2276-2278.
- Joughin, I. R., Winebrenner, D. P., and Fahnestock, M. A., 1995. Observation of complex ice-sheet motion in Greenland using satellite radar interferometry. *Geophysical Research Letters*, vol. 22, pp. 571-574.
- Joughin, I. R., Winebrenner, D. P., and Percival, D. B., 1994. Probability density functions for multi-look polarimetric signatures. *IEEE Transactions on Geoscience and Remote Sensing*, vol. 32, pp. 562-574.
- Just, D. and Bamler, R., 1994. Phase statistics of interferograms with applications to synthetic aperture radar. *Applied Optics*, vol. 33, no. 20, pp. 4361-4368.
- Karnevi, S., Dean, E., Carter, D. J. Q., and Hartley, S. S., 1994. Envisat's advanced synthetic aperture radar: ASAR. *ESA Bulletin*, vol. 76, pp. 30-35.
- Kreyszig, E., 1988. *Advanced Engineering Mathematics*, 6th ed. John Wiley & Sons, Inc.

- Kwock, R. and Fahnestock, M. A., 1996. Ice sheet motion and topography from radar interferometry. *IEEE Transactions on Geoscience and Remote Sensing*, vol. 34, pp. 189-220.
- Lee, H. and Liu, J. G., 1999. Spatial decorrelation due to the topography in the interferometric SAR coherence imagery. *Proceedings of the IEEE International Geoscience and Remote Sensing Symposium (IGARSS'99), Hamburg, Germany*, vol. 1, pp. 485-487.
- Lee, H. and Liu, J. G., 2000a. Analysis of topographic decorrelation in SAR interferometry using ratio coherence imagery. *IEEE Transactions on Geoscience and Remote Sensing*, accepted for publication.
- Lee, H. and Liu, J. G., 2000b. Topographic phase corrected coherence estimation using multi-pass differential SAR interferometry: differential coherence. *Proceedings of the IEEE International Geoscience and Remote Sensing Symposium (IGARSS2000), Honolulu, Hawaii*, vol. 2, pp. 776-778.
- Lee, J. S., Hoppel, K. W., Mango, S. A., and Miller, A. R., 1994. Intensity and phase statistics of multilook polarimetric and interferometric SAR imagery. *IEEE Transactions on Geoscience and Remote Sensing*, vol. 32, no. 5, pp. 1017-1028.
- Li, F. K. and Goldstein, R. M., 1990. Studies of multibaseline spaceborne interferometric synthetic aperture radars. *IEEE Transactions on Geoscience and Remote Sensing*, vol. 28, no. 1, pp. 88-97.
- Li, F. K. and Johnson, W. T. K., 1983. Ambiguities in spaceborne synthetic aperture radar systems. *IEEE Transactions on Aerospace and Electronic Systems*, vol. AES-19, pp. 389-97.
- Liu, J. G., Black, A., Lee, H., Hanaizumi, H., and Moore, J. M., 1999a. Change detection and interpretation in a desert area using multi-temporal ERS SAR coherence images. *Proceedings of the 13th International Conference and Workshop on Applied Geological Remote Sensing (ERIM), Vancouver, Canada*, 1-3 March, 1999, pp. 263-270.
- Liu, J. G., Black, A., Lee, H., Hanaizumi, H., and Moore, J. M., 1999b. Land surface change detection in a desert area in Algeria using multi-temporal ERS SAR coherence images. *International Journal of Remote Sensing*, accepted for publication.

- Liu, J. G., Capes, R., Haynes, M., and Moore, J. M., 1997. An experiment of ERS SAR multi-temporal coherence image as a tool for sand desert study (dune movement, sand encroachment and erosion). *Proceedings of the 12th International Conference and Workshop on Applied Geological Remote Sensing (ERIM), Denver, Colorado*, vol. 1, pp. 478-485.
- Liu, J. G., Lee, H., Hu, G., and Chen, J. G., 1999c. Land subsidence in Guanzhong basin, Shanxi, China - A SAR interferometric study. *Proceedings of the International Symposium on Digital Earth, Beijing, China*, vol. 2, pp. 910 - 919.
- Liu, J. G., Lee, H., and Pearson, T., 1999d. Detection of rapid erosion in SE Spain using ERS SAR interferometric coherence imagery. *Proceedings of the EOS/SPIE Symposium on Remote Sensing, Florence, Italy, 20-24 September 1999*, vol. 3868, ch. 66, pp. 525-535.
- Liu, J. G., Lee, H., and Pearson, T., 1999e. Erosion and landuse change detection using ERS SAR interferometric coherence imagery (ESA ERS AO3-113), *Second International Workshop on ERS SAR Interferometry (Fringe '99), Liege, Belgium*, website: <http://www.esa.int/fringe99>.
- Livingstone, I., Warren, A., 1996. *Aeolian Geomorphology: An Introduction*, Addison Wesley Longman, Essex.
- Madsen, S. N., Zebker, H. A., and Martin, J., 1993. Topographic mapping using radar interferometry: Processing techniques. *IEEE Transactions on Geoscience and Remote Sensing*, vol. 31, pp. 246-256.
- Massonnet, D., Briole, P., and Arnaud, A., 1995. Deflation of mount Etna monitored by spaceborne radar interferometry. *Nature*, vol. 375, pp. 567-570.
- Massonnet, D. and Feigl, K., 1995. Satellite radar interferometric map of the coseismic deformation field of the $M=6.1$ Eureka Valley California earthquake of May 17, 1993. *Geophysical Research Letters*, vol. 22, pp. 1541-1544.
- Massonnet, D., Holzer, T., and Vadon, H., 1997. Land subsidence caused by the East Mesa geothermal field, California, observed using SAR interferometry. *Geophysical Research Letters*, vol. 24, pp. 901-904.
- Massonnet, D., Rossi, M., Carmona, C., Adragna, F., Peltzer, G., Feigl, K., and Rabaute, T., 1993. The displacement field of the Landers earthquakes mapped by radar interferometry. *Nature*, vol. 364, pp. 138-142.

- Massonnet, D., Thatcher, W., and Vadon, H., 1996a. Detection of postseismic fault zone collapse following the Landers earthquake. *Nature*, vol. 382, pp. 612-616.
- Massonnet, D., Vadon, H., Rossi, M., 1996b. Reduction of the need for phase unwrapping in radar interferometry. *IEEE Transactions on Geoscience and Remote Sensing*, vol. 34, no. 2, pp. 489–497.
- McDonough, R. N., Raff, B. E., and Kerr, J. L., 1985. Image formation from spaceborne synthetic aperture radar signals, *Johns Hopkins APL Technical Digest*, vol. 6, no. 4, pp. 300-312.
- Meyer, B., Armijo, R., Massonnet, D., de Chabali er, J. B., Delacourt, C., Ruegg, C., Achache, J., Briole, P., and Papanastassiou, D., 1996. The 1995 Grevena (Northern Greece) earthquake: Fault model constrained with tectonic observations and SAR interferometry. *Geophysical Research Letters*, vol. 23, pp. 2677-2680.
- Moore, R. K., Claassen, J. P., and Lin, Y. H., 1981. Scanning spaceborne synthetic aperture radar with integrated radiometer. *IEEE Transactions on Aerospace Electronic Systems*, vol. 17, pp. 410-420.
- Moreira, A., Mittermayer, J., and Scheiber, R., 1996. Extended chirp scaling algorithm for air- and spaceborne SAR data processing in stripmap and ScanSAR image modes. *IEEE Transactions on Geoscience and Remote Sensing*, vol. 34, pp. 1123-1136.
- Munson, D. C., O'Brien, J. D., and Jenkins, W. K., 1983. A tomographic formulation of spotlight-mode synthetic aperture radar. *Proceedings of the IEEE*, vol. 71, pp. 917-925.
- Nesti, G., Tarchi, D., Despan, D., Rudant, J. P., Bedidi, A., Borderies, P., and Bachelier, E., 1998. Phase shift and decorrelation of radar signal related to soil moisture changes. *Proceedings of the 2nd International Workshop on Retrieval of Bio- & Geo-physical Parameters from SAR Data for Land Applications (ESTEC), Noordwijk, The Netherlands, ESA SP-441*, pp. 423- 430.
- Olmsted, C., 1993. *Alaska SAR Facility – Scientific SAR User’s Guide*, Alaska SAR Facility, ASF-SD-003.
- Papathanassiou, K. P. and Cloude, S. R., 1997. Polarimetric effects in repeat-pass SAR interferometry. *Proceedings of the IEEE International Geoscience and Remote Sensing Symposium (IGARSS'97), Singapore*, pp. 1926-1928.

- Papoulis, A., 1991. *Probability, Random Variables, and Stochastic Processes*. 3rd ed., McGraw-Hill, Inc.
- Pearson, T. D., 1999. *Land surface change detection using ERS-SAR coherence imagery in southeast Spain*, unpublished MSc. Dissertation, University of London.
- Pearson, T. D., Liu, J. G., and Lee, H., 2000. Detection of rapid erosion in southeast Spain using ERS SAR interferometric coherence imagery. *The Remote Sensing Society Newsletter, February 2000*.
- Pettengill, G. H., Campbell, D. B., and Masursky, H., 1980. The surface of Venus. *Scientific American*, vol. 243, pp. 54-65.
- Prati, A. and Rocca, F., 1993. Improving slant range resolution of stationary objects with multiple SAR surveys. *IEEE Transactions on Aerospace Electronic Systems*, vol. 29, pp. 135-144.
- Prati, C., Rocca, F., and Guarnieri, A. M., 1989. Effect of speckle and additive noise on the altimetric resolution of interferometric SAR (ISAR) surveys. *Proceedings of the IEEE International Geoscience and Remote Sensing Symposium (IGARSS'89), Vancouver, Canada*, pp. 2469-2472.
- Pritt, M. D., 1996. Phase unwrapping by means of multigrid techniques for interferometric SAR. *IEEE Transactions on Geoscience and Remote Sensing*, vol. 34, no. 3, pp. 728 –738.
- Pritt, M. D. and Shipman, J. S., 1994. Least-squares two-dimensional phase unwrapping using FFT's. *IEEE Transactions on Geoscience and Remote Sensing*, vol. 32, no. 3, pp. 706 –708.
- Raney, R. K., 1980. SAR processing of partially coherent phenomena. *International Journal of Remote Sensing*, vol. 1, pp. 29-51.
- Raney, R. K., 1982. Processing synthetic aperture radar data. *International Journal of Remote Sensing*, vol. 3, pp. 243-257.
- Raney, R. K., Runge, H., Bamler, R., Cumming, I. G., and Wong, F. H., 1994. Precision SAR processing using chirp scaling. *IEEE Transactions on Geoscience and Remote Sensing*, vol. 32, pp. 786-799.

- Raney, R. K. and Vachon, P. W., 1988. Synthetic aperture radar imaging of ocean waves from an airborne platform: focus and tracking issues. *Journal of Geophysical Research*, vol. 93, pp. 475-486.
- Raymond, D., and Rudant, J-P., 1997. ERS-SAR interferometry; potential and limits for mining subsidence detection. *3rd ERS Workshop (Florence'97)*, Florence, Italy, <http://earth.esa.int/florence/papers/>.
- Reigber, C., Xia, Y., Michel, G. W., Klotz, J., and Angermann, D., 1997. The Antofagasta 1995 earthquake: Crustal deformation patterns as observed by GPS and D-InSAR. *3rd ERS Workshop (Florence'97)*, Florence, Italy, <http://earth.esa.int/florence/papers/>.
- Rignot, E. J. M. and van Zyl, J. J., 1993. Change detection techniques for ERS-1 SAR data. *IEEE Transactions on Geoscience and Remote Sensing*, vol. 31, no. 4, pp. 896-906.
- Rodriguez, E. J. and Martin, M., 1992. Theory and design of interferometric synthetic aperture radars. *IEE Proceedings Part F Radar and Signal Processing*, vol. 139, no. 2, pp. 147-159.
- Rogers, A. E. E. and Ingalls, R. P., 1969. Venus: Mapping the surface reflectivity by radar interferometry. *Science*, vol. 165, pp. 797-799.
- Rosen, P. A., Hensley, S., Zebker, H. A., Webb, F. H., and Fielding, E. J., 1996. Surface deformation and coherence measurements of Kilauea volcano, Hawaii, from SIR-C radar interferometry. *Journal of Geophysical Research*, vol. 23, pp. 109-125.
- Roth, A., Adam, N., Schwäbisch, M., Müschen, B., Böhm, C., and Lang, O., 1997. Observation of the effects of the subglacial volcano eruption underneath the Vatnajökull glacier in Iceland with ERS-SAR data. *3rd ERS Workshop (Florence'97)*, Florence, Italy, <http://earth.esa.int/florence/papers/>.
- Roth, L. E. and Wall, S. D., 1995. *The Face of Venus, the Magellan Radar-Mapping Mission*, NASA, Washington, D.C.
- Rouse, J. W., Haas, R. H., Schell, J. A., and Deering, D. W., 1974. Monitoring vegetation systems in the great plains with ERTS. *3rd ERTS Symposium*, NASA, vol. SP-351, no. 1, pp. 309-317.
- Rudolf, B., Hauschild, H., Rueth, W., and Schneider, U., 1994. Terrestrial precipitation analysis: Operational method and required density of point measurements. In: *Global*

- Precipitations and Climate Change* (Ed. M. Desbois, F. Desalmond), NATO ASI Series I, Vol. 26, Springer-Verlag, p. 173-186.
- Runge, H. and Bamler, R., 1992. A novel high precision SAR focusing algorithm based on chirp scaling. *Proceedings of the IEEE International Geoscience and Remote Sensing Symposium (IGARSS'92), Houston, TX*, pp. 372-375.
- Sarabandi, K., 1992. Derivation of phase statistics from the Mueller matrix. *Radio Science*, vol. 27, pp. 553-560.
- Sarabandi, K., 1997. Δk equivalent of interferometric SAR's: A theoretical study for determination of vegetation height. *IEEE Transactions on Geoscience and Remote Sensing*, vol. 35, pp. 1267-1276.
- Scharroo, R. and Visser, P. N. A. M., 1998. Precise orbit determination and gravity field improvement for the ERS satellites. *Journal of Geophysical Research*, vol. 103, C4, pp. 8113-8127.
- Scheuer, T. E. and Wong, F. H., 1991. Comparison of SAR processors based on a wave equation formulation. *Proceedings of the IEEE International Geoscience and Remote Sensing Symposium (IGARSS'91)*, pp. 635-639.
- Schwäbisch, M., Lehner, S., and Winkel, N., 1997. Coastline extraction using ERS SAR interferometry. *3rd ERS Symposium (Florence'97), Florence, Italy*, <http://earth.esa.int/florence/papers/>.
- Seymour M. S. and Cumming, I. G., 1996. An iterative algorithm for ERS baseline estimation. *The ERS Fringe Workshop on SAR Interferometry (Fringe'96), Zurich, Switzerland*, <http://www.geo.unizh.ch/rsl/fringe96/papers/seymour-cumming>.
- Sherwin, C. W, Ruina, J. P., and Rawcliffe, R. D., 1962. Some early developments in synthetic aperture radar systems. *IRE Transactions on Military Electronics*, vol. MIL-6, pp. 111-115.
- Singh, K., Stussi, N., Kwong, K. L., and Hock, L., 1997. Baseline estimation in interferometric SAR. *3rd ERS symposium (Florence'97), Florence, Italy*, <http://earth.esa.int/florence/papers/>.
- Smith, A., 1998a. *Phoenix Systems – Pulsar User Guide*, Phoenix Systems and Associates Ltd., Surrey, UK.

- Smith, A., 1998b. *Phoenix Systems – InSAR Toolkit User Guide*, Phoenix Systems and Associates Ltd., Surrey, UK.
- Smith, L. C. and Alsdorf, D. E., 1997. Flood monitoring from tandem ERS phase coherence maps: Ob River, Siberia. *3rd ERS Symposium (Florence'97)*, Florence, Italy, <http://earth.esa.int/florence/papers/>.
- Spagnolini, U., 1995. 2-D phase unwrapping and instantaneous frequency estimation. *IEEE Transactions on Geoscience and Remote Sensing*, vol. 33, no. 3, pp. 579–589.
- Tarayre, H. and Massonnet, D., 1994. Effects of a refractive atmosphere on interferometric processing. *Proceedings of the IEEE International Geoscience and Remote Sensing Symposium (IGARSS'94)*, Pasadena, California, pp. 717-719.
- The Weather Underground, Inc., <http://www.wunderground.com>.
- Thiel, K-H., Hartl, P., and Wu, X., 1995. Monitoring the ice movement with ERS SAR interferometry in the Antarctic region. *2nd ERS Application Workshop, London*.
- Thiel, K-H. and Wu, X., 1996. Monitoring ice movement in Antarctica. *Sixth International Offshore and Polar Engineering Conference, Los Angeles, CA*, pp. 401-405.
- Thiel, K-H., Wu, X., and Hartl, P., 1997. ERS-Tandem interferometric observation of volcano activities in Iceland. *3rd ERS Workshop (Florence'97)*, Florence, Italy, <http://earth.esa.int/florence/papers/>.
- Tomiyasu, K., 1978. Tutorial review of synthetic-aperture radar (SAR) with applications to imaging of the ocean surface. *Proceedings of the IEEE*, vol. 66, pp. 563-583.
- Tomiyasu, K., 1981. Conceptual performance of a satellite borne, wide swath synthetic aperture radar. *IEEE Transactions on Geoscience and Remote Sensing*, vol. GE-19, pp. 108-116.
- Tough, R. J. A., 1991. Interferometric detection of sea ice surface features. *Memorandum 4446 Royal Signals and Radar Establishment, UK*.
- Touzi, R. and Lopes, A., 1996. Statistics of the Stokes parameters and the complex coherence parameters in one-look and multilook speckle fields. *IEEE Transactions on Geoscience and Remote Sensing*, vol. 34, pp. 519-531.

- Touzi, R., Lopes, A., Bruniquel, J., and Vachon, P. W., 1999. Coherence Estimation for SAR Imagery. *IEEE Transactions on Geoscience and Remote Sensing*, vol. 37, no. 1, pp. 135-149.
- Trouve, E., Nicolas, J. M., and Maitre, H., 1998. Improving phase unwrapping techniques by the use of local frequency estimates. *IEEE Transactions on Geoscience and Remote Sensing*, vol. 36, no. 6, pp. 1963–1972.
- Ulaby, F. T., Moore, R. K., and Fung, A. K., 1981. *Microwave Remote Sensing, Active, and Passive, Volume I: Microwave Remote Sensing Fundamentals and Radiometry*, Addison-Wesley, Reading, MA.
- Ulaby, F. T., Moore, R. K., and Fung, A. K., 1982. *Microwave Remote Sensing, Active, and Passive, Volume II: Radar Remote Sensing and Surface Scattering and Emission Theory*, Addison-Wesley, Reading, MA.
- Ulaby, F. T., Moore, R. K., and Fung, A. K., 1986. *Microwave Remote Sensing, Active, and Passive, Volume III: From Theory to Applications*, Artech House, Dedham, MA.
- Ulander, L. M. H., 1996. Radiometric slope correction of synthetic-aperture radar images. *IEEE Transactions on Geoscience and Remote Sensing*, vol. 34, no. 5, pp. 1115–1122.
- Walker, 1980. Range-Doppler imaging of rotating objects. *IEEE Transactions on Aerospace Electronic Systems*, vol. 16, pp. 23-52.
- Wegmuller, U. and Werner, C. L., 1997. Retrieval of vegetation parameters with SAR interferometry. *IEEE Transactions on Geoscience and Remote Sensing*, vol. 35, pp. 18-24.
- Wegmuller, U., Werner, C. L., Nuesch, D., and Borgeaud, M., 1995. Landsurface analysis using ERS-1 SAR interferometry. *ESA Bulletin*, vol. 81, pp. 30-37.
- Werner, C. L., Wegmuller, U., Small, D. L., and Rosen, P. A., 1993. Applications of interferometrically derived terrain slopes: Normalization of SAR backscatter and the interferometric correlation coefficient. *Proceedings of the Second ERS-1 Symposium, Hamburg, Germany*, pp. 723-726.
- Whalen, A. D., 1971. *Detection of Signals in Noise*, Academic Press, New York.
- Wu, C., Barkan, B., Karplus, W. J., and Caswell, D., 1982a. Seasat synthetic-aperture radar data reduction using parallel programmable array processors. *IEEE Transactions on Geoscience and Remote Sensing*, vol. GE-20, no. 3, pp. 352-358.

- Wu, C., Liu, K. Y., and Jin, M., 1982b. Modeling and a correlation algorithm for spaceborne SAR signals. *IEEE Transactions on Aerospace Electronic Systems*, vol. AES-18, pp. 563-574.
- Wu, X., Thiel, K-H., and Hartl, P., 1997. Estimating ice changes by SAR interferometry. *3rd International Airborne Remote Sensing Conference and Exhibition, Copenhagen*, pp. 110-117.
- Xu, W. and Cumming, I., 1999. A region-growing algorithm for InSAR phase unwrapping. *IEEE Transactions on Geoscience and Remote Sensing*, vol. 37, no. 1, pp. 124 –134.
- Xu, W. and Massonnet, D., 1997. Comments on “Reduction of the need for phase unwrapping in radar interferometry”. *IEEE Transactions on Geoscience and Remote Sensing*, vol. 35, no. 4, pp. 1073 –1074.
- Zebker, H. A. and Goldstein, R. M., 1986. Topographic mapping from interferometry Synthetic Aperture Radar observations. *Journal of Geophysical Research*, vol. 91, pp. 4993-4999.
- Zebker, H. A., Rosen, P. A., Goldstein, R. M., Gabriel, A., and Werner, C. L., 1994a. On the derivation of coseismic displacement fields using differential radar interferometry: The Landers earthquake. *Journal of Geophysical Research*, vol. 99, no. B10, pp. 19617-19634.
- Zebker, H. A., Madsen, S. N., Martin, J., Sheeler, K. B., Miller, T., Lou, Y., Alberti, G., Vettorella, S., and Cucci, A., 1992. The TOPSAR interferometric radar topographic mapping instrument. *IEEE Transactions on Geoscience and Remote Sensing*, vol. 30, pp. 933-940.
- Zebker, H. A. and Villasenor, J., 1992. Decorrelation in interferometric radar echoes. *IEEE Transactions on Geoscience and Remote Sensing*, vol. 30, no. 5, pp. 950-959.
- Zebker, H. A., Werner, C. L., Rosen, P. A., and Hensley, S., 1994b. Accuracy of topographic maps derived from ERS-1 interferometric radar. *IEEE Transactions on Geoscience and Remote Sensing*, vol. 32, no. 4, pp. 823-836.

Appendix A. Mathematical Symbols

| Symbol | Description | Units |
|---------------------------------|---|----------|
| A | A constant ($= c/\lambda RB_v$) | m^{-1} |
| B | Baseline | m |
| B_μ | Azimuth (Doppler) bandwidth | Hz |
| B_v | Range (chirp) bandwidth | Hz |
| $B_{//}$ | Baseline parallel component | m |
| B_\perp | Baseline perpendicular component | m |
| $B_{\perp,c}$ | Critical baseline perpendicular component | m |
| $B_{\perp,c}^0$ | Critical baseline perpendicular component on flat surface | m |
| c | Speed of light $= 2.998 \times 10^8$ | m/s |
| D | Antenna length in range direction | m |
| $E[\]$ | Mathematical expectation operator | |
| f | Frequency | Hz |
| f_c | Carrier frequency | Hz |
| f_{Dc} | Doppler centroid frequency | Hz |
| f_p | Pulse repetition frequency (PRF) | Hz |
| f_R | Doppler rate | Hz/s |
| f_ϕ | Interferometric phase fringe frequency ($= \nu_0$) | Hz |
| $\hat{g}(s x_c, R_c)$ | Range compressed complex data at (x_c, R_c) | |
| H | Altitude | m |
| H_1, H_2 | System transfer function | |
| I_1, I_2 | Image intensity | |
| K | Frequency rate of linear FM waveform (chirp rate) | Hz/s |
| k_c^{sim} | Critical topographic phase fringe number of simulation | m^{-1} |
| $k_m^{sim}, k_n^{sim}, k^{sim}$ | Simulated topographic phase fringe number in pixel | m^{-1} |

| | | |
|------------------|--|-----------------|
| k_ϕ | Interferometric phase fringe number | m^{-1} |
| k_{ϕ_0} | System geometric phase fringe number | m^{-1} |
| L_a | Antenna length in azimuth direction | m |
| R | Slant range | m |
| R_c | Slant range at radar beam centre | m |
| R_g | Ground range | m |
| r_e | Earth radius | m |
| S | Azimuth integration time | s |
| s | Azimuth time (slow time) | s |
| s_c | Azimuth time at radar beam centre | s |
| t | Range time (fast time) | s |
| V_{st} | Relative speed between platform and target | m/s |
| $W(\mu), W(\nu)$ | Hamming filter in azimuth and range | |
| W_1, W_2 | Bandwidth of range (or azimuth) spectral filter | Hz |
| x | Azimuth spatial coordinate | m |
| x_c | Azimuth coordinate at radar beam centre | m |
| y | Ground range coordinate | m |
| z | Target elevation (earth centred) | m |
| α | Terrain slope | degree |
| α_c | Critical terrain slope | degree |
| β | Angle of baseline from horizon | degree |
| γ | Complex correlation coefficient | |
| ΔR | Slant range difference | m |
| Δs | Azimuth time shift | s |
| ΔT | Time separation | s |
| δR | Slant range spatial resolution, or Slant range pixel size | m |
| δs | Azimuth time resolution, or Azimuth time offset | s |
| δt | Range time resolution | s |
| δx | Azimuth spatial resolution | m |

| | | |
|--------------------------|---|--------|
| $\delta(x, y)$ | Two-dimensional Dirac delta function | |
| δy | Ground range spatial resolution | m |
| δz | Penetration depth | m |
| $\delta\theta_i$ | Difference of incidence angle | degree |
| ϵ_{10} | Azimuth misregistration | |
| ϵ_{20} | Phase error from azimuth defocusing | |
| ϵ_{11} | Residual range walk (linear range migration) | |
| ϵ_{21} | Residual range curvature (quadratic range migration) | |
| ϵ_r | Relative complex dielectric coefficient ($= \epsilon' + j\epsilon''$) | |
| ζ | Surface displacement | m |
| $\zeta(s'_c s_c, R_c)$ | Azimuth and range compressed complex data | |
| $\eta_{spatial}$ | Spatial ratio coherence | |
| $\eta_{temporal}$ | Temporal ratio coherence | |
| η_{total} | Total ratio coherence | |
| θ_d | Slope of total topographic decorrelation | |
| θ_i | Incidence angle | degree |
| θ_i^0 | Nominal incidence angle at beam centre | degree |
| $\theta_{i,c}$ | Critical incidence angle | degree |
| θ_l | Radar look angle | degree |
| θ_l^0 | Radar look angle at zero elevation | degree |
| θ_s | Squint angle | degree |
| λ | Carrier wavelength | m |
| μ | Azimuth frequency | Hz |
| μ_0 | Azimuth spectral envelope misalignment | Hz |
| μ_1, μ_2 | Centre frequency of azimuth spectral filter | Hz |
| ν | Range frequency | Hz |
| ν_0 | Range spectral envelope misalignment ($= f_\phi$) | Hz |
| ν_1, ν_2 | Centre frequency of range spectral filter | Hz |
| ρ | Coherence | |

| | | |
|---------------------|--|---|
| $\rho_{spatial}$ | Spatial decorrelation function | |
| $\rho_{surface}$ | Spatial decorrelation from surface scattering | |
| $\rho_{temporal}$ | Temporal decorrelation function | |
| ρ_{total} | Total decorrelation function | |
| ρ_{volume} | Spatial decorrelation from volume scattering | |
| σ^0 | Mean specific backscatter coefficient | |
| σ_y | rms surface motion in ground range direction | m |
| σ_z | rms surface motion in vertical direction | m |
| $\sigma_{\Delta R}$ | Coregistration error | m |
| σ_ϕ | Phase error | |
| τ_p | Radar pulse length in time | s |
| ϕ | Phase | |
| | Phase difference of InSAR image pair | |
| ϕ_0 | System geometric phase | |
| ϕ_a | Atmospheric phase | |
| ϕ_d | Differential phase (coherent surface displacement phase) | |
| ϕ_{flat} | Earth-flattened phase | |
| ϕ_{topo} | Topographic phase | |
| ψ | Phase aberration coefficient | |
| ω_c | Angular carrier frequency = $2\pi f_c$ | |

Appendix B: Abbreviations and Acronyms

| | |
|--------|---|
| ALG | Algeria SAR scene |
| ALM | Almeria SAR scene |
| ASAR | Advanced Synthetic Aperture Radar (of ESA) |
| ATI | Along-Track Interferometry |
| CCRS | Canadian Centre for Remote Sensing |
| DEOS | Delft Institute for Earth-Oriented Space Research |
| DEM | Digital Elevation Model |
| DInSAR | Differential Interferometric Synthetic Aperture Radar |
| DN | Digital Number (or Data Number) |
| EMSL | European Microwave Signature Laboratory |
| ERIM | Environmental Research Institute of Michigan |
| ERS | Earth Resources Satellite (ESA) |
| ESA | European Space Agency |
| FFT | Fast Fourier Transform |
| FM | Frequency Modulation |
| GCP | Ground Control Point |
| GRA | Granada SAR scene |
| InSAR | Interferometric Synthetic Aperture Radar |
| JERS-1 | Japanese Earth Resources Satellite (NASDA) |
| JPL | Jet Propulsion Laboratory (NASA) |
| LUT | Look Up Table |
| NASA | National Aeronautics and Space Administration (U.S.A) |
| NASDA | National Aeronautics and Space Development Agency |
| PRF | Pulse Repetition Frequency |
| RGB | Red, Green, and Blue colour composite |
| SAR | Synthetic Aperture Radar |
| SIR | Shuttle Imaging Radar |
| SLC | Single Look Complex (SAR intensity image) |
| SNR | Signal to Noise Ratio |
| VOIR | Venus Orbiting Imaging Radar |